Title
Two Tests of New Physics Using Top Quarks at the CMS Experiment

Author
Klein, Daniel

Publication Date
2018

UNIVERSITY OF CALIFORNIA SAN DIEGO

Two Tests of New Physics Using Top Quarks at the CMS Experiment

A dissertation submitted in partial satisfaction of the
requirements for the degree
Doctor of Philosophy

in

Physics

by

Daniel Stuart Klein

Committee in charge:

Professor Frank Würthwein, Chair
Professor Avraham Yagil, Co-Chair
Professor Rommie Amaro
Professor Pamela Cosman
Professor Benjamín Grinstein

2018

The dissertation of Daniel Stuart Klein is approved, and it is acceptable in quality and form for publication on microfilm and electronically:

Co-Chair

Chair

University of California San Diego

2018

DEDICATION

This dissertation is dedicated

to the memory of my grandmother, Dr. Isabelle Rapin (1927-2017).

To everyone else, a titan of pediatric neurology.

To me, one of my staunchest supporters.

EPIGRAPH

Now you see why your father
and I call it 'gradual school'.
—Mom

TABLE OF CONTENTS

LIST OF FIGURES

LIST OF TABLES

ACKNOWLEDGEMENTS

I always knew graduate school would be a long and difficult road. But I never anticipated just how much I would grow along the way, both as a scholar and a human being. The fresh young college graduate who began this PhD seven years ago feels like a different person entirely. I owe tremendous thanks to the many people who helped me learn and grow as a scientist, and to those who supported me personally, giving me the strength and endurance to see this program through to the end.

It has been a true privilege to belong to the Surf 'n' Turf group. You have all taught me the true meaning of hard work and commitment. Thank you to my advisors, Frank Würthwein and Avi Yagil, for guiding me all this way, and for never giving up on me. Thank you to the postdocs and scientists who were my day-to-day mentors: Yanjun Tu, Jacob Linacre, Sergo Jindariani, John Wood, and Hannsjörg Weber. If I've learned anything in seven years, it's only because you sat patiently by my side, passing on your knowledge and experience. To the older students, my former officemates, Ian, Ryan, and Vince, thank you for teaching me how to be a grad student, for paving the road ahead of me, and for showing me what I could accomplish if I kept working at it.

A huge thank you goes out to my parents, Anne Louise Oaklander and Max Klein. Your love and support has been indispensable, but your first-hand advice on surviving a PhD has been a godsend. To my mother-in-law, Leigh: you treated me like family from day one. Because of that, San Diego is not just a place I went to school for a while. Rather, it's become my second home. Thank you for everything. And finally, to my beloved wife, Katelyn: I could write a second dissertation on all the ways you've helped me through my PhD. You've given me superhuman levels of support through this difficult and chaotic phase of my life. You've been patient with me and all the uncertainties of the student life. You've sacrificed for my benefit. I really can't thank you enough for all of it.

Chapters 2, 3, and 4 contain material that was authored by the CMS Collaboration, which has over 4000 members. Thus, that material represents the collective contributions of thousands of scientists. The CMS-authored materials in Chapter 2 were published standalone by CERN, or in the journal JINST; those in Chapter 3 were published in Physics Letters and Physical Review D; and those in Chapter 4 were published in JHEP and EPJ.

VITA

2011	B. A. in Physics and Mathematics, Cornell University, Ithaca
2013	M. S. in Physics, University of California San Diego
2018	Ph. D. in Physics, University of California San Diego

PUBLICATIONS

“Search for top squark pair production in pp collisions at $\sqrt{s} = 13$ TeV using single lepton events”, CMS Collaboration, *JHEP* **10**, 019 (2017)

“Searches for pair production for third-generation squarks in $\sqrt{s} = 13$ TeV pp collisions”, CMS Collaboration, *Eur. Phys. Jour.* **C77**, 327 (2017)

“Measurements of $t\bar{t}$ charge asymmetry using dilepton final states in pp collisions at $\sqrt{s} = 8$ TeV”, CMS Collaboration, *Phys. Lett.* **B760**, 365 (2016)

“Measurements of $t\bar{t}$ spin correlations and top quark polarization using dilepton final states in pp collisions at $\sqrt{s} = 8$ TeV”, CMS Collaboration, *Phys. Rev.* **D93**, 052007 (2016)

“Measurements of the $t\bar{t}$ charge asymmetry using the dilepton decay channel in pp collisions at $\sqrt{s} = 7$ TeV”, CMS Collaboration, *JHEP* **04**, 191 (2014)

ABSTRACT OF THE DISSERTATION

Two Tests of New Physics Using Top Quarks at the CMS Experiment

by

Daniel Stuart Klein

Doctor of Philosophy in Physics

University of California San Diego, 2018

Professor Frank Würthwein, Chair
Professor Avraham Yagil, Co-Chair

Two related analyses of data from the CMS Experiment are presented. The first is performed using 19.5 inverse femtobarns of proton-proton collision data from CMS Run I. In this analysis, six different asymmetry variables are measured in events with top-antitop quark pairs decaying to final states with two leptons. Unfolding techniques are used to extrapolate these measurements to parton level. No deviations from the predictions of the Standard Model are found, implying the absence of any influence from physics beyond the Standard Model. The second analysis is performed using 35.9 inverse femtobarns of proton-proton collision data collected during CMS Run II. In this analysis, a search is performed for evidence of stop squark pair production and decay to single-lepton final states. Several backgrounds, including dileptonic top-pair production, are estimated using control regions in the data. No excess above the Standard Model backgrounds is found, and exclusion limits are placed on three models of stop squark pair production.

Chapter 1

Particle Physics

Particle physics is the study of the elementary particles and fundamental forces of nature. By “elementary particles” we mean the smallest, most basic building blocks of all structures in the universe. By “fundamental forces” we mean the most basic kinds of interactions between particles, from which all other known interactions in the universe arise.

This chapter will provide a simple introduction to the concepts and terminology of particle physics, with the dual goals of motivating the research in this dissertation, and of making that research understandable to readers inexperienced in particle physics. Pursuant to those goals, this introduction will focus on the concepts most relevant to the research, and will use plain, non-technical language as much as possible. These self-imposed constraints risk hiding some of the considerable beauty and richness of particle physics, so I encourage the interested reader to seek deeper explanations elsewhere.

1.1 The Standard Model

1.1.1 Description

The Standard Model (SM) is the scientific theory that describes (almost) all the fundamental particles and forces we know of and their properties. It is a relativistic quantum field theory, meaning it describes the behavior of particles at speeds up to and including the speed of light, as well as their quantum mechanical nature. The Standard Model was developed beginning in the early 1970s, through the joint efforts of theoretical and experimental physicists. Although it is not a perfect description of all known physical phenomena, it has correctly predicted numerous discoveries, cementing its place as one of the most successful physical theories of all time [1, 2].

The Standard Model describes two families of matter particles – that is to say, particles that may give rise to tangible structures at the macro scale. These two families are called quarks and leptons. In addition, it describes several force-carrying particles, as well as the Higgs boson. A sort of "periodic table" of these particles is given in Figure 1.1. A diagram showing which particles interact with which other particles is given in Figure 1.2.

Quarks

There are six quarks in the SM. In order from lightest to heaviest, these quarks are named *up, down, strange, charm, bottom,* and *top*. They are often referred to using only the first letter of their names. Up and down quarks are essential to our lives, as they make up the nuclei of atoms: ignoring short-lived quantum fluctuations, the proton is composed of two up quarks and a down quark bound together (uud), and the neutron is composed of one up quark and two down quarks bound together (udd). The four heavier quarks tend to decay into lighter quarks within a fraction of a second, so they are generally not found in everyday matter. The up, charm, and top quarks all have a positive charge with $\frac{2}{3}$ the magnitude of the electron's charge, and the down, strange, and bottom quarks have a negative charge that is $\frac{1}{3}$ that of the electron.

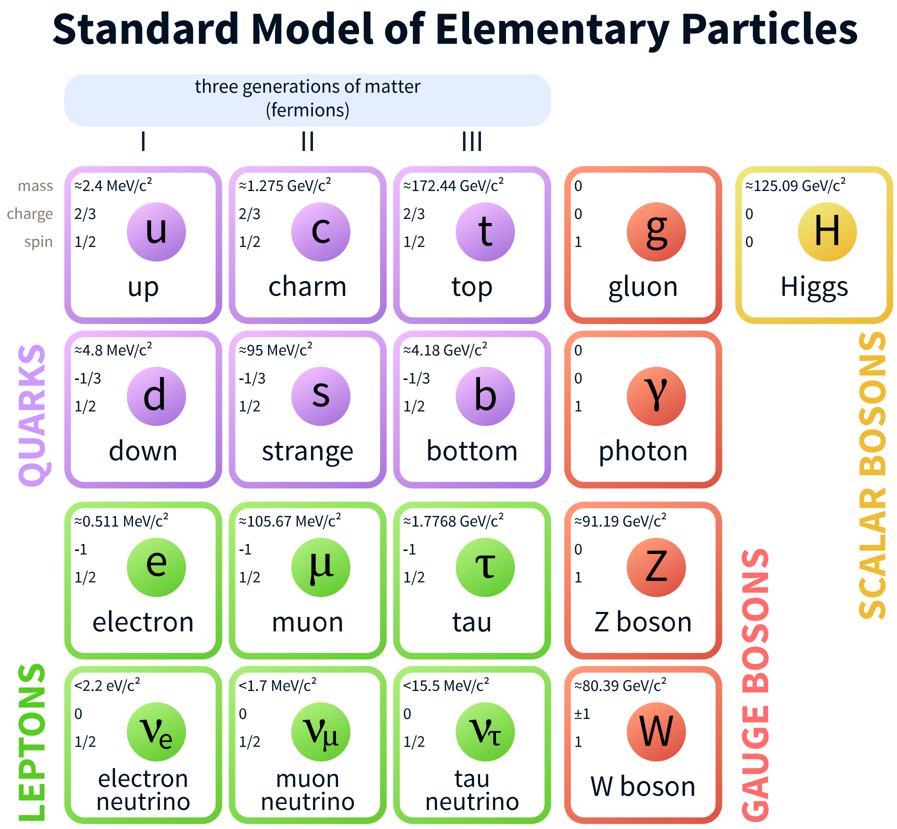

Figure 1.1: A diagram of all the particles of the Standard Model, grouped into families of related particles. Mass measurements are constantly being improved, so the listed mass values may not reflect the latest and best measurements.

The top quark has several unique properties that make it important in particle physics. Not only is it the heaviest quark, but it is also the heaviest elementary particle we know of, with a measured mass of approximately 173 giga-electron volts (GeV). This figure is comparable to the mass of an entire tungsten atom, which contains a multitude of quarks and electrons. For comparison, the mass of the up quark is only about 2.2 mega-electron volts (MeV) [3]. In addition, when the top quark decays, it has a 96% chance of decaying into a bottom quark and a W boson, and it decays more rapidly than any other quark [3]. Few other particles have such predictable decay products. The reasons why these properties are so important will be articulated in Section 3.1.

Leptons

There are three defining members of the lepton family. In order of increasing mass, they are: the electron (e^-), the muon (μ^-), and the tau (τ^-). As their symbols denote, these leptons each have a negative electric charge. They are often referred to collectively as the charged leptons. The electron is well known as the part of an atom responsible for the majority of its chemical interactions with other atoms. Muons and taus tend to decay within a fraction of a second, so they also tend not to be found in everyday matter. However, muons are often produced in Earth's upper atmosphere due to bombardment by cosmic rays (particles streaming in from outer space) [1].

For each charged lepton, there is a corresponding particle called a neutrino. They are the electron neutrino (ν_e), the muon neutrino (ν_μ), and the tau neutrino (ν_τ). As their name suggests, neutrinos are electrically neutral - they have no charge. In addition, neutrinos have extremely small masses. In fact, the SM considers them to be massless particles, though experimental results show they have non-zero masses of less than one electron volt (eV) [3]. Neutrinos also have an extremely small probability of interacting with matter. In practice, this makes neutrinos difficult or impossible to detect. The experimental implications of this difficulty will be described in Section 2.4.2.

Force Carriers

The Standard Model describes four force-carrying particles. These particles are the physical manifestations, or *quanta*, of the forces they convey. In general, matter particles interact with other matter particles through the force-carriers. However, not all particles are able to interact with all forces.

The photon (γ), commonly known as the particle of light, is in fact the quantum of the electromagnetic force. Thus every time two particles interact electrically or magnetically, they do so by exchanging photons. Only particles that have a non-zero electric charge can interact electromagnetically. Thus we say the photon *couples to* charged particles. All quarks, as well as

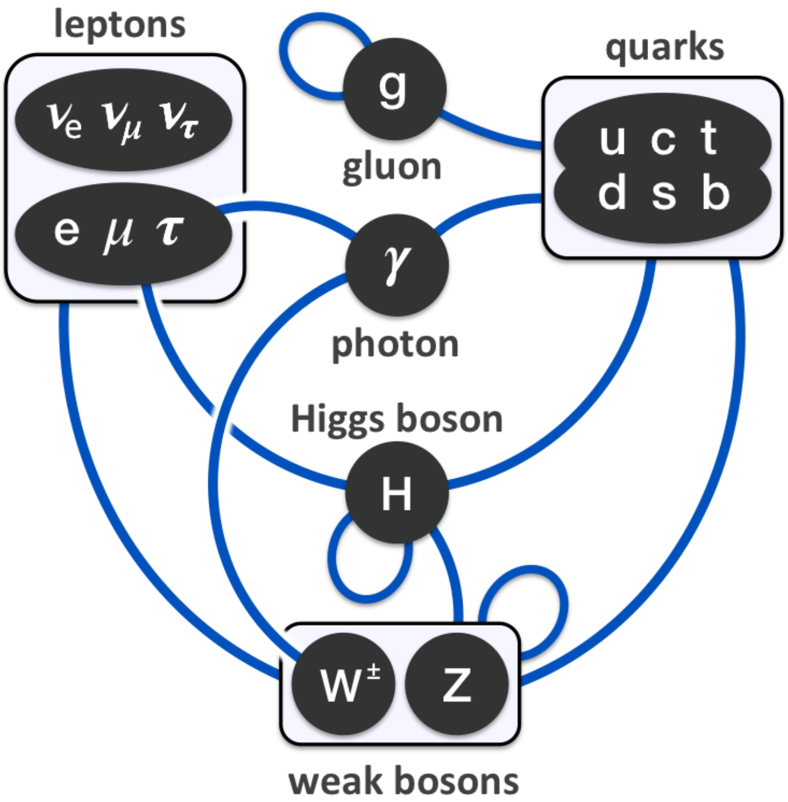

Figure 1.2: A diagram of the interactions, or couplings, between the particles of the Standard Model. Particles or groups of particles connected by blue lines are able to interact with each other.

the charged leptons, carry electric charge. The photon travels at the speed of light, and has no mass or electric charge.

The gluon (g) is the carrier of the strong nuclear force. The strong force is responsible for binding together quarks to form protons, neutrons, and other composite particles (known collectively as *hadrons*). This same interaction also binds protons and neutrons together into atomic nuclei. Gluons couple to any particle that has so-called *color charge*, namely quarks and other gluons. Although gluons are in principle massless, the energy of their collective interactions actually makes up more than 98% of the mass of protons and neutrons [4].

The strong force has a unique property that is of great importance experimentally. When two particles (usually quarks) connected via the strong force are pulled apart, the energy of the bond increases with the separation distance, like a spring or rubber band. When the bond energy is great enough, it becomes energetically favorable for additional quarks and gluons to be created out of the vacuum and form shorter bonds with the original particles. In practice, this means that single quarks or gluons separated from their bound states will produce sprays of hadrons as they recruit new fellows to keep their bond lengths short. We refer to these hadronic sprays as *jets*.

The W and Z bosons (W^+, W^-, Z) carry the weak nuclear force. The best known instance of this force is radioactive β-decay, which is mediated by the W boson. In fact, the W boson mediates all Standard Model processes where a quark or lepton changes flavor [1]. Particle physicists know the Z boson best for its role in the Drell-Yan process, where pairs of quarks convert into pairs of charged leptons. The W and Z bosons couple to all matter particles. In addition, they are capable of coupling to each other, though such interactions are rare. The W bosons have a mass of around 80 GeV, and the Z boson has a mass of around 91 GeV [3].

One more force of nature is conspicuous by its absence from the Standard Model: gravity. Although gravity is the most apparent force of nature in our everyday lives, and was the first to be described mathematically, the Standard Model is still unable to incorporate the workings of gravity. Einstein's general theory of relativity does a marvelous job describing gravity on the scale of large objects, such as stars and galaxies. However, physicists have so far been unable to formulate a theory of gravity consistent with quantum mechanics, a necessary step to incorporate gravity into the Standard Model.

Higgs Boson

The Higgs boson is neither a force-carrying particle nor a matter particle, but something else entirely. It is the manifestation, or quantum, of the Higgs field, a field that permeates the entire universe, and endows mass upon most elementary particles [5, 6, 7]. For example, the top quark is so massive because it couples very strongly to the Higgs field. Similarly, the photon is massless because it does not couple to the Higgs field at all. The Higgs boson was discovered in 2012, and measured to have a mass of about 125 GeV [8]. Thus the Higgs must also couple to itself.

Spin

All particles (both elementary and composite) have a property known as spin. Spin is an intrinsic property, just like mass or electric charge. But unlike those properties, spin is quantum mechanical in nature. All particles can be divided into two categories based on their intrinsic spin: particles whose spin is an integer (0, 1, 2, 3,...) are called *bosons*, and particles whose spin is a half-integer ($\frac{1}{2}, \frac{3}{2}, \frac{5}{2}, \ldots$) are called *fermions*. Figure 1.1 labels which particles are fermions and which are bosons, but even absent those labels, it is apparent that quarks and leptons are all fermions because they have spins of $\frac{1}{2}$, and the force carriers and the Higgs particle are all bosons, with spins of 0 or 1.

Antimatter

For every matter particle, there also exists a corresponding antiparticle. These are collectively referred to as antimatter. Antiparticles have mostly the exact same properties as their normal-matter partners, the key exception being that their electrical charge (if they have one) is opposite in sign. Thus the anti-electron (also called a positron) has a positive electrical charge instead of negative. The antimatter versions of the charged leptons are indicated with a plus in their symbol (e^+, μ^+, τ^+), and all other antiparticles have a bar on top of their symbol ($\bar{u}, \bar{b}, \bar{\nu}_\mu$, etc.). Since the properties of antiparticles are mostly identical to those of normal-matter particles, particle physicists seldom distinguish between matter and antimatter in speech or writing.

When a particle meets its own antiparticle, they usually annihilate, and produce high-energy photons, or sometimes Z bosons. Because of this instant annihilation, antimatter is not generally found in large quantities in our universe. However, very small quantities can be produced by energetic collisions in nature, radioactive decays, and in manmade particle colliders.

1.1.2 Successes

The predictions of the Standard Model have been confirmed in a staggering number of experiments over the last several decades. Some of the greatest successes of the SM include the correct predictions of the Higgs boson, the W and Z bosons, and the top and bottom quarks. On a less exciting but equally telling note, thousands of deliberate searches for phenomena that violate the Standard Model have been conducted by a wide variety of experimental groups; the overwhelming majority have failed to find any such violations. This unprecedented success has led the Standard Model to be labeled as one of the most successful physics theories ever formulated [1, 2].

1.1.3 Shortcomings

Despite the Standard Model's vast successes, it is not a complete theory of all particles and interactions in the universe. Physicists have observed a number of phenomena that are not described within the framework of the Standard Model. Additionally, the Standard Model does not contain all the information needed to build a stable universe from scratch. Some of these shortcomings are presented here, as they provide strong motivations for further research in particle physics and related fields.

The Hierarchy Problem

When the Higgs boson was discovered in 2012, its mass was measured to be 125 GeV [8]. This measurement also fixed the value of the "Higgs mass squared" variable in the equation for the Standard Model: $m_H^2 = -(92.9\text{GeV})^2$. Unfortunately, this value of the parameter is strikingly inconsistent with what we expect from theory. Because the Higgs boson couples to all particles with mass, the value of m_H^2 should be sensitive to the masses of all the other heavy particles in existence. By themselves, the other heavy Standard Model particles should be enough to drive the value of m_H^2 up by thirty orders of magnitude, to say nothing of any undiscovered heavy particles [9]. Yet the m_H^2 value remains steadfastly small. The hierarchy problem thus boils down to: why is the Higgs mass squared not incredibly large?

Arbitrary Parameters

Another perceived deficit of the Standard Model is the fact that many of the fundamental constants of nature are not given in the theory. For example, the Standard Model predicts the existence of the elementary particles described in Section 1.1.1, but it does not predict what their masses will be; the masses must be measured experimentally. Similarly, the Standard Model offers no clue to the strength of the various forces of nature, only their existence. In total, the Standard Model has 19 independent parameters that cannot be derived from other information in the theory, and must be determined experimentally [10]. Some physicists object to this large number as being clunky and inelegant, feeling that a fundamental description of the universe should have fewer unexplained parameters [1].

Dark Matter

Beginning in the late 19th century, and continuing into the 20th, scientists tried to calculate the masses of the Milky Way and other galaxies. They made their estimates based on the masses of the stars and gas they could see through their telescopes. But when these scientists tried to construct models of the internal motions of galaxies, they noticed a problem: galaxies rotate so quickly that the observed stars and gas shouldn't have enough gravitational pull to keep everything together [11]. They hypothesized that there must be some extra matter that supplies the missing gravitational pull, but that cannot be seen through telescopes (hence *dark*). This theory eventually gained widespread acceptance. We now estimate that only about $\frac{1}{6}$ of the mass of the universe consists of visible matter such as stars, planets, and nebulae, and the remainder consists of this mysterious dark matter [12].

Since everything is made of particles, the particle physics community is naturally curious to learn what particles make up dark matter. The observation that dark matter neither absorbs nor emits light indicates that it does not interact electromagnetically, and thus cannot be charged. Observations of distant stars, and calculations of nucleus formation after the Big Bang, have ruled out the possibility that dark matter is made of baryons (three-quark hadrons, such as the proton and neutron). Finally, simulations have shown that neutrinos could not give rise to the large-scale structures we see in the universe [11]. This exhausts all possibilities from among standard-model particles. Therefore, the existence of dark matter seems to require physics Beyond the Standard Model (BSM).

Dark Energy

In a universe filled with ordinary matter and dark matter, it is natural to believe that the inexorable pull of gravity would slow the expansion of that universe, until the universe eventually begins to contract again. However, observations of distant supernovae [13, 14], the cosmic microwave background (CMB), galaxy clusters, and more have shown that the expansion of the universe is *accelerating*, not slowing [15]. The mysterious energy that drives this outward expansion is given the name “dark energy”. Thus far, the Standard Model offers no explanation for how this kind of energy could exist.

Neutrino Masses and Oscillations

The Standard Model predicts that neutrinos should be entirely massless. And for many years, observations of processes that produced neutrinos, such as β-decay, seemed consistent with this belief. However, beginning in 1968, observations of neutrinos produced in the sun showed that the rate of electron neutrinos reaching the earth was only a third of the predicted rate [16, 17].

Further measurements of neutrinos from the sun [18, 19], the atmosphere [20], and other sources eventually led to the conclusion that neutrinos change back and forth between their three flavors as they travel through space [21]. This mutability makes it impossible for neutrinos to be massless, because massless particles must travel at the speed of light, and therefore cannot experience the passage of time. But since neutrinos morph between different states, clearly they must have some experience of time passing. These oscillations require an extension of the Standard Model to explain how neutrinos acquire mass, and how they are able to change identities.

1.2 Supersymmetry

Physicists have proposed a number of theories to explain the various shortcomings of the Standard Model. One particular class of theories, known as supersymmetry (or SUSY for short), is extremely popular for the elegant ways it can fill some of these gaps. Although there are numerous variations of supersymmetric theories, they all have one defining feature in common. For every standard-model particle, SUSY postulates the existence of another particle with mostly the same properties, but with a spin that differs by $\frac{1}{2}$. Thus every standard-model fermion would have a corresponding "superpartner" that is a boson, and every standard-model boson would have a superpartner that is a fermion [9].

1.2.1 Sparticles

Supersymmetry uses a unique, sometimes quirky nomenclature to refer to the new particles it postulates. The partners of Standard Model fermions are named by prefixing the existing name with an 's'. Thus the two families become *squarks* and *sleptons*, and the individual members of those families are named, e.g., *sup, sbottom, selectron, sneutrino*, etc. Meanwhile the partners of Standard Model bosons gain the suffix *-ino*, which replaces the suffix *-on* if present. Thus we arrive at the names *gluino, photino, zino, wino*, and *Higgsino*. The symbols for these particles are generally formed by adding a tilde on top of the original particle's symbol, so that a scharm squark is notated $\tilde{c}$, a gluino is notated $\tilde{g}$, etc. To avoid conflict with the tilde, anti-sparticles are notated using a star (as in $\tilde{c}^*$) instead of a bar.

These superpartners are capable of mixing with each other to form different sparticles, which may not correspond exactly to Standard Model particles. Of particular note are the neutralinos ($\tilde{\chi}_1^0, \tilde{\chi}_2^0, \tilde{\chi}_3^0, \tilde{\chi}_4^0$), made by mixing the photino, zino, and Higgsino; and the charginos ($\tilde{\chi}_1^{\pm}, \tilde{\chi}_2^{\pm}$), made by mixing charged winos and charged Higgsinos.

It is worth noting that if SUSY were a perfect symmetry, all sparticles would have the same masses as their corresponding particles. However, to date, no sparticles have been observed, implying that most sparticles (if they exist) must be too heavy to produce using our current particle colliders. Since the equality of masses is destroyed, we say SUSY is a *broken symmetry* [9].

1.2.2 Motivation

One of the features that makes SUSY very attractive is its ability to solve the hierarchy problem. If the masses of the SM particles tend to drive m_H^2 to a high value, the introduction of a new boson for every SM fermion and a fermion for every SM boson will create large cancellations, and allow m_H^2 to take on the moderate value derived from experiments [9].

In addition, SUSY provides particles that may be good candidates to explain dark matter. At the moment, the most popular explanation for the composition of dark matter is weakly-interacting massive particles (WIMPs). These are particles that primarily interact through the weak force, and that also have mass, allowing them to exert a gravitational pull. The neutralinos fit this bill nicely. In addition, the dark matter particle must be stable. The lightest supersymmetric particle (LSP) would be stable due to conservation laws associated with supersymmetry. In fact, many SUSY models predict that the lightest neutralino, $\tilde{\chi}_1^0$, actually *is* the LSP. Thus the lightest neutralino makes a tantalizing dark matter candidate [9, 22]. We will assume moving forward that $\tilde{\chi}_1^0$ is the LSP, and will use the terms LSP and neutralino interchangeably.

If the theoretical considerations were not enough to make SUSY an attractive target for study, there is a strong experimental case as well. *Naturalness* is the idea that it makes sense for the parameters of a model to be not-too-dissimilar in size (the hierarchy problem is an example of un-naturalness). If SUSY is to be "natural", as many theorists hope it is, then the lightest sparticles are likely to have masses in the terra-electron volt (TeV) range [9, 22]. This is exactly the energy scale probed by current and near-future collider experiments. Therefore, there is reason to believe that searches at the Large Hadron Collider, or a close successor, should uncover evidence for the existence of supersymmetry.

Chapter 2

The Large Hadron Collider and the CMS Experiment

In order to study the properties of the Standard Model particles, and to search for physics beyond the Standard Model, we need a way to produce particles other than the simple up and down quarks and electrons that make up everyday matter. And once we have produced such particles, we need a way to detect their presence, identify them, and measure their properties.

This chapter will describe the machines used to perform the analyses described in Chapters 3 and 4, namely the Large Hadron Collider and the CMS Detector. It will also describe how the CMS Collaboration uses software to make sense of the readings it has collected from the CMS Detector. Because these systems are immensely complex, this chapter will not attempt to describe them in exhaustive detail, but will focus on the aspects that are important for understanding the science presented in the remaining chapters.

2.1 The Large Hadron Collider

In order to study heavy particles, we must first create them, since it is impractical to find them in nature. Einstein's famous equation, $E = mc^2$, tells us that mass and energy are equivalent to one another. Physicists employ this principle to create heavier particles by taking lightweight particles, accelerating them to very high speeds, and smashing them together. Particles moving at high speed have high kinetic energy, and when those particle collide, that energy can be converted into mass, creating heavier particles. Because it is so often conducted at high energies, particle physics is sometimes referred to as high energy physics, or HEP.

The Large Hadron Collider, or LHC, is the largest and most powerful particle collider ever built. It is the flagship project of CERN, the European Organization for Nuclear Research, located in Geneva, Switzerland. The LHC is a ring-shaped structure about 27 kilometers (17 miles) in circumference, buried underground beneath the border between Switzerland and France, as shown in Figure 2.1. The ring encloses two pipes, through which beams of protons normally circulate in opposite directions for eventual collision. Strong electric fields propel the protons along the beam pipes, and strong magnetic fields steer the protons around the ring [23]. The LHC tunnel and a cutaway view inside the accelerator may be seen in Figure 2.2.

The LHC is fed by a chain of smaller accelerators at CERN that shape the beams and bring them partway up to speed so they can be injected into the LHC. The LHC was designed to collide protons at an energy of 14 trillion electron volts (TeV). However, during early testing, a defective weld caused severe damage to the LHC; as a precaution against future damage, the LHC was operated at 7 and 8 TeV energy in its first run (Run I), and has been colliding at 13 TeV so far in its second run (Run II). At these energies, the protons in the beam are moving at 99.999999% of the speed of light.

The proton beams are not continuous streams of particles. Rather, the protons are grouped into bunches. The LHC is designed to circulate 2808 bunches of protons in each direction, with

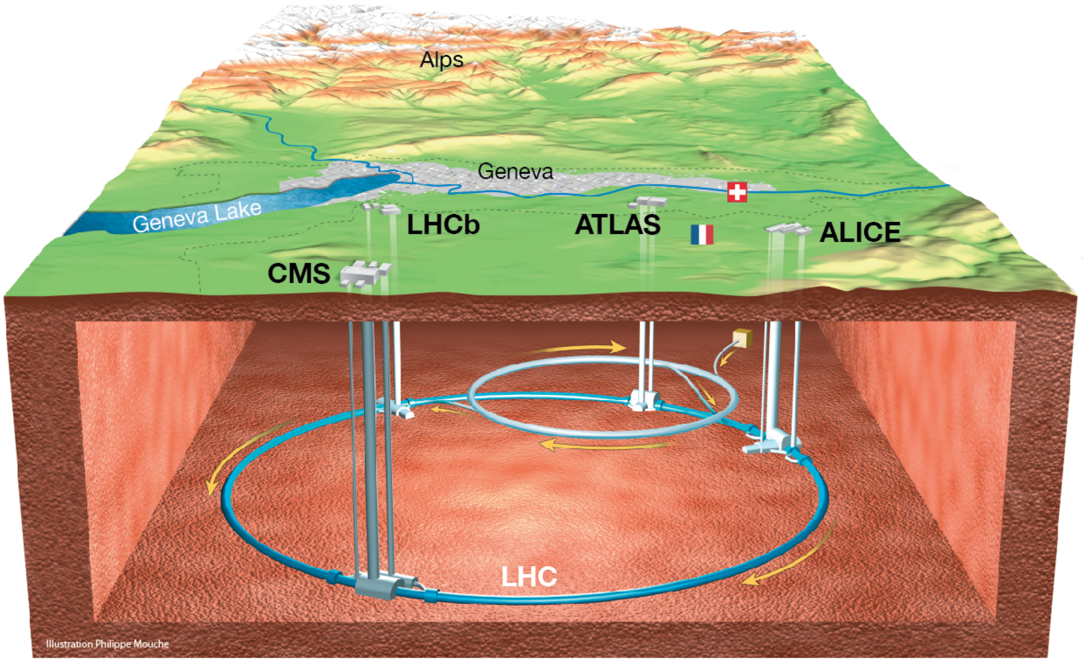

Figure 2.1: Situation of the Large Hadron Collider near Geneva, Switzerland [24].

each bunch containing about 120 billion protons when it is first injected. The total "amount of beam" delivered per unit time is called *luminosity*, denoted $\mathcal{L}$. Unrelated to the measure of optical power, luminosity in accelerator physics is expressed in units of 1/(area×time); the typical luminosity of the LHC integrated over one year of running is on the order of several dozen *inverse femtobarns* (fb^{-1}). The strange choice of units for luminosity allows us to express it as the inverse of *cross section* (denoted σ), which is measured in units of area. The cross section for a particular process is a kind of relative probability of that process occurring. Because time-integrated luminosity has units of inverse area, the number of occurrences, N, of a given process observed in some time is given by:

$$N = \mathcal{L}_{\text{int}} \cdot \sigma \tag{2.1}$$

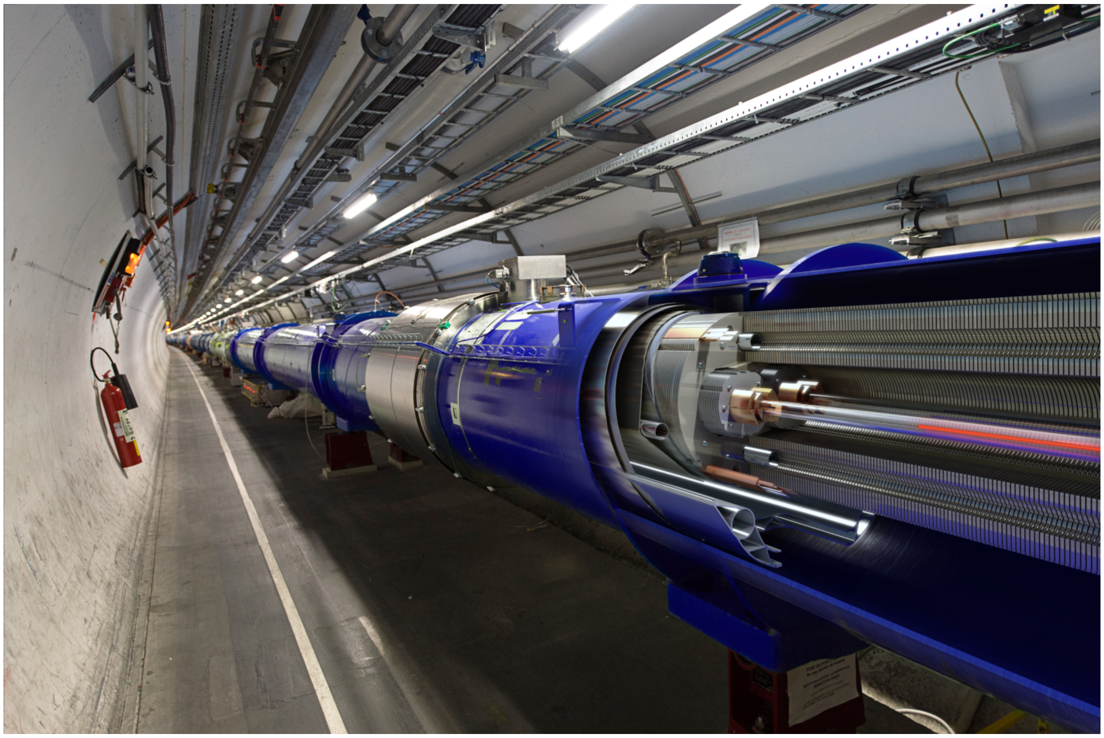

Figure 2.2: Interior of the LHC tunnel, with cutaway view inside the accelerator [24].

Thus a process with a cross section of 50 fb may be expected to occur 1000 times in 20 fb^{-1} of data.

The proton beams are made to collide every 25 ns, or 40 million times per second. Each beam crossing is referred to as an "event". A single event may contain anywhere from 20-60 collisions between the protons in the bunches, though only one collision in the event will be analyzed. Usually this is the most energetic collision. The products of any other pp collisions are known as *pileup*, and are treated as general background debris to be subtracted out.

Although we have been describing protons as simple particles, in fact they are anything but. Protons contain two up quarks and a down quark, and innumerable gluons binding them together. But in addition, protons contain a sort of froth of quarks and antiquarks that are constantly popping into and out of existence on ultrashort timescales, in accordance with the laws of quantum mechanics. Collectively, all of these components of a proton are known as *partons*, and any of them may be involved when two protons collide. Studies on the relative momentum of the various partons tell us that at the LHC, most of the time it is the gluons that are colliding with each other.

At the LHC, there are four places where the beam pipes intersect and the proton beams are made to collide with one another. At each of these four locations, a detector is placed where it can observe the particles that are produced by these collisions. Two of the detectors are large, general-purpose machines, designed to support a broad range of particle physics research. These detectors are called CMS and ATLAS. There are two general-purpose detectors so that the results from one may be cross-checked by the other. The other two main detectors are moderately sized and designed to study specific kinds of physics phenomena. One is LHCb, which is designed to study the physics of bottom quarks. The other is ALICE; a few weeks each year, the LHC collides lead nuclei instead of protons, and ALICE is designed to study the physics of these collisions. In recent years, three smaller detectors have been added: ToTeM, which shares an interaction point with CMS; MoEDAL, which is colocated with LHCb; and LHCf, installed around the ATLAS detector.

2.2 The CMS Detector

The research described in Chapters 3 and 4 was conducted using proton-proton collision data gathered by the CMS detector. CMS stands for Compact Muon Solenoid, a name whose origin will become apparent in the next few sections. In brief, though, this detector is a complex, multilayered array of sensors designed to detect, and measure the properties of, as many of the particles emerging from the collision point as possible [25]. Figure 2.3 provides a cutaway view inside these layers.

The CMS detector was designed with a wide array of physics goals in mind. Some of these goals included discovering the Higgs boson, especially in decays to leptons or photons; discovering signs of supersymmetry, if such signs exist; searching for extra dimensions; and

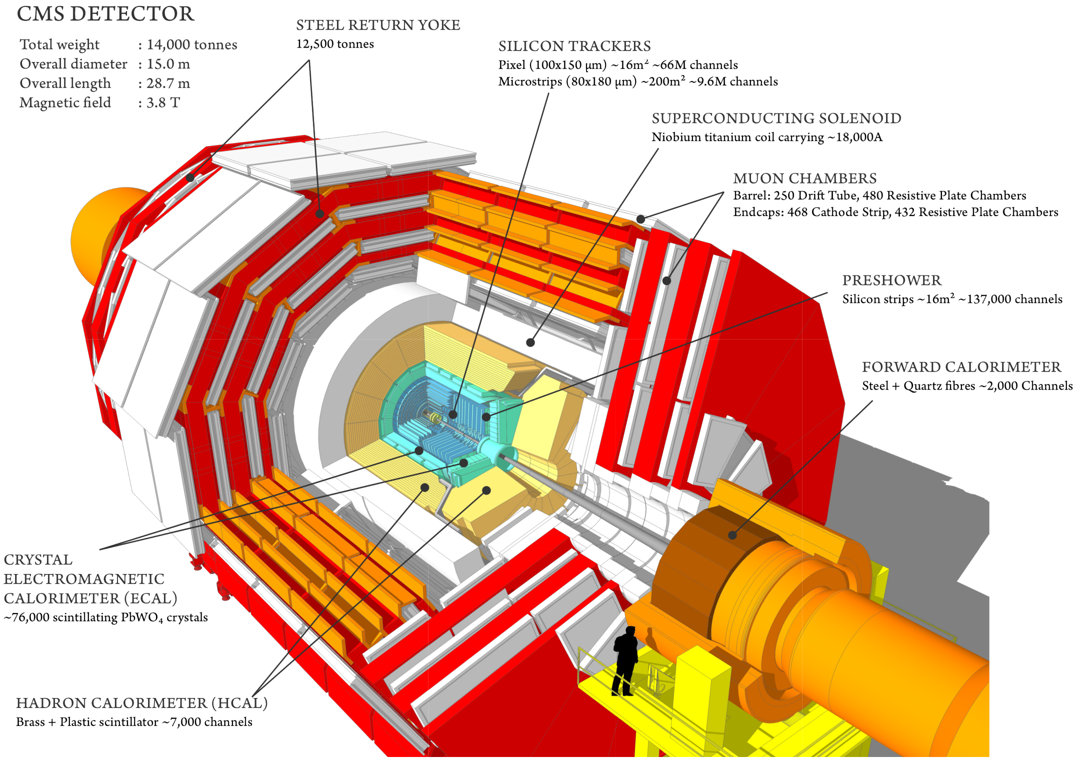

Figure 2.3: Perspective view of the CMS detector, with cutaway showing the many layers inside [26].

conducting precision tests of the predictions of the Standard Model [27]. These and other goals had to be balanced against practical constraints, such as budget, durability, and ease of readout. The detector that resulted from the convergence of these factors is described in detail in Sections 2.2.2-2.2.6.

2.2.1 Coordinate System

Before we can understand the design of the CMS detector, or the physics it studies, we must assign a coordinate system to the detector. Because the beam pipe has cylindrical symmetry, the CMS detector is similarly cylindrical. It is shaped like a giant barrel wrapped around the beam pipe, some 5 stories tall and wide, and 7 stories long. The middle region of the detector is actually referred to as the *barrel*, and the two plugs that cap off either end of the barrel are known as the *endcaps*.

The coordinate system attached to the detector may be seen in plots throughout this Section. The longitudinal axis running down the center of the beam pipe is defined to be the z-axis. The $+z$ direction points counterclockwise along the LHC, and the $-z$ direction clockwise. If we consider a circular cross-section of the detector, as depicted atop Figure 2.4, the radial coordinate r expresses distance out from the center, and the azimuthal angle is labeled ϕ.

Because the proton beams are compressed and stabilized in the transverse direction before they enter the collision area, we expect that the system of two colliding protons has no net momentum transverse to the beam pipe, i.e. in the r direction. We can therefore expect the total *transverse momentum* (or p_T) of the collision products to be zero. However, because the individual partons inside a proton have constantly-changing momenta, we cannot know the total longitudinal momentum (p_z) of the pp collision. Because the total p_T of the system is known *a priori*, but the p_z is not, we consider the p_T of particles almost exclusively, and seldom spare a thought for p_z.

Because particle collisions take place near the origin of the detector, it is often helpful to describe the trajectories of particles in terms of a sort of angle that they make in the $r-z$ plane. We could use the polar angle θ from spherical coordinates. But in a world of particles moving at relativistic speeds, we will often need to boost between different reference frames, and θ becomes cumbersome. Physicists came up with a more useful coordinate, which they termed *rapidity*. In collider physics, the rapidity, y, of a particle is given by:

$$y = \frac{1}{2} \ln \frac{E + p_z}{E - p_z} \tag{2.2}$$

This coordinate has the advantage that the rapidity difference Δy between two particles is Lorentz invariant–it remains the same no matter what reference frame it is measured in.

Rapidity will be used to define other variables in Section 3.3.1, but on the whole, it turns out to be not very convenient, because it requires us to know the energy of the particle. So physicists have devised a related quantity that behaves somewhat better, calling it *pseudorapidity*. The pseudorapidity, η, of a moving particle is defined by

$$\eta = -\ln\left[\tan\left(\frac{\theta}{2}\right)\right] \tag{2.3}$$

This coordinate depends only on the polar angle, not the energy, of a particle. And like its cousin, the pseudorapidity difference $\Delta\eta$ between two particles is also a relativistic invariant. In fact, at velocities approaching the speed of light, rapidity and pseudorapidity become equal to one another. η is used widely in collider physics, even to the extent that parts of the CMS detector are referred to by their (η, ϕ) coordinates. Thus, you will see labels employing the η coordinate in Figures 2.5, 2.6, 2.7, and 2.8.

We have established that differences $\Delta\eta$ in pseudorapidity are invariant under Lorentz boosts along the z-axis. So too are differences $\Delta\phi$ in the azimuthal angle, because ϕ is measured transverse to the z-axis. So particle physicists often use a 3-dimensional "angle" ΔR, defined by:

$$(\Delta R)^2 = (\Delta\eta)^2 + (\Delta\phi)^2 \tag{2.4}$$

This not-quite-an-angle will be used in this and subsequent chapters to measure the separation between two objects, and to define cones around single objects, in a relativistically invariant way.

2.2.2 Superconducting Solenoid

Figure 2.4 shows a small cross-sectional wedge of the detector, and demonstrates how each of the components contributes to measurements of the particles produced in the collisions.

The defining feature of CMS, which gives rise to the 'S' in its name, is the superconducting solenoid. This component is a large electromagnet; it is made from superconducting niobium-

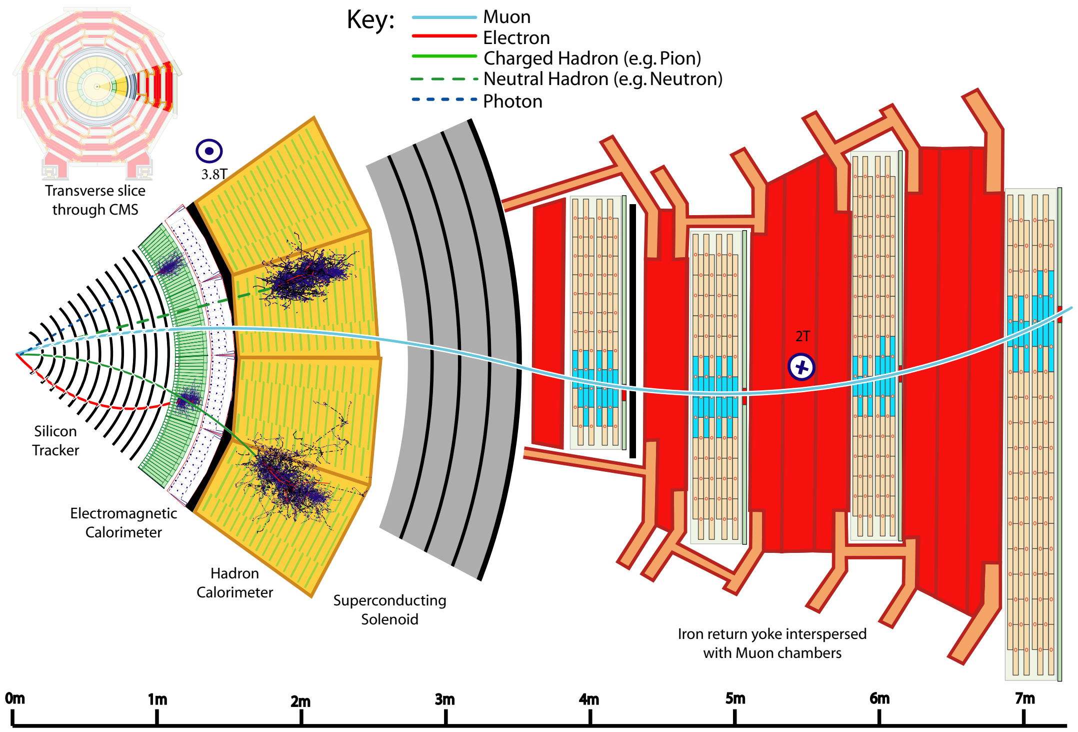

Figure 2.4: Diagram showing particles interacting with a typical cross-sectional wedge of the CMS detector [28].

titanium material, taking the form of a giant coil 12.9m long and with an inner bore of 5.9m [27]. When cooled to about 4 Kelvin using liquid helium, the magnet can generate a longitudinal magnetic field of up to 4T inside the solenoid, though in practice it is run at 3.8T to help it last longer. The return field outside the solenoid is lower, and is not uniform [29].

The purpose of this magnet is to bend the trajectories of particles passing through the detector. The tracker and the muon system (described below) can measure the radius of curvature of a track, from which we can determine how much momentum the particle was carrying. The strength of the magnetic field was chosen based on the requirement that the CMS detector be able to determine the charge of a muon carrying 1 TeV of momentum [27].

2.2.3 Inner Tracker

The innermost component of the detector, wrapped immediately around the beam pipe, is the inner tracker. This component is made of several layers of silicon sensors. Every time a charged particle passes through a layer of silicon, it creates a blip of electrical current in the silicon that can be read out electronically. We can "connect the dots" to reconstruct the path the particle took. Because of the magnetic field inside the detector, charged particles will have curving trajectories. Using the tracker, we can measure the radius of curvature of these tracks, and thus determine the momentum of the particle that created the tracks. Because the magnetic field is only in the z-direction, we can only measure the p_T of the charged tracks, not the p_z. Importantly, neutral particles do not leave any hits in the tracker, and thus their trajectories and momenta cannot be measured.

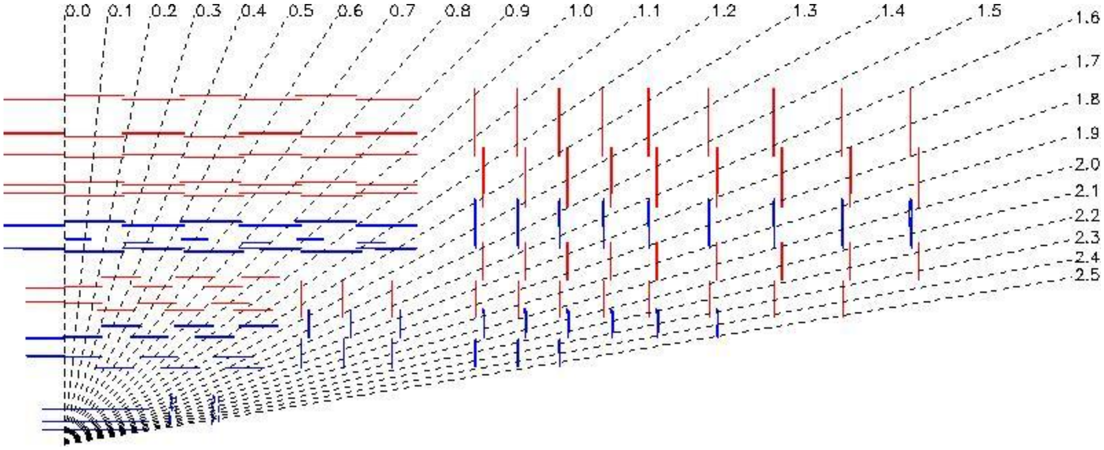

Figure 2.5: One-quarter (r,z) view of the layout of the CMS inner tracker [27].

Figure 2.5 shows the geometry of the tracker as originally designed. The innermost part of the tracker ($r \lesssim 10$ cm), where the tracks are densest, consists of silicon pixels. At installation, there were three pixel layers in the barrel and two in the endcaps. Each pixel is $100\times150\ \mu$m in size. At this scale, the expect occupancy of a pixel was 10^{-4} per bunch crossing [27]. The pixel tracker was upgraded during the 2016/2017 winter shutdown, adding a fourth pixel layer in the barrel and a third in the endcaps, while slimming down the hardware that supports the functioning of the pixels [30].

The remaining layers of the tracker consist of silicon strips. In the region $20 < r < 55$ cm in the barrel (Tracker Inner Barrel, TIB), there are four layers of silicon microstrips, with a size of at least 10 cm $\times$ 80 μm. In the Tracker Outer Barrel (TOB), defined by $r > 55$ cm, there are six layers of microstrips with a size of no more than 25 cm $\times$ 180 μm. In the endcap regions, the Tracker Inner Disks (TID) sit just outside the TIB, and consist of three layers of disks of strips. The Tracker Endcaps (TEC) sit just outside the TOB, and consists of nine disks of silicon strips. These various layers provide tracker coverage out to $|\eta| \approx 2.5$.

The electrical impulses produced in the silicon pixels and strips are read out by “APV25” chips that amplify and process the signals. The signals are then passed out of the detector using optical cable, and further processed in hardware outside the detector volume [27]. Additional hardware circulates a refrigerant liquid that maintains the silicon sensors at a temperature no higher than -10 °C [29]. The materials and geometry of the tracker were chosen to minimize the amount of energy absorbed from particles as they pass through.

The performance of the inner tracker has been measured using both muons and pions. The p_T resolution for muons ranges from about 0.5 - 2.0%, depending on p_T and η. The efficiency of global muon track reconstruction is generally around 99%. For pions, the global track resolution is somewhat less, ranging from 85-95% for 100 GeV pions and 75-90% for 1 GeV pions [27].

2.2.4 Electromagnetic Calorimeter (ECAL)

Just outside the tracker, the next component in the CMS detector is the electromagnetic calorimeter, or ECAL. The purpose of this device is to measure the energy of electromagnetic particles (electrons and photons) produced in collisions. The ECAL consists of a giant array of lead tungstate ($PbWO_4$) crystals; when struck by electromagnetic particles, these crystals scintillate with a blue light that can be read out by optical sensors. The amount of light gives us a measure of how much energy the particle was carrying. In addition, the pattern of energy deposition in the crystals can provide clues to the identity of the particle.

Lead tungstate has a number of properties that make it an ideal material to use in the ECAL. For one thing, it is quick to read out: lead tungstate crystals can release 80% of their scintillation photons in the 25 ns window between bunch crossings. In addition, lead tungstate is highly resistant ("hard") to the high levels of radiation emitted by the collisions, tolerating a total absorbed dose of up to 10 Mrad (100 kGy). But perhaps most importantly, lead tungstate allows the ECAL to be built relatively compactly, because the material has a short radiation length (X_0) and Molière radius (R_M).

Radiation length and Molière radius are two properties that describe a material's ability to absorb electromagnetic energy. When an electron passes into a material, the radiation length is the characteristic distance over which that electron will lose all but $1/e$ of its energy. To put it mathematically:

$$E(x) = E_0 \cdot e^{-x/X_0} \tag{2.5}$$

It is also equal to 7/9 of the mean free path for pair production by photons [3]. So the shorter the radiation length for a material, the shorter the distance needed for electromagnetic particles to be stopped and their energy absorbed. Lead tungstate has a radiation length $X_0 = 0.89$ cm [27]. Similarly, the Molière radius governs the absorption of energy in the direction transverse to the particle's trajectory. It is the characteristic lateral distance over which 90% of an EM shower's energy will be contained. So materials with a shorter Molière radius will have on average a smaller transverse shower size. For lead tungstate, $R_M = 2.2$ cm [27]. These characteristic distances play an important role in determining the size of the ECAL crystals.

The ECAL is divided into barrel and endcap components. These may be seen in Figure 2.6. The $PbWO_4$ crystals are shaped like tapered rectangular prisms. In the barrel region, they are 230 mm long, corresponding to 25.8 X_0, and have front faces that are 22×22 mm, corresponding to 1×1 R_M. These dimensions ensure that very little EM energy will escape out the back of the crystals, and that about 94% of a given shower will be contained in a 3×3 array of crystals. In

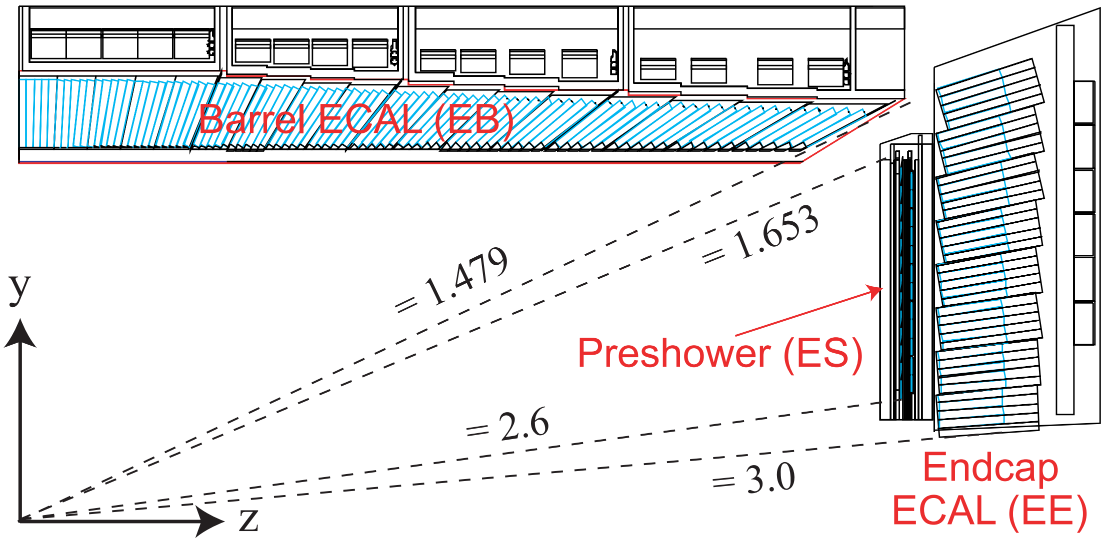

Figure 2.6: One-quarter (r,z) view of the layout of the CMS ECAL [27].

the endcaps, the crystals are 220 mm long (24.7 X_0), and have front faces of 28.6×28.6 mm (1.3×1.3 R_M). The barrel section is composed of 36 “supermodules”. Each supermodule is an array of 85×20 crystals, covering half the barrel length and 20° in ϕ. Each of the two endcaps is composed of two half-circle structures called “Dees”. Each dee holds 138 groupings of 5×5 crystals (called“supercrystals”) plus 18 partial supercrystals. The endcaps are also fronted with preshower detectors, whose purpose is primarily to study neutral pions produced at high η. These preshower detecters are composed of lead absorbers that initiate pion showering, and silicon strip detectors that measure the size and shape of the shower. All told, there are 75,848 crystals in the entire ECAL, providing very fine spatial granularity. As Figure 2.6 shows, ECAL coverage extends out to $|\eta| = 3.0$. However, there is a gap in coverage between the barrel and the endcaps. Electromagnetic particles that fall into this “crack” will not be measured, a fact that we must account for when attempting to reconstruct electrons and photons [27].

Lead tungstate produces a blue-green scintillation light, peaking near 420mm. The amount of light produced in each crystal must be measured, and the information digitized, in order to determine the energy of incident EM particles. In the barrel, scintillation photons are read out by silicon avalanche photodiodes (APDs) stuck to the backs of each crystal. In the endcaps, vacuum phototriodes (VPTs) are used for readout instead. These sensors feed their signals to amplification and digitization hardware attached to the CMS detector, and from there are sent to computing equipment outside the detector volume [27].

The performance of the ECAL was measured using a controlled beam of electrons. The measured energy resolution in groups of 3×3 crystals is better than 1% for electron energies above about 20 GeV [27].

2.2.5 Hadron Calorimeter (HCAL)

Outside the ECAL but (mostly) inside the magnet lies the hadron calorimeter, or HCAL. This component is designed to measure the energy of hadronic particles produced in collisions. The HCAL is composed of alternating layers of metal, used to absorb some of the incident hadronic energy, and scintillating materials, used to measure the hadronic energy deposited in the calorimeter. The HCAL thus has an important role in measuring the energy of jets, as well as in measuring pileup from secondary collisions in the event.

The power of materials to stop relativistic particles is described in terms of the interaction length, λ_I. When a number of particles are incident on some material, this parameter describes the length over which all but a $1/e$ fraction of those particles will be absorbed. In other words:

$$N(x) = N_0 \cdot e^{-x/\lambda_I} \tag{2.6}$$

So the shorter a material's interaction length, the shorter the distance over which it will absorb incident particles.

The CMS HCAL is a *sampling* calorimeter, meaning that it uses different materials to produce the shower and to measure the energy. Hadronic showering is induced by the absorber layers, most of which are made of brass (70/30% Cu/Zn). Brass is used because it is relatively affordable, and also because it is non-magnetic, and thus won't perturb the magnetic field inside the detector. This particular brass alloy has an interaction length $\lambda_I = 16.42$ cm. Stainless steel is also used as an absorber in places. Interleaved with the absorber materials are layers of scintillating material. Most of the scintillators are made of radiation-hard plastic, either Kuraray SCSN81 or Bicron BC408, though where extreme particle flux and radiation is an issue, quartz fiber is used instead for its superior radiation hardness. The amount of light produced by these scintillators corresponds to how much hadronic energy was deposited in them. Note that any energy deposited in the absorber layers is not measured, and must be extrapolated from the measurements in the scintillating layers.

The HCAL is divided into four subcomponents: the barrel (HB), the endcaps (HE), the outer calorimeter (HO), and the forward calorimeter (HF). Each of these components operates on the same principles, though the design of each differs slightly. These components are all cleverly overlapped to avoid any cracks like that of the ECAL. The arrangement of the components is shown in Figure 2.7.

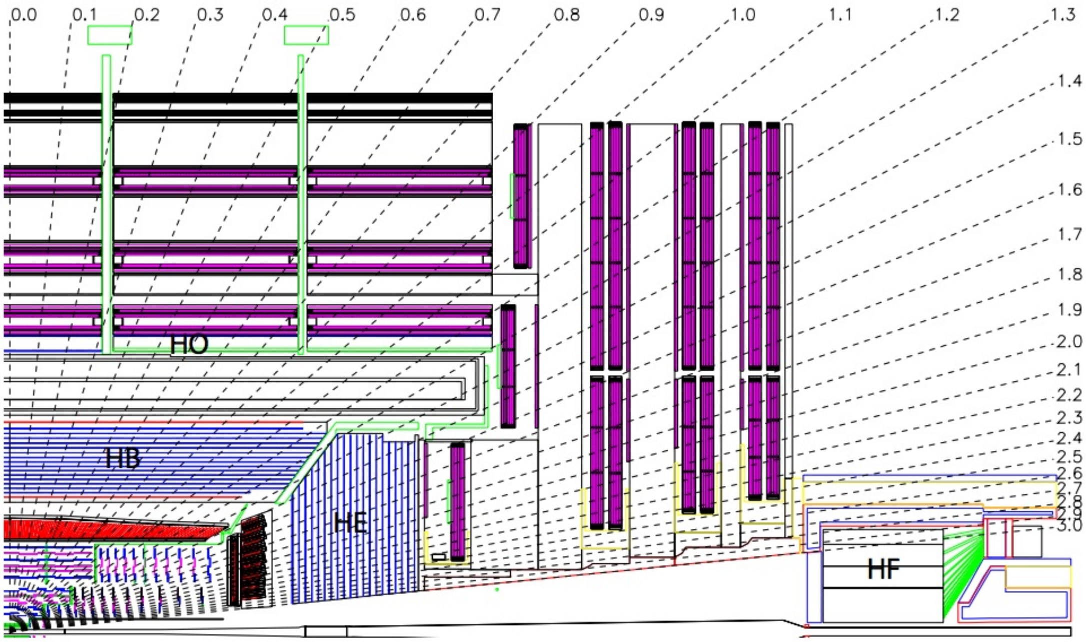

Figure 2.7: One-quarter (r, z) view showing the layout of the HCAL components within the CMS detector [25].

The barrel covers the range $|\eta| < 1.3$. The absorber material in the HB is segmented into 36 wedges; each wedge encompasses half the length of the HB and 20° in ϕ, corresponding exactly to the size and position of the ECAL supermodules. There are 16 layers of absorber material in each wedge; the innermost and outermost layers are made of stainless steel, for strength, and the middle 14 layers are brass. The total thickness of these absorber layers is 5.82 λ_I at $\eta = 0$, increasing to 10.6 λ_I at $|\eta| = 1.3$. Within each wedge, the scintillating material is further divided into segments of size 0.087×0.087 in $\Delta\eta - \Delta\phi$ space, providing fine granularity. The innermost layer of scintillating material in the HB is Bicron BC408, and the remaining 16 layers are Kuraray SCSN81 [29].

The endcaps cover the regions $1.3 < |\eta| < 3.0$, and use the same absorber and scintillator materials as the barrel, with one exception: stainless steel is only used as the outer absorber layer, to prevent any magnetic interference inside the magnet bore. The scintillators are divided into segments of size 0.087×0.087 in $\Delta\eta - \Delta\phi$ space for $|\eta| < 1.6$, and approximately 0.17×0.17 for $|\eta| \geq 1.6$. The total thickness of the endcaps (including attached ECAL dees) is about 10 λ_I [29].

The outer calorimeter is designed to augment the stopping power of the HB and the EB, and covers the region $|\eta| < 1.3$. It consists of tiles of Bicron BC408 scintillator embedded in the iron yoke that gathers the returning magnetic field outside the solenoid. Thus the HO actually uses the solenoid material itself as an absorber. Following the shape of the return yoke, the HO is divided into 5 rings along the z-axis, each of which has 12 sectors in ϕ. There are gaps between the rings, and in some azimuth sectors, for the cryogenic and power lines that supply the magnet. The scintillator tiles roughly follow the 0.087×0.087 segmentation of the HB, within the constraints of the yoke geometry [29].

The forward calorimeter is located in the region $3.0 < |\eta| < 5.2$. This area receives an extremely high flux of particles due to its small angle with respect to the beamline. As such, this component must be considerably more radiation hard than any other part of the HCAL. To meet this requirement, the HF uses quartz fibers with polymer cladding as its measuring material, and reads out Cherenkov light rather than scintillation light. Each end of the HF is composed of stainless steel absorbers arranged in 18 azimuthal wedges, each of which is penetrated by quartz fibers that run parallel to the beamline. Some of these fibers only penetrate partway through the steel plate, allowing the HF to differentiate between electromagnetic and hadronic showers based on penetration depth. The fibers form towers of size 0.175×0.175 in $\Delta\eta - \Delta\phi$ space [29].

The scintillation light from the plastic tiles in the HB, HE, and HO is read out by Kuraray Y-11 wavelength-shifting (WLS) fibers. These fibers are embedded into the tiles themselves. Once outside the tiles, the WLS fibers are spliced to clear optical fibers that send the light to hybrid photodiodes for electronic processing. The Cherenkov light from the quartz fibers in the HF is transmitted to air-core light guides, which carry the light through layers of radiation shielding to photomultiplier tubes outside the shielding [29].

2.2.6 Muon System

The outermost component of the CMS detector is the muon system. The strong penetrating power of muons allows us to place this system outside all the other layers without fear that the muons will be attenuated or absorbed en route. As its name suggests, the muon system is responsible for measuring the momentum of muons as they fly away from the collision point. It employs three different gas-and-electrode technologies to reconstruct the trajectories of muons, from which momentum can be inferred. These trajectories can be combined with measurements from the tracker for greater precision.

The layout of the muon system is presented in Figure 2.8. Like many other components, it is divided into barrel and endcap regions. The barrel region detects muons using a combination of drift tubes (DTs) and resistive plate chambers (RPCs), whereas the endcaps use cathode strip chambers (CSCs) and RPCs. All three of these technologies detect muons by the trail of ionization the muons leave after passing through a gas. The liberated electrons will be attracted to positively charged electrodes, and the ions to negatively charged electrodes. When electrons and ions hit the

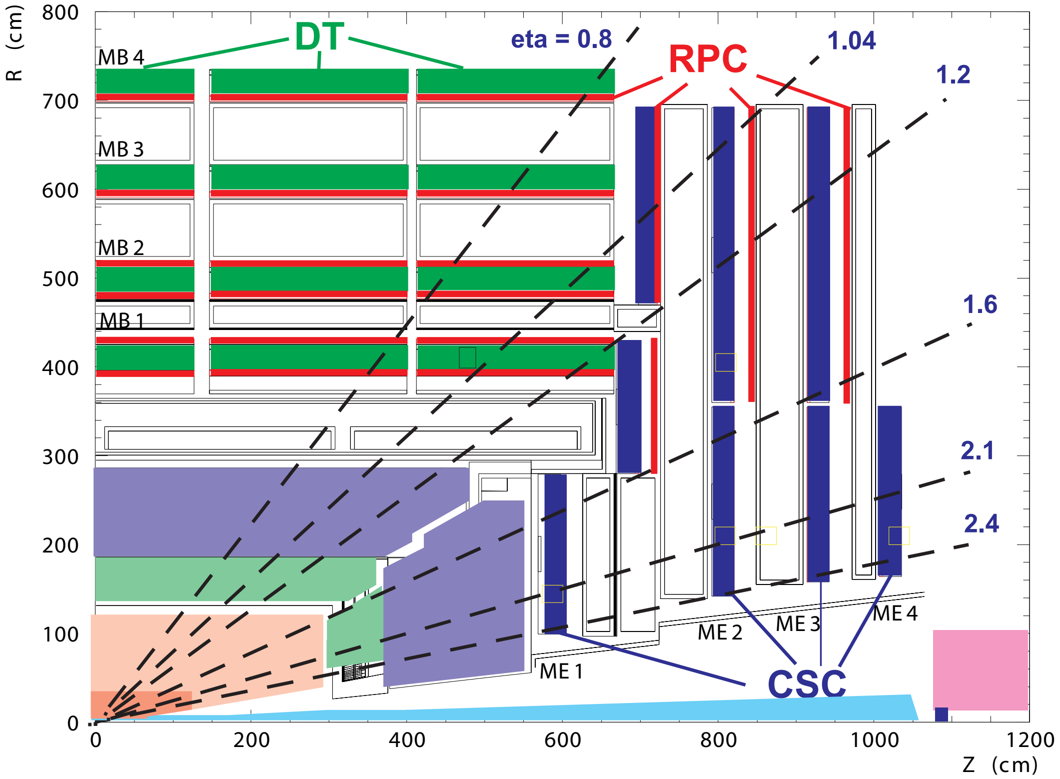

Figure 2.8: One-quarter (r,z) view of the layout of the CMS muon system [27].

electrodes, they produce an electrical signal that is read out, and timing information is used to tell how far along the electrode the impact occurred.

The drift tubes are long, thin chambers filled with a mixture of 85% Ar and 15% CO_2 gases, and with a positively charged wire running down their centers. Drift times in these chambers are a maximum of 380 ns. These tubes provide 1D position measurements, but multiple layers may be stacked at right angles to provide 2D measurements. These devices are used because they are precise and inexpensive, and can function well in the muon barrel, where the particle flux and magnetic field are both low [29, 31]. The cathode strip chambers are planar chambers filled with a mix of 40% Ar, 50% CO_2, and 10% CF_4. They contain positively charged wires running in one direction, and negatively charged strips running perpendicularly, providing native 2D position measurements. CSCs are employed in the endcap because they are precise, moderately fast (< 225 ns), and can operate in the high magnetic fields at the fringes of the solenoid [29, 32]. Resistive plate chambers are planar chambers filled with a mixture of 96.2% $C_2H_2F_4$, 3.5% iC_4H_{10}, and 0.3% SF_6. They have a positively charged plate on one face, and a negatively charged plate on the opposite face. Electrons are actually detected by metal strips just outside the chambers. RPCs are used to supplement the DTs and CSCs mainly for their 1 ns timing resolution; their spatial resolution is not as fine as the DTs or the CSCs [29, 33]. The signals from these subsystems are processed in electronics both within the detector volume and outside it.

The barrel section of the muon system, covering $|\eta| < 1.2$, is interleaved with the iron return yokes, structures that concentrate the magnetic field exiting the solenoid and return it around to the other end. As such, the muon barrel follows the geometry of the yokes. The return yokes consist of five rings that are about 2 meters long in z and divided into 12 sectors in ϕ. As Figure 2.8 shows, the DTs and RPCs are stacked in four layers, or *stations*. These are offset in ϕ so that all muons will pass through at least three stations. The three innermost stations contain 12 planes of DTs, 8 of which provide (r, ϕ) measurements, and 4 of which provide z measurements. The outer station lacks the z measuring planes. The inner two stations are coupled to two RPCs each, and the outer two stations have one RPC each. With this geometry, each individual station can provide position measurements with a precision of better than 100 μm in space and about 1 mrad in ϕ [27].

The endcap muon system covers the range $0.9 < |\eta| < 2.4$. The CSCs are arrayed in four layers of disks, with each disk being made up of several trapezoidal chambers 10 or 20° wide in ϕ, arranged in concentric rings. Each chamber contains 6 gas gaps and electrode grids. There are 36 chambers in each ring, except the centermost rings of stations 2-4, which have only 18 chambers. The CSCs provide a spatial resolution of about 200 μm and an angular resolution in ϕ of about 10 mrad [27]. During Run I, the first three disks had RPCs attached to all but the central ring; for Run II, the outer CSC ring of disk 4 was added, and was instrumented with attached RPCs.

2.3 Triggers

As previous sections have described, the LHC collides protons at a rate of 40 million collisions per second. However, the number of collisions per second that can actually be recorded is ultimately dictated by the medium used to store the data. Magnetic disk drives are prohibitively slow for our uses, while solid-state drives are both prohibitively slow and expensive. So in particle physics, we store our data on magnetic tape (like one might find in a video or audio cassette). The data recording system allows us to keep only about one out of every 100,000 events.

Fortunately, this constraint is less harmful than it might seem, because not every event is worth saving. Even with the considerable beam focusing power of the LHC, most bunch crossings only produce near-misses or grazing contact between protons. True head-on pp collisions, producing particles with a high transverse component to their momentum, are somewhat rare. Thus we can reach a manageable threshold of $<$1000 events per second using a system of "triggers" to store only events where interesting physics is taking place.

The first stage of the trigger system is the Level 1 trigger (L1). The L1 trigger is integrated directly into the detector hardware, and does not use any computational resources. It is tripped by basic signatures such as ionization tracks in the muon system, ECAL deposits consistent with electrons or photons, HCAL deposits consistent with jets, and a few others. This trigger system is able to make extremely fast decisions, and outputs events at a rate of 100 kHz [34].

Events passing the L1 triggers are handed off to the second trigger stage, called the high-level trigger (or HLT). This stage uses banks of commodity computers running physics reconstruction software to make a much more sophisticated determination of what physics objects are present in the event. Thanks to this more detailed reconstruction, the HLT allows one to trigger on a wide variety of signatures with a high degree of specificity. The HLT outputs events at an average rate of about 400 Hz; these are then stored for eventual use in physics research [34].

The use of these trigger systems can create certain difficulties that must be compensated for during physics analysis. For one, the triggers are not perfectly *efficient*, meaning they miss some fraction of the events they are intended to trigger on. For example, a trigger designed to select events containing muons with $p_T > 17$ GeV might only select 98% of those target muons, and this fraction might even vary with the muon p_T. This effect must be measured, and accounted for when we compare our data against theoretical predictions. Another problem is that certain very common signatures (e.g. a single electron) occur more frequently than the triggers can handle. To cope with this flood of events, we may have to program the trigger to record only every n^{th} event, and weight that event to count n times. This is called *prescaling* the trigger. Because weighting up prescaled events reduces our statistical precision, we try to use non-prescaled triggers whenever possible.

2.4 Reconstruction and Identification

In order to perform meaningful particle physics analysis, we must translate the electronic output from the CMS detector into a picture of what particles and objects are present in the event. This is the process of event reconstruction ("reco") and particle identification ("ID"). There are any number of possible algorithms for converting detector signatures into particles. The CMS Collaboration performs its basic reconstruction using a system called particle flow (PF).

2.4.1 Particle Flow

The particle flow algorithm attempts to associate all of the detector readings with particles. It begins by reconstructing all the tracks, calorimeter energy clusters, and vertices in the event. Then, using this information, the algorithm iteratively attempts to reconstruct all the particles in the event using all available detector information. It starts with the easiest objects to identify (muons); once all the muons in an event are reconstructed, the corresponding detector signatures are removed, and the next easiest identifications are attempted, and so on. Each successive ID step uses only the information that has not been consumed by a previous step. Some postprocessing is performed at the end [28].

Charged Tracks and Vertices

As a prelude to reconstructing particles, the PF algorithm begins by reconstructing tracks from the pixel and strip hits in the inner tracker. These tracks are reconstructed using a sophisticated method based on Kalman filtering, which is described in References [35] and [36]. In short, this method attempts to connect hits in successive layers and fit them to a helical trajectory. The method places tunable constraints on the minimum number of sequential hits required, the maximum number of missing “expected” hits, and other quantities to ensure that tracks may be reconstructed to a desired level of quality.

Once all the tracks in the event are identified, they must be grouped into vertices. A vertex is a spot where a collision or decay took place and some number of particles were emitted. Vertices are reconstructed by extrapolating tracks backward to see where they originated from, and finding spots where several tracks intersect. As mentioned previously, a single event may contain multiple proton-proton interactions, as well as decays of intermediate particles, and thus multiple vertices. The vertex associated with the highest sum of squares of track p_T is known as the *primary vertex*, and any others are called secondary. When analyzing an event, we primarily study particles emanating from the primary vertex. Secondary vertices that give rise to pileup are mostly ignored, though displaced secondary vertices may be used in reconstructing other particle signatures.

Calorimeter Clusters

The next step before reconstructing particles is to group the energy deposits in the ECAL and HCAL into clusters. The clustering process is important for differentiating between electrons and photons, and between charged hadrons and neutral hadrons. Each cluster begins with a *seed*–a calorimeter cell whose measured energy is above some defined threshold. From the seed, a cluster is formed by recursively adding in any adjacent cells with sufficient energy, and then fitting the energy distribution with a 2D Gaussian. Separate calibrations are applied in the endcap and barrel of each calorimeter, to account for the differences in geometry and detector layout between the regions [28].

Muons

Once the tracks, vertices, and clusters have been formed, the particle flow algorithm attempts to reconstruct any muons in the event. Among particles, muons are the natural starting point because their signature is very distinctive and usually quite clean. The ideal muon is made by joining a track in the muon system with a track in the inner tracker that lines up appropriately. A muon that comes directly from the collision is expected to have a low value for its *isolation*, a measurement of how much energy and momentum is found within a cone of radius $\Delta R < 0.3$ around the prospective muon. A muon that uses both tracker and muon-system information is known as a *global* muon. Sometimes it may also be possible to reconstruct *tracker-only* muons or *standalone* muons, which use only information from the inner tracker, or the muon system, respectively. Once a muon candidate is identified, the associated tracks are removed from consideration in future identification steps [28].

Electrons and Isolated Photons

Electrons and isolated photons are processed in the same step because the identification of both particles relies on ECAL energy deposits. A potential electron starts out as a charged track that matches up with a suitable ECAL energy deposit; a photon is suspected when there is an ECAL deposit that has no corresponding track. To solidify the identification, a number of further identification criteria are checked in each case.

The shape of the ECAL energy deposit is a key clue used in identifying electrons and photons. As they pass through the tracker, electrons tend to produce *bremsstrahlung*, a shower of photons that radiate off as the electron's path bends. These photons tend to then convert into electron-positron pairs, which may produce further bremsstrahlung, and so on. This cascade, emitted tangent to the curved trajectory of electrons, means that electrons often appear in the ECAL as a pronounced energy deposit with a long tail in the ϕ direction. Photons, by contrast, are not bent by the magnetic field, and thus tend to create rounder energy deposits wherever they strike the ECAL [28].

A number of other criteria are also used in identifying electrons and photons. For example, the track of an electron must be well-aligned with its corresponding ECAL cluster, and the magnitude of the track momentum must be compatible with the energy of the cluster. In addition, the ECAL deposits associated with an electron or photon must not overlap significant HCAL deposits, because certain hadrons can emit photons when they decay. In the case of electrons, these and other criteria are combined and optimized using machine learning techniques. Photons are also subject to an isolation requirement [28].

Hadrons

Once isolated muons, electrons, and isolated photons are removed from the event, the final task is to identify charged and neutral hadrons. However, particle flow also attempts to reconstruct non-isolated photons and muons at this point, because they may be produced when hadrons decay. Wherever a (non-isolated) ECAL deposit is found that is not linked to a track, it becomes a photon; similarly, any HCAL deposits not linked to tracks become neutral hadrons. Any remaining HCAL deposits must be linked to tracks, and are therefore considered to be charged hadrons. When overlaps of ECAL deposits, HCAL deposits, and/or tracks are found, they may be reconstructed as combinations of charged and neutral hadrons and photons [28].

2.4.2 Missing Transverse Energy

As Section 2.2.1 described, the proton beams are stabilized so that they have negligible momentum in the transverse direction. Thus, conservation of momentum implies that the total momentum of all the collision products should also have a negligible transverse component. However, if some particles pass through the detector without interacting, it would look like the total transverse momentum of the event is not zero. Neutrinos are well known for their low probability of interacting with standard detector hardware. In addition, some theories of new physics (such as supersymmetry) predict particles that wouldn't be detected by CMS. It is therefore important to quantify the apparent transverse momentum imbalance in our events.

Momentum conservation tells us that the missing p_T from the invisible particles should be equal and opposite to the vector sum of the p_T of the visible particles:

$$p_T^{\text{miss}} = -1 \cdot \sum_i \vec{p}_T^{\,i} \tag{2.7}$$

For historical reasons, this quantity tends to be called *missing transverse energy*, even though it is actually a momentum. It is formally denoted $E_{\mathrm{T}}^{\text{miss}}$, or in shorthand, MET (for Missing E-sub-T). The particle flow algorithm computes the $E_{\mathrm{T}}^{\text{miss}}$ of the event using the negative vector sum of the p_T of the PF candidates:

$$\text{Particle flow } E_{\mathrm{T}}^{\text{miss}} \text{ (PFMET) } = -1 \cdot \sum_{\text{PF cands}} \vec{p}_T(\text{cand}) \tag{2.8}$$

This information is used in nearly all analyses that involve neutrino production, or are searching for new invisible particles.

2.4.3 Jets

As Section 1.1.1 described, a jet is a spray of hadronic particles produced when a lone parton is ejected from a bound state, and hadronizes with other partons produced from the vacuum. At the reconstruction level, then, a jet is simply a set of charged and neutral hadrons that appear to originate from a common source. If a given event contains only jets that are clearly separated from one another, then grouping particles together into a jet is a simple problem. However, in practice, jets frequently overlap each other, necessitating the use of clustering algorithms to group particles into jets with reasonable boundaries. Numerous jet clustering algorithms have been developed, but the one preferred by CMS is the anti-k_t algorithm [37].

Like many clustering algorithms, the anti-k_t method works by grouping particles together that are "nearby" according to a distance metric d_{ij}. Previous algorithms either ignored the p_T of the particles when computing d_{ij}, or had d_{ij} proportional to the p_T squared. The anti-k_t method is unique in that d_{ij} is *inversely* proportional to the p_T squared of the particles. The advantage of clustering particles this way is that low-momentum particles have less influence on the final shape of the jet, an attribute that is important for accurately measuring the jet energy [37].

2.4.4 Downstream Identification

Particle flow and anti-k_t clustering provide a useful foundation for the reconstruction of particles and jets. However, in practice, these IDs are usually too broad or error-prone for the purposes of cutting-edge science. Therefore, particle physicists will generally add further identification criteria to the objects they plan to use in their research.

The CMS collaboration includes a number of Physics Object Groups (POGs) and Physics Analysis Groups (PAGs) whose mandates include developing and disseminating identification criteria that are suitable for use in analysis. For example, the Muon POG provides recommended muon ID criteria, and the SUSY PAG provides recommended ID criteria for use when searching for supersymmetry.

It is common for a POG to release multiple versions or “working points” (WPs) of their ID criteria, with varying levels of purity vs. acceptance. For example, a “tight” electron ID will contain very stringent criteria, ensuring that very nearly all of the objects selected by such criteria really are electrons, even if a number of genuine electrons are missed. Conversely, a “loose” electron ID will use less stringent criteria, ensuring that nearly all true electrons in the event are selected, even if a number of fake electrons are selected as well.

B-tagging

Certain hadrons formed from bottom quarks have uniquely long lifetimes, carry uniquely high fractions of their parent quark momentum, or tend to decay into leptons. On the basis of these characteristics, it is often possible to identify jets that originated from a bottom quark, a process called *b-tagging*. There exist numerous methods for tagging b-jets, but the one favored by CMS up to this point has generally been the Combined Secondary Vertex (CSV) method [38, 39].

The CSV method relies primarily on information about any secondary vertices within a jet. Even if a jet contains no secondary vertex, it may often be possible to approximate one from the tracks in the jet. The algorithm takes in measurements such as the displacement of the vertex, the number of tracks produced from it, the impact parameter of the tracks with respect to the primary vertex, and many others. This information is fed into a machine learning system, which returns a discriminator value between zero and one, with higher values denoting a greater likelihood that the jet comes from a b-quark [38, 39]. The Btag POG provides recommended WPs for identifying b-tags using this and other discriminators.

2.5 Monte Carlo Simulations

So far, we have discussed in considerable detail how proton-proton collision data are processed at the CMS experiment. After these intricate steps of reconstruction and identification, it becomes difficult to compare measurements of the data against the equations of the Standard Model or BSM theories. We would do better to compare "apples to apples". To facilitate such a comparison, we use Monte Carlo (MC) simulation methods to generate "fake" or simulated data that reflect the predictions of the theories we're interested in testing.

Monte Carlo simulations are typically produced using "generator" software such as aMC@NLO [40], MadGraph [40], or POWHEG [41]. A physicist inputs a desired process, such as top quark pair production, and the generator will simulate a large number of events where that process takes place. These simulations are often then passed to more specialized software such as PYTHIA [42] to add realistic jets.

Once the physics processes in the event have been simulated, the results are run through a simulated version of the CMS detector using the GEANT4 software [43]. GEANT4 is a toolkit for simulating the interactions of particles with matter; using it, we can mimic the responses of the CMS detector to the simulated physics events. We can thus run the same reconstruction algorithms on simulated data as are run on real data. In some cases, the GEANT4 representation (FullSim) is not fast enough for specific needs, so the Monte Carlo simulations are run through *FastSim*, a faster, but sometimes less accurate, reproduction of the CMS detector [44].

Armed with MC datasets that contain the same kind of information as real datasets, we can make detailed comparisons between theoretical predictions and measured results. As an added bonus, we can use the simulated data to better understand the physics behind our real data. The simulated events contain information about the true physics process being simulated, as well as what the detector and reconstruction algorithms would see in such a case, allowing us to map the "reconstruction-level" information about the event back to the underlying "truth-level" information.

2.6 Acknowledgements

This chapter draws from several works authored by the CMS Collaboration. I am but one of over 3000 members of the collaboration. Thus, the work in this chapter represents the collective contributions of thousands of scientists.

All of the works authored by CMS are either technical notes [30, 35, 36], books [27, 29], or websites [24, 26, 31, 32, 33] published by CERN, or are papers published in JINST [23, 25, 28, 34, 38, 39].

Chapter 3

Top Asymmetry Measurements

This chapter will describe the measurements of several asymmetries in events where a top-antitop ($t\bar{t}$) pair decays to a two-lepton final state (2ℓ). This work was performed using the CMS experiment during Run I of the LHC, at both 7 TeV and 8 TeV center-of-mass energies; I will focus on the 8 TeV results, and in particular, my work with the unfolding technique. The 8 TeV analysis led to two publications, which are References [45] and [46].

3.1 Motivation

As mentioned in Section 1.1.1, the top quark is the heaviest known elementary particle, with a mass of ~ 173 GeV [3]. This large mass gives the top quark a number of properties that make it uniquely interesting to study.

In general, a particle's lifetime – how long it tends to exist before decaying to lighter particles – is inversely related to its mass [1]. The top quark, being so heavy, has an extremely short lifetime of $O(10^{-25})$ seconds. This is shorter than the timescales on which hadronization (10^{-24}s) and spin decorrelation (10^{-21}s) normally occur [3, 47], processes that wipe out some information about a quark. Since the top quark decays before these processes can happen, it passes on information about its spin correlation and polarization to its decay products. So studying the decay products of the top quark is one of the only ways we have to measure these properties from a bare, unbound quark.

Additionally, the top quark's large mass places it on the edge of unexplored territory. Because the likelihood of a decay is proportional to the mass difference between the particles involved, many of the heavy new particles predicted by BSM theories would have strong couplings to the top quark. These couplings would naturally cause some of the top quark's properties to deviate from the values predicted by the SM. Thus, precise measurements of properties such as charge asymmetry may tease out links to possible new physics.

There are a few different final states that can result from the decay of $t\bar{t}$ pairs. The top decays to a W boson and a b quark, and the W boson can decay to quarks, or to a lepton and a neutrino. The hadronic W decay has a higher cross-section than the leptonic decay [3], meaning that the more hadrons in the final state, the more data we would have to work with. However, the CMS detector was designed with high-precision lepton reconstruction in mind, and precision is important to these asymmetry measurements. So we choose to study the two-lepton final state, valuing the precision of the lepton reconstruction over higher statistics. The production of a top-antitop pair and its decay to a dilepton final state is depicted in Figure 3.1.

3.2 Previous Measurements

The CDF and D0 experiments on the Tevatron collider at Fermilab made several previous measurements of top charge asymmetry [49, 50, 51, 52], and CDF, D0, and ATLAS made prior measurements of top spin correlation and polarization [53, 54, 55, 56, 57, 58]. The early charge asymmetry measurements [49, 50] were particularly interesting, because they revealed a 2σ deviation from the SM expectation, though later results [51, 52] showed a reduced discrepancy. During Run I of the LHC, it was natural to want to confirm and extend the Tevatron measurements, and to cross-check the ATLAS measurements.

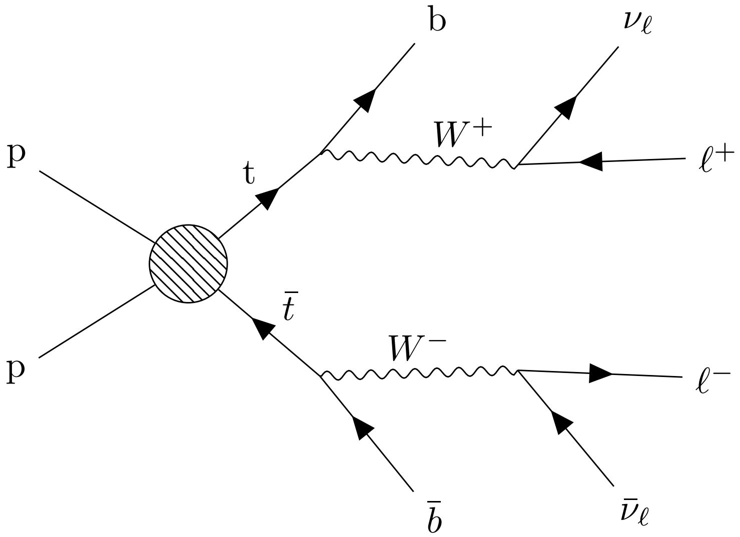

Figure 3.1: Feynman diagram showing a proton-proton collision that produces a $t\bar{t}$ pair, which subsequently decays dileptonically. The two leptons (ℓ) are not necessarily of the same flavor. This diagram was made using the Tikz-Feynman package [48].

The Tevatron collided beams of protons against beams of antiprotons. When such $p\bar{p}$ collisions produce $t\bar{t}$ pairs, we expect the top will tend to travel more along the direction of the proton beam, and the antitop will tend to travel more along the direction of the antiproton beam, so that the difference in their rapidities tends to be positive ($y_t - y_{\bar{t}} > 0$). This case was called “forward”, and the reverse was called “backward”. Thus, given a number of $t\bar{t}$ events from the Tevatron, we can define a forward-backward asymmetry by subtracting the number of backward events from the number of forward ones, and dividing by the total:

$$A_{FB} = \frac{N(\Delta y > 0) - N(\Delta y < 0)}{N(\Delta y > 0) + N(\Delta y < 0)} \tag{3.1}$$

However, the LHC is a proton-proton collider, and as such, there is no naturally favored direction for the top or antitop to travel. As the next section will explain, we must define “forward” and “backward” events somewhat differently.

3.3 Asymmetry Variables

In this analysis, we evaluate six different asymmetries in $t\bar{t} \to \ell\ell$ events, including two charge asymmetries, one polarization variable, and three measures of spin correlation. If any of these variables deviate from their expected SM values, it could potentially be a sign of new physics.

3.3.1 Definitions

As at the Tevatron, the top charge asymmetry was measured at CMS using the rapidity of the top quarks. However, absent a natural direction for the top and antitop to travel, we categorized events as "forward" and "backward" based on which quark had a higher *absolute value* of rapidity. Thus we define our **top charge asymmetry** as:

$$A_C = \frac{N(|y_t| > |y_{\bar{t}}|) - N(|y_t| < |y_{\bar{t}}|)}{N(|y_t| > |y_{\bar{t}}|) + N(|y_t| < |y_{\bar{t}}|)} \tag{3.2}$$

In addition to the top charge asymmetry, we define a similar **leptonic charge asymmetry** to be:

$$A_C^{lep} = \frac{N(|\eta_{\ell^+}| > |\eta_{\ell^-}|) - N(|\eta_{\ell^+}| < |\eta_{\ell^-}|)}{N(|\eta_{\ell^+}| > |\eta_{\ell^-}|) + N(|\eta_{\ell^+}| < |\eta_{\ell^-}|)} \tag{3.3}$$

Though similar to the top charge asymmetry, this variable is based purely on the pseudorapidity of the leptons produced in the decay. We may use the leptons as a proxy for the tops because we expect their direction to be correlated with the directions of their parent tops. One advantage of using only the leptons is that it obviates the need to reconstruct the $t\bar{t}$ system (a process described in Section 3.5), thereby allowing us to include more events in our calculation of this variable. However, this variable also has some dependence on the polarization, so it is not fully correlated with A_C.

Before proceeding further, we must define the *helicity angle*, which will be used in the next two asymmetry variables. The helicity angle θ^*_ℓ is defined as the angle a charged lepton makes in the rest frame of its parent top, relative to the parent top's direction in the $t\bar{t}$ center-of-mass (CM) reference frame. This angle may be defined separately for the positive and negative charged lepton in an event.

The **top polarization** is an asymmetry based on the helicity angles of the charged leptons, and is given by:

$$A_P = \frac{N(\cos(\theta^*_\ell) > 0) - N(\cos(\theta^*_\ell) < 0)}{N(\cos(\theta^*_\ell) > 0) + N(\cos(\theta^*_\ell) < 0)} \tag{3.4}$$

We use both the positively and negatively charged leptons in this asymmetry measurement. A different, commonly used polarization variable, P, can be calculated as $P = 2A_P = 2(A_{P+} + A_{P-})$, if we assume CP-invariance.

Our **top spin correlation** asymmetry, which also depends on the lepton helicity angles, is defined as:

$$A_{c1c2} = \frac{N(\cos(\theta^*_{\ell+}) \times \cos(\theta^*_{\ell-}) > 0) - N(\cos(\theta^*_{\ell+}) \times \cos(\theta^*_{\ell-}) < 0)}{N(\cos(\theta^*_{\ell+}) \times \cos(\theta^*_{\ell-}) > 0) + N(\cos(\theta^*_{\ell+}) \times \cos(\theta^*_{\ell-}) < 0)} \tag{3.5}$$

From this variable, we may also obtain the C spin correlation coefficient, which is given by $C = -4 \times A_{c1c2}$ [59].

We also obtain an indirect measurement of the spin correlation using the **lepton azimuthal asymmetry**. This variable depends on the azimuthal angle between the two leptons, and is defined as:

$$A_{\Delta\phi} = \frac{N(\Delta\phi_{\ell^+\ell^-} > \pi/2) - N(\Delta\phi_{\ell^+\ell^-} < \pi/2)}{N(\Delta\phi_{\ell^+\ell^-} > \pi/2) + N(\Delta\phi_{\ell^+\ell^-} < \pi/2)} \tag{3.6}$$

As with the leptonic charge asymmetry, this variable also relies solely on the charged leptons, and does not require reconstruction of the $t\bar{t}$ system, permitting us to use more events than are available for the top spin correlation.

Finally, we define our **lepton opening angle** asymmetry as:

$$A_{\cos\phi} = \frac{N(\cos(\phi_{\ell\ell}) > 0) - N(\cos(\phi_{\ell\ell}) < 0)}{N(\cos(\phi_{\ell\ell}) > 0) + N(\cos(\phi_{\ell\ell}) < 0)} \tag{3.7}$$

This variable is based on the opening angle between the two leptons in their respective parent top reference frames. From this measured asymmetry, we can calculate the D spin correlation coefficient to be $D = -2 \times A_{\cos\phi}$ [59].

3.3.2 Differential Measurements

In addition to measuring the above six asymmetries in one dimension (*inclusively*), we also measure them in two dimensions (*differentially*), against other physical variables. We chose to make differential measurements because the CDF charge asymmetry discrepancy was more pronounced at $t\bar{t}$ invariant masses above 450 GeV than below 450 GeV [49]. If similar behavior occurs at CMS, in any variable, we would like to observe it. We measured all six of our asymmetry variables differentially with respect to the $t\bar{t}$ invariant mass ($m_{t\bar{t}}$), absolute rapidity ($|y_{t\bar{t}}|$), and transverse momentum ($p_T^{t\bar{t}}$).

3.4 Datasets and Triggers

For this analysis, we use 19.5 fb^{-1} of data from the 8 TeV portion of CMS Run I, encompassing the 2012A through 2012D eras. Because the analysis focuses on a process that produces two leptons in the final state, we use the dilepton datasets A complete list of these datasets is given in Table 3.1.

We use several Monte Carlo datasets to model both the $t\bar{t} \to \ell\ell$ process and any potential background processes. A list of all Monte Carlo datasets used is given in Table 3.2.

To select events from the datasets listed in Table 3.1, we use a set of dilepton triggers that

Table 3.1: List of CMS datasets used in this analysis.

Dataset Name	run range
/DoubleMu/Run2012A-13Jul2012-v1/AOD	190456-193621
/DoubleElectron/Run2012A-13Jul2012-v1/AOD	190456-193621
/MuEG/Run2012A-13Jul2012-v1/AOD	190456-193621
/DoubleMu/Run2012A-recover-06Aug2012-v1/AOD	190949 190945 190906 190895 190782
/DoubleElectron/Run2012A-recover-06Aug2012-v1/AOD	190949 190945 190906 190895 190782
/MuEG/Run2012A-recover-06Aug2012-v1/AOD	190949 190945 190906 190895 190782
/DoubleElectron/Run2012B-13Jul2012-v1/AOD	193834-196531
/DoubleMu/Run2012B-13Jul2012-v1/AOD	193834-196531
/MuEG/Run2012B-13Jul2012-v1/AOD	193834-196531
/DoubleElectron/Run2012C-24Aug2012-v1/AOD	197770- 198913
/DoubleMu/Run2012C-24Aug2012-v1/AOD	197770- 198913
/MuEG/Run2012C-24Aug2012-v1/AOD	197770- 198913
/DoubleElectron/Run2012C-PromptReco-v2/AOD	198934 - 203755
/DoubleMu/Run2012C-PromptReco-v2/AOD	198934 - 203755
/MuEG/Run2012C-PromptReco-v2/AOD	198934 - 203755
/DoubleElectron/Run2012D-PromptReco-v1/AOD	203768 - 208686
/DoubleMu/Run2012D-PromptReco-v1/AOD	203768 - 208686
/MuEG/Run2012D-PromptReco-v1/AOD	203768 - 208686

capture the four possible dilepton flavors. These triggers are listed in Table 3.3.

3.5 Object and Event Selection

We employ a set of physics object and event selections designed to accept as many $t\bar{t} \to \ell\ell$ events as possible while minimizing the number of background events selected.

3.5.1 Object Definitions

For the purpose of our analysis, we consider a lepton to mean an electron or muon. Taus are excluded because of the difficulties in correctly reconstructing and identifying them. We define our leptons using the following criteria:

- Electrons and muons are defined using the recommended 2012 identification criteria provided by their respective POGs. Specifically, electrons use the recommended medium working point, and muons use the recommended tight WP.

Table 3.2: List of CMS Monte Carlo samples used in this analysis.

With Pileup: Processed dataset name is (53) Summer12_DR53X-PU_S10_START53_V7A-v*/AODSIM		
Description	Primary Dataset Name	cross-section [pb]
$t\bar{t}$	/TT_TuneZ2Star_8TeV-mcatnlo (S3)	234
$t\bar{t}$ (alternative)	/TT_CT10_TuneZ2Star_8TeV-powheg-tauola (53)	234
W $\to \ell\nu$+ jets	/WJetsToLNu_TuneZ2Star_8TeV-madgraph-tarball	37509
W $\to \ell\nu$+1 jets	/W1JetsToLNu_TuneZ2Star_8TeV-madgraph-tauola (53)	6663
W $\to \ell\nu$+2 jets	/W2JetsToLNu_TuneZ2Star_8TeV-madgraph-tauola (53)	2159
W $\to \ell\nu$+3 jets	/W3JetsToLNu_TuneZ2Star_8TeV-madgraph-tauola (53)	640
W $\to \ell\nu$+$\geq$ 4 jets	/W4JetsToLNu_TuneZ2Star_8TeV-madgraph-tauola (53)	264
WW	/WWJetsTo2L2Nu_TuneZ2star_8TeV-madgraph-tauola (53)	5.8123
WZ	/WZJetsTo3LNu_TuneZ2_8TeV-madgraph-tauola (53)	1.0575
	/WZJetsTo2L2Q_TuneZ2star_8TeV-madgraph-tauola (53)	2.206
ZZ	/ZZJetsTo2L2Nu_TuneZ2star_8TeV-madgraph-tauola (53)	0.365
	/ZZJetsTo4L_TuneZ2star_8TeV-madgraph-tauola (53)	0.176908
	/ZZJetsTo2L2Q_TuneZ2star_8TeV-madgraph-tauola (53)	2.4487
WG^*	/WGstarToLNu2E_TuneZ2star_8TeV-madgraph-tauola (53)	
	/WGstarToLNu2Mu_TuneZ2star_8TeV-madgraph-tauola (53)	
	/WGstarToLNu2Tau_TuneZ2star_8TeV-madgraph-tauola (53)	
t (s-chan)	/T_TuneZ2Star_s-channel_8TeV-powheg-tauola (53)	3.9
$\bar{t}$ (s-chan)	/Tbar_TuneZ2Star_s-channel_8TeV-powheg-tauola (53)	1.8
t (t-chan)	/T_TuneZ2Star_t-channel_8TeV-powheg-tauola (53)	55.5
$\bar{t}$ (t-chan)	/Tbar_TuneZ2Star_t-channel_8TeV-powheg-tauola (53)	30.0
tW	/T_TuneZ2Star_tW-channel-DR_8TeV-powheg-tauola (53)	11.2
$\bar{t}W$	/Tbar_TuneZ2Star_tW-channel-DR_8TeV-powheg-tauola (53)	11.2
$Z/\gamma^* \to \ell\ell$	/DYJetsToLL_TuneZ2Star_M-10To50filter_8TeV-madgraph (53)	860.5
$Z/\gamma^* \to \ell\ell$	/DYJetsToLL_TuneZ2Star_M-50_8TeV-madgraph-tarball (53)	3532.8
$Z/\gamma^* \to \ell\ell$+$\geq$ 1 jets	/DY1JetsToLL_M-50_TuneZ2Star_8TeV-madgraph (53)	671.83
$Z/\gamma^* \to \ell\ell$+$\geq$ 2 jets	/DY2JetsToLL_M-50_TuneZ2Star_8TeV-madgraph (53)	216.76
$Z/\gamma^* \to \ell\ell$+$\geq$ 3 jets	/DY3JetsToLL_M-50_TuneZ2Star_8TeV-madgraph (53)	61.2
$Z/\gamma^* \to \ell\ell$+$\geq$ 4 jets	/DY4JetsToLL_M-50_TuneZ2Star_8TeV-madgraph (53)	27.6
$t\bar{t}W$	/TTW_TuneZ2Star_8TeV-madgraph (53)	0.23
$t\bar{t}Z$	/TTZ_TuneZ2Star_8TeV-madgraph (53)	0.21
$t\bar{t}\gamma$	/TTGJets_TuneZ2Star_8TeV-madgraph (53)	2.166
$t\bar{t}WW$	/TTWW_TuneZ2Star_8TeV-madgraph (53)	0.002037
WWW	/WWW_TuneZ2Star_8TeV-madgraph (53)	0.08058
WWZ	/WWZNoGstar_TuneZ2Star_8TeV-madgraph (53)	0.05798
WZZ	/WZZNoGstar_TuneZ2Star_8TeV-madgraph (53)	0.01698
ZZZ	/ZZZNoGstar_TuneZ2Star_8TeV-madgraph (53)	0.0055269
WWG	/ WWGJets_TuneZ2Star_8TeV-madgraph (53)	0.528

Table 3.3: List of triggers used in this analysis.

Triggers
Dilepton Sample
`HLT_Mu17_Mu8_v*`
`HLT_Mu17_Ele8_CaloIdT_CaloIsoVL_TrkIdVL_TrkIsoVL_v*`
`HLT_Mu8_Ele17_CaloIdT_CaloIsoVL_TrkIdVL_TrkIsoVL*`
`HLT_Ele17_CaloIdT_CaloIsoVL_TrkIdVL_TrkIsoVL_Ele8_CaloIdT_CaloIsoVL_TrkIdVL_TrkIsoVL_v*`

- We require the leptons to have $p_T > 20$ GeV and $|\eta| < 2.4$.
- We use particle flow-based isolation within a cone of $\Delta R < 0.3$, where absolute isolation must be < 5 GeV, and relative isolation (isolation / p_T) must be < 0.15.
- The PF lepton and the reconstructed lepton must have p_T that differ by < 10 GeV.
- For electrons, we require $E/p_{in} < 4$.

Jets are defined using particle flow. They must have $p_T > 30$ GeV and $|\eta| < 2.4$. They must pass the tight Multi-Variate Analysis (MVA) pileup ID, and they must be separated from leptons by $\Delta R > 0.4$. B-tagging of jets is done using the CSV medium working point, as provided by the b-tag POG. $\vec{E}_{\mathrm{T}}^{\mathrm{miss}}$ is computed by summing up the vector momenta of all particle flow objects, and multiplying by -1.

3.5.2 Event Selections

Using the above object definitions, we select events with exactly two leptons of opposite-sign charge, and at least two jets, including at least one b-tagged jet. Some additional requirements on these objects include:

- To suppress events with low-mass resonances, we require the dilepton invariant mass $M_{\ell\ell} > 20$ GeV.

- For events where the leptons have the same flavor, we require $|M_{\ell\ell} - M_Z| > 15$ GeV to exclude dileptons produced by the Drell-Yan (DY) process.
- We also require $E_{\mathrm{T}}^{\mathrm{miss}} > 40$ GeV in same-flavor events, which further helps to reduce the DY background.

Additionally, we clean our data events using a number of standard event filters. These filters are:

- At least one primary vertex
- Beam scraping events
- Tracking failure
- HBHE noise filter
- EE noise filter
- ECAL/HCAL laser events
- CSCHaloFilter
- Anomalous ρ

3.5.3 Corrections

We make several corrections to our data to remove spurious effects, and to our Monte Carlo simulations to more accurately reflect the properties of the data. In particular:

- We measure the efficiencies of our chosen triggers vs. p_T and η, and reweight MC events to reflect these efficiencies. The measurement technique is described below.

- We use lepton identification and isolation efficiencies measured in a previous but related analysis [60]. As these values agree well with the efficiencies of our MC, we apply no correction, but we do assign a systematic uncertainty, as described in Section 3.9.
- We correct the MC for the efficiency of b-tagging using the CSV discriminator reshaping method.
- We apply the standard Jet Energy Corrections (JECs).
- JECs are propagated to the $E_{\mathrm{T}}^{\mathrm{miss}}$ calculation for jets with $p_T > 10$ GeV, and the $E_{\mathrm{T}}^{\mathrm{miss}}$ is also corrected to remove modulation in ϕ.

Trigger efficiency measurements

We measure the efficiencies of the dilepton triggers listed in Table 3.3 using a method called *tag-and-probe*. The key to this method is the fact that the process $Z \to \ell\ell$ is very clean to reconstruct and has a much higher cross section than its backgrounds. We begin by selecting pairs of leptons that are consistent with a Z boson origin. We require that one of the leptons pass some very tight selection (we call this lepton a tag). The other lepton must pass some looser selection (we call it a probe). The efficiency of a lepton trigger is thus given by the fraction of tag-probe pairs where the probe passes the trigger.

For this analysis, tags must pass our full analysis selections, must have $p_T > 30$ GeV and $|\eta| < 2.1$, and must be matched to the dilepton trigger. Probes need only pass our analysis selections. A tag-probe pair must have opposite charge, and must have an invariant mass within 15 GeV of the Z boson mass. We evaluate the efficiencies of the leading and trailing legs of the dilepton triggers separately. The muon trigger efficiencies are given in Tables 3.4 and 3.5, and the electron trigger efficiencies are given in Tables 3.6 and 3.7.

Table 3.4: Measured efficiency of the Mu8 leg of the HLT_Mu17_Mu8_v* trigger. Uncertainties are statistical only.

p_T range [GeV]	$\|\eta\| < 0.8$	$0.8 < \|\eta\| < 1.2$	$1.2 < \|\eta\| < 2.1$	$2.1 < \|\eta\| < 2.5$
20 - 30	0.979 ± 0.001	0.948 ± 0.002	0.945 ± 0.002	0.925 ± 0.003
30 - 40	0.978 ± 0.001	0.949 ± 0.001	0.939 ± 0.001	0.931 ± 0.002
40 - 60	0.978 ± 0.001	0.948 ± 0.001	0.935 ± 0.001	0.934 ± 0.002
>60	0.979 ± 0.002	0.949 ± 0.004	0.930 ± 0.004	0.932 ± 0.007

Table 3.5: Measured efficiency of the Mu17 leg of the HLT_Mu17_Mu8_v* trigger. Uncertainties are statistical only.

p_T range [GeV]	$\|\eta\| < 0.8$	$0.8 < \|\eta\| < 1.2$	$1.2 < \|\eta\| < 2.1$	$2.1 < \|\eta\| < 2.5$
20 - 30	0.977 ± 0.001	0.937 ± 0.003	0.931 ± 0.002	0.863 ± 0.004
30 - 40	0.976 ± 0.001	0.939 ± 0.001	0.928 ± 0.001	0.890 ± 0.002
40 - 60	0.977 ± 0.001	0.939 ± 0.001	0.926 ± 0.001	0.899 ± 0.002
>60	0.978 ± 0.002	0.941 ± 0.004	0.922 ± 0.004	0.904 ± 0.008

Table 3.6: Measured efficiency of the Ele8 leg of the HLT_Ele17_CaloIdT_CaloIsoVL_TrkIdVL_TrkIsoVL_Ele8_CaloIdT_CaloIsoVL_TrkIdVL_TrkIsoVL_v* trigger. Uncertainties are statistical only.

p_T range [GeV]	$\|\eta\| < 1.5$	$1.5 < \|\eta\| < 2.5$
20 - 30	0.964 ± 0.001	0.979 ± 0.001
30 - 40	0.978 ± 0.001	0.986 ± 0.001
40 - 60	0.982 ± 0.001	0.989 ± 0.001
>60	0.985 ± 0.001	0.991 ± 0.001

Table 3.7: Measured efficiency of the Ele17 leg of the HLT_Ele17_CaloIdT_CaloIsoVL_TrkIdVL_TrkIsoVL_Ele8_CaloIdT_CaloIsoVL_TrkIdVL_TrkIsoVL_v* trigger. Uncertainties are statistical only.

p_T range [GeV]	$\|\eta\| < 1.5$	$1.5 < \|\eta\| < 2.5$
20 - 30	0.964 ± 0.001	0.982 ± 0.001
30 - 40	0.981 ± 0.001	0.990 ± 0.001
40 - 60	0.987 ± 0.001	0.993 ± 0.001
>60	0.988 ± 0.001	0.994 ± 0.001

3.5.4 $t\bar{t}$ System Reconstruction

For some of the asymmetry variables described in Section 3.3.1, it is necessary to reconstruct the $t\bar{t}$ system and its decay chain. This process is challenging because we do not know the exact momenta of the two neutrinos (only the total $E_{\mathrm{T}}^{\mathrm{miss}}$ for the event), and because there is an ambiguity as to which lepton corresponds with which b-jet. In addition, some events have only one medium CSV jet, not two.

In cases with only one medium CSV jet, we treat the next-highest-CSV jet like a second b-tag. We then plug the two b-jets, the lepton four-momenta, and the $E_{\mathrm{T}}^{\mathrm{miss}}$ into an analytical neutrino solver that attempts to reconstruct the $t\bar{t}$ system, assuming a fixed top mass of 172.5 GeV [61]. Of the up to eight possible solutions for each event, this software chooses the one with the greatest matrix weight. In cases where no solution is found, it returns the closest approach to a real solution. If no closest approach solution is possible, we do not use the event in measuring the asymmetries that require $t\bar{t}$ reconstruction (about 16% of events, in both data and MC).

3.6 Background Estimation

In general, the backgrounds in this analysis are estimated using Monte Carlo simulations, normalized based on next-to-leading order (NLO) or next-to-next-to-leading order (NNLO) cross sections. However, we validate these estimates and derive scale factors (SFs) and uncertainties for the backgrounds by comparing them to data in certain control regions. Our largest background is irreducible, namely single-top production in the tW channel. However, this background is known to be well-modeled by MC [62], a fact we verify for ourselves, and therefore it requires no correction. And fortunately, our measurements depend on the shape of the data, and thus are not very sensitive to the normalization of the background components. Finally, as we will see in Section 3.7, our background yields are very small compared to the $t\bar{t} \to \ell\ell$ signal.

Since our signal region (SR) is designed to target the $t\bar{t} \to \ell\ell$ process and exclude backgrounds, we can create control regions (CRs) that target specific background processes by inverting one to two cuts and selections from the SR. We form three broad categories of CRs, each targeting a particular background component, as diagrammed in Figure 3.2. These CRs are described in detail in Table 3.8.

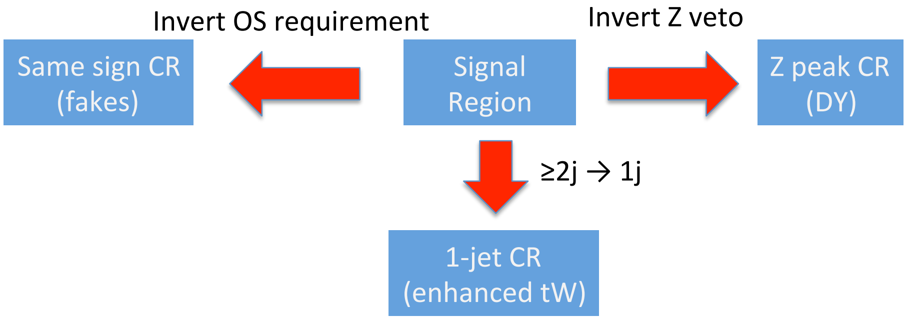

Figure 3.2: Relationships between the SR and the different categories of CRs.

Table 3.8: Summary of control regions. For each "CR*N*" other than CR0, there is a corresponding "CR*N*v", with a b-veto added.

Selection Criteria	Name	Target process
b veto	CR0	DY
Z peak	CR1	DY
Z peak, no $E_{\mathrm{T}}^{\mathrm{miss}}$ cut	CR2	DY
No $E_{\mathrm{T}}^{\mathrm{miss}}$ cut	CR3	DY
1 jet	CR4	tW
Same sign	CR5	Fakes
Same sign, no $E_{\mathrm{T}}^{\mathrm{miss}}$ cut	CR6	Fakes

In each control region, we vary the normalization of the targeted background process until the MC yield matches the data yield in that region. The SF for the DY process is taken from CR1, and the SF for fakes is taken from CR5; in each case, the related CRs are used to derive an envelope of variation that defines the systematic uncertainties on the SFs. These envelopes are depicted in Figure 3.3, and the final SFs and uncertainties are given in Table 3.9. Since CR4 validates the modeling of the tW background, and thus our decision not to apply a SF, we take the

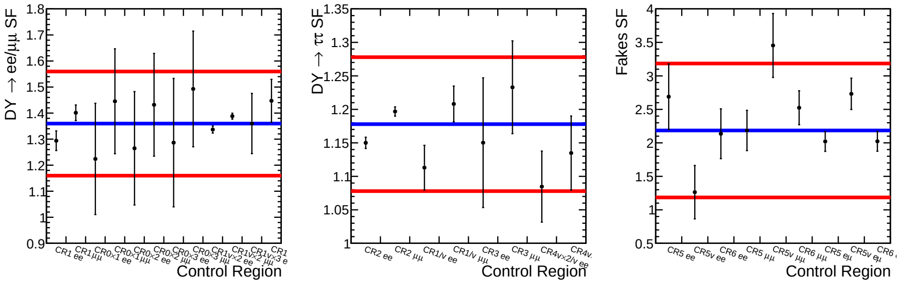

Figure 3.3: SFs measured in different CRs. The blue line depicts the central value, and the red lines give the systematic uncertainty band.

uncertainty on this background component from a CMS cross section measurement of 23.4 ± 5.4 pb [62].

There are a few more backgrounds that come from rare processes. These include $t\bar{t}$ production in association with a W or Z boson or a photon; diboson production (WW, ZZ, WZ); and triboson production (WWW, WWZ, WZZ, ZZZ). The cross sections for these processes are extremely small compared to that for $t\bar{t} \to \ell\ell$, so we predict them directly from MC, and assign a 50% systematic uncertainty. The background from QCD processes is expected to be negligible, a fact we verify in a loosened version of CR5.

Table 3.9: SFs applied to the background components, and their associated uncertainties.

Process	SF
DY→ $ee/\mu\mu$	1.36 ± 0.02 (stat) ± 0.2 (syst)
DY→ $\tau\tau$	1.18 ± 0.01 (stat) ± 0.1 (syst)
fakes	2.18 ± 0.30 (stat) ± 1.0 (syst)
tW	1.00 ± 0.25 (syst)

3.7 Comparison Between Data and Simulation

After applying the event selections and scale factors described in the previous section, our MC-predicted and observed event yields are as shown in Table 3.10. The dileptonic $t\bar{t}$ MC has been rescaled so that the total MC yield equals the total data yield, because we assume that anything that isn't background must be signal. This $t\bar{t} \to \ell\ell$ sample was generated using MC@NLO, and required a scale factor of 0.95 to match the data yield. The original cross section was verified using Powheg. After all scale factors are applied, the total yield is approximately 91% signal and 9% background.

Figure 3.4 provides comparisons between data and Monte Carlo predictions for several of the observables that describe the $t\bar{t}$ system, after all corrections and scale factors have been applied. Figure 3.5 gives the same comparisons for the variables used to calculate our asymmetries. As the plots themselves and the associated ratios show, the MC predictions match the data fairly well, indicating good quality modeling of the background processes and the $t\bar{t} \to \ell\ell$ process.

Table 3.10: Observed and expected yields after applying preselection and scale factors. Yields are scaled to a luminosity of 19.5 fb^{-1}. Uncertainties are statistical only.

Sample	ee	$\mu\mu$	$e\mu$	Total
$t\bar{t} \to \ell\ell$	6313.6 ± 37.7	8975.7 ± 44.1	24651.6 ± 73.4	39940.9 ± 93.6
$t\bar{t} \to \ell+$ jets	107.1 ± 7.7	62.2 ± 5.4	327.4 ± 13.4	496.7 ± 16.4
W+jets	7.3 ± 3.6	1.8 ± 1.8	10.0 ± 3.5	19.1 ± 5.3
single top (s/t-chan, 1ℓ)	2.6 ± 0.6	4.6 ± 0.9	18.8 ± 1.6	26.1 ± 1.9
single top (tW, 2ℓ)	298.0 ± 1.6	425.9 ± 1.9	1161.9 ± 3.1	1885.8 ± 4.0
WW/WZ/ZZ	27.6 ± 1.4	40.7 ± 1.4	89.3 ± 2.3	157.5 ± 3.0
DY $\to ee/\mu\mu$+jets	211.0 ± 16.0	368.0 ± 22.8	1.6 ± 0.5	580.6 ± 27.9
DY $\to \tau\tau$+jets	33.9 ± 2.5	51.5 ± 3.0	137.6 ± 5.1	223.0 ± 6.4
$ttW/Z/\gamma$	86.4 ± 6.5	141.3 ± 8.2	331.6 ± 12.8	559.2 ± 16.5
triboson	1.5 ± 0.1	2.3 ± 0.2	5.2 ± 0.3	9.0 ± 0.4
Total SM MC	7089.0 ± 42.5	10074.0 ± 50.8	26735.0 ± 76.1	43898.0 ± 100.9
Data	7089	10074	26735	43898

3.8 Unfolding

The CMS detector and reconstruction software described in Section 2.2 are not perfect. Neither are our object and event selections and reconstruction methods described in Section 3.5. Because of these imperfections, our measured asymmetry values may be distorted from their true values. In addition, The unique attributes of other experiments may cause their measured

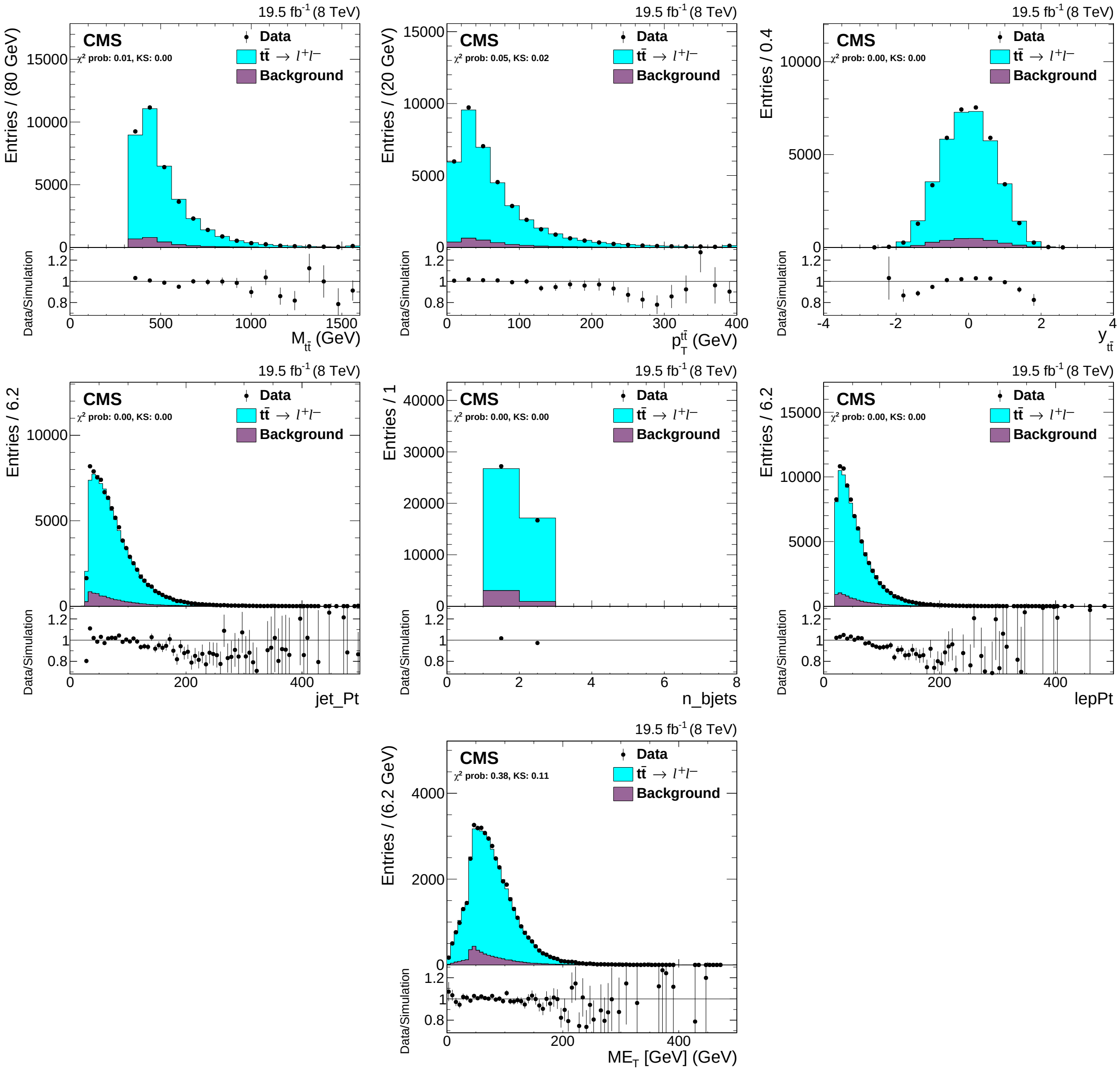

Figure 3.4: Comparison of data with Monte Carlo predictions for selected $t\bar{t}$ observables.

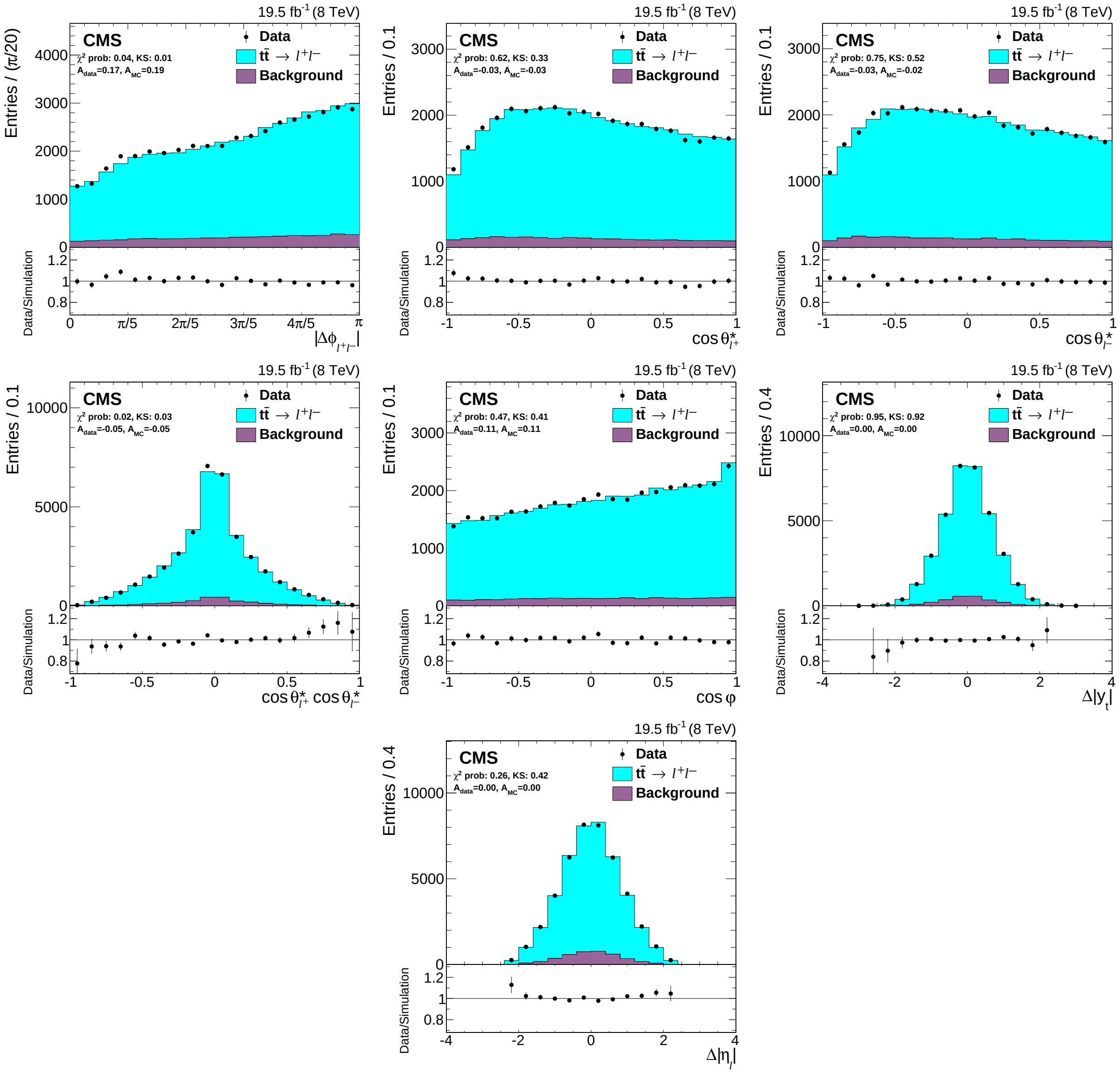

Figure 3.5: Comparison of data with Monte Carlo predictions for the variables used to compute asymmetries. Helicity angles are presented separately for the positively and negatively charged leptons.

asymmetry values to differ from those at CMS. And finally, when theorists make predictions for these asymmetries, they predict the true values, not the values that would be measured by any individual experiment. So in order to compare our results with theoretical predictions, as well as with results measured at other experiments, it behooves us to extrapolate from our measurements backward to the true asymmetry values. We do this using a technique known as *unfolding*.

3.8.1 Background

Unfolding is a technique that can be used to reverse blurring or smearing effects. In other fields it may be known as *deconvolution* or *unsmearing*. The technique originated in signal processing and image processing, but its broad utility has seen it spread to various other scientific and technical disciplines. General unfolding for particle physics is described in detail in References [63] and [64]. For our asymmetry measurements, we use the technique as follows:

Each of the physical observables we use to calculate our asymmetries, such as $\Delta\phi_{\ell\ell}$, may be plotted in a histogram, so that the contents of each bin correspond to some number of events. If the bin contents of our measured histogram are expressed as a vector $\vec{b}$, and the bin contents of the hypothetical "true" histogram for that variable are expressed as a vector $\vec{x}$, then we can model the distorting effects of our detector, reconstruction, etc. using a response matrix that transforms $\vec{x}$ into $\vec{b}$. We choose to split the response matrix into two components, giving us the matrix equation:

$$\vec{b} = SA\vec{x} \tag{3.8}$$

Here, A is the *acceptance* matrix, a diagonal matrix that expresses the fraction of true events from each bin that are actually measured, and not lost to event selection. S is the *smearing* matrix, which describes the fraction of true events from each bin that get measured in other bins due to distortion from reconstruction effects. If we know the values of the matrices S and A, and they are invertible, then we can invert Equation 3.8 to solve for the true distribution, $\vec{x}$, of our variables:

$$\vec{x} = A^{-1}S^{-1}\vec{b} \tag{3.9}$$

Unfolding is an example of an *inverse problem*, because it takes effects and attempts to extrapolate back to their causes. And like many other inverse problems, this one is mathematically *ill-posed*, because a small fluctuation in the measured distribution, $\vec{b}$, can cause a much larger fluctuation in the unfolded solution, $\vec{x}$ [64]. To curtail these fluctuations, we employ a technique called *regularization*.

Regularization is the act of adding additional constraints to the unfolding process, in the hope of making the unfolded result more accurate to the true distribution. If we know (or believe) that the true distribution $\vec{x}$ should have certain properties, we can constrain the unfolding process so that the output will be more likely to have those properties too [63].

To regularize our unfolded results, we supply the truth-level Monte Carlo distributions of our variables as *bias distributions*, essentially templates for what the unfolded result should resemble. In particular, we ask that the unfolded result should attempt to mimic the curvature (i.e. the second derivative) of the bias distribution. The strength of the regularization constraint is determined by a parameter τ. Choosing a small value for τ will give less regularization, and lead to more statistical fluctuations in the output; choosing a large value of τ will give heavy regularization, and strongly constrain the output to resemble the bias distribution. In truth, any amount of regularization must introduce some degree of bias into our measurements. So, in Section 3.8.4 I describe the tests we perform to quantify the amount of introduced bias.

3.8.2 One-Dimensional Unfolding Procedure

When choosing how to bin histograms that will be unfolded, one must strike a balance. If there are too many narrow bins, one risks causing statistical fluctuations in the output. But with too few bins, one loses resolution in the measurement. For the asymmetry variables that require us to reconstruct the $t\bar{t}$ system, we discovered the ideal balance was to have six bins in the truth level distribution $\vec{x}$. However, for the variables that only require lepton reconstruction, we have more statistics and finer resolution, allowing us to use 12 bins at truth level. In both cases we use twice as many bins for the reconstruction-level distribution $\vec{b}$ to avoid a quirk of the numerical method that would make the problem seem artificially well-posed [64]. We choose to bin our variables so that the number of events in each bin is approximately equal. The specific bins chosen are given in Table 3.11. The reconstruction-level bins are formed by simply dividing the truth-level bins in half.

For each asymmetry variable, we calculate the fraction of true Monte Carlo events in each bin that pass our selections. These values then become the diagonal entries of the acceptance matrix, A. Because our event selections are slightly different for same-flavor and opposite-flavor dileptons, we calculate and apply separate acceptance matrices for each case. In Figure 3.6, we show the acceptance matrices for each asymmetry, after combining the two dilepton flavors in appropriate proportion.

The smearing matrices S are generated based on Monte Carlo simulations. Each simulated event is placed into a 2D histogram with the gen-level asymmetry variable on the y-axis and the reco-level asymmetry variable on the x-axis. The unfolding software then converts the histogram bins into elements of the smearing matrix. These histograms are presented in Figure 3.7. The histograms that represent the smearing matrices for the leptonic variables have almost no off-diagonal components, reflecting the high quality of our lepton reconstruction. For the variables that require $t\bar{t}$ system reconstruction, the smearing is noticeable, and may be due to detector effects or to the limitations of the $t\bar{t}$ reconstruction software. At any rate, these smearing matrices are nearly symmetric about the diagonal. This fact indicates that reconstruction introduces little to no bias, and simply dilutes the true asymmetry.

As described in Section 3.8.1, the choice of the regularization strength parameter, τ, will

Table 3.11: Truth-level bins chosen for 1D unfolding of asymmetry variables.

Variable	B1	B2	B3	B4	B5	B6
A_C	[-∞,-22/30]	[-22/30,-10/30]	[-10/30,0]	[0, 10/30]	[10/30, 22/30]	[22/30, ∞]
A_P	[-1,-2/3]	[-2/3,-1/3]	[-1/3,0]	[0, 1/3]	[1/3, 2/3]	[2/3, 1]
A_{c1c2}	[-1,-2/5]	[-2/5,-1/6]	[-1/6,0]	[0, 1/6]	[1/6, 2/5]	[2/5, 1]
$A_{\cos\phi}$	[-1,-2/3]	[-2/3,-1/3]	[-1/3,0]	[0, 1/3]	[1/3, 2/3]	[2/3, 1]

Variable	B1	B2	B3	B4	B5	B6
A_C^{lep}	[-∞,-34/30]	[-34/30,-24/30]	[-24/30,-16/30]	[-16/30, -10/30]	[-10/30, -4/30]	[-4/30, 0]
$A_{\Delta\phi}$	[0, $5\pi/60$]	[$5\pi/60$,$10\pi/60$]	[$10\pi/60$,$15\pi/60$]	[$15\pi/60$, $20\pi/60$]	[$20\pi/60$, $25\pi/60$]	[$25\pi/60$, $30\pi/60$]
	B7	B8	B9	B10	B11	B12
A_C^{lep}	[0, 4/30]	[4/30, 10/30]	[10/30, 16/30]	[16/30, 24/30]	[24/30, 34/30]	[34/30, ∞]
$A_{\Delta\phi}$	[$30\pi/60$, $35\pi/60$]	[$35\pi/60$,$40\pi/60$]	[$40\pi/60$,$45\pi/60$]	[$45\pi/60$, $50\pi/60$]	[$50\pi/60$, $55\pi/60$]	[$55\pi/60$, π]

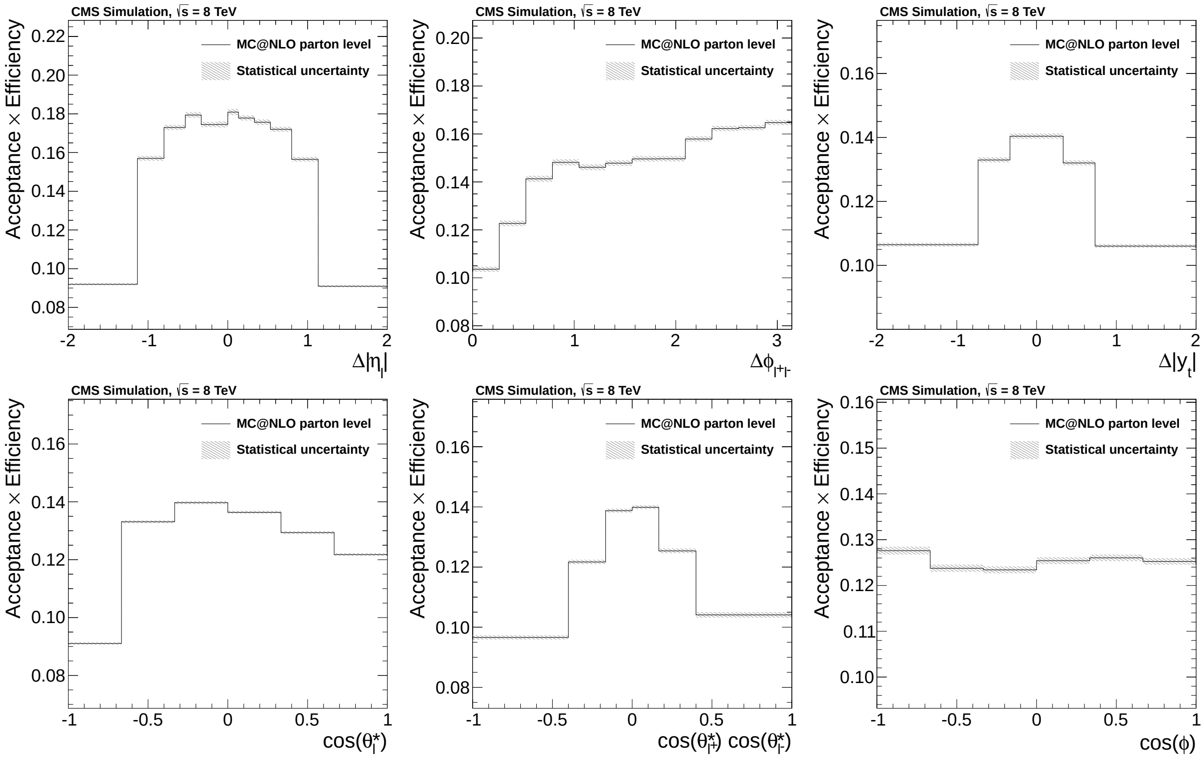

Figure 3.6: Acceptance matrices for the six asymmetry variables. Since all off-diagonal matrix elements are zero, only the diagonal elements are plotted.

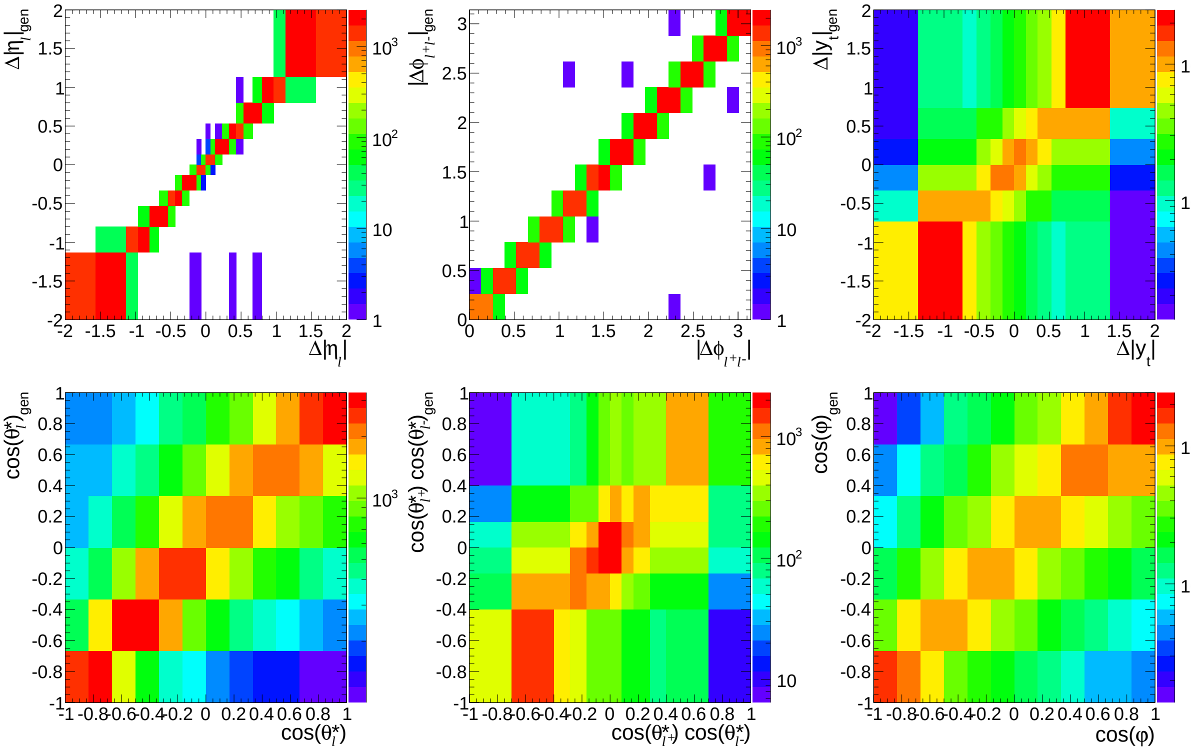

Figure 3.7: Smearing matrices for the six asymmetry variables.

impact both the amount of statistical fluctuation in the unfolded distribution, and the amount of bias. There are many ways to choose the optimal value of this parameter. We use the method of minimizing the mean of the global correlation coefficients, which is also favored by Blobel [64]. The values of τ we arrive at this way are presented in Table 3.12. To validate these values, we check how the unfolded asymmetries and their uncertainties vary as we scale τ up and down by up to a factor of 100. As expected, the uncertainties become larger as τ is decreased; as τ is increased, the asymmetry central value shifts, indicating the addition of bias. From this behavior, we deduce that our choices for τ are appropriate. The dependence of the asymmetries and their uncertainties on the choice of τ is shown in Figure 3.8.

Table 3.12: Optimized τ values chosen for each asymmetry.

Asymmetry	A_C^{lep}	$A_{\Delta\phi}$	A_C	A_P	A_{c1c2}	$A_{\cos\phi}$
τ value	0.000185	0.000166	0.000110	0.000075	0.000089	0.000098

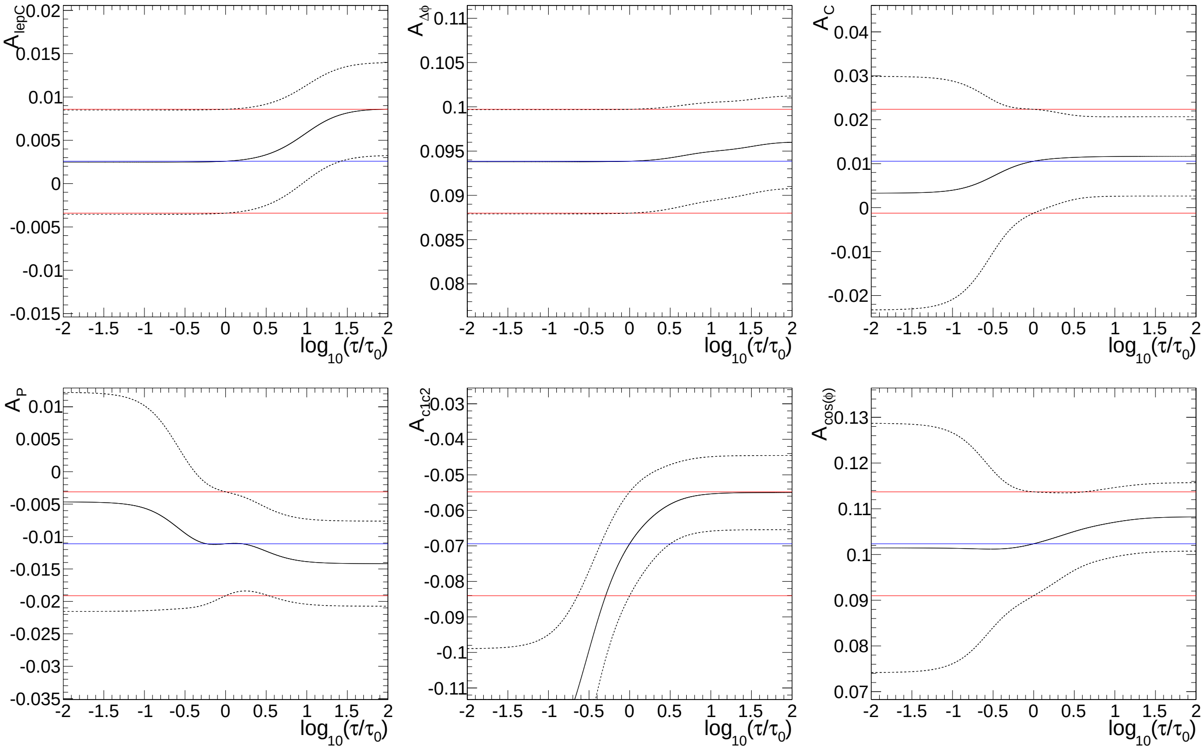

Figure 3.8: Dependence of unfolded asymmetries and uncertainties on the regularization strength, τ. Blue lines denote the nominal unfolded asymmetry, and red lines denote the nominal uncertainty bounds. Black lines show how these values vary with τ.

We perform the actual regularized unfolding using the TUnfold package [65]. We chose TUnfold because it provides good support for two-dimensional unfolding, a process described in the next section. The results of the one-dimensional unfolding are presented in Section 3.10.1. The tests for bias due to regularization are presented in Section 3.8.4.

3.8.3 Two-Dimensional Unfolding Procedure

As described in Section 3.3.2, we also wish to measure our asymmetries differentially with respect to three different kinematic variables – the mass, absolute rapidity, and transverse momentum of the $t\bar{t}$ system. For our asymmetry variables, we use the same binning described in Table 3.11. For the secondary variables, our chosen binning is described in Table 3.13.

The procedure for unfolding these two-dimensional distributions is nearly identical to

Table 3.13: Bins chosen for kinematic variables in differential measurements.

Secondary Variable	B1	B2	B3
$m_{t\bar{t}}$ (GeV)	[0, 430]	[430,530]	[530,∞]
$p_T^{t\bar{t}}$ (GeV)	[0,41]	[41,92]	[92,∞]
$\lvert y_{t\bar{t}} \rvert$	[0,0.34]	[0.34,0.75]	[0.75,∞]

the procedure for unfolding one-dimensional distributions. We convert our two-dimensional distributions into one-dimensional distributions by essentially "unwrapping" the 2D histogram into a 1D histogram. If the 2D histogram has the familiar 6(12) bins on the x-axis, and 3 rows (i.e. bins) on the y-axis, we concatenate those three rows together to form a 1D histogram (a single row) with 18(36) bins. We can then unfold the unwrapped distribution, and re-wrap it to obtain the differential asymmetry measurements. The correspondence between the wrapped and unwrapped histograms is shown in Figure 3.9.

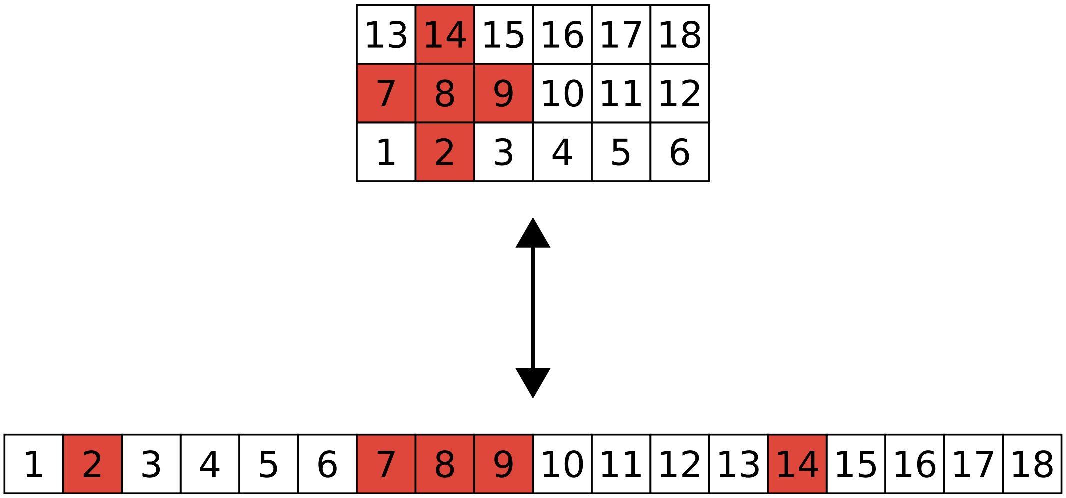

Figure 3.9: Comparison between wrapped 2D histogram and unwrapped 1D histogram. Each numbered box corresponds to a histogram bin. Bin 8 and its adjacent bins are highlighted in red to illustrate how adjacency is not always preserved by the unwrapping process.

The smearing and acceptance matrices used for unfolding in two dimensions follow this same unwrapping scheme, but are otherwise derived identically to those for 1D unfolding. The regularization parameter τ is chosen for 2D unfolding just as it was for 1D unfolding, by finding the value that minimizes the mean of the global correlation coefficients. As an example, the τ values used for 2D unfolding vs. $m_{t\bar{t}}$ are given in Table 3.14.

Table 3.14: Optimized τ values used to unfold each asymmetry differentially with respect to $m_{t\bar{t}}$.

Asymmetry	A_C^{lep}	$A_{\Delta\phi}$	A_C	A_P	A_{c1c2}	A_ϕ
τ value	0.000426	0.000422	0.000144	0.000102	0.000120	0.000121

Our regularization procedure was already described in Section 3.8.1; however, there is an additional subtlety introduced in two-dimensional unfolding. Because the distribution we are unfolding is actually an “unwrapped” two-dimensional distribution, we do not want to regularize the curvature at the boundaries between unwrapped rows. In addition, we also wish to regularize in the secondary variable. In the unwrapped distribution, this means we must regularize bins that are no longer adjacent. Using Figure 3.9 as an example, bin 8 must be regularized with bins 7, 9, 2, and 14; however, bins 12 and 13 must not be regularized with each other. We specifically chose to use TUnfold because it natively supports such complex regularization schemes [65]. The results of the 2D unfolding procedure are presented in Section 3.10.2, and the bias tests are described in the next section.

3.8.4 Bias Tests

As described in Section 3.8.1, regularization introduces some amount of bias to our unfolded results because it forces the results to take on characteristics of a distribution we supply. But since regularization is important for controlling statistical fluctuations in the output, we cannot abandon it entirely. We must therefore try to quantify the amount of bias introduced by regularization, and judge whether or not it is acceptable.

To test the amount of bias introduced by regularization, we perform *linearity tests* on our asymmetries. For each asymmetry, we begin by reweighting the $t\bar{t} \to \ell\ell$ Monte Carlo events using a linear function of the measured variable. For example, the top charge asymmetry is defined in terms of the measured variable $|y_t| - |y_{\bar{t}}|$ (see Equation 3.2), so the reweighting equation would be:

$$\text{weight} = 1 + K \cdot (|y_t| - |y_{\bar{t}}|) \tag{3.10}$$

For other asymmetries, substitute the appropriate measured variable into this expression. The parameter K is varied between -0.3 and 0.3 in steps of 0.1. This reweighting artificially induces asymmetries of up to 25% in the simulated data, which is much larger than anything we would expect from Standard Model or BSM physics.

For each K value, we make 10,000 copies of the measurement histogram, and in each copy we fluctuate the various bin contents randomly up and down according to Poisson statistics. Each of these fluctuated histograms is called a *pseudoexperiment* (PE), because the Poisson fluctuation approximates what we might see if we ran our experiment again. Each of the 10,000 pseudoexperiments is unfolded, and we compare the average of those unfolded asymmetries against the original, artificially-induced asymmetry. Figure 3.10 shows plots of the average unfolded asymmetry vs. the induced asymmetry for each of the seven K values. We fit these plots with a straight line, and record the slope and offset (or intercept) of the line. The slope tells us by what factor any asymmetry in the data will be scaled up or down by regularization. The offset tells us how much asymmetry will be added or subtracted by the regularization. These slopes and offsets are listed in Table 3.15. Most of the offsets are zero (the largest is 0.2%), meaning regularization will add essentially zero asymmetry that isn't there. The slopes are all close to 1.0, meaning regularization will not enhance or reduce any asymmetry in our data by any appreciable amount. The largest slope is 1.024 for A_{c1c2}, meaning this asymmetry could be exaggerated by up to 2.4% by regularization. We consider this an acceptably small amount of bias. This information is also taken into consideration when evaluating our systematic uncertainty due to regularization, described in Section 3.9.

In addition to the linearity tests, we also verify that the unfolding uncertainties are

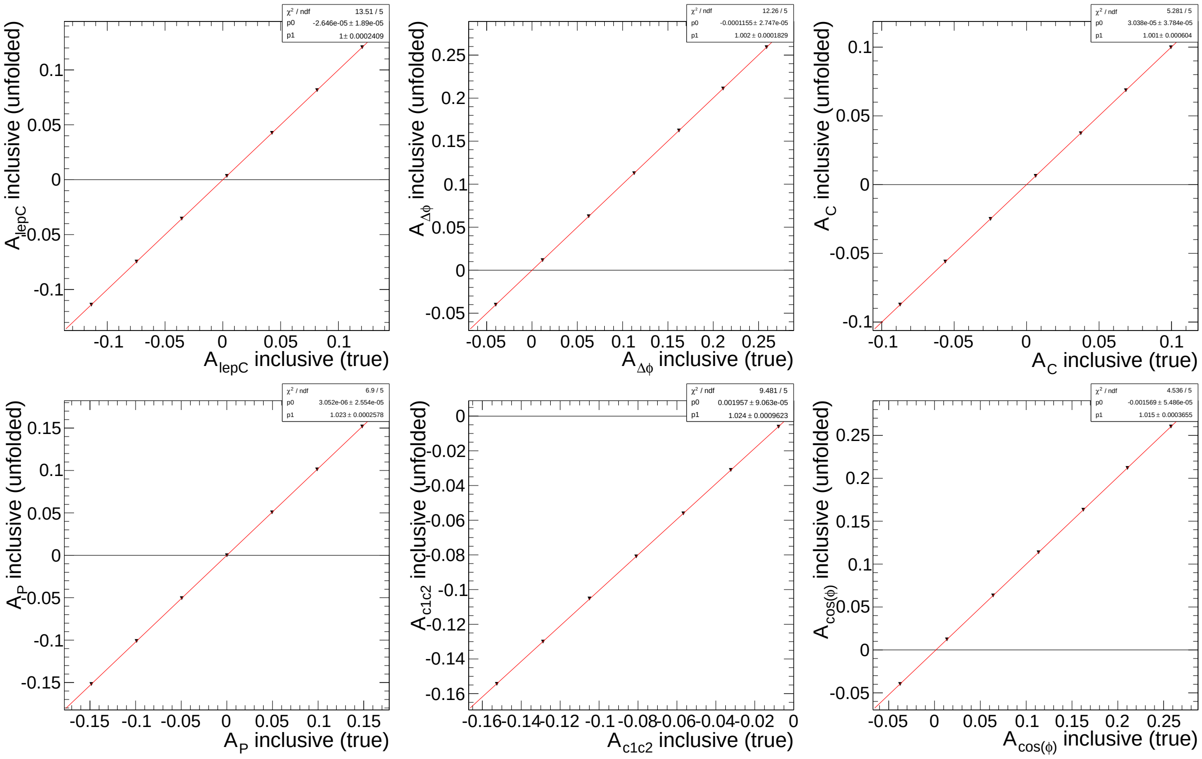

Figure 3.10: Results of the linearity tests. Artificially induced asymmetry values are on the x-axis, and average unfolded asymmetries are on the y-axis.

Table 3.15: Parameters describing the fit to the linearity test results.

Variable	offset	slope
A_C^{lep}	0.000 ± 0.000	1.000 ± 0.000
$A_{\Delta\phi}$	0.000 ± 0.000	1.002 ± 0.000
A_C	0.000 ± 0.000	1.001 ± 0.000
A_P	0.000 ± 0.000	1.023 ± 0.000
A_{c1c2}	0.002 ± 0.000	1.024 ± 0.000
A_ϕ	-0.002 ± 0.000	1.015 ± 0.000

estimated correctly by examining the *pulls* of the pseudoexperiments for each value of K. The pull is defined as:

$$\text{Pull} = \frac{A_{\text{true}} - A_{\text{unfolded}}}{\sigma(A_{\text{unfolded}})} \tag{3.11}$$

When we plot these pulls for all observables and all values of K, we find that they are gaussian distributed with a width of 1.0, meaning that $\sigma(A_{\text{unfolded}})$ is estimated correctly. Figure 3.11 shows these pull distributions for the example case of $K = 0$. Figure 3.12 shows the pull widths as a function of the induced asymmetries.

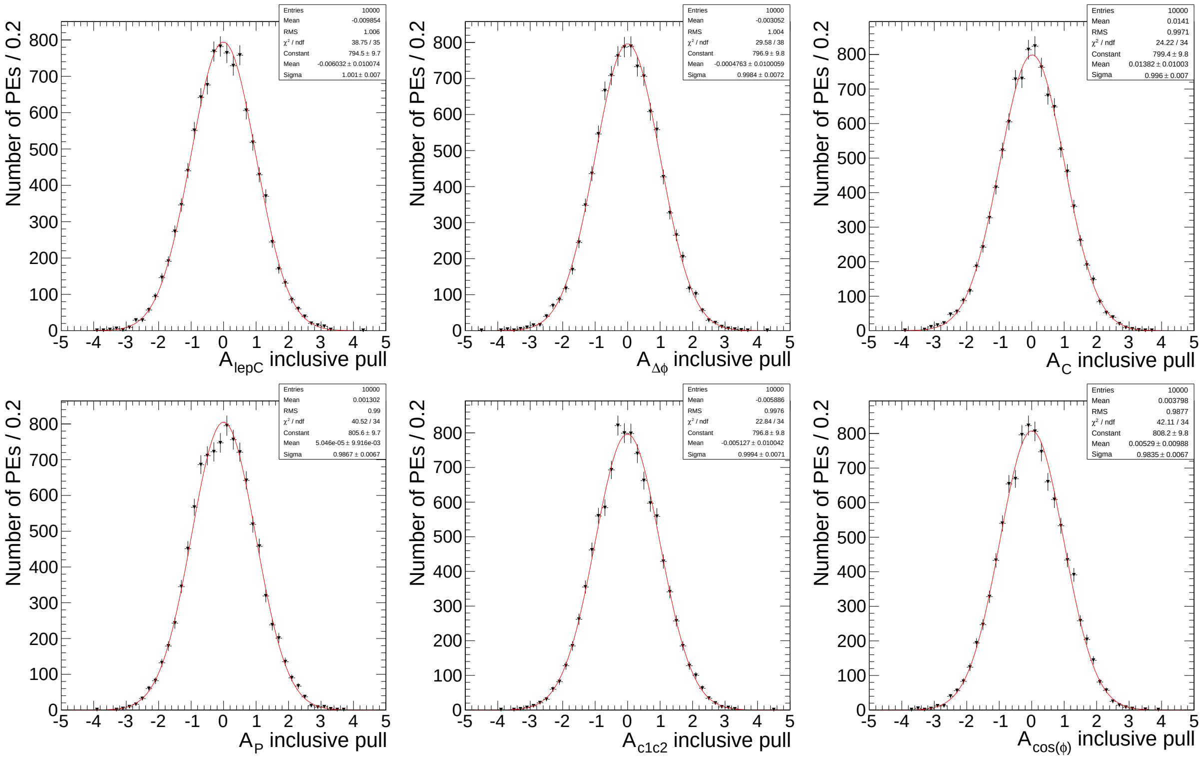

Figure 3.11: Pull distributions for the example case $K = 0$.

3.9 Systematic Uncertainties

There are a number of possible mechanisms by which uncertainty may be introduced into our asymmetry measurements. Most of these sources of systematic uncertainty relate to imperfect

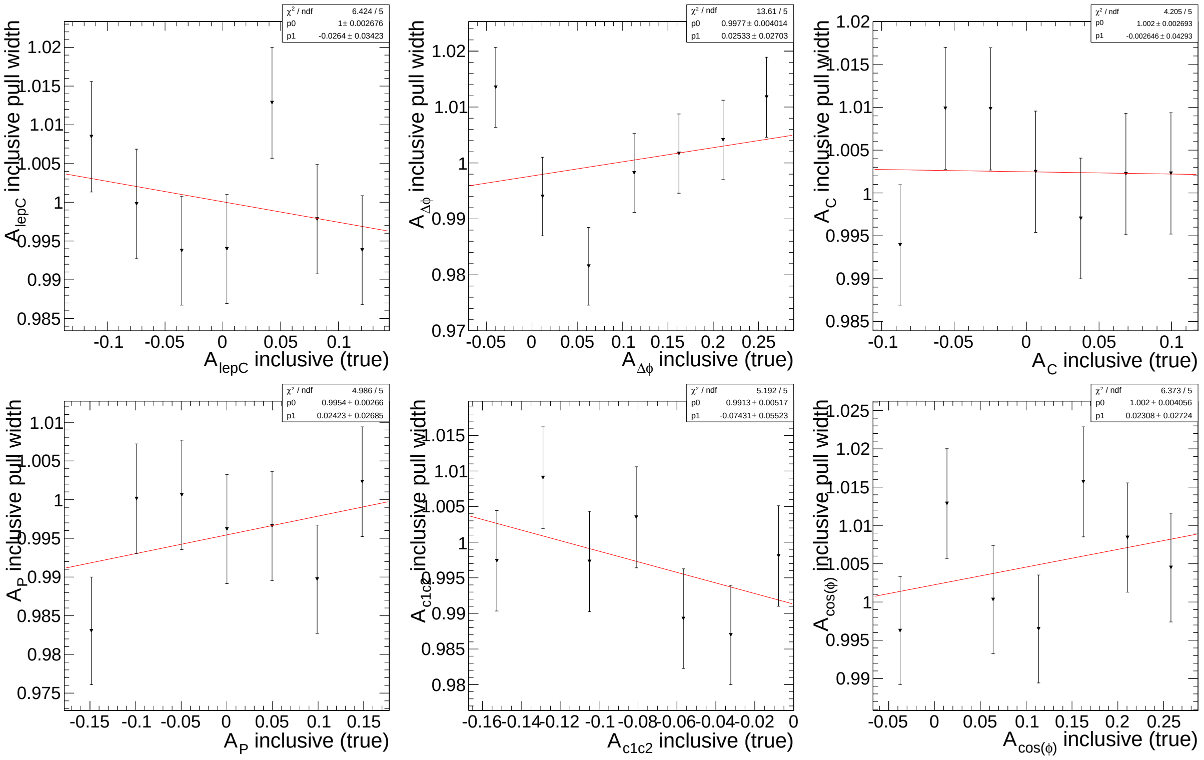

Figure 3.12: Pull widths for unfolded asymmetries vs. induced asymmetry values. Each data point corresponds to a single K value. These results are consistent with pull widths of 1.

modeling of the physics in our Monte Carlo simulations, or to the workings of the CMS detector and software. The ways in which we assign uncertainties to these effects are discussed below. We will give special consideration to the uncertainty due to regularization.

Our experimental systematic uncertainties are evaluated as follows:

- **Lepton selection:** We correct the Monte Carlo simulations so that the lepton trigger efficiencies, and the efficiencies of lepton identification and isolation, reflect those measured in actual data. The scale factors used in these corrections never deviate from 1.0 by more than 2%, so we vary all the scale factors by 2% to obtain the lepton selection systematic.
- **Lepton energy scale:** Comparisons between data and Monte Carlo for $Z \to \ell\ell$ events have shown that the uncertainty on electron energy scales is approximately 0.5%; for muons, this uncertainty is negligible. Therefore we evaluate a systematic on the electron energy

scale by varying that scale by 0.5%.

- **Jet energy scale (JES):** The uncertainty from JES corrections is evaluated by varying those corrections within their uncertainties, and propagating the effect to the $E_{\mathrm{T}}^{\mathrm{miss}}$. We properly account for the effects this has on our event selections, and on the $t\bar{t}$ system reconstruction.
- **Jet energy resolution (JER):** This uncertainty is evaluated similarly to the uncertainty on the JES. However, the JER is varied by 5-10% depending on the η of the jet.
- **Background estimation:** We vary the normalizations of our backgrounds by the uncertainties evaluated in Section 3.6.
- **Pileup (PU) modeling:** We vary the pileup reweighting scale factors by $\pm 1\sigma$.
- **b-tagging:** We reweight MC events to correctly model the efficiency of b-tagging b and c quarks. These scale factors are varied by $\pm 1\sigma$.

In addition, there are several uncertainties on our modeling of the $t\bar{t} \to \ell\ell$ process. These uncertainties are evaluated as follows:

- **Factorization and renormalization scales:** We evaluate the uncertainty by substituting MC@NLO $t\bar{t}$ samples that have these two values scaled both up and down by a factor of 2.
- **Top quark mass:** As described in Section 3.5.4, we use 172.5 GeV for our top quark mass. To evaluate the systematic on this value, we use $t\bar{t}$ MC samples with the top mass varied by ± 3 GeV, and interpolate down to an effective variation of ± 1 GeV.
- **Parton distribution functions (PDFs):** The systematic uncertainty on PDFs was evaluated using the then-current PDF4LHC recommendations [66].
- **Top p_T reweighting:** Since the effects of top p_T reweighting were not fully understood, we assigned a conservative 100% systematic to the reweighting.

Evaluating most of these systematics requires us to regenerate the smearing and acceptance matrices using reweighted Monte Carlo simulations, and then reapply the unfolding procedure. In addition, we evaluate the systematic uncertainty due to limited **Monte Carlo statistics** by propagating the uncertainty on the smearing matrix to the unfolded result.

Regularization Systematic

At the time this analysis was published, there was no standard way to evaluate a systematic uncertainty on regularization. We therefore had to devise our own method. We wished to isolate the effect of regularization from other potential systematics related to the unfolding. Specifically, we wished to separate regularization uncertainty from any uncertainty that might arise if the MC used to fill the smearing matrix is discrepant from real data. We argued that any mismodeling in S is already covered by the other systematic uncertainties described above.

To evaluate the systematic uncertainty due to regularization, we reweight the bias distribution to match the data, and compare that unfolded result to the nominal. This procedure should isolate the effect of the regularization from any other sources of uncertainty. As Section 3.10 shows, the uncertainty we obtain this way is less than 0.001 on all asymmetry variables – far smaller than the statistical uncertainty on the results.

As a cross-check on the small size of this uncertainty, we use pseudoexperiments to estimate the statistical uncertainty on our choice of regularization strength, τ. This check also gives an uncertainty of < 0.001 on all asymmetries. Further, this small uncertainty is consistent with the findings from Section 3.8.4, that the bias induced by regularization is a very small fraction of the total asymmetry.

To validate the claim that any mismodeling of the smearing matrix is covered by other systematics, we try reweighting both the bias distribution and S together. The uncertainty produced by this test is still smaller in magnitude than the sum of the other systematics, so we can be confident that those systematics cover any mismodeling in S.

Finally, we verify that the regularization term contributes only a small amount to the χ^2 that is minimized in the unfolding procedure.

The systematic uncertainties on our asymmetry measurements are summarized in Table 3.16.

Table 3.16: Systematic uncertainties on the inclusive unfolded asymmetry measurements.

Asymmetry variable	A_C	A_C^{lep}	$A_{\Delta\phi}$	$A_{\cos\phi}$	A_{c1c2}	A_P
experimental systematic uncertainties						
Jet energy scale	0.001	0.000	0.001	0.005	0.007	0.018
Jet energy resolution	0.002	0.000	0.000	0.001	0.002	0.003
Lepton energy scale	0.001	0.000	0.001	0.002	0.005	0.003
b-tagging efficiency	0.001	0.000	0.000	0.001	0.001	0.001
Lepton selection	0.000	0.000	0.001	0.000	0.000	0.002
Pileup	0.000	0.000	0.000	0.000	0.000	0.000
Background	0.001	0.001	0.001	0.001	0.001	0.002
$t\bar{t}$ modeling uncertainties						
Top quark mass	0.001	0.001	0.001	0.001	0.007	0.008
Fact. and renorm. scales	0.003	0.002	0.002	0.003	0.005	0.002
Parton distribution functions	0.001	0.001	0.004	0.005	0.005	0.001
Hadronization	0.003	0.000	0.001	0.004	0.005	0.019
Unfolding (simulation statistics)	0.005	0.002	0.002	0.005	0.006	0.003
Unfolding (regularization)	0.000	0.000	0.000	0.000	0.000	0.000
Top quark p_T	0.001	0.000	0.011	0.006	0.006	0.004
Total systematic uncertainty	0.007	0.003	0.012	0.012	0.016	0.028
Total uncertainty (inc. data stat.)	0.013	0.006	0.013	0.016	0.021	0.029

3.10 Results

3.10.1 One-Dimensional Results

After subtracting the background and unfolding, distributions for our six asymmetry variables are shown in Figure 3.13, along with SM parton-level predictions using MC@NLO and NLO+EW predictions. The measured asymmetry values with uncertainties and the MC@NLO

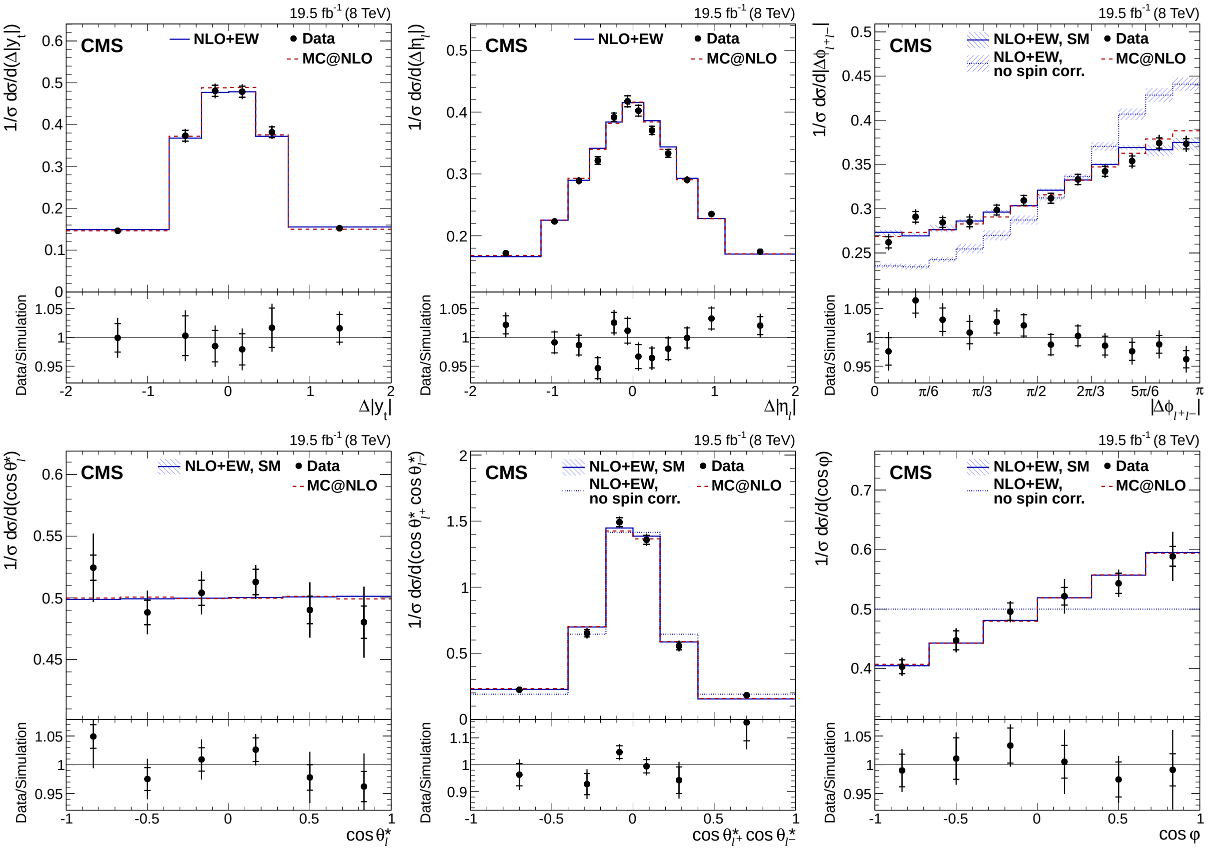

Figure 3.13: Distributions of asymmetry variables after unfolding, and simulations and theoretical predictions.

Table 3.17: Asymmetry values measured after unfolding, compared to predictions from simulation. Uncertainties on measurements are statistical and systematic; uncertainties on simulation are statistical only.

Variable	Data	MC
A_C	$0.011 \pm 0.011 \pm 0.007$	0.006 ± 0.001
A_C^{lep}	$0.003 \pm 0.006 \pm 0.003$	0.004 ± 0.001
$A_{\Delta\phi}$	$0.094 \pm 0.005 \pm 0.012$	0.113 ± 0.001
$A_{\cos\phi}$	$0.102 \pm 0.010 \pm 0.012$	0.114 ± 0.001
A_{c1c2}	$-0.069 \pm 0.013 \pm 0.016$	-0.081 ± 0.001
A_P	$-0.011 \pm 0.007 \pm 0.028$	0.000 ± 0.001

predictions are presented numerically in Table 3.17. All six asymmetries are consistent with the predictions; thus, we do not observe any significant deviations from the Standard Model expectation.

3.10.2 Two-Dimensional Results

After 2D unfolding, the six asymmetries, along with MC@NLO and NLO+EW predictions, are presented differentially with respect to $m_{t\bar{t}}$, $|y_{t\bar{t}}|$, and $p_T^{t\bar{t}}$ in Figures 3.14 and 3.15. The overall values of these 2D-unfolded asymmetries, and the corresponding MC predictions, are presented in Table 3.18. The asymmetry values for each bin in the secondary variables are presented in Table 3.19. The overall 2D-unfolded asymmetries are consistent with the MC predictions; therefore, we do not observe any discrepancy from the Standard Model expectation.

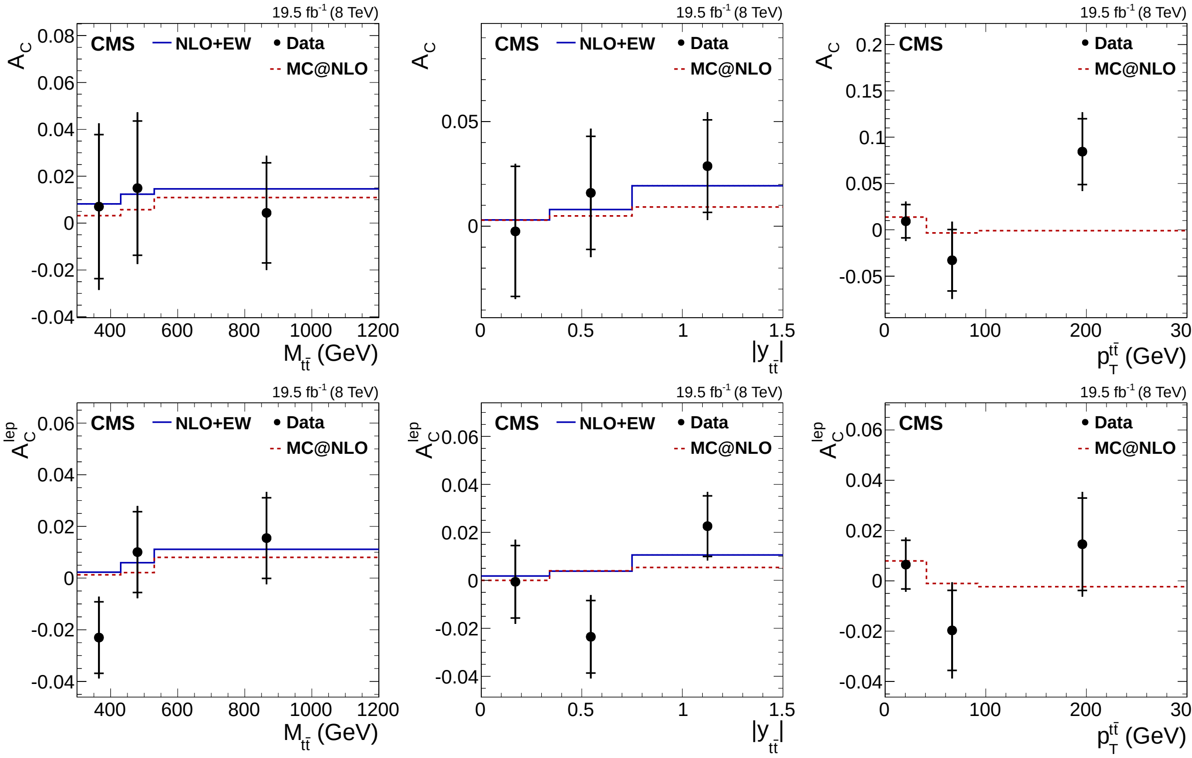

Figure 3.14: Unfolded charge asymmetry values as a function of the three secondary kinematic variables. The last bin includes any overflow.

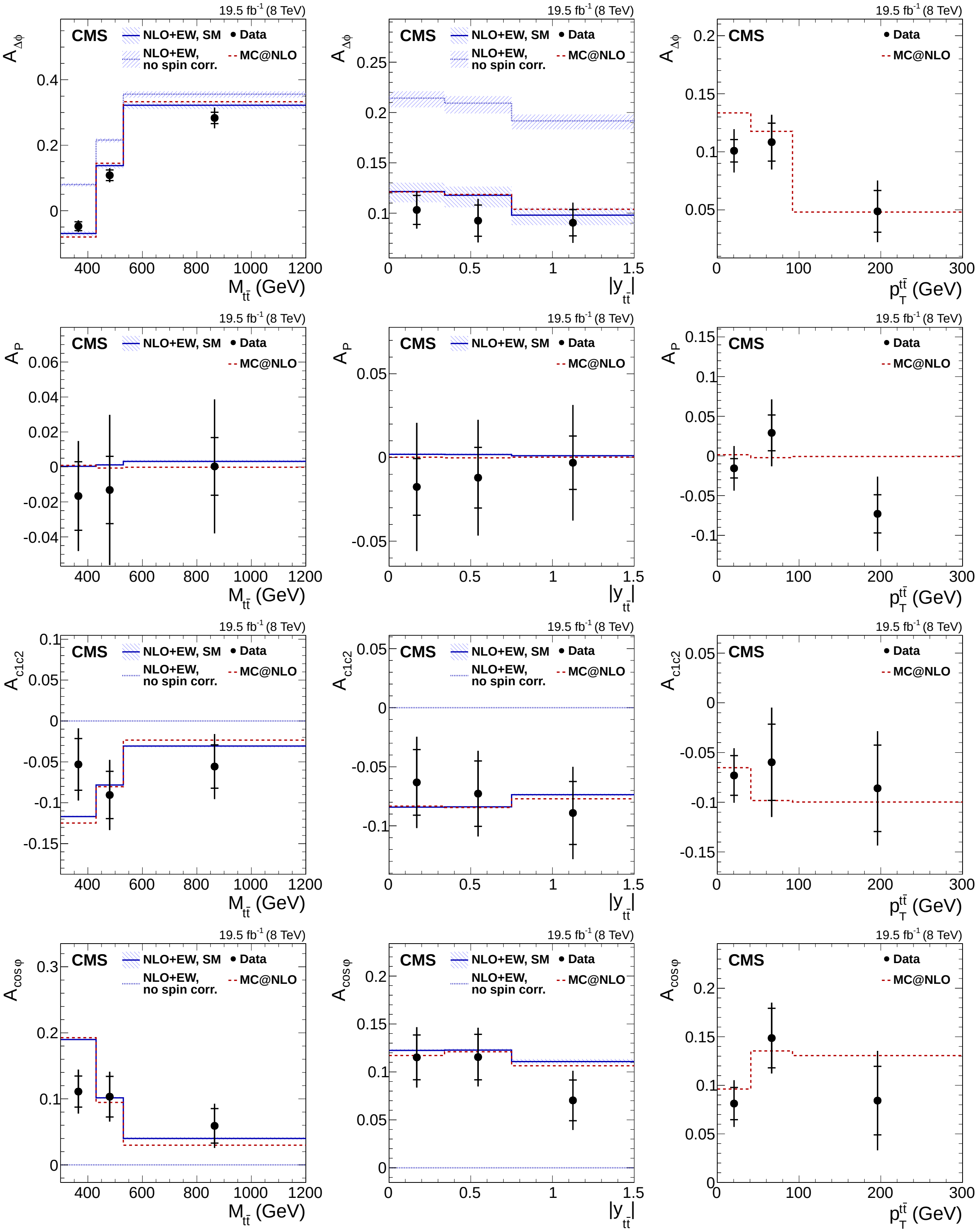

Figure 3.15: Unfolded spin correlation and polarization asymmetry values as a function of the three secondary kinematic variables. The last bin includes any overflow.

Table 3.18: Measured asymmetries after 2D unfolding, for each of the secondary kinematic variables. Uncertainties on measured asymmetries are statistical and systematic; uncertainties on simulation are statistical only.

Variable	Unfolded vs $M_{t\bar{t}}$	MC
A_C	0.009 ± 0.013 ± 0.008	0.006 ± 0.001
A_C^{lep}	-0.002 ± 0.006 ± 0.003	0.004 ± 0.001
$A_{\Delta\phi}$	0.095 ± 0.006 ± 0.007	0.113 ± 0.001
A_{c1c2}	-0.065 ± 0.015 ± 0.015	-0.081 ± 0.001
A_P	-0.011 ± 0.008 ± 0.028	0.000 ± 0.001
$A_{\cos\phi}$	0.094 ± 0.012 ± 0.009	0.114 ± 0.001
Variable	Unfolded vs $y_{t\bar{t}}$	MC
A_C	0.016 ± 0.012 ± 0.007	0.006 ± 0.001
A_C^{lep}	0.002 ± 0.006 ± 0.003	0.004 ± 0.001
$A_{\Delta\phi}$	0.095 ± 0.006 ± 0.012	0.113 ± 0.001
A_{c1c2}	-0.077 ± 0.015 ± 0.019	-0.081 ± 0.001
A_P	-0.010 ± 0.008 ± 0.029	0.000 ± 0.001
$A_{\cos\phi}$	0.097 ± 0.011 ± 0.012	0.114 ± 0.001
Variable	Unfolded vs $p_T^{t\bar{t}}$	MC
A_C	0.011 ± 0.012 ± 0.008	0.006 ± 0.001
A_C^{lep}	0.001 ± 0.006 ± 0.003	0.004 ± 0.001
$A_{\Delta\phi}$	0.094 ± 0.006 ± 0.012	0.113 ± 0.001
A_{c1c2}	-0.072 ± 0.014 ± 0.017	-0.081 ± 0.001
A_P	-0.014 ± 0.008 ± 0.028	0.000 ± 0.001
$A_{\cos\phi}$	0.100 ± 0.011 ± 0.011	0.114 ± 0.001

3.11 Conclusion

We performed a measurement of six different asymmetries in $t\bar{t} \rightarrow \ell\ell$ events recorded by the CMS experiment at the LHC. The data sample was gathered at an energy of 8 TeV, and corresponds to 19.5 fb^{-1} of luminosity. We selected events where top-antitop pairs decayed to a final state with two leptons (electrons or muons), giving a sample that was estimated to be 91% signal and 9% background. After subtracting the backgrounds, we used the unfolding technique to extrapolate our results to parton level. These results included inclusive measurements of the asymmetries, and differential measurements with respect to the mass, transverse momentum, and absolute rapidity of the $t\bar{t}$ system. Our results are consistent with the predictions of the Standard

Table 3.19: Measured asymmetry values after 2D unfolding, presented bin-by-bin in the secondary kinematic variables. Uncertainties on measured values are statistical and systematic.

Variable	$M_{t\bar{t}}$ bin 1	$M_{t\bar{t}}$ bin 2	$M_{t\bar{t}}$ bin 3
A_C	$0.007 \pm 0.031 \pm 0.019$	$0.015 \pm 0.029 \pm 0.015$	$0.004 \pm 0.021 \pm 0.013$
A_C^{lep}	$-0.023 \pm 0.014 \pm 0.009$	$0.010 \pm 0.016 \pm 0.009$	$0.015 \pm 0.016 \pm 0.010$
$A_{\Delta\phi}$	$-0.048 \pm 0.014 \pm 0.012$	$0.108 \pm 0.016 \pm 0.014$	$0.283 \pm 0.017 \pm 0.026$
$A_{\cos\phi}$	$0.111 \pm 0.024 \pm 0.024$	$0.103 \pm 0.031 \pm 0.022$	$0.059 \pm 0.026 \pm 0.021$
A_{c1c2}	$-0.053 \pm 0.032 \pm 0.031$	$-0.090 \pm 0.029 \pm 0.032$	$-0.056 \pm 0.026 \pm 0.030$
A_P	$-0.017 \pm 0.020 \pm 0.025$	$-0.013 \pm 0.019 \pm 0.038$	$0.000 \pm 0.017 \pm 0.035$
Variable	$y_{t\bar{t}}$ bin 1	$y_{t\bar{t}}$ bin 2	$y_{t\bar{t}}$ bin 3
A_C	$-0.002 \pm 0.031 \pm 0.013$	$0.016 \pm 0.027 \pm 0.017$	$0.029 \pm 0.022 \pm 0.014$
A_C^{lep}	$-0.001 \pm 0.015 \pm 0.009$	$-0.024 \pm 0.015 \pm 0.010$	$0.023 \pm 0.013 \pm 0.006$
$A_{\Delta\phi}$	$0.103 \pm 0.014 \pm 0.012$	$0.092 \pm 0.016 \pm 0.015$	$0.090 \pm 0.013 \pm 0.015$
$A_{\cos\phi}$	$0.115 \pm 0.023 \pm 0.021$	$0.115 \pm 0.024 \pm 0.019$	$0.070 \pm 0.021 \pm 0.022$
A_{c1c2}	$-0.063 \pm 0.028 \pm 0.027$	$-0.073 \pm 0.028 \pm 0.023$	$-0.089 \pm 0.027 \pm 0.029$
A_P	$-0.018 \pm 0.017 \pm 0.034$	$-0.012 \pm 0.018 \pm 0.029$	$-0.003 \pm 0.016 \pm 0.031$
Variable	$p_T^{t\bar{t}}$ bin 1	$p_T^{t\bar{t}}$ bin 2	$p_T^{t\bar{t}}$ bin 3
A_C	$0.009 \pm 0.018 \pm 0.012$	$-0.033 \pm 0.033 \pm 0.027$	$0.084 \pm 0.036 \pm 0.026$
A_C^{lep}	$0.006 \pm 0.010 \pm 0.005$	$-0.020 \pm 0.016 \pm 0.015$	$0.015 \pm 0.018 \pm 0.010$
$A_{\Delta\phi}$	$0.101 \pm 0.010 \pm 0.016$	$0.108 \pm 0.016 \pm 0.017$	$0.049 \pm 0.018 \pm 0.020$
$A_{\cos\phi}$	$0.081 \pm 0.017 \pm 0.017$	$0.149 \pm 0.031 \pm 0.020$	$0.084 \pm 0.035 \pm 0.037$
A_{c1c2}	$-0.073 \pm 0.020 \pm 0.019$	$-0.060 \pm 0.038 \pm 0.039$	$-0.086 \pm 0.043 \pm 0.038$
A_P	$-0.016 \pm 0.012 \pm 0.025$	$0.029 \pm 0.023 \pm 0.036$	$-0.073 \pm 0.024 \pm 0.040$

Model, and as a result, we see no evidence of deviations from theory that could indicate the presence of new physics.

3.12 Acknowledgements

Although the bulk of this analysis was the work of a few physicists, the analysis would not be possible without the efforts of the entire CMS collaboration, more than 3,000 members strong. They were responsible for maintaining the detector, software, and computing platforms necessary to perform the analysis. In addition, numerous members contributed feedback that enhanced the quality of the analysis. Finally, I thank W. Bernreuther and Z.-G. Si for their theoretical predictions, and for discussions of how this work can be applied to searches for new physics.

This analysis was published in two parts. The charge asymmetry measurements were published in Physics Letters [45], and the spin correlation and polarization measurements were published in Physical Review D [46].

Chapter 4

Single-Lepton Stop Search

This chapter will describe a search for evidence of supersymmetry, with the target signal being stop-antistop squark pairs decaying to a single-lepton (1ℓ) final state. This work was performed using the CMS experiment during Run II of the LHC, at 13 TeV center-of-mass energy. This analysis resulted in two publications: the search performed using 2016 data [67], and a combined single-lepton and all-hadronic search using 2015 data [68]. Two public research documents (PASes) were also produced to support conference results [69, 70], however these are superseded by the published results. I will focus on the analysis as described in the most recent publication [67], particularly my work developing, validating, and executing the compressed T2tt search strategy.

4.1 Motivation

As Section 1.2.2 has described, supersymmetry (SUSY) is a very important class of theories in particle physics. It has the potential to solve the hierarchy problem, and may provide the answer to the difficult question of what particles make up dark matter. And the notion of naturalness would seem to imply that our current or near-future particle colliders have just the right energies to search for evidence of SUSY.

Many models predict that in order for SUSY to solve the hierarchy problem, the stop squark must have a mass that is relatively close to the mass of the top quark. In other words, the stop squark should be one of the lighter sparticles. The Lightest Supersymmetric Particle ($\tilde{\chi}_1^0$) and the chargino ($\tilde{\chi}_1^{\pm}$) are also expected to be relatively light, so it is only natural that a search for evidence of SUSY should focus on stops, LSPs, and charginos.

When planning how to search for a desired physics process, especially when said process represents new physics, one must balance cross section and branching ratio against ease of identification. As Section 3.1 has described, hadronic W-boson decays have a higher branching fraction than leptonic decays; however, the CMS detector is better able to cleanly reconstruct leptons than jets. Our signals contain two W-boson decays, and we choose to take the middle ground: we target the case where one W-boson decays to a lepton, to help us more easily identify our signal, and the other W-boson decays hadronically, to ensure our targeted process is not too rare. These signal models will be described more fully in Section 4.3.

4.2 Previous Searches

Various searches for stop pairs have previously been performed at CMS during Run I, including in the one-lepton final state [60]. This previous single-lepton search used 19.5 fb^{-1} of 8 TeV collision data. The analyzers performed a traditional cut-based search, and also a search employing a boosted decision tree (BDT). This machine-learning technique allows a computer to decide how best to discriminate between signal and background. Ultimately, neither search strategy detected any evidence of the production of stop squarks. This result allowed the analyzers to set limits on the possible masses of stops and LSPs. Specifically, stop squarks were excluded up to masses of about 650 GeV in the case where the LSP is massless, and LSPs were excluded up to a maximum of about 250 GeV for stop masses around 550 GeV.

The LHC and the CMS detector received a number of upgrades for Run II, some of which have greatly benefitted the single-lepton stop search. Of particular note, the LHC collision energy was raised from 8 to 13 TeV, increasing the likelihood of producing heavy new particles, and the luminosity was raised considerably, allowing us to record more data in the same amount of running time. In addition, we have learned from the Run I analysis, and attempted to improve our analysis techniques for Run II. To avoid the obfuscation inherent in results produced by machine learning, we declined to perform a BDT search. We also added a new signal model to our search. Finally, we added dedicated signal regions to address the unique kinematics of several particular regions of phase space.

The ATLAS collaboration has also taken advantage of improvements to its detector and to the LHC as a whole, and has published its own single-lepton stop search at 13 TeV [71]. They have also previously published searches for stop squarks using data from Run I.

4.3 Signal Models

Because supersymmetry is still purely theoretical, and the masses of the sparticles are unknown, there are a number of possible ways that a stop squark pair could decay to a single lepton final state. We consider three possible signal models, each with its own unique signature. In addition, we consider a wide range of possible values for the masses of the stop and LSP, and the kinematics that result.

4.3.1 Bulk Signals

T2tt

One of the primary models we target is known by the identifier **T2tt**. In this model, the stop squarks decay to top quarks and LSPs ($\tilde{t} \rightarrow t\tilde{\chi}_1^0$). The top quarks then decay to bottoms and W bosons, as normal; one of the Ws decays leptonically, and the other hadronically. The two free parameters in this model are the stop mass, $m_{\tilde{t}}$, and the LSP mass, $m_{\tilde{\chi}_1^0}$; we scan a wide range of possible values for these two variables. The kinematics of the decay products are determined entirely by the stop and LSP masses. We may sometimes refer to regions of the parameter space in terms of ΔM, which is given by $m_{\tilde{t}} - m_{\tilde{\chi}_1^0}$, the difference in stop and LSP masses. A Feynman diagram of the T2tt model is given at the top left of Figure 4.1.

T2bW

The second primary model we consider is known as **T2bW**. In this model, the stop squarks decay to bottom quarks and charginos, skipping the top quarks entirely. The charginos then decay to W bosons and neutralinos ($\tilde{t} \to b\tilde{\chi}_1^{\pm}, \tilde{\chi}_1^{\pm} \to W\tilde{\chi}_1^0$). One W boson then decays leptonically, and the other hadronically. In this case, the free parameters are $m_{\tilde{t}}$, $m_{\tilde{\chi}_1^0}$, and also the chargino mass, $m_{\tilde{\chi}_1^{\pm}}$. For the purposes of this analysis, we fix the chargino mass at the average of the stop and neutralino masses, $m_{\tilde{\chi}_1^{\pm}} = (m_{\tilde{t}} + m_{\tilde{\chi}_1^0})/2$. We then scan a broad range of possible values for $m_{\tilde{t}}$ and $m_{\tilde{\chi}_1^0}$. The T2bW model is diagrammed in the top right of Figure 4.1.

T2tb

For the Run II search, we have added a new signal model that was not evaluated in the Run I search. This model is called **T2tb**. It is essentially a mixture of the T2tt and T2bW models, in that it covers the case where one of the stop squarks decays to a top quark and an LSP, and the other decays to a bottom quark and a chargino. For this analysis, we fix $m_{\tilde{\chi}_1^{\pm}}$ to be $m_{\tilde{\chi}_1^0} + 5$ GeV, a choice that allows us to target the T2tb model with dedicated signal regions. We then scan a range of possible values for $m_{\tilde{t}}$ and $m_{\tilde{\chi}_1^0}$. The T2tb model is pictured at the bottom of Figure 4.1.

4.3.2 Compressed T2tt

There is a region of the $m_{\tilde{t}}$ and $m_{\tilde{\chi}_1^0}$ phase space that is of particular interest to us in this analysis. In the T2tt model, if the difference between the stop and LSP masses is less than the mass of the top quark, $\Delta M \lesssim m_t$, then the top quark must be produced off-shell (i.e. with a

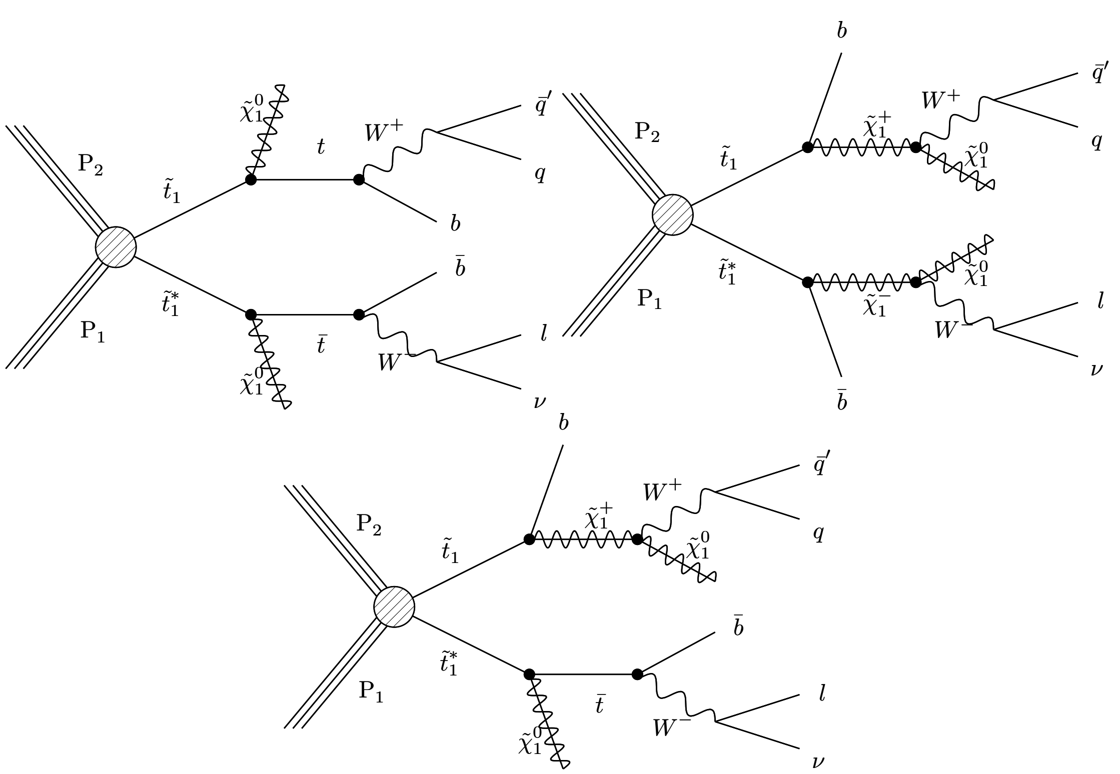

Figure 4.1: Feynman diagrams showing the production of stop pairs that subsequently decay to single-lepton final states. Pictured are the T2tt (top left), T2bW (top right), and T2tb (bottom) models, respectively.

mass less than its normal 173 GeV). This kind of process would be difficult to detect because the production of off-shell top quarks is suppressed, and because there is also less energy and momentum available to the top decay products. We may also consider what happens if we go one step further, to the region where $m_{\tilde{t}} - m_{\tilde{\chi}_1^0} \lesssim m_W$. In this case, not only the top quark but also its daughter W boson must be produced off-shell, making it even harder to detect this signal. We call these cases *compressed* T2tt decays, because the particles are squeezed into a smaller mass window.

The difficulties in detecting compressed T2tt signals are evident in the results plot of the Run I analysis [60]. The exclusion curve for the T2tt model has no coverage in the narrow strip where $m_{\tilde{t}} - m_{\tilde{\chi}_1^0} \approx m_t$, or the strip where $m_{\tilde{t}} - m_{\tilde{\chi}_1^0} \approx m_W$. We call these two regions the *top corridor* and the *W corridor*, respectively. In this analysis we wish to fill in these two gaps, and achieve exclusion in the corridor regions. To that end, I developed a specialized set of signal regions that target the kinematics of compressed decays, with the aim of increasing our sensitivity to these signals. These specialized signal regions will be described in Section 4.7.

4.4 Search Strategy

Because we are searching for single-lepton stop decays, we must of course select events with one and only one lepton in them. In addition to a lepton, all of our signal models have two LSPs and a neutrino in the final state. The LSPs should go undetected by the CMS detector, just as neutrinos do, so we must also search for the presence of large $E_{\mathrm{T}}^{\mathrm{miss}}$.

Many other physics processes can produce a single lepton plus high $E_{\mathrm{T}}^{\mathrm{miss}}$, or can produce signatures that resemble these. We must therefore identify these backgrounds, and attempt to reduce their size using a series of cuts and selections. When it is not possible to mitigate the backgrounds with cuts, we must attempt to estimate how many background events fall into our signal regions so we can subtract them from the final measurements.

Before applying any cuts and selections, the largest background will naturally be SM processes that produce one true lepton and large $E_{\mathrm{T}}^{\mathrm{miss}}$. The largest component of this background is $t\bar{t} \to 1\ell$, though other processes can contribute as well, such as W boson production with jets, where the W decays leptonically. In order to reduce the true single-lepton background, we first add a cut on the transverse mass of the lepton-plus-$E_{\mathrm{T}}^{\mathrm{miss}}$ system, called M_{T}. The exact definition of this variable is given in Section 4.6.7. This cut works in concert with our high-$E_{\mathrm{T}}^{\mathrm{miss}}$ requirement to help reduce the single-lepton background component.

Figure 4.2 shows the results of several investigations into the M_{T} variable. The left plot shows the reconstructed value of M_{T} in a sample of W($\ell\nu$)+jets MC events, with three different $E_{\mathrm{T}}^{\mathrm{miss}}$ cuts applied. As the plot shows, higher $E_{\mathrm{T}}^{\mathrm{miss}}$ requirements cause the W-boson mass edge to become more sharply defined, making it easier to set a cut threshold.

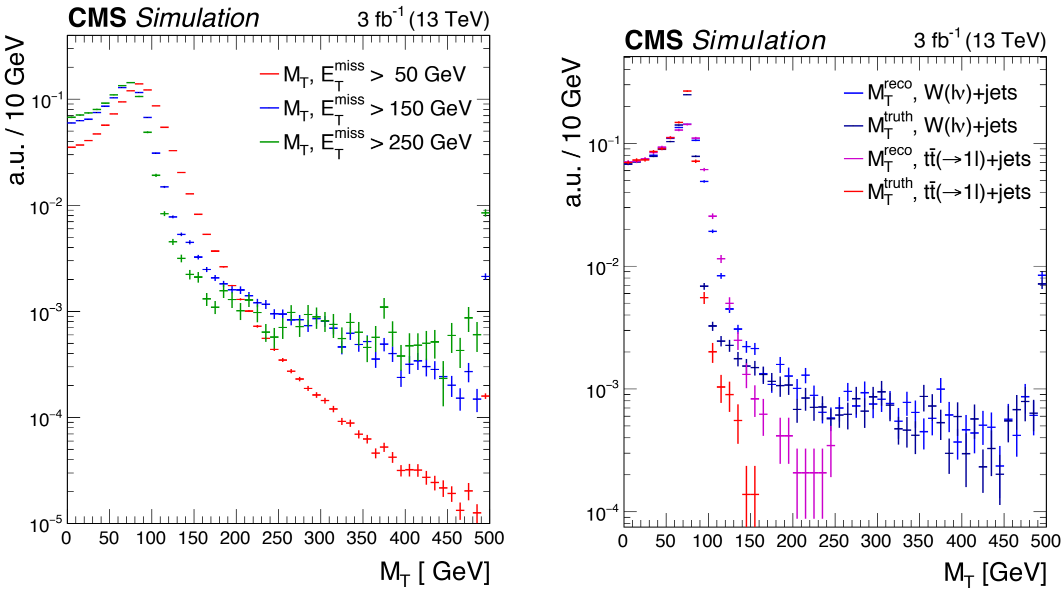

Figure 4.2: M_{T} distributions in W+jets with various $E_{\mathrm{T}}^{\mathrm{miss}}$ selections applied, and comparison between gen and reco M_{T} in W+jets and $t\bar{t} \rightarrow 1\ell$.

The right plot in Figure 4.2 shows generator-level M_{T} and reconstructed M_{T} for both W+jets and $t\bar{t} \rightarrow 1\ell$ simulated events. These events were selected by requiring a single lepton and at least 2 jets, all with $p_T > 30$ GeV, and $E_{\mathrm{T}}^{\mathrm{miss}} > 250$ GeV. The generator-level M_{T} was calculated using the neutrino momentum in place of the $E_{\mathrm{T}}^{\mathrm{miss}}$. The plot shows that the tails of the M_{T} distribution look very different for W+jets and $t\bar{t} \rightarrow 1\ell$. In the case of $t\bar{t} \rightarrow 1\ell$, the top mass restricts the mass spectrum of the W boson, so that most events in the tail are present because of the limited resolution of $E_{\mathrm{T}}^{\mathrm{miss}}$ reconstruction. This is seen in the difference between the gen and reco M_{T} spectra. By contrast, in W+jets events, there is no constraint on the W mass, so the tail is attributable to the natural width of the W boson mass spectrum. Thus, by selecting an appropriate M_{T} cut, we can effectively reduce the single lepton background to mostly W+jets events. We can then estimate the size of the remaining background component using techniques that will be described in Sections 4.8.2 and 4.8.3.

After reducing the single lepton background using $E_{\mathrm{T}}^{\mathrm{miss}}$ and M_{T} cuts, the next largest background comes from events with two genuine leptons, such as $t\bar{t} \rightarrow \ell\ell$, where one of the leptons is not reconstructed. Although we veto events that have a second electron, muon, or tau, as well as events with an isolated track in them, these vetos are not perfect. And often, a second lepton falls outside our range of acceptance in p_T or η, is not isolated, or is not reconstructed. We call this component the "lost lepton" background. As Chapter 3 has demonstrated, we have a good understanding of the $t\bar{t} \to \ell\ell$ process, and can model it fairly well. On the basis of that strong understanding, we estimate this background using data-driven techniques described in Section 4.8.1.

The final background to consider is events with one genuine lepton, but where the high $E_{\mathrm{T}}^{\mathrm{miss}}$ comes from a $Z \to \nu\nu$ decay, and not from SUSY particles. The largest contributor to this background is ttZ events, where the $t\bar{t}$ pair decays semileptonically and the Z decays to invisible neutrinos; the next largest contributor is WZ production. There is little we can do to exclude such events with cuts; fortunately, this background component is relatively small. We estimate the $Z \to \nu\nu$ component using MC with theoretical uncertainties applied, as described in Section 4.8.4.

4.5 Datasets and Triggers

4.5.1 Data samples

As Section 4.4 described, our two main experimental signatures are a single lepton and large $E_{\mathrm{T}}^{\mathrm{miss}}$. With these two signatures in mind, we select our data from the Single Lepton and $E_{\mathrm{T}}^{\mathrm{miss}}$ datasets produced by the CMS experiment. We also employ the muon+electron dataset for a set of crosscheck regions to be described in Appendix A, and the single photon dataset for $E_{\mathrm{T}}^{\mathrm{miss}}$ resolution studies to be described in Appendix B. These datasets were recorded during the 2016 datataking period, encompassing eras 2016B through 2016H, and represent a total integrated luminosity of 35.9 fb^{-1}. Table 4.1 gives a complete listing of all datasets used in this analysis.

Table 4.1: List of CMS datasets used in the single lepton stop search.

Dataset	Run Range
/SingleMuon/Run2016B-03Feb2017_ver2-v2/MINIAOD	273150-275376
/SingleMuon/Run2016C-03Feb2017-v1/MINIAOD	275656-276283
/SingleMuon/Run2016D-03Feb2017-v1/MINIAOD	276315-276811
/SingleMuon/Run2016E-03Feb2017-v1/MINIAOD	276831-277420
/SingleMuon/Run2016F-03Feb2017-v1/MINIAOD	277932-278808
/SingleMuon/Run2016G-03Feb2017-v1/MINIAOD	278820-280385
/SingleMuon/Run2016H-03Feb2017_ver2-v1/MINIAOD	281613-284035
/SingleMuon/Run2016H-03Feb2017_ver3-v1/MINIAOD	284036-284044
/SingleElectron/Run2016B-03Feb2017_ver2-v2/MINIAOD	273150-275376
/SingleElectron/Run2016C-03Feb2017-v1/MINIAOD	275656-276283
/SingleElectron/Run2016D-03Feb2017-v1/MINIAOD	276315-276811
/SingleElectron/Run2016E-03Feb2017-v1/MINIAOD	276831-277420
/SingleElectron/Run2016F-03Feb2017-v1/MINIAOD	277932-278808
/SingleElectron/Run2016G-03Feb2017-v1/MINIAOD	278820-280385
/SingleElectron/Run2016H-03Feb2017_ver2-v1/MINIAOD	281613-284035
/SingleElectron/Run2016H-03Feb2017_ver3-v1/MINIAOD	284036-284044
/MET/Run2016B-03Feb2017_ver2-v2/MINIAOD	273150-275376
/MET/Run2016C-03Feb2017-v1/MINIAOD	275656-276283
/MET/Run2016D-03Feb2017-v1/MINIAOD	276315-276811
/MET/Run2016E-03Feb2017-v1/MINIAOD	276831-277420
/MET/Run2016F-03Feb2017-v1/MINIAOD	277932-278808
/MET/Run2016G-03Feb2017-v1/MINIAOD	278820-280385
/MET/Run2016H-03Feb2017_ver2-v1/MINIAOD	281613-284035
/MET/Run2016H-03Feb2017_ver3-v1/MINIAOD	284036-284044
/MuonEG/Run2016B-03Feb2017_ver2-v2/MINIAOD	273150-275376
/MuonEG/Run2016C-03Feb2017-v1/MINIAOD	275656-276283
/MuonEG/Run2016D-03Feb2017-v1/MINIAOD	276315-276811
/MuonEG/Run2016E-03Feb2017-v1/MINIAOD	276831-277420
/MuonEG/Run2016F-03Feb2017-v1/MINIAOD	277932-278808
/MuonEG/Run2016G-03Feb2017-v1/MINIAOD	278820-280385
/MuonEG/Run2016H-03Feb2017_ver2-v1/MINIAOD	281613-284035
/MuonEG/Run2016H-03Feb2017_ver3-v1/MINIAOD	284036-284044
/SinglePhoton/Run2016B-03Feb2017_ver2-v2/MINIAOD	273150-275376
/SinglePhoton/Run2016C-03Feb2017-v1/MINIAOD	275656-276283
/SinglePhoton/Run2016D-03Feb2017-v1/MINIAOD	276315-276811
/SinglePhoton/Run2016E-03Feb2017-v1/MINIAOD	276831-277420
/SinglePhoton/Run2016F-03Feb2017-v1/MINIAOD	277932-278808
/SinglePhoton/Run2016G-03Feb2017-v1/MINIAOD	278820-280385
/SinglePhoton/Run2016H-03Feb2017_ver2-v1/MINIAOD	281613-284035
/SinglePhoton/Run2016H-03Feb2017_ver3-v1/MINIAOD	284036-284044

4.5.2 Triggers

For each of the datasets described above, we select events using appropriate HLT triggers. Of particular note, we select data events for our signal regions using the union of the single lepton and $E_{\mathrm{T}}^{\mathrm{miss}}$ triggers. This strategy allows us to use leptons that are below their trigger thresholds, and to compensate for any inefficiency in the turn-on phase of the $E_{\mathrm{T}}^{\mathrm{miss}}$ trigger. The triggers we use are listed in Table 4.2.

Table 4.2: HLT trigger paths corresponding to each of the primary datasets used in the analysis. The trigger version is suppressed.

Type	HLT path
SingleMuon	HLT_Iso(Tk)Mu22 OR HLT_Iso(Tk)Mu24
SingleElectron	HLT_Ele25_eta2p1_WPTight_Gsf OR HLT_Ele27_eta2p1_WPTight_Gsf
MET	HLT_PFMET170_HBHECleaned OR HLT_PFMET(NoMu)110_PFMHT110(NoMu)_IDTight OR HLT_PFMET(NoMu)120_PFMHT120(NoMu)_IDTight
MuonEG	HLT_Mu8_TrkIsoVVL_Ele23_CaloIdL_TrackIdL_IsoVL(_DZ) OR HLT_Mu8_TrkIsoVVL_Ele17_CaloIdL_TrackIdL_IsoVL_v* OR HLT_Mu23_TrkIsoVVL_Ele12_CaloIdL_TrackIdL_IsoVL(_DZ) OR HLT_Mu17_TrkIsoVVL_Ele12_CaloIdL_TrackIdL_IsoVL_v*
SinglePhoton	HLT_Photon*_R9Id90_HE10_IsoM OR HLT_Photon165_HE10 OR HLT_Photon175 OR HLT_Photon250_NoHE

4.5.3 Trigger Efficiency Measurements

We measure the efficiency of our combined single lepton and $E_{\mathrm{T}}^{\mathrm{miss}}$ triggers in a sample of events from the JetHT primary dataset, selected using the `HLT_(PF)HT*` trigger paths. We use events triggered on H_T because this trigger is expected to be orthogonal to the $E_{\mathrm{T}}^{\mathrm{miss}}$ and lepton p_T triggers, allowing us to examine the full spectrum of these variables. The trigger efficiency is parameterized in $E_{\mathrm{T}}^{\mathrm{miss}}$ and lepton p_T. We select events with at least one lepton and two jets. Our definitions of leptons, jets, and $E_{\mathrm{T}}^{\mathrm{miss}}$ are presented later, in Section 4.6. For any given bin in the efficiency histogram, the efficiency is computed as the number of events in that bin passing our triggers divided by the total number of events in that bin.

Figure 4.3 shows the parameterized trigger efficiencies, separated by flavor of the leading lepton. Using 35.9 fb^{-1} of data, our overall trigger efficiency is 99.1% in the region $E_{\mathrm{T}}^{\mathrm{miss}} > 250$ GeV and lepton $p_T > 20$ GeV. Because this efficiency is so close to 100%, we do not correct for the small inefficiency. However, we assign a systematic uncertainty of 2% for events with $E_{\mathrm{T}}^{\mathrm{miss}}$ below 300 GeV, and 4% for events with $E_{\mathrm{T}}^{\mathrm{miss}}$ greater than 300 GeV.

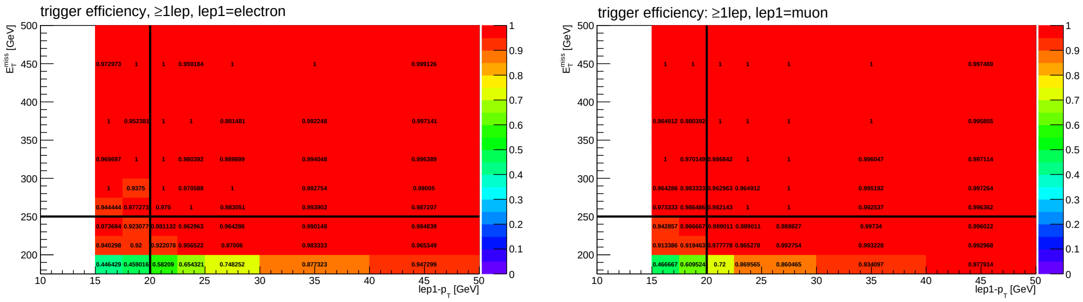

Figure 4.3: Measured efficiencies for the union of the single lepton and $E_{\mathrm{T}}^{\mathrm{miss}}$ triggers. Efficiency is represented by the z-axis color scale. The efficiencies are presented separately for the case where the leading lepton is an electron (left), and a muon (right).

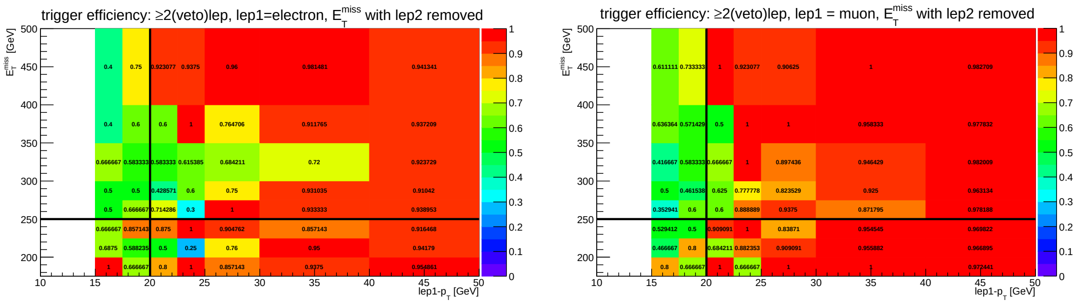

Figure 4.4: Measured efficiencies for the union of the single lepton and $E_{\mathrm{T}}^{\mathrm{miss}}$ triggers, when the sub-leading lepton p_T is added to the $E_{\mathrm{T}}^{\mathrm{miss}}$. Efficiency is represented by the z-axis color scale. The efficiencies are presented separately for the case where the leading lepton is an electron (left), and a muon (right).

As Section 4.4 has described, we sometimes fail to reconstruct a true second lepton in the event. When that happens, the p_T of the lost lepton effectively contributes to the $E_{\mathrm{T}}^{\mathrm{miss}}$ of the event. When considering such events, we must re-evaluate the efficiency of our combined single lepton and $E_{\mathrm{T}}^{\mathrm{miss}}$ triggers. We do so using the exact same procedures described above, except that we additionally require events to have a second lepton with $p_T > 10$ GeV. These efficiencies are presented in Figure 4.4. Because the combined triggers have substantial inefficiency at low $E_{\mathrm{T}}^{\mathrm{miss}}$

and low lepton p_T, we do correct our Monte Carlo simulations for these trigger efficiencies when considering dilepton events.

4.5.4 Monte Carlo Samples

Our analysis relies on modeling a number of background and signal processes using Monte Carlo simulation. Table 4.3 presents the complete list of Monte Carlo samples used. All samples are produced as MINIAODSIM. Our SM samples were made using FullSim, while the SUSY signal samples were made using FastSim [44].

4.6 Object and Event Selection

We define our physics objects, and use them to select events, with an eye to maximizing our acceptance of SUSY signals, while rejecting SM backgrounds.

4.6.1 Vertex Selections

For an event to be selected, at least the first vertex in the event must be a good vertex. A vertex is considered to be “good” if it meets the following criteria:

- The tracks used to create the vertex must have trajectory fits with positive χ^2 values.
- The vertex fit must have at least 5 degrees of freedom.
- The distance between the vertex and the nominal center of the detector must have a z-component of less than 24 cm.
- The same distance must have a transverse component, ρ, of less than 2 cm.

Table 4.3: Monte Carlo simulation datasets used in this analysis, and their theoretical cross sections. The symbol * replaces the string RunIISummer16MiniAODv2-PUMoriond17_80X_mcRun2_asymptotic_2016_TrancheIV_v6, and the † replaces RunIISpring16MiniAODv2-PUSpring16Fast_80X_mcRun2_asymptotic_2016_miniAODv2_v0.

Sample	Cross Section [pb]
/TTJets_SingleLeptFromT_TuneCUETP8M1_13TeV-madgraphMLM-pythia8/*(_ext)-v1	182.7
/TTJets_SingleLeptFromTbar_TuneCUETP8M1_13TeV-madgraphMLM-pythia8/*(_ext)-v1	182.7
/TTJets_DiLept_TuneCUETP8M1_13TeV-madgraphMLM-pythia8/*_ext-v1 (and *-v4)	87.3
/ST_tW_top_5f_NoFullyHadronicDecays_13TeV-powheg_TuneCUETP8M1/*-v1	19.6
/ST_tW_antitop_5f_NoFullyHadronicDecays_13TeV-powheg_TuneCUETP8M1/*-v1	19.6
/ST_t-channel_top_4f_leptonDecays_13TeV-powheg-pythia8_TuneCUETP8M1/*-v1	44.1
/ST_t-channel_antitop_4f_leptonDecays_13TeV-powheg-pythia8_TuneCUETP8M1/*-v1	26.2
/ST_s-channel_4f_leptonDecays_13TeV-amcatnlo-pythia8_TuneCUETP8M1/*-v1	3.7
/W1JetsToLNu_TuneCUETP8M1_13TeV-madgraphMLM-pythia8/*-v1	11782
/W2JetsToLNu_TuneCUETP8M1_13TeV-madgraphMLM-pythia8/*-v1	3841
/W3JetsToLNu_TuneCUETP8M1_13TeV-madgraphMLM-pythia8/*-v1	1160
/W4JetsToLNu_TuneCUETP8M1_13TeV-madgraphMLM-pythia8/*-v1	600
/W1JetsToLNu_NuPt-200_TuneCUETP8M1_13TeV-madgraphMLM-pythia8/*-v1	2.36
/W2JetsToLNu_NuPt-200_TuneCUETP8M1_13TeV-madgraphMLM-pythia8/*-v1	4.95
/W3JetsToLNu_NuPt-200_TuneCUETP8M1_13TeV-madgraphMLM-pythia8/*-v1	4.94
/W4JetsToLNu_NuPt-200_TuneCUETP8M1_13TeV-madgraphMLM-pythia8/*-v1	8.83
/ttWJets_13TeV_madgraphMLM/*-v1	0.61
/ttZJets_13TeV_madgraphMLM/*-v1	0.78
/WWTo2L2Nu_13TeV-powheg/*-v1	12.18
/WWToLNuQQ_13TeV-powheg/*-v1	50.00
/WZTo3LNu_TuneCUETP8M1_13TeV-powheg-pythia8/*-v1	4.43
/WZTo2L2Q_13TeV_amcatnloFXFX_madspin_pythia8/*-v1	5.60
/WZTo1L1Nu2Q_13TeV_amcatnloFXFX_madspin_pythia8/*-v1	10.74
/WZTo1L3Nu_13TeV_amcatnloFXFX_madspin_pythia8/*-v1	3.05
/ZZTo4L_13TeV_powheg_pythia8/*-v1	1.25
/ZZTo2L2Q_13TeV_amcatnloFXFX_madspin_pythia8/*-v1	3.22
/ZZTo2L2Nu_13TeV_powheg_pythia8/*-v1	0.56
/ZZTo2Q2Nu_13TeV_amcatnloFXFX_madspin_pythia8/*-v1	4.73
/SMS-T2tt_mStop-150to250_TuneCUETP8M1_13TeV-madgraphMLM-pythia8/†-v1	
/SMS-T2tt_mStop-250to350_TuneCUETP8M1_13TeV-madgraphMLM-pythia8/†-v1	
/SMS-T2tt_mStop-350to400_TuneCUETP8M1_13TeV-madgraphMLM-pythia8/†-v1	
/SMS-T2tt_mStop-400to1200_TuneCUETP8M1_13TeV-madgraphMLM-pythia8/†-v1	
/SMS-T2bW_TuneCUETP8M1_13TeV-madgraphMLM-pythia8/†-v1	
/SMS-T2bt_TuneCUETP8M1_13TeV-madgraphMLM-pythia8/†-v1	

If multiple vertices in an event meet these criteria, we choose the one whose associated tracks have the highest $\sum p_T^2$ to be our primary vertex (PV), from which all of our physics objects originate.

4.6.2 Lepton Selections and Veto

We select events that have one well-identified reconstructed lepton (electron or muon), and veto events with additional leptons. All our identification criteria are based on the POG recommendations, and are described in Table 4.4.

For our electrons, we remove the POG-recommended isolation cut, and substitute a cut based on *relative mini-isolation*, as is standard for SUSY searches at CMS. Relative mini-isolation is defined as the sum of the p_T of the particle flow candidates within a cone-shaped region around the lepton, where the cone size varies with the lepton p_T. For lepton $p_T < 50$ GeV, the cone size is 0.2 in ΔR. For p_T between 50 and 200 GeV, the cone size is defined to be 10.0 GeV / p_T^{lep}. Finally, for lepton p_T above 200 GeV, the cone size is fixed at 0.05. The rationale for reducing the cone size as lepton p_T rises is to avoid vetoing signal events where a boosted top decays to a lepton and b-jet that are nearly colinear. Pileup correction is performed using the average energy density in the event, and the same effective area used in the mini-isolation calculation.

Table 4.4: Criteria used to identify electrons or muons. We select exactly one good lepton, and veto any additional leptons, using two different sets of criteria.

type	variable	selected	veto
electron	p_T	> 20 GeV	> 5 GeV
	$\|\eta\|$	< 1.442	< 2.4
	POG ID without ISO	Medium	Veto
	relative miniisolation	< 0.1	< 0.2
muon	p_T	> 20 GeV	> 5 GeV
	$\|\eta\|$	< 2.4	< 2.4
	POG ID	Medium	Loose
	relative miniisolation	< 0.1	< 0.2

4.6.3 Isolated Track Veto

In addition to vetoing events with a second electron/muon, we must also reject events with a tau in them. Taus mostly decay in flight, so to reject taus, we must reject their decay products. Some 50% of the time, taus decay to a charged pion or kaon. Decays to an electron and a muon account for another 17.5% each. Summing these cases up, we see that 85% of all tau decays produce a single charged track. So the most powerful way to veto taus is to veto isolated charged tracks. These tracks are found in the pfChargedHadrons collection. The event is vetoed if at least one pfChargedHadron is found that meets these criteria:

- $p_T > 10$ GeV
- $|\eta| < 2.4$
- Charge is opposite in sign from the selected lepton
- $\Delta R > 0.4$ from the selected lepton
- z-component of the distance to the PV is < 0.1 cm

We measure the isolation of charged tracks using tracker-only isolation, because tau decays sometimes produce multiple neutral hadrons along with the charged track, and these hadrons should not be counted against the track isolation. With that in mind, we require our veto tracks to have the following isolation values:

- For track $p_T > 60$ GeV, absolute tracker iso within a cone of 0.3 must be < 6 GeV.
- For track $p_T \leq 60$ GeV, relative tracker iso within a cone of 0.3 must be < 0.1.

Relative isolation is, again, isolation divided by the p_T of the object being considered. We use absolute isolation above p_T of 60 GeV because relative isolation becomes a weak requirement at high p_T.

4.6.4 Hadronic Tau Veto

Although highly effective, the isolated track veto does not address cases where the tau decays to three charged hadrons (3-pronged decay). So we add another veto targeting hadronic tau decays, using an ID recipe approved by the tau POG within CMS. We veto events if we find a hadronic tau that meets these criteria:

- $p_T > 20$ GeV
- $|\eta| < 2.4$
- Passes tau identification algorithm *byDecayModeFinding*
- Passes isolation selection *byMediumCombinedIsolationDeltaBetaCorr3Hits*
- Charge is opposite in sign from the selected lepton
- $\Delta R > 0.4$ from the selected lepton

4.6.5 Jets

We reconstruct jets using the anti-k_t jet clustering algorithm [37] with a distance parameter of 0.4. These jets must have $p_T > 30$ GeV, must have $|\eta| < 2.4$, and must pass the established jet ID at the loose working point. The jet ID requirement is waived for our signal MC samples, because the jet ID has some inefficiencies in samples made using FastSim. We apply the official CMS jet energy corrections. Each event is required to have at least two jets, though most signal regions have higher requirements to suit their purposes, as Section 4.7 will describe.

We also require each event to have at least one b-tagged jet, where b-tagging is performed using the CSVv2 algorithm. Depending on the signal region in question, the b-tag may be required to pass the loose WP (CSV discriminant > 0.8) or the tight WP (CSV discriminant > 0.935). Section 4.7 will list which WP is used for each signal region.

4.6.6 Missing Transverse Energy ($E_{\mathrm{T}}^{\mathrm{miss}}$)

As described earlier, $\vec{E}_{\mathrm{T}}^{\mathrm{miss}}$ is calculated as the negative of the vector sum of all the particle flow candidates in the event. We recalculate the $E_{\mathrm{T}}^{\mathrm{miss}}$ after the jet energy corrections have been applied to the jets in the event. We require each event to have $E_{\mathrm{T}}^{\mathrm{miss}} > 250$ GeV. We also employ the following $E_{\mathrm{T}}^{\mathrm{miss}}$ filters, as recommended by the JetMET group in CMS:

- Primary vertex filter
- CSC beam halo filter
- HBHE noise filter
- HBHEiso noise filter
- ee badSC noise filter
- ECAL TP filter
- Bad muon filter
- Bad charged hadron filter
- Bad muons filter
- Duplicate muons filter

These filters reject events where the $E_{\mathrm{T}}^{\mathrm{miss}}$ (or a significant fraction of it) is believed to originate from detector noise, spurious particles in the event, interference from the proton beams, etc., and not from invisible particles produced in the hard collision.

4.6.7 Transverse Mass (M_{T})

As alluded to in Section 4.4, we use the transverse mass of the lepton-$E_{\mathrm{T}}^{\mathrm{miss}}$ system to reduce the prevalence of the single-lepton background, especially $t\bar{t} \to 1\ell$. By transverse mass, we mean the solution to the relativistic equation $M^2 = E^2 - p^2$, but using only the transverse components of the energy and momentum of the lepton-$E_{\mathrm{T}}^{\mathrm{miss}}$ system. So:

$$\begin{aligned} M_{\mathrm{T}}^2 &= E_T^2 - p_T^2 \\ &= (E_{\mathrm{T}}^{\mathrm{miss}} + E_{\mathrm{T}}^{\ell})^2 - (\vec{p}_{\mathrm{T}}^{\mathrm{miss}} + \vec{p}_{\mathrm{T}}^{\ell})^2 \end{aligned} \tag{4.1}$$

Transverse energy is defined as:

$$E_{\mathrm{T}}^2 = m^2 + p_{\mathrm{T}}^2 \tag{4.2}$$

In the case of $E_{\mathrm{T}}^{\mathrm{miss}}$, the missing momentum and energy are the same thing, giving us:

$$M_{\mathrm{T}}^2 = m_\ell^2 + 2E_{\mathrm{T}}^{\mathrm{miss}} E_{\mathrm{T}}^{\ell} - 2\vec{E}_{\mathrm{T}}^{\mathrm{miss}} \cdot \vec{p}_{\mathrm{T}}^{\ell} \tag{4.3}$$

In our case, m_ℓ is negligible compared to p_{T}^{ℓ}. This also means $E_{\mathrm{T}}^{\ell} \approx p_{\mathrm{T}}^{\ell}$. So if ϕ denotes the azimuthal angle between $\vec{E}_{\mathrm{T}}^{\mathrm{miss}}$ and $\vec{p}_{\mathrm{T}}^{\ell}$, then we find:

$$M_{\mathrm{T}} = \sqrt{2E_{\mathrm{T}}^{\mathrm{miss}} p_{\mathrm{T}}^{\ell}(1 - \cos\phi)} \tag{4.4}$$

In events with an on-shell W-boson decaying to a single lepton and no other sources of $E_{\mathrm{T}}^{\mathrm{miss}}$, the largest possible value M_{T} can take on is the W-boson mass, around 80 GeV. Thus, by cutting on M_{T}, we can strongly reduce the presence of $t\bar{t} \to 1\ell$, W+jets, and single-top events. This fact is illustrated in Figure 4.5. As described in Section 4.4, background events in the tail of the M_{T} distribution are mostly due to off-shell W bosons and $E_{\mathrm{T}}^{\mathrm{miss}}$ resolution effects.

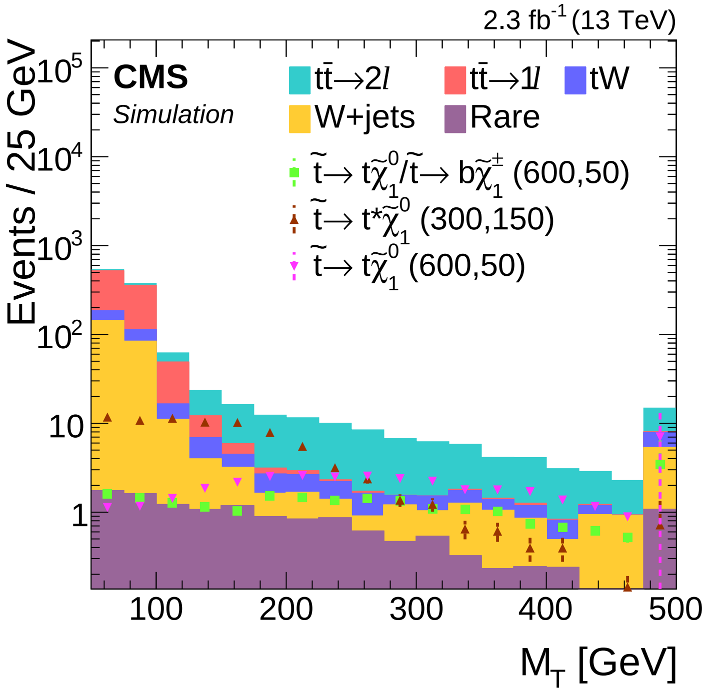

Figure 4.5: Distribution of M_{T} after all other selections have been applied.

4.6.8 Modified Topness (t_{mod})

In a previous search for stop squarks, particle physicists developed a variable they called *topness*, denoted t. This complicated variable attempts to quantify the degree to which an event is consistent with being a $t\bar{t} \to \ell\ell$ event [72]. Although our analysis must also suppress the $t\bar{t} \to \ell\ell$ background, our investigations showed that we could achieve better discrimination between signal and $t\bar{t} \to \ell\ell$ by removing two of the terms in the topness variable (specifically, the center-of-mass constraint, and the χ^2 for leptonic top decay). We thus arrive at a variable we call *modified topness*, or t_{mod}. To calculate this variable, we must minimize an expression that constrains the neutrino-lepton system to have a mass similar to the W-boson mass, and the b-quark-W-boson system to have a mass similar to the top quark mass. Thus we define:

$$\begin{aligned} t_{\text{mod}} &= \ln(\min S), \text{ where} \\ S(\vec{p}_W, p_{\nu,z}) &= \frac{(m_W^2 - (p_\nu + p_\ell)^2)^2}{a_W^4} + \frac{(m_t^2 - (p_{b_2} + p_W)^2)^2}{a_t^4} \end{aligned} \tag{4.5}$$

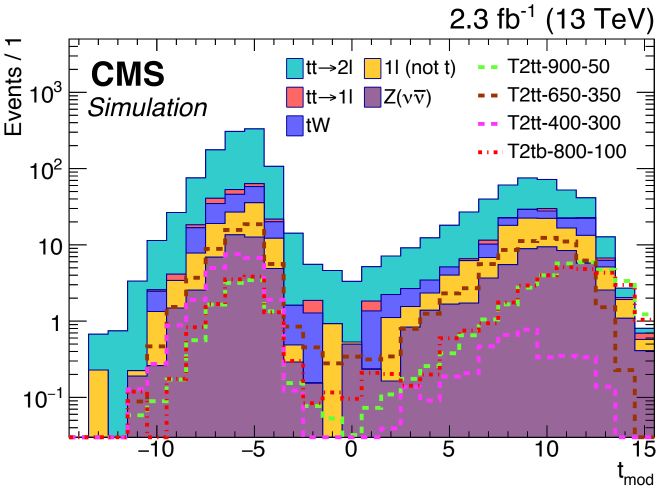

Figure 4.6: Distribution of t_{mod} after all other selections have been applied. Normalization is arbitrary.

The parameters a_W and a_t provide the scale for the W-boson and top quark masses; we set them to 5 GeV and 15 GeV, respectively. There is some ambiguity as to which jets should be used in this calculation. We find that t_{mod} behaves best across signal models with both low and high mass splittings if we chose our jets according to these rules:

- Consider all combinations of the three jets with the highest CSVv2 discriminator values. If at least one such jet is b-tagged, only consider permutations that include at least one b-tagged jet.
- Choose the combination of jets that minimizes the ultimate t_{mod} value.

Ultimately, modified topness is effective in discriminating against both $t\bar{t} \to \ell\ell$ events and single top tW events. However, it also suppresses signal models with certain kinematics. For that reason, we choose to bin our signal regions in t_{mod}, instead of making a strict cut on it. Figure 4.6 shows the distribution of t_{mod} for our background processes and various signal mass points.

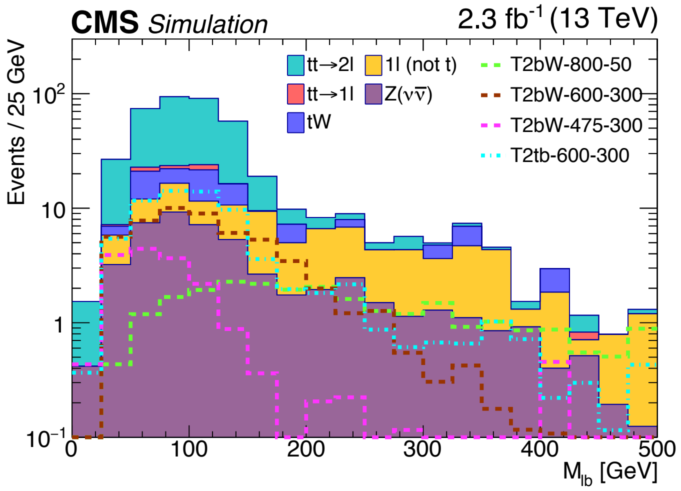

Figure 4.7: Distribution of $M_{\ell b}$ variable after baseline selections, in the region $t_{\text{mod}} > 0$. Normalization is arbitrary.

4.6.9 Lepton-b Invariant Mass ($M_{\ell b}$)

Another variable that can help us discriminate signal from background is the invariant mass of the lepton and its corresponding b-jet, denoted $M_{\ell b}$. In the case of $t\bar{t} \to \ell\ell$ and $t\bar{t} \to 1\ell$ backgrounds, as well as T2tt signals, assuming we pair our lepton with the correct b-jet, then $M_{\ell b}$ is constrained by kinematics:

$$M_{\ell b} \leq \sqrt{m_t^2 - m_W^2} \approx 153\text{GeV} \tag{4.6}$$

This inequality does not hold true for the W+jets background, nor for T2bW signals. So a low-$M_{\ell b}$ requirement will reduce W+jets content compared to the T2tt signal, and a high-$M_{\ell b}$ requirement will reduce the $t\bar{t}$ backgrounds compared to the T2bW signal. As Section 4.7 will describe, we use different bins of $M_{\ell b}$ in the definitions of some of our signal regions.

We define $M_{\ell b}$ to be the invariant mass of the system of the leading lepton and the b-tag nearest the lepton in ΔR. Figure 4.7 shows an example distribution of this variable. Because the W+jets background is dominant at higher $M_{\ell b}$, and because W+jets has a much higher prevalence of light-flavor jets over b-jets, we also tighten our b-tagging WP at high $M_{\ell b}$.

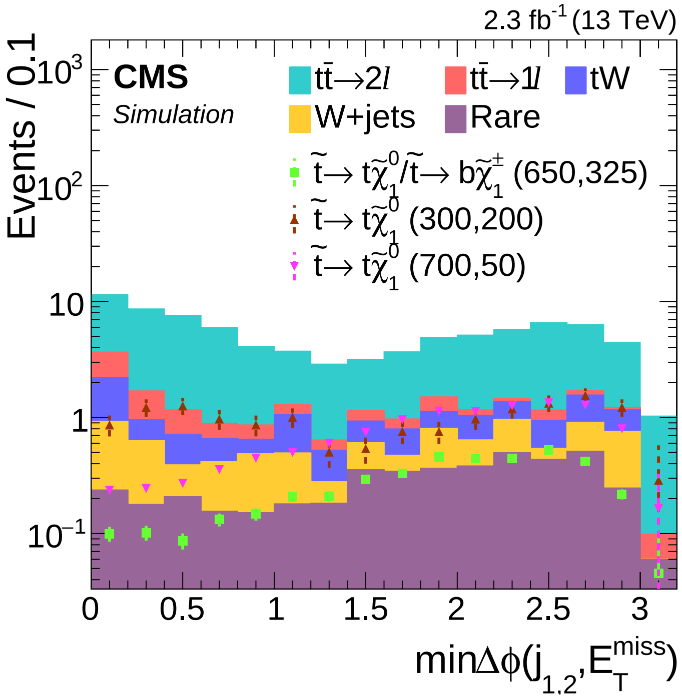

Figure 4.8: Distribution of $\min\Delta\phi(j_{1,2},\vec{E}_{\mathrm{T}}^{\mathrm{miss}})$ after all other selections have been applied.

4.6.10 Minimum Delta-Phi ($\min\Delta\phi(j_{1,2},\vec{E}_{\mathrm{T}}^{\mathrm{miss}})$)

The final variable we consider in selecting our events is the minimum $\Delta\phi$ between the $\vec{E}_{\mathrm{T}}^{\mathrm{miss}}$ and either of the two leading jets. In other words:

$$\min\Delta\phi(j_{1,2},\vec{E}_{\mathrm{T}}^{\mathrm{miss}}) = \min\left\{\Delta\phi(\vec{E}_{\mathrm{T}}^{\mathrm{miss}},j_1),\ \Delta\phi(\vec{E}_{\mathrm{T}}^{\mathrm{miss}},j_2)\right\} \tag{4.7}$$

This variable allows us to reduce backgrounds such as $t\bar{t} \to \ell\ell$ and $t\bar{t} \to 1\ell$ with relatively little loss of signal, because in these backgrounds we expect the neutrino (i.e. the source of the $E_{\mathrm{T}}^{\mathrm{miss}}$) to be relatively close to the high-p_T quark produced in the top decay. Figure 4.8 shows the distribution of this variable. We require a $\min\Delta\phi > 0.8$ for our bulk signal regions; for the compressed T2tt search, this requirement is relaxed to $\min\Delta\phi > 0.5$.

4.6.11 Corrections

Our Monte Carlo simulations seldom reproduce the aggregate properties of real data with perfect accuracy. Therefore, we must reweight our simulated events to reproduce the properties of the data more exactly. The nominal weights applied to our MC simulations are described here. Sections 4.8 and 4.10.1 will describe the systematic uncertainties on these and other weights, and how we propagate those uncertainties to our final results.

- As was described in Section 4.5.3, we evaluate the efficiencies of all triggers used in this analysis. For our signal regions, the combined trigger efficiency is so near 100% that we do not reweight our MC; in the regions where we use dilepton triggers, we do apply a weight for the efficiency of those triggers.

- We apply the official jet energy corrections from CMS, as mentioned in Sections 4.6.5 and 4.6.6.

- We apply weights to correct the efficiency of our b-tagging algorithms. These weights are provided by the b-tagging POG within CMS. There are separate weights for heavy flavor (HF) and light flavor (LF) jets, as well as for the medium and tight WPs used in the analysis.

- We apply weights for the efficiency of lepton identification and isolation, as provided by the SUSY PAG in CMS. We also account for the efficiency of vetoing a second lepton where applicable. Separate weights must be applied to our signal samples because they were generated using FastSim.

- Initial state radiation (ISR) refers to partons (and the jets they produce) that radiate off the initial particles in the hard collision process. ISR is not necessarily modeled correctly in our Monte Carlo samples. We reweight our simulated events using a prescription from the SUSY group to obtain a more accurate distribution of the number of jets per event.

- All of our signal and control regions involve binning in $E_{\mathrm{T}}^{\mathrm{miss}}$. If the $E_{\mathrm{T}}^{\mathrm{miss}}$ resolution differs between data and MC, we run the risk of badly estimating how simulated events are distributed among these bins. In Appendix B, we perform a separate study on the effects of $E_{\mathrm{T}}^{\mathrm{miss}}$ resolution mismodeling, and the results are used to reweight our $t\bar{t}$, single top tW, and W+jets simulated events.
- As Appendix A describes, there is a disagreement between data and MC in the tail of the $E_{\mathrm{T}}^{\mathrm{miss}}$ spectra of dileptonic $t\bar{t}$ and tW events. Thus, we correct this discrepancy by applying a weight to dileptonic $t\bar{t}$ and tW MC events in the upper $E_{\mathrm{T}}^{\mathrm{miss}}$ range where this effect would impact our measurements.
- To correct for discrepancies in the pileup distribution, we reweight events using the official corrections prescribed by CMS.

4.7 Signal Regions

As Section 4.6 has described, we preselect events for our search using the following criteria:

- The first vertex must meet certain quality criteria.
- The event must have one well-reconstructed electron or muon. There must be no other electrons or muons in the event, even of low reconstruction quality.
- The event must not have a tau in it, or an isolated track that could be a tau.
- The event must have at least two jets, of which at least one must be b-tagged.
- The $E_{\mathrm{T}}^{\mathrm{miss}}$ must be at least 250 GeV.
- The M_{T} must be at least 150 GeV.

- The minimum $\Delta\phi$ between the $E_{\mathrm{T}}^{\mathrm{miss}}$ and the two leading jets must be at least 0.8 (at least 0.5 for the corridor search).

After those criteria have been met, events are further subdivided among several different signal regions to increase our sensitivity to a wide variety of SUSY scenarios.

4.7.1 Nominal Signal Regions

Our nominal signal regions are tailored to the search for most T2tt signals, the T2bW signals, and the T2tb signals. To that end, our signal regions are divided by the number of jets in the event, the modified topness variable, the lepton-b-jet invariant mass, and the amount of $E_{\mathrm{T}}^{\mathrm{miss}}$. These signal regions are enumerated in Table 4.5. At times I will refer to these regions using a letter for the series and a number for the specific $E_{\mathrm{T}}^{\mathrm{miss}}$ bin, as A3, D1, G4, etc.

Table 4.5: Definitions of the signal regions used in the nominal search.

Label	N_J	t_{mod}	$M_{\ell b}$ [GeV]	$E_{\mathrm{T}}^{\mathrm{miss}}$ [GeV]				
A	2-3	> 10	≤ 175	250-350	350-450	450-600	> 600	
B	2-3	> 10	> 175	250-450	450-600	> 600		
C	≥ 4	≤ 0	≤ 175	250-350	350-450	450-550	550-650	> 650
D	≥ 4	≤ 0	> 175	250-350	350-450	450-550	> 550	
E	≥ 4	0-10	≤ 175	250-350	350-550	> 550		
F	≥ 4	0-10	> 175	250-450	> 450			
G	≥ 4	> 10	≤ 175	250-350	350-450	450-600	> 600	
H	≥ 4	> 10	> 175	250-450	> 450			

The signal regions that require 2-3 jets and $t_{\mathrm{mod}} > 10$ (the A and B series) are designed to target T2tb signals. Because we take the mass difference between the chargino and the LSP to be only 5 GeV in this model, the W boson produced in the chargino decay will be very off shell. Thus the lepton will come from the top decay, and the off-shell W will decay into very weak jets that we cannot resolve. In addition, these regions will also have sensitivity to any of our signal models where the stops are highly boosted and cause two jets to merge into one.

The remaining nominal signal regions (C-H) target T2tt and T2bW models. They include a four jet requirement because we expect two b-jets from the top or stop decays and two more jets from the hadronic W decay.

Each of our three signal models peaks in a different part of the t_{mod} range. So by creating three distinct bins in t_{mod} (but not applying a cut), we can target each model with a different region, while effectively dividing the background events into three parts. As Figure 4.6 shows, the compressed case (small ΔM) is most prominent when t_{mod} is < 0. When $0 < t_{\mathrm{mod}} < 10$, signal models with moderate ΔM will stand out most against $t\bar{t} \rightarrow \ell\ell$. And when $t_{\mathrm{mod}} > 10$, the $t\bar{t} \rightarrow \ell\ell$ background drops off substantially faster than signals with a large ΔM.

The binning in $M_{\ell b}$ follows from the facts explained in Section 4.6.9. At low $M_{\ell b}$, the W+jets background is reduced with little loss in the T2tt signal, and at high $M_{\ell b}$, the $t\bar{t}$ backgrounds are reduced for little loss in the T2bW signal. Because this reduction in $t\bar{t}$ leaves W+jets as the dominant background, we also require that our one b-tag pass a tight WP in the high $M_{\ell b}$ regions.

Finally, the higher the mass splitting, the more $E_{\mathrm{T}}^{\mathrm{miss}}$ we generally expect in an event. So binning in $E_{\mathrm{T}}^{\mathrm{miss}}$ increases the likelihood that any one particular signal model will stand out against the SM background. We choose how many $E_{\mathrm{T}}^{\mathrm{miss}}$ bins to use in each series, and where their boundaries should be, in order to give reasonable statistics in all signal regions.

4.7.2 Corridor Signal Regions

As Section 4.3.2 described, previous stop searches have struggled to achieve sensitivity in the top corridor region because compressed T2tt decays are suppressed and difficult to detect. In order to address this deficit, I developed a dedicated search strategy focused on increasing our acceptance of compressed T2tt signals, while maintaining a low rate of SM background events. I also validated that this strategy was compatible with our established techniques for background and signal estimation. The final product of my work was four additional signal regions to add to our overall search strategy.

The dedicated corridor signal regions use the same event selections as the nominal signal regions, except for the following changes:

- I require at least 5 jets in the event.
- The highest-p_T jet must not be b-tagged using the medium WP.
- The p_T of the lepton in the event must be < 150 GeV.
- The azimuthal angle between the $E_{\mathrm{T}}^{\mathrm{miss}}$ and the lepton, $\Delta\phi(E_{\mathrm{T}}^{\mathrm{miss}}, \ell)$, must be < 2.0.
- As described earlier, the $\min\Delta\phi(j_{1,2}, \vec{E}_{\mathrm{T}}^{\mathrm{miss}})$ must be > 0.5.

In addition to these selections, the four corridor signal regions are defined by four bins in $E_{\mathrm{T}}^{\mathrm{miss}}$, given by Table 4.6:

Table 4.6: $E_{\mathrm{T}}^{\mathrm{miss}}$ bins used in the dedicated corridor signal regions.

Label	$E_{\mathrm{T}}^{\mathrm{miss}}$ [GeV]			
I	250-350	350-450	450-550	> 550

To develop these signal regions, I considered the unique kinematics of compressed T2tt signals, and how they might affect the variables already measured in our stop search. I also considered whether any new variables might be able to discriminate compressed T2tt from the SM background. Although several variables had the potential to discriminate compressed T2tt from background, I made the final choice by measuring which added cuts provided the greatest increases in expected sensitivity, measured using a simplified version of the limit-setting procedure described later in Section 4.10.

Compressed stop decays, by virtue of their off-shell top quark, tend to have lower $E_{\mathrm{T}}^{\mathrm{miss}}$ than the bulk signals. So one of the first modifications I considered was relaxing our $E_{\mathrm{T}}^{\mathrm{miss}}$ requirement. However, I found that any reduction in $E_{\mathrm{T}}^{\mathrm{miss}}$ would cause a proportionally larger increase in background yield than in signal yield. With the 250 GeV $E_{\mathrm{T}}^{\mathrm{miss}}$ cut firmly fixed in place, we then asked how might a compressed stop decay generate such large $E_{\mathrm{T}}^{\mathrm{miss}}$? The answer to that question ultimately became the defining element of the corridor search strategy.

We concluded that in the corridor region, in order to generate at least 250 GeV of $E_{\mathrm{T}}^{\mathrm{miss}}$, a stop pair must have a large boost. Momentum conservation dictates that in order to have a large boost, the stop pair should be recoiling off some other physics object. The most likely candidate was a high-p_T jet produced as ISR. Because we expected another jet in the event, in addition to the four from stop decay, I imposed the $N_J > 5$ requirement. Additionally, ISR jets seldom originate from b-quarks, because b-quarks are fairly heavy, and thus hard to produce. So I further target the compressed signal by requiring that the leading jet not be b-tagged.

The $E_{\mathrm{T}}^{\mathrm{miss}}$ in a stop decay comes from the two LSPs, as well as the neutrino produced alongside the single lepton. In the case where the stop squarks are boosted, we expect the products of the stop decays, including the main contributors to the $E_{\mathrm{T}}^{\mathrm{miss}}$, to continue in the rough direction of their parents. Thus the cut $\Delta\phi(E_{\mathrm{T}}^{\mathrm{miss}}, \ell) < 2$ selects events where the lepton and the $E_{\mathrm{T}}^{\mathrm{miss}}$ are not separated by a large angle. Similarly, by relaxing the cut on $\min\Delta\phi(j_{1,2}, \vec{E}_{\mathrm{T}}^{\mathrm{miss}})$ to > 0.5, we allow jets produced in the stop decays to be more colinear with the lepton. Finally, the upper bound on the lepton p_T is because compressed top quarks have less momentum to pass on to their decay products. The distributions of these variables are pictured in Figure 4.9.

It is worth noting that the dedicated corridor signal regions are not orthogonal to the nominal signal regions. In fact, if not for the relaxed $\min\Delta\phi$ cut, the corridor signal regions would constitute a strict subset of the nominal signal regions. To avoid double-counting events in multiple signal regions, we decided to use the corridor and nominal signal regions in non-overlapping regions of parameter space. Using the statistical tools described in Section 4.10.2, I calculated the expected sensitivity to T2tt signals for both the nominal and corridor signal regions at a variety of mass points. The sensitivity is expressed as a number, r, the smallest value by which one could scale the signal cross section and be able to exclude the signal hypothesis. Put simply, lower values of r indicate greater sensitivity to the signal. In Figure 4.10, I plotted

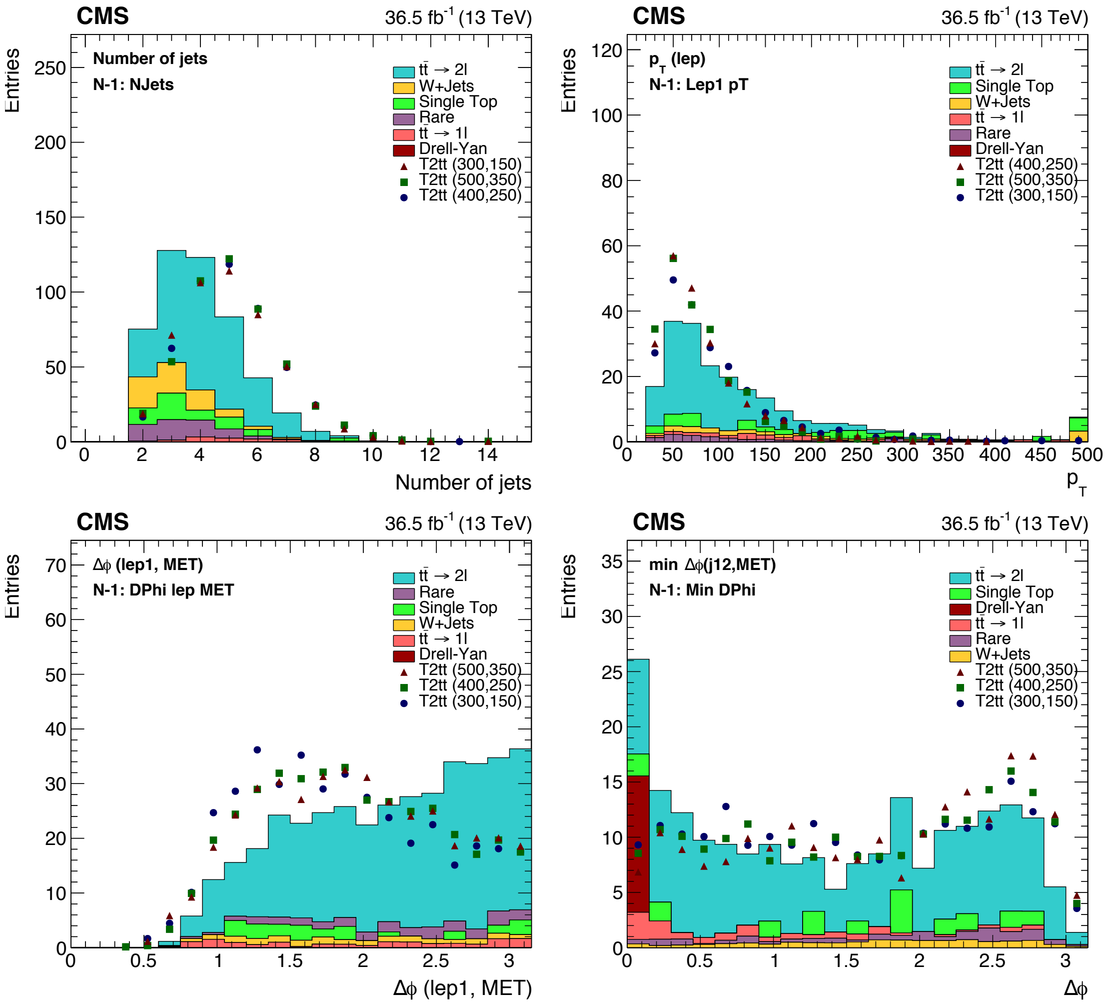

Figure 4.9: Comparison between background and selected signal points for the four (non-boolean) variables that define the corridor signal regions. Each cut is removed, to illustrate the rationale for its threshold.

the ratio $r_{\mathrm{corridor}}/r_{\mathrm{nominal}}$ for T2tt signals; wherever that value is less than 1, the corridor signal regions are expected to be more sensitive than the nominal signal regions. Perhaps unsurprisingly, the corridor search regions have higher expected sensitivity for ΔM between 100 and 225 GeV–in other words, in the area around the top and W corridors. The size of the improvement in sensitivity ranges from about 10-30%. We therefore use the corridor signal regions for T2tt models with ΔM between 100 and 225 GeV, and we use the nominal signal regions everywhere else in the T2tt plane, as well as for the T2bW and T2tb signal models.

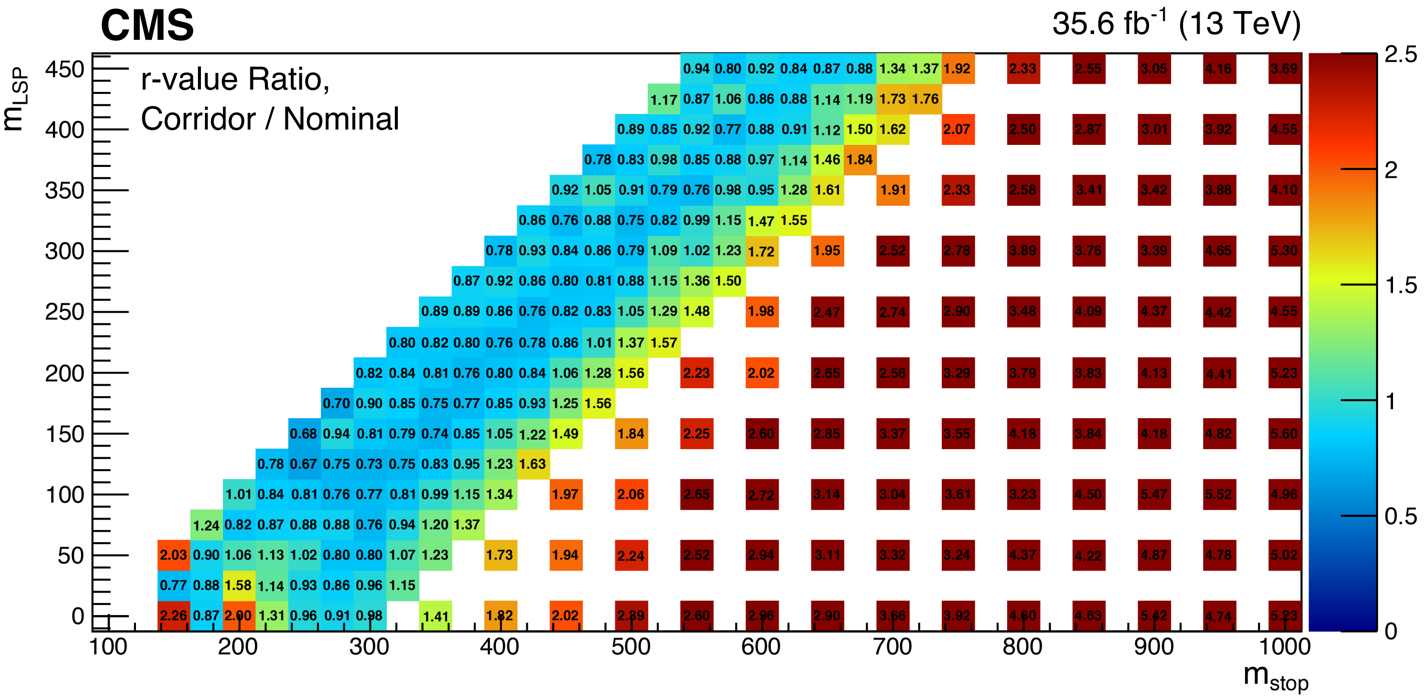

Figure 4.10: Ratio of expected sensitivities for the corridor and nominal signal regions, at every mass point in the T2tt signal scan.

4.8 Background Estimation

As previous sections have described, we apply a number of preselections that reduce the prevalence of the SM backgrounds in our search. In addition, we divide our search up into signal regions so that we can be sensitive to several possible signal models while spreading out the backgrounds. However, even after these measures, we still expect our signal regions to be dominated by SM background events. If we hope to find any signal from SUSY among the backgrounds, we must be able to reliably estimate the size of the backgrounds so we can subtract them from the measured data. We make these estimates using a variety of techniques that will be described below. Wherever possible, we make data-driven estimates based on control regions that are adjacent or complementary to our signal regions. This section will also describe how we estimate the systematic uncertainties on each background component.

4.8.1 Lost Lepton

Across all our signal regions, the largest total background is the lost lepton background. These are events that have two true leptons in them, but for various reasons, one lepton is not caught by our second lepton veto, hadronic tau veto, or isolated track veto. Often this loss occurs because the additional lepton is poorly reconstructed, or falls outside the $|\eta|$ or p_T ranges of our detect or ID criteria. Because the second lepton is not detected, it effectively creates additional $E_{\mathrm{T}}^{\mathrm{miss}}$, helping the event to pass our $E_{\mathrm{T}}^{\mathrm{miss}}$ requirement. Plus, the additional neutrino associated with the second lepton can help the event pass our M_{T} cut. The dominant physics process contributing to this background is $t\bar{t} \to \ell\ell$, however there is a strong contribution from single-top production in the tW channel. Other contributors include $t\bar{t}$ + vector boson production, and diboson production. The strong understanding of the $t\bar{t} \to \ell\ell$ process gained in the top asymmetry measurements (Chapter 3) gives us confidence we can accurately estimate this background component.

Estimation Method

We estimate the number of lost lepton events in our signal regions based on the number of events in a set of dilepton control regions, to be defined below. We assume that Monte Carlo simulations correctly model the ratio of lost lepton events to dilepton events, so that the following relationship holds true:

$$\frac{N_{\text{lost}\,\ell}^{\text{Data, SR}}}{N_{\ell\ell}^{\text{Data, CR}}} = \frac{M_{\text{lost}\,\ell}^{\text{MC, SR}}}{M_{\ell\ell}^{\text{MC, CR}}} \tag{4.8}$$

In this and future equations, N will denote the number of events in actual data, and M will denote the number of events in Monte Carlo simulations.

By rearranging Equation 4.8, we can derive the formula for a data-driven estimate of the number of lost lepton events in the signal region. The estimate is given by the data yield in the corresponding control region times the SR/CR ratio derived from Monte Carlo. This ratio is known as the lepton transfer factor, TF_{lep}. So:

$$N_{\text{lost}\,\ell}^{\text{SR}} = N_{\ell\ell}^{\text{CR}} \times \frac{M_{\text{lost}\,\ell}^{\text{SR}}}{M_{\ell\ell}^{\text{CR}}} \tag{4.9}$$

Five of the high-$E_{\mathrm{T}}^{\text{miss}}$ CRs have very small data yields, a fact that would contribute to large statistical uncertainty using the estimation method described above. To mitigate this uncertainty, we combine the low-statistics bins with their neighboring bins that have higher statistics, and add another term where we use MC to extrapolate from the merged $E_{\mathrm{T}}^{\text{miss}}$ bins to the single $E_{\mathrm{T}}^{\text{miss}}$ bins:

$$N_{\text{lost}\,\ell}^{\text{SR, bin}} = N_{\ell\ell}^{\text{CR, merged}} \times \frac{M_{\text{lost}\,\ell}^{\text{SR, merged}}}{M_{\ell\ell}^{\text{CR, merged}}} \times \left(\frac{M_{\text{lost}\,\ell}^{\text{SR, bin}}}{M_{\text{lost}\,\ell}^{\text{SR, merged}}} \right) \tag{4.10}$$

The specific regions that are merged in this way are: B2/3, E2/3, F1/2, and H1/2.

This process of extrapolating in $E_{\mathrm{T}}^{\text{miss}}$ has the potential to introduce errors in our measurements if the $E_{\mathrm{T}}^{\text{miss}}$ distribution or $E_{\mathrm{T}}^{\text{miss}}$ resolution are mismodeled in MC. In Appendix A, we study the modeling of dileptonic $t\bar{t}$ and tW events using an e/μ cross-check region, and in

Appendix B we study the modeling of the $E_{\mathrm{T}}^{\mathrm{miss}}$ resolution. Based on these studies, we assign appropriate scale factors and systematic uncertainties to account for any effects due to mismodeling. The $E_{\mathrm{T}}^{\mathrm{miss}}$ extrapolation also introduces some additional uncertainty due to limited MC statistics.

Control Region Definitions

To form our dilepton control regions, we use the same selections and binning as the signal regions, except that we invert the veto on additional leptons. Whereas the signal regions require the absence of a second electron or muon, our dilepton control regions require the presence of a second reconstructed electron or muon passing the veto ID (described earlier), and with $p_T > 10$ GeV. To simplify our estimate and its uncertainties, we do not invert the hadronic tau or isolated track vetos. Because lost leptons contribute to $E_{\mathrm{T}}^{\mathrm{miss}}$ in our signal regions, when working with the dilepton control regions we add the trailing lepton p_T to the $E_{\mathrm{T}}^{\mathrm{miss}}$, and recalculate all derived quantities that are based on $E_{\mathrm{T}}^{\mathrm{miss}}$. This helps us keep the conditions as similar as possible between the CRs and the SRs.

The data and MC yields in the dilepton control regions are given in Table 4.7. The events in the control regions receive all the same corrections as the SR events, with two exceptions. For dilepton events with a hadronic tau in them, we apply a scale factor to correct the efficiency of tau identification. We also apply different trigger weights, because we select dilepton events using dilepton triggers. Our control regions are over 95% pure in dilepton events, so we make no correction for impurities. The last column of Table 4.7 presents the ratio of the data to MC yields. In some regions, this ratio differs considerably from unity. Such differences in normalization between data and MC actually have no effect on our final background estimate. Looking at Equation 4.9, we see that the background normalization comes entirely from the CR data, and that MC is used only to calculate the transfer factor from the CRs to SRs (and the $E_{\mathrm{T}}^{\mathrm{miss}}$ extrapolation factor, where relevant).

Table 4.7: Data and Monte Carlo yields in the dilepton control regions, based on 35.9 fb^{-1} of luminosity.

Region	≥ 2 leptons	1 lepton, from W	1 lepton, from t	$Z \to \nu\nu$	Sum Bkg.	Data	Data/MC
< 4 jets, $t_{\text{mod}} \geq 10$, $M_{\ell b} < 175$, $250 < E_T^{\text{miss}} < 350$	215.40 ± 4.56	4.27 ± 2.62	6.49 ± 0.95	1.35 ± 0.06	227.51 ± 5.35	217 ± 14.73	0.95 ± 0.07
< 4 jets, $t_{\text{mod}} \geq 10$, $M_{\ell b} < 175$, $350 < E_T^{\text{miss}} < 450$	77.88 ± 2.80	0.27 ± 0.13	2.61 ± 0.62	0.65 ± 0.04	81.40 ± 2.87	75 ± 8.66	0.92 ± 0.11
< 4 jets, $t_{\text{mod}} \geq 10$, $M_{\ell b} < 175$, $450 < E_T^{\text{miss}} < 600$	25.01 ± 1.63	3.33 ± 3.08	1.37 ± 0.44	0.23 ± 0.03	29.95 ± 3.51	25 ± 5.00	0.83 ± 0.19
< 4 jets, $t_{\text{mod}} \geq 10$, $M_{\ell b} < 175$, $E_T^{\text{miss}} > 600$	6.62 ± 0.84	0.02 ± 0.02	0.47 ± 0.27	0.06 ± 0.01	7.17 ± 0.88	3 ± 1.73	0.42 ± 0.25
< 4 jets, $t_{\text{mod}} \geq 10$, $M_{\ell b} \geq 175$, $250 < E_T^{\text{miss}} < 450$	9.44 ± 0.92	3.15 ± 2.80	0.88 ± 0.36	0.22 ± 0.02	13.68 ± 2.97	11 ± 3.32	0.80 ± 0.30
< 4 jets, $t_{\text{mod}} \geq 10$, $M_{\ell b} \geq 175$, $450 < E_T^{\text{miss}} < 650$	2.64 ± 0.51	0.05 ± 0.03	—	0.04 ± 0.01	2.72 ± 0.51	3 ± 1.73	1.10 ± 0.67
< 4 jets, $t_{\text{mod}} \geq 10$, $M_{\ell b} \geq 175$, $E_T^{\text{miss}} > 600$	0.75 ± 0.26	0.05 ± 0.03	0.15 ± 0.15	0.01 ± 0.00	0.95 ± 0.31	—	—
≥ 4 jets, $t_{\text{mod}} < 0.0$, $M_{\ell b} < 175$, $250 < E_T^{\text{miss}} < 350$	667.08 ± 7.32	0.71 ± 0.21	27.62 ± 1.81	4.87 ± 0.11	700.28 ± 7.54	675 ± 25.98	0.96 ± 0.04
≥ 4 jets, $t_{\text{mod}} < 0.0$, $M_{\ell b} < 175$, $350 < E_T^{\text{miss}} < 450$	140.51 ± 3.45	2.45 ± 2.19	5.53 ± 0.84	1.28 ± 0.06	149.76 ± 4.17	150 ± 12.25	1.00 ± 0.09
≥ 4 jets, $t_{\text{mod}} < 0.0$, $M_{\ell b} < 175$, $450 < E_T^{\text{miss}} < 550$	34.80 ± 1.75	0.18 ± 0.10	1.00 ± 0.38	0.33 ± 0.03	36.31 ± 1.79	27 ± 5.20	0.74 ± 0.15
≥ 4 jets, $t_{\text{mod}} < 0.0$, $M_{\ell b} < 175$, $550 < E_T^{\text{miss}} < 650$	10.44 ± 0.95	0.08 ± 0.04	0.27 ± 0.19	0.13 ± 0.02	10.92 ± 0.97	7 ± 2.65	0.64 ± 0.25
≥ 4 jets, $t_{\text{mod}} < 0.0$, $M_{\ell b} < 175$, $E_T^{\text{miss}} > 650$	3.97 ± 0.59	—	0.14 ± 0.14	0.05 ± 0.01	4.17 ± 0.60	8 ± 2.83	1.92 ± 0.73
≥ 4 jets, $t_{\text{mod}} < 0.0$, $M_{\ell b} \geq 175$, $250 < E_T^{\text{miss}} < 350$	95.64 ± 2.73	0.83 ± 0.24	5.54 ± 0.82	1.02 ± 0.05	103.03 ± 2.86	73 ± 8.54	0.71 ± 0.09
≥ 4 jets, $t_{\text{mod}} < 0.0$, $M_{\ell b} \geq 175$, $350 < E_T^{\text{miss}} < 450$	25.32 ± 1.45	0.28 ± 0.11	1.39 ± 0.42	0.25 ± 0.03	27.25 ± 1.52	24 ± 4.90	0.88 ± 0.19
≥ 4 jets, $t_{\text{mod}} < 0.0$, $M_{\ell b} \geq 175$, $450 < E_T^{\text{miss}} < 550$	7.16 ± 0.78	0.00 ± 0.00	0.61 ± 0.28	0.09 ± 0.02	7.86 ± 0.83	4 ± 2.00	0.51 ± 0.26
≥ 4 jets, $t_{\text{mod}} < 0.0$, $M_{\ell b} \geq 175$, $E_T^{\text{miss}} > 550$	4.92 ± 0.65	0.02 ± 0.02	0.40 ± 0.23	0.05 ± 0.01	5.38 ± 0.69	2 ± 1.41	0.37 ± 0.27
≥ 4 jets, $0.0 < t_{\text{mod}} < 10$, $M_{\ell b} < 175$, $250 < E_T^{\text{miss}} < 350$	119.79 ± 3.04	1.02 ± 0.74	12.02 ± 1.24	1.46 ± 0.11	134.29 ± 3.36	119 ± 10.91	0.89 ± 0.08
≥ 4 jets, $0.0 < t_{\text{mod}} < 10$, $M_{\ell b} < 175$, $350 < E_T^{\text{miss}} < 550$	33.87 ± 1.68	0.37 ± 0.14	4.69 ± 0.80	0.50 ± 0.04	39.42 ± 1.86	33 ± 5.74	0.84 ± 0.15
≥ 4 jets, $0.0 < t_{\text{mod}} < 10$, $M_{\ell b} < 175$, $E_T^{\text{miss}} > 550$	1.64 ± 0.41	0.02 ± 0.02	—	0.05 ± 0.01	1.71 ± 0.42	1 ± 1.00	0.58 ± 0.60
≥ 4 jets, $0.0 < t_{\text{mod}} < 10$, $M_{\ell b} \geq 175$, $250 < E_T^{\text{miss}} < 450$	7.95 ± 0.79	0.53 ± 0.19	1.58 ± 0.44	0.18 ± 0.02	10.24 ± 0.92	16 ± 4.00	1.56 ± 0.42
≥ 4 jets, $0.0 < t_{\text{mod}} < 10$, $M_{\ell b} \geq 175$, $E_T^{\text{miss}} > 450$	1.31 ± 0.32	0.15 ± 0.10	0.26 ± 0.18	0.13 ± 0.11	1.85 ± 0.39	1 ± 1.00	0.54 ± 0.55
≥ 4 jets, $t_{\text{mod}} \geq 10$, $M_{\ell b} < 175$, $250 < E_T^{\text{miss}} < 350$	23.14 ± 1.35	0.13 ± 0.11	7.34 ± 0.95	0.44 ± 0.03	31.04 ± 1.65	29 ± 5.39	0.93 ± 0.18
≥ 4 jets, $t_{\text{mod}} \geq 10$, $M_{\ell b} < 175$, $350 < E_T^{\text{miss}} < 450$	18.13 ± 1.24	0.26 ± 0.14	3.37 ± 0.66	0.29 ± 0.03	22.05 ± 1.41	23 ± 4.80	1.04 ± 0.23
≥ 4 jets, $t_{\text{mod}} \geq 10$, $M_{\ell b} < 175$, $450 < E_T^{\text{miss}} < 600$	11.54 ± 0.98	0.03 ± 0.02	2.15 ± 0.54	0.16 ± 0.02	13.88 ± 1.12	15 ± 3.87	1.08 ± 0.29
≥ 4 jets, $t_{\text{mod}} \geq 10$, $M_{\ell b} < 175$, $E_T^{\text{miss}} > 600$	3.22 ± 0.51	0.05 ± 0.03	0.22 ± 0.15	0.21 ± 0.14	3.71 ± 0.55	2 ± 1.41	0.54 ± 0.39
≥ 4 jets, $t_{\text{mod}} \geq 10$, $M_{\ell b} \geq 175$, $250 < E_T^{\text{miss}} < 450$	2.01 ± 0.36	0.10 ± 0.09	1.05 ± 0.37	0.07 ± 0.01	3.22 ± 0.53	1 ± 1.00	0.31 ± 0.31
≥ 4 jets, $t_{\text{mod}} \geq 10$, $M_{\ell b} \geq 175$, $E_T^{\text{miss}} > 450$	1.91 ± 0.40	0.21 ± 0.13	0.37 ± 0.21	0.02 ± 0.01	2.51 ± 0.47	3 ± 1.73	1.20 ± 0.73
Compressed search, $250 < E_T^{\text{miss}} < 350$	109.78 ± 2.79	0.43 ± 0.14	8.20 ± 0.97	1.19 ± 0.06	119.60 ± 2.96	114.00 ± 10.68	0.95 ± 0.09
Compressed search, $350 < E_T^{\text{miss}} < 450$	31.39 ± 1.53	0.30 ± 0.13	2.01 ± 0.49	0.35 ± 0.03	34.05 ± 1.61	27.00 ± 5.20	0.79 ± 0.16
Compressed search, $450 < E_T^{\text{miss}} < 550$	8.04 ± 0.81	0.07 ± 0.04	0.30 ± 0.22	0.11 ± 0.02	8.52 ± 0.83	4.00 ± 2.00	0.47 ± 0.24
Compressed search, $E_T^{\text{miss}} > 550$	4.76 ± 0.61	0.05 ± 0.03	0.23 ± 0.16	0.08 ± 0.01	5.12 ± 0.63	5.00 ± 2.24	0.98 ± 0.45

Systematic Uncertainties

Our use of Monte Carlo simulations introduces several sources of systematic uncertainty on our lost lepton background estimate. Some uncertainties cancel out in the ratio $M^{\mathrm{SR}}/M^{\mathrm{CR}}$, such as the flat 2.6% uncertainty on the luminosity of the data, though most do not. The procedures used to estimate our uncertainties are as follows:

- **Data and MC statistics:** The largest sources of uncertainty on our background estimates are the statistical uncertainties on our data and Monte Carlo yields.
- **Trigger efficiency:** The efficiencies of our dilepton triggers are parameterized in leading lepton flavor, leading lepton p_T, and $E_{\mathrm{T}}^{\mathrm{miss}}$ (with second lepton added). We take the uncertainties on these efficiency measurements and propagate them through the background estimate.
- **JES:** We vary the jet energy scale within its uncertainties. This effect cancels out to first order in $M^{\mathrm{SR}}/M^{\mathrm{CR}}$.
- **ISR:** The uncertainties on the ISR n_{jets} corrections are propagated through the background estimate.
- **$E_{\mathrm{T}}^{\mathrm{miss}}$ resolution:** The effects of $E_{\mathrm{T}}^{\mathrm{miss}}$ resolution are studied in Appendix B. These effects cancel in all regions except those where we perform $E_{\mathrm{T}}^{\mathrm{miss}}$ extrapolation. We assign an uncertainty of half the distance between the scale factor and unity.
- **$t\bar{t}$ and tW $E_{\mathrm{T}}^{\mathrm{miss}}$:** The modeling of $E_{\mathrm{T}}^{\mathrm{miss}}$ in our dilepton CRs is studied in Appendix A. The scale factors we derive are not applied where $E_{\mathrm{T}}^{\mathrm{miss}}$ extrapolation is not used. The uncertainty on these scale factors is propagated through the background estimate.
- **b-tagging efficiencies:** We apply the uncertainties on the heavy flavor (HF) and light flavor (LF) b-tagging scale factors provided by CMS. To first order, this effect cancels out in

$M^{\mathrm{SR}}/M^{\mathrm{CR}}$.

- **Lepton efficiencies:** The variations on the lepton ID and isolation scale factors are applied.
- **Hadronic tau and isolated track efficiencies:** Our method for assigning this uncertainty is based on the method used in the all-hadronic M_{T2} search [73]. Most of our tau rejection power comes from the isolated track veto. The isolation efficiency for 1-prong hadronic taus may differ by up to 15% from the efficiency for electrons and muons, so we take half this figure (about 7%) as the uncertainty on the isolated track veto. Meanwhile, the (3-prong) hadronic tau veto is less than 10% efficient. We thus assign a 100% uncertainty to this component of the veto.
- **Pileup reweighting:** The cross section for the data sample used to reweight the distribution of the number of primary vertices is varied by 5%.
- **PDF:** We take the average of 100 different PDF variations from the NNPDF3.0 set [74], and use the standard deviation of this average to reweight our Monte Carlo events up and down.
- α_S**:** We vary the QCD scale of our events, deriving the uncertainty from only the change in acceptance. To first order, this uncertainty cancels out in $M^{\mathrm{SR}}/M^{\mathrm{CR}}$
- Q^2**:** We take the largest two variations in factorization and normalization scales (up to 2.0 and down to 0.5 for each) as an envelope, and calculate the uncertainty based only on the change in acceptance. This effect cancels out to first order in $M^{\mathrm{SR}}/M^{\mathrm{CR}}$.

The size of these uncertainties is presented in Table 4.8.

Results

The results of the full background estimation procedure, including systematic uncertainties, are presented in Table 4.9.

Table 4.8: Summary of systematic uncertainties on the lost lepton background estimate.

Region	Data Stats	MC Stats	CR2l Trig.	JES	ISR	MET res.	MET $t\bar{t}$ SF	b-tag (HF)	b-tag (LF)	Lepton Eff.	τ Eff.	PU	PDF	α_S	Q^2	Total
A $250 < E_T^{miss} < 350$	6.8%	5.0%	2.1%	0.6%	0.1%	0.0%	0.0%	0.0%	0.1%	6.3%	0.3%	0.9%	3.0%	2.7%	0.5%	11.6%
A $350 < E_T^{miss} < 450$	11.5%	9.1%	1.6%	5.7%	0.2%	0.0%	0.0%	0.0%	0.2%	6.5%	0.5%	2.2%	0.7%	0.5%	0.9%	17.3%
A $450 < E_T^{miss} < 600$	20.0%	21.6%	1.9%	5.3%	0.1%	0.0%	0.0%	0.7%	0.2%	5.3%	0.4%	2.5%	5.2%	2.5%	1.4%	31.1%
A $E_T^{miss} > 600$	57.7%	37.9%	1.8%	5.2%	0.3%	0.2%	0.0%	0.3%	0.6%	40.1%	0.5%	0.8%	5.8%	5.0%	3.2%	80.5%
B $250 < E_T^{miss} < 450$	30.2%	30.9%	4.3%	15.2%	0.3%	0.0%	0.0%	1.2%	3.2%	4.9%	0.2%	4.9%	2.2%	3.1%	0.7%	46.8%
B $450 < E_T^{miss} < 600$	57.7%	29.2%	1.1%	3.3%	0.1%	5.3%	0.0%	0.6%	0.1%	4.5%	0.3%	2.4%	4.6%	3.4%	3.7%	65.6%
B $E_T^{miss} > 600$	57.7%	45.4%	1.1%	3.3%	0.1%	5.3%	0.0%	0.8%	3.2%	18.0%	0.2%	14.1%	2.3%	1.8%	7.5%	77.7%
C $250 < E_T^{miss} < 350$	3.8%	2.0%	2.1%	3.0%	1.2%	0.0%	0.0%	0.1%	0.2%	6.5%	0.5%	0.5%	0.3%	0.5%	0.1%	8.8%
C $350 < E_T^{miss} < 450$	8.2%	4.9%	2.4%	1.2%	0.9%	0.0%	0.0%	0.2%	0.4%	6.7%	0.7%	0.1%	0.3%	0.1%	0.2%	12.0%
C $450 < E_T^{miss} < 550$	19.2%	9.3%	1.6%	1.0%	0.5%	0.0%	0.0%	0.2%	0.3%	7.9%	0.6%	0.7%	1.1%	0.1%	0.1%	22.9%
C $550 < E_T^{miss} < 650$	37.8%	17.3%	1.6%	9.3%	0.6%	0.1%	0.0%	0.2%	0.7%	6.8%	0.7%	2.3%	6.0%	0.3%	0.1%	43.6%
C $E_T^{miss} > 650$	35.4%	25.9%	2.2%	8.8%	2.7%	0.4%	0.0%	0.2%	0.7%	12.0%	0.5%	3.0%	7.6%	8.2%	1.7%	47.9%
D $250 < E_T^{miss} < 350$	11.7%	5.8%	1.2%	5.5%	0.5%	0.0%	0.0%	0.0%	0.1%	8.1%	0.6%	1.1%	1.5%	1.2%	0.8%	16.6%
D $350 < E_T^{miss} < 450$	20.4%	10.9%	1.3%	5.4%	1.3%	0.1%	0.0%	0.2%	0.8%	6.2%	0.5%	2.1%	4.0%	2.0%	0.3%	25.1%
D $450 < E_T^{miss} < 550$	50.0%	20.4%	1.1%	4.1%	4.1%	0.2%	0.0%	0.3%	0.3%	6.7%	0.9%	1.6%	4.3%	3.8%	1.2%	55.1%
D $E_T^{miss} > 550$	70.7%	23.7%	1.0%	5.7%	6.5%	0.2%	0.0%	0.9%	1.6%	8.5%	1.0%	6.0%	6.6%	5.2%	1.6%	76.3%
E $250 < E_T^{miss} < 350$	9.2%	5.2%	2.2%	5.2%	0.8%	0.0%	0.0%	0.0%	0.1%	6.5%	0.4%	0.3%	0.9%	0.8%	0.4%	13.7%
E $350 < E_T^{miss} < 550$	17.1%	4.9%	1.9%	7.3%	0.3%	0.0%	9.3%	0.2%	0.5%	5.7%	0.6%	2.0%	1.3%	0.7%	0.4%	22.4%
E $E_T^{miss} > 550$	17.1%	28.3%	1.9%	23.4%	4.8%	1.6%	29.0%	0.2%	0.1%	4.7%	0.6%	0.2%	3.4%	6.2%	2.1%	50.9%
F $250 < E_T^{miss} < 450$	24.3%	8.5%	1.5%	0.9%	4.2%	0.3%	4.6%	0.2%	0.7%	17.2%	0.4%	0.4%	5.0%	3.0%	0.2%	32.1%
F $E_T^{miss} > 450$	24.3%	82.1%	1.5%	132.0%	12.4%	2.1%	15.0%	1.5%	0.7%	5.4%	0.1%	1.9%	50.7%	27.6%	5.6%	168.9%
G $250 < E_T^{miss} < 350$	18.6%	11.5%	2.1%	2.0%	1.0%	0.0%	0.0%	0.2%	0.8%	7.9%	0.6%	1.5%	2.3%	2.5%	0.3%	23.7%
G $350 < E_T^{miss} < 450$	20.9%	14.4%	1.9%	3.7%	3.0%	0.0%	0.0%	0.2%	0.2%	9.8%	0.6%	1.5%	7.2%	7.2%	2.2%	29.6%
G $450 < E_T^{miss} < 600$	25.8%	18.5%	1.8%	6.6%	3.0%	0.0%	0.0%	0.1%	0.4%	7.9%	0.8%	3.2%	4.7%	3.0%	2.0%	34.2%
G $E_T^{miss} > 600$	70.7%	36.2%	1.8%	6.8%	4.1%	0.2%	0.0%	0.6%	1.1%	9.6%	0.7%	5.6%	3.3%	2.3%	2.8%	80.8%
H $250 < E_T^{miss} < 450$	50.0%	22.9%	1.3%	7.4%	3.9%	1.1%	4.4%	0.4%	0.2%	18.7%	0.8%	0.6%	5.3%	4.9%	3.1%	59.4%
H $E_T^{miss} > 450$	50.0%	47.8%	1.3%	4.9%	4.9%	1.2%	14.3%	1.0%	0.2%	7.5%	0.3%	1.2%	9.4%	5.8%	0.5%	72.2%
I $250 < E_T^{miss} < 350$	9.4%	4.5%	1.3%	2.2%	1.6%	0.0%	0.0%	0.1%	0.1%	7.5%	0.5%	0.8%	0.8%	0.5%	0.2%	13.2%
I $350 < E_T^{miss} < 450$	19.2%	8.8%	1.9%	0.7%	2.4%	0.0%	0.0%	0.2%	0.7%	8.1%	0.5%	1.1%	1.6%	1.8%	0.1%	23.0%
I $450 < E_T^{miss} < 550$	50.0%	16.5%	1.4%	2.0%	0.7%	0.1%	0.0%	0.4%	0.4%	8.1%	0.8%	1.7%	1.6%	2.0%	1.3%	53.5%
I $E_T^{miss} > 550$	44.7%	22.5%	2.2%	7.3%	2.4%	0.2%	0.0%	0.1%	0.1%	9.5%	0.6%	1.6%	6.3%	6.4%	0.3%	52.4%

Table 4.9: Summary of the lost lepton background estimate and its key components.

Region	$E_{\mathrm{T}}^{\mathrm{miss}}$ bin	Observed$_{CR}$	TF_{lepton}	$TF_{\mathrm{SR\ bin}}$	TF_{Total}	SR Estimate
< 4 jets, $t_{\mathrm{mod}} \geq 10.0$, $M_{\ell b} < 175$	$250 < E_{\mathrm{T}}^{\mathrm{miss}} < 350$	217 ± 14.73	0.25 ± 0.02	1.00 ± 0.00	0.25 ± 0.02	53.89 ± 6.23
< 4 jets, $t_{\mathrm{mod}} \geq 10.0$, $M_{\ell b} < 175$	$350 < E_{\mathrm{T}}^{\mathrm{miss}} < 450$	75 ± 8.66	0.19 ± 0.02	1.00 ± 0.00	0.19 ± 0.02	14.16 ± 2.45
< 4 jets, $t_{\mathrm{mod}} \geq 10.0$, $M_{\ell b} < 175$	$450 < E_{\mathrm{T}}^{\mathrm{miss}} < 600$	25 ± 5.00	0.12 ± 0.03	1.00 ± 0.00	0.12 ± 0.03	2.95 ± 0.92
< 4 jets, $t_{\mathrm{mod}} \geq 10.0$, $M_{\ell b} < 175$	$E_{\mathrm{T}}^{\mathrm{miss}} > 600$	3 ± 1.73	0.20 ± 0.11	1.00 ± 0.00	0.20 ± 0.11	0.61 ± 0.49
< 4 jets, $t_{\mathrm{mod}} \geq 10.0$, $M_{\ell b} \geq 175$	$250 < E_{\mathrm{T}}^{\mathrm{miss}} < 450$	11 ± 3.32	0.15 ± 0.06	1.00 ± 0.00	0.15 ± 0.06	1.70 ± 0.79
< 4 jets, $t_{\mathrm{mod}} \geq 10.0$, $M_{\ell b} \geq 175$	$450 < E_{\mathrm{T}}^{\mathrm{miss}} < 600$	3 ± 1.73	0.01 ± 0.00	0.64 ± 0.16	0.01 ± 0.00	0.02 ± 0.01
< 4 jets, $t_{\mathrm{mod}} \geq 10.0$, $M_{\ell b} \geq 175$	$E_{\mathrm{T}}^{\mathrm{miss}} > 600$	3 ± 1.73	0.01 ± 0.00	0.36 ± 0.16	0.00 ± 0.00	0.01 ± 0.01
≥ 4 jets, $t_{\mathrm{mod}} < 0.0$, $M_{\ell b} < 175$	$250 < E_{\mathrm{T}}^{\mathrm{miss}} < 350$	675 ± 25.98	0.51 ± 0.04	1.00 ± 0.00	0.51 ± 0.04	345.68 ± 30.33
≥ 4 jets, $t_{\mathrm{mod}} < 0.0$, $M_{\ell b} < 175$	$350 < E_{\mathrm{T}}^{\mathrm{miss}} < 450$	150 ± 12.25	0.44 ± 0.04	1.00 ± 0.00	0.44 ± 0.04	66.25 ± 7.93
≥ 4 jets, $t_{\mathrm{mod}} < 0.0$, $M_{\ell b} < 175$	$450 < E_{\mathrm{T}}^{\mathrm{miss}} < 550$	27 ± 5.20	0.45 ± 0.06	1.00 ± 0.00	0.45 ± 0.06	12.11 ± 2.77
≥ 4 jets, $t_{\mathrm{mod}} < 0.0$, $M_{\ell b} < 175$	$550 < E_{\mathrm{T}}^{\mathrm{miss}} < 650$	7 ± 2.65	0.48 ± 0.11	1.00 ± 0.00	0.48 ± 0.11	3.38 ± 1.48
≥ 4 jets, $t_{\mathrm{mod}} < 0.0$, $M_{\ell b} < 175$	$E_{\mathrm{T}}^{\mathrm{miss}} > 650$	8 ± 2.83	0.74 ± 0.24	1.00 ± 0.00	0.74 ± 0.24	5.92 ± 2.84
≥ 4 jets, $t_{\mathrm{mod}} < 0.0$, $M_{\ell b} \geq 175$	$250 < E_{\mathrm{T}}^{\mathrm{miss}} < 350$	73 ± 8.54	0.36 ± 0.04	1.00 ± 0.00	0.36 ± 0.04	26.05 ± 4.31
≥ 4 jets, $t_{\mathrm{mod}} < 0.0$, $M_{\ell b} \geq 175$	$350 < E_{\mathrm{T}}^{\mathrm{miss}} < 450$	24 ± 4.90	0.43 ± 0.06	1.00 ± 0.00	0.43 ± 0.06	10.41 ± 2.61
≥ 4 jets, $t_{\mathrm{mod}} < 0.0$, $M_{\ell b} \geq 175$	$450 < E_{\mathrm{T}}^{\mathrm{miss}} < 550$	4 ± 2.00	0.42 ± 0.10	1.00 ± 0.00	0.42 ± 0.10	1.68 ± 0.93
≥ 4 jets, $t_{\mathrm{mod}} < 0.0$, $M_{\ell b} \geq 175$	$E_{\mathrm{T}}^{\mathrm{miss}} > 550$	2 ± 1.41	0.54 ± 0.16	1.00 ± 0.00	0.54 ± 0.16	1.08 ± 0.83
≥ 4 jets, 0.0 <tmod< 10.0, $M_{\ell b} < 175$	$250 < E_{\mathrm{T}}^{\mathrm{miss}} < 350$	119 ± 10.91	0.36 ± 0.04	1.00 ± 0.00	0.36 ± 0.04	42.99 ± 5.89
≥ 4 jets, 0.0 <tmod< 10.0, $M_{\ell b} < 175$	$350 < E_{\mathrm{T}}^{\mathrm{miss}} < 550$	34 ± 5.83	0.28 ± 0.04	0.94 ± 0.02	0.27 ± 0.04	9.13 ± 2.05
≥ 4 jets, 0.0 <tmod< 10.0, $M_{\ell b} < 175$	$E_{\mathrm{T}}^{\mathrm{miss}} > 550$	34 ± 5.83	0.28 ± 0.04	0.06 ± 0.02	0.02 ± 0.01	0.55 ± 0.28
≥ 4 jets, 0.0 <tmod< 10.0, $M_{\ell b} \geq 175$	$250 < E_{\mathrm{T}}^{\mathrm{miss}} < 450$	17 ± 4.12	0.27 ± 0.06	0.98 ± 0.03	0.26 ± 0.05	4.43 ± 1.42
≥ 4 jets, 0.0 <tmod< 10.0, $M_{\ell b} \geq 175$	$E_{\mathrm{T}}^{\mathrm{miss}} > 450$	17 ± 4.12	0.27 ± 0.06	0.02 ± 0.03	0.01 ± 0.01	0.10 ± 0.16
≥ 4 jets, $t_{\mathrm{mod}} \geq 10.0$, $M_{\ell b} < 175$	$250 < E_{\mathrm{T}}^{\mathrm{miss}} < 350$	29 ± 5.39	0.33 ± 0.05	1.00 ± 0.00	0.33 ± 0.05	9.48 ± 2.25
≥ 4 jets, $t_{\mathrm{mod}} \geq 10.0$, $M_{\ell b} < 175$	$350 < E_{\mathrm{T}}^{\mathrm{miss}} < 450$	23 ± 4.80	0.26 ± 0.05	1.00 ± 0.00	0.26 ± 0.05	5.92 ± 1.75
≥ 4 jets, $t_{\mathrm{mod}} \geq 10.0$, $M_{\ell b} < 175$	$450 < E_{\mathrm{T}}^{\mathrm{miss}} < 600$	15 ± 3.87	0.26 ± 0.06	1.00 ± 0.00	0.26 ± 0.06	3.83 ± 1.31
≥ 4 jets, $t_{\mathrm{mod}} \geq 10.0$, $M_{\ell b} < 175$	$E_{\mathrm{T}}^{\mathrm{miss}} > 600$	2 ± 1.41	0.38 ± 0.15	1.00 ± 0.00	0.38 ± 0.15	0.75 ± 0.61
≥ 4 jets, $t_{\mathrm{mod}} \geq 10.0$, $M_{\ell b} \geq 175$	$250 < E_{\mathrm{T}}^{\mathrm{miss}} < 450$	4 ± 2.00	0.19 ± 0.04	0.70 ± 0.15	0.14 ± 0.04	0.55 ± 0.32
≥ 4 jets, $t_{\mathrm{mod}} \geq 10.0$, $M_{\ell b} \geq 175$	$E_{\mathrm{T}}^{\mathrm{miss}} > 450$	4 ± 2.00	0.19 ± 0.04	0.30 ± 0.15	0.06 ± 0.03	0.23 ± 0.17
Compressed search	$250 < E_{\mathrm{T}}^{\mathrm{miss}} < 350$	114 ± 10.68	0.59 ± 0.06	1.00 ± 0.00	0.59 ± 0.06	67.55 ± 8.95
Compressed search	$350 < E_{\mathrm{T}}^{\mathrm{miss}} < 450$	27 ± 5.20	0.56 ± 0.07	1.00 ± 0.00	0.56 ± 0.07	15.11 ± 3.48
Compressed search	$450 < E_{\mathrm{T}}^{\mathrm{miss}} < 550$	4 ± 2.00	0.61 ± 0.12	1.00 ± 0.00	0.61 ± 0.12	2.44 ± 1.31
Compressed search	$E_{\mathrm{T}}^{\mathrm{miss}} > 550$	5 ± 2.24	0.77 ± 0.21	1.00 ± 0.00	0.77 ± 0.21	3.86 ± 2.02

4.8.2 Single Lepton not from Top

The second largest background component across all signal regions comprises events with one true lepton that originates from a W boson, where the W boson is not the daughter of a top quark. We sometimes refer to this background as 1ℓW. By far the largest physics process contributing to this background is the production of W+jets, where the W boson decays leptonically. Other small contributions come from single top tW and ttW production where no top quarks decay leptonically, as well as diboson production. Note that if an event has any Z-boson decaying to neutrinos, it is automatically counted in the rare background category, even if it has a leptonic W decay.

Estimation Method

The method used to estimate the 1ℓW background is very similar to the method used for the lost lepton background, as described in Section 4.8.1. We estimate the number of 1ℓW background events in our signal regions based on the number of events in a set of 0-btag control regions, described below. We assume that Monte Carlo simulations correctly model the ratio of $\geq$1-btag events to 0-btag events, so that this ratio holds true:

$$\frac{N^{\text{data}}_{\geq 1\text{ btag}}}{N^{\text{data}}_{0\text{ btag}}} = \frac{M^{\text{MC}}_{\geq 1\text{ btag}}}{M^{\text{MC}}_{0\text{ btag}}} \tag{4.11}$$

We can rearrange this equation to derive the formula for a data-driven estimate of the 1ℓW background component in our signal regions. The estimate is given by the data yield from the control regions times the SR/CR ratio derived in Monte Carlo. We will refer to this ratio as the b-tag transfer factor, TF_{btag}.

$$N^{\text{SR}}_{\geq 1\text{ btag}} = N^{\text{CR}}_{0\text{ btag}} \times \frac{M^{\text{SR}}_{\geq 1\text{ btag}}}{M^{\text{CR}}_{0\text{ btag}}} \tag{4.12}$$

The 0-btag control regions are not totally pure; they contain significant contamination from non-1ℓW events. So in order for our background estimate to reflect only the 1ℓW content in the signal regions, we must multiply our estimate by the purity of the CR. The purity is the fraction of events in the CR that are true 1ℓW events, and is derived from simulation. So the estimate is now given by:

$$N_{1\ell W}^{\geq 1\text{ btag, SR}} = N_{\text{total}}^{0\text{ btag, CR}} \times \frac{M_{\text{total}}^{\geq 1\text{ btag, SR}}}{M_{\text{total}}^{0\text{ btag, CR}}} \times \frac{M_{1\ell W}^{0\text{ btag, CR}}}{M_{\text{total}}^{0\text{ btag, CR}}} \tag{4.13}$$

Control Region Definitions

Because bottom quarks are heavy, processes without top decays tend not to have b-jets in them. So one of the easiest ways to make a sample enriched in 1ℓW events is to require the absence of b-tags. Thus, we generally form our 0-btag control regions from the corresponding signal regions by simply inverting the b-tag requirement. The low-$M_{\ell b}$ signal regions, which require 1 medium b-tag, are inverted to form control regions that require no medium b-tags. Similarly, the high-$M_{\ell b}$ signal regions, which require 1 tight b-tag, are inverted to form control regions that require no tight b-tags.

This naïve inversion does give rise to some high-$M_{\ell b}$ control regions with low purity of 1ℓW events. We later assess a systematic uncertainty on impurities (or *contamination*), so any low-purity CRs would wind up with an outsize uncertainty. To reduce the number of CRs with excessive uncertainties, we change certain high-$M_{\ell b}$ CRs to require 0 medium b-tags, instead of 0 tight b-tags. This modification is made on a case-by-case basis; we apply the change only in CRs where we see a 0 medium b-tag requirement would substantially increase the purity without cutting out too many data events. These regions are:

- All CRs in the D series (≥ 4 jets, $t_{\text{mod}} < 0$, high $M_{\ell b}$)
- All CRs in the F series (≥ 4 jets, $0 < t_{\text{mod}} < 10$, high $M_{\ell b}$)

Clearly, in these regions, the b-tag transfer factor must take on a slightly new meaning, as it maps

CRs with 0 medium b-tags to SRs with ≥ 1 tight b-tag:

$$TF_{\text{btag}} = \frac{M^{\text{total}}_{\geq 1\text{ (tight) btag, SR}}}{M^{\text{total}}_{0\text{ (med) btag, CR}}} \tag{4.14}$$

Because these control regions are defined by the absence of b-tagged jets, the definition of $M_{\ell b}$ from Section 4.6.9 will no longer serve. In the absence of formally b-tagged jets, we instead calculate $M_{\ell b}$ using the jet with the highest CSV discriminator value. In Figure 4.11, we plot this makeshift $M_{\ell b}$ from our CRs against the nominal $M_{\ell b}$ from the SRs, both using MC, and verify that they agree to within uncertainties. We also check the shape of $M_{\ell b}$ in data vs MC within a high-statistics crosscheck region, defined only by $60 < M_{\text{T}} < 120$ GeV, $E_{\text{T}}^{\text{miss}} > 250$ GeV, and 1-2 jets. As Figure 4.12 shows, the shape agreement is quite good. Therefore we do not assess a systematic uncertainty on $M_{\ell b}$ shape modeling. Note that any issues with $M_{\ell b}$ modeling would not affect the corridor regions because they are not binned in $M_{\ell b}$.

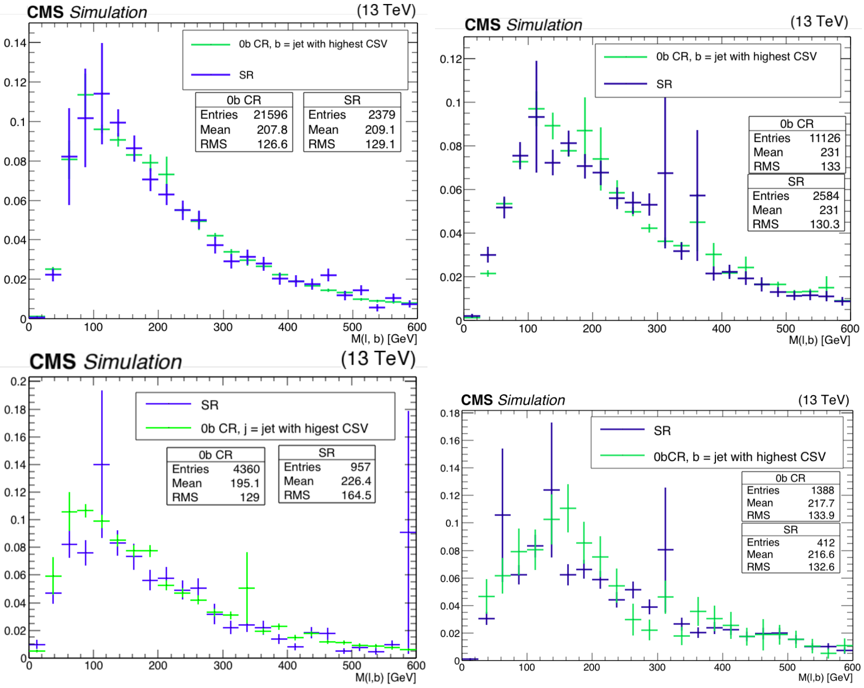

Figure 4.11: Comparison between $M_{\ell b}$ from SRs and makeshift $M_{\ell b}$ from CRs, using simulated data. The four plots are made in the combined A+B regions, the C+D regions, the E+F regions, and the G+H regions, respectively.

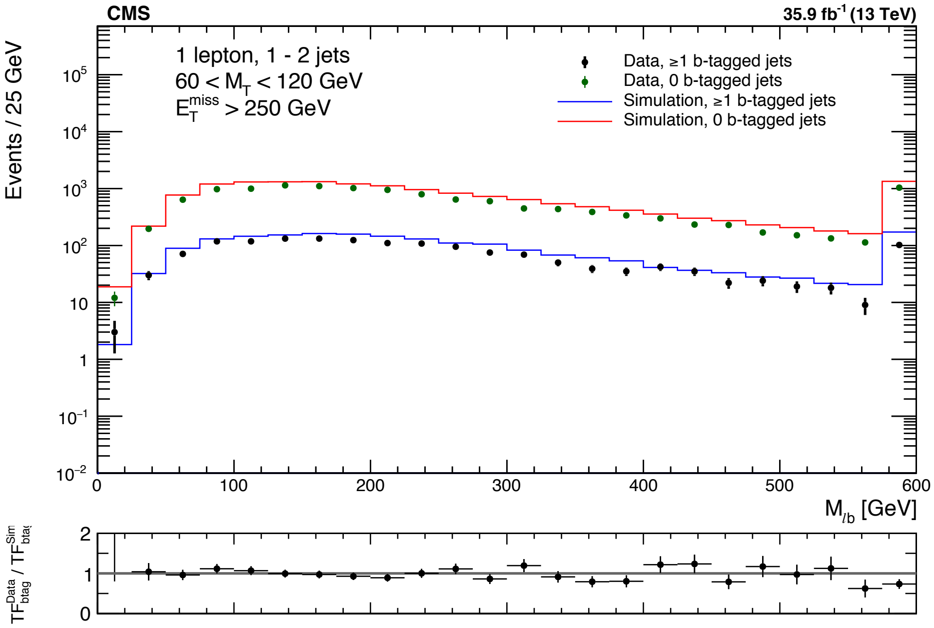

Figure 4.12: Comparison of $M_{\ell b}$ shape for data and MC, in 0-btag and ≥1-btag crosscheck regions.

The yields for data and MC in the control regions are given in Table 4.10. The MC simulations receive all the same corrections as in the SRs. The purity of these control regions ranges from a high of 83% to a low of 37%. The impurity of these regions will be addressed further on with a systematic uncertainty.

Systematic Uncertainties

Many of the systematic uncertainties on the 1ℓW background are assessed the same way as for the lost lepton background, as described in Section 4.8.1. These uncertainties are:

- Data and MC statistics
- b-tagging efficiencies
- JES
- PDF

Table 4.10: Data and Monte Carlo yields in the 0-btag control regions, based on 35.9 fb^{-1} of luminosity.

Region	≥ 2 leptons	1 lepton, from W	1 lepton, from t	$Z \rightarrow \nu\nu$	Sum Bkg.	Data	Data/MC
< 4 jets, $t_{\mathrm{mod}} \geq 10$, $M_{\ell b} < 175$, $250 < E_{\mathrm{T}}^{\mathrm{miss}} < 350$	31.59 ± 2.40	99.79 ± 3.00	0.49 ± 0.28	14.59 ± 2.05	146.46 ± 4.36	151 ± 12.29	1.03 ± 0.09
< 4 jets, $t_{\mathrm{mod}} \geq 10$, $M_{\ell b} < 175$, $350 < E_{\mathrm{T}}^{\mathrm{miss}} < 450$	10.15 ± 1.33	48.50 ± 2.25	0.33 ± 0.23	9.55 ± 1.40	68.52 ± 2.97	68 ± 8.25	0.99 ± 0.13
< 4 jets, $t_{\mathrm{mod}} \geq 10$, $M_{\ell b} < 175$, $450 < E_{\mathrm{T}}^{\mathrm{miss}} < 600$	3.44 ± 0.84	24.34 ± 1.79	—	4.68 ± 1.08	32.45 ± 2.25	31 ± 5.57	0.96 ± 0.18
< 4 jets, $t_{\mathrm{mod}} \geq 10$, $M_{\ell b} < 175$, $E_{\mathrm{T}}^{\mathrm{miss}} > 600$	0.39 ± 0.20	6.66 ± 0.37	—	1.20 ± 0.53	8.25 ± 0.68	11 ± 3.32	1.33 ± 0.42
< 4 jets, $t_{\mathrm{mod}} \geq 10$, $M_{\ell b} \geq 175$, $250 < E_{\mathrm{T}}^{\mathrm{miss}} < 450$	19.15 ± 1.90	167.31 ± 1.88	—	22.63 ± 2.37	209.09 ± 3.57	234 ± 15.30	1.12 ± 0.08
< 4 jets, $t_{\mathrm{mod}} \geq 10$, $M_{\ell b} \geq 175$, $450 < E_{\mathrm{T}}^{\mathrm{miss}} < 650$	3.22 ± 0.80	44.17 ± 1.46	—	9.67 ± 1.44	57.06 ± 2.20	49 ± 7.00	0.86 ± 0.13
< 4 jets, $t_{\mathrm{mod}} \geq 10$, $M_{\ell b} \geq 175$, $E_{\mathrm{T}}^{\mathrm{miss}} > 600$	0.40 ± 0.27	26.11 ± 1.76	—	4.38 ± 1.10	30.89 ± 2.09	27 ± 5.20	0.87 ± 0.18
≥ 4 jets, $t_{\mathrm{mod}} < 0.0$, $M_{\ell b} < 175$, $250 < E_{\mathrm{T}}^{\mathrm{miss}} < 350$	81.70 ± 3.39	55.64 ± 2.31	5.02 ± 0.87	8.92 ± 1.19	151.28 ± 4.37	143 ± 11.96	0.95 ± 0.08
≥ 4 jets, $t_{\mathrm{mod}} < 0.0$, $M_{\ell b} < 175$, $350 < E_{\mathrm{T}}^{\mathrm{miss}} < 450$	16.78 ± 1.62	17.05 ± 1.69	0.53 ± 0.26	3.78 ± 0.88	38.14 ± 2.51	31 ± 5.57	0.81 ± 0.16
≥ 4 jets, $t_{\mathrm{mod}} < 0.0$, $M_{\ell b} < 175$, $450 < E_{\mathrm{T}}^{\mathrm{miss}} < 550$	4.27 ± 0.85	3.89 ± 0.28	0.17 ± 0.17	1.76 ± 0.61	10.08 ± 1.09	5 ± 2.24	0.50 ± 0.23
≥ 4 jets, $t_{\mathrm{mod}} < 0.0$, $M_{\ell b} < 175$, $550 < E_{\mathrm{T}}^{\mathrm{miss}} < 650$	0.84 ± 0.33	1.66 ± 0.25	—	0.09 ± 0.02	2.59 ± 0.41	3 ± 1.73	1.16 ± 0.69
≥ 4 jets, $t_{\mathrm{mod}} < 0.0$, $M_{\ell b} < 175$, $E_{\mathrm{T}}^{\mathrm{miss}} > 650$	0.97 ± 0.40	1.18 ± 0.15	0.13 ± 0.13	0.32 ± 0.27	2.60 ± 0.52	4 ± 2.00	1.54 ± 0.83
≥ 4 jets, $t_{\mathrm{mod}} < 0.0$, $M_{\ell b} \geq 175$, $250 < E_{\mathrm{T}}^{\mathrm{miss}} < 350$	36.35 ± 2.31	81.05 ± 3.77	2.58 ± 0.59	6.82 ± 1.28	126.80 ± 4.64	104 ± 10.20	0.82 ± 0.09
≥ 4 jets, $t_{\mathrm{mod}} < 0.0$, $M_{\ell b} \geq 175$, $350 < E_{\mathrm{T}}^{\mathrm{miss}} < 450$	10.93 ± 1.30	31.43 ± 3.80	0.42 ± 0.24	5.69 ± 1.05	48.47 ± 4.15	27 ± 5.20	0.56 ± 0.12
≥ 4 jets, $t_{\mathrm{mod}} < 0.0$, $M_{\ell b} \geq 175$, $450 < E_{\mathrm{T}}^{\mathrm{miss}} < 550$	3.77 ± 0.78	10.41 ± 0.51	0.00 ± 0.00	1.57 ± 0.67	15.74 ± 1.15	9 ± 3.00	0.57 ± 0.20
≥ 4 jets, $t_{\mathrm{mod}} < 0.0$, $M_{\ell b} \geq 175$, $E_{\mathrm{T}}^{\mathrm{miss}} > 550$	3.99 ± 1.36	8.50 ± 0.45	0.13 ± 0.13	1.23 ± 0.58	13.84 ± 1.55	12 ± 3.46	0.87 ± 0.27
≥ 4 jets, $0.0 < t_{\mathrm{mod}} < 10$, $M_{\ell b} < 175$, $250 < E_{\mathrm{T}}^{\mathrm{miss}} < 350$	16.96 ± 1.51	28.65 ± 3.66	0.29 ± 0.21	4.87 ± 0.81	50.78 ± 4.05	54 ± 7.35	1.06 ± 0.17
≥ 4 jets, $0.0 < t_{\mathrm{mod}} < 10$, $M_{\ell b} < 175$, $350 < E_{\mathrm{T}}^{\mathrm{miss}} < 550$	4.17 ± 0.80	12.99 ± 0.53	0.12 ± 0.12	1.71 ± 0.63	19.00 ± 1.15	13 ± 3.61	0.68 ± 0.19
≥ 4 jets, $0.0 < t_{\mathrm{mod}} < 10$, $M_{\ell b} < 175$, $E_{\mathrm{T}}^{\mathrm{miss}} > 550$	0.32 ± 0.18	1.38 ± 0.16	—	0.75 ± 0.41	2.45 ± 0.48	2 ± 1.41	0.82 ± 0.60
≥ 4 jets, $0.0 < t_{\mathrm{mod}} < 10$, $M_{\ell b} \geq 175$, $250 < E_{\mathrm{T}}^{\mathrm{miss}} < 450$	6.60 ± 0.90	34.16 ± 1.52	—	5.12 ± 0.96	45.88 ± 2.01	51 ± 7.14	1.11 ± 0.16
≥ 4 jets, $0.0 < t_{\mathrm{mod}} < 10$, $M_{\ell b} \geq 175$, $E_{\mathrm{T}}^{\mathrm{miss}} > 450$	1.68 ± 0.81	8.35 ± 0.40	—	2.54 ± 0.63	12.58 ± 1.10	5 ± 2.24	0.40 ± 0.18
≥ 4 jets, $t_{\mathrm{mod}} \geq 10$, $M_{\ell b} < 175$, $250 < E_{\mathrm{T}}^{\mathrm{miss}} < 350$	1.83 ± 0.47	1.82 ± 0.19	0.16 ± 0.16	0.58 ± 0.24	4.38 ± 0.58	8 ± 2.83	1.82 ± 0.69
≥ 4 jets, $t_{\mathrm{mod}} \geq 10$, $M_{\ell b} < 175$, $350 < E_{\mathrm{T}}^{\mathrm{miss}} < 450$	1.98 ± 0.52	3.88 ± 1.13	—	0.26 ± 0.03	6.11 ± 1.24	7 ± 2.65	1.15 ± 0.49
≥ 4 jets, $t_{\mathrm{mod}} \geq 10$, $M_{\ell b} < 175$, $450 < E_{\mathrm{T}}^{\mathrm{miss}} < 600$	1.42 ± 0.57	2.96 ± 0.24	—	0.52 ± 0.44	4.89 ± 0.76	3 ± 1.73	0.61 ± 0.37
≥ 4 jets, $t_{\mathrm{mod}} \geq 10$, $M_{\ell b} < 175$, $E_{\mathrm{T}}^{\mathrm{miss}} > 600$	0.68 ± 0.39	2.54 ± 1.16	—	0.32 ± 0.45	3.54 ± 1.30	2 ± 1.41	0.57 ± 0.45
≥ 4 jets, $t_{\mathrm{mod}} \geq 10$, $M_{\ell b} \geq 175$, $250 < E_{\mathrm{T}}^{\mathrm{miss}} < 450$	2.04 ± 0.84	6.03 ± 0.34	0.11 ± 0.11	0.41 ± 0.14	8.60 ± 0.92	10 ± 3.16	1.16 ± 0.39
≥ 4 jets, $t_{\mathrm{mod}} \geq 10$, $M_{\ell b} \geq 175$, $E_{\mathrm{T}}^{\mathrm{miss}} > 450$	0.93 ± 0.45	8.10 ± 0.39	—	2.14 ± 0.53	11.17 ± 0.80	7 ± 2.65	0.63 ± 0.24
Compressed search, $250 < E_{\mathrm{T}}^{\mathrm{miss}} < 350$	19.70 ± 1.43	23.62 ± 4.24	1.80 ± 0.45	2.36 ± 0.52	47.47 ± 4.53	49 ± 7.00	1.03 ± 0.18
Compressed search, $350 < E_{\mathrm{T}}^{\mathrm{miss}} < 450$	7.49 ± 0.92	12.07 ± 3.64	0.40 ± 0.21	2.43 ± 0.76	22.38 ± 3.83	11 ± 3.32	0.49 ± 0.17
Compressed search, $450 < E_{\mathrm{T}}^{\mathrm{miss}} < 550$	2.98 ± 0.67	3.68 ± 0.27	0.30 ± 0.22	1.75 ± 0.53	8.71 ± 0.92	5 ± 2.24	0.57 ± 0.26
Compressed search, $E_{\mathrm{T}}^{\mathrm{miss}} > 550$	1.43 ± 0.43	3.26 ± 0.26	—	1.13 ± 0.48	5.82 ± 0.70	3 ± 1.73	0.52 ± 0.30

- Q^2

Because our TF_{btag} is derived from simulation, we must ensure that the relative cross-sections of W+b and W+non-b jets are correctly modeled in MC. We check the agreement between data and MC on the number of b-jets in the high-statistics crosscheck region described above. As Figure 4.13 shows, a 50% systematic uncertainty on the W+b cross section adequately covers any mismodeling that may exist. Additionally, the 0-btag CRs have considerable impurity from non-1ℓW backgrounds, so we assess a 50% systematic uncertainty on that contamination. The systematic uncertainties on the single lepton from W estimate are presented in Table 4.11.

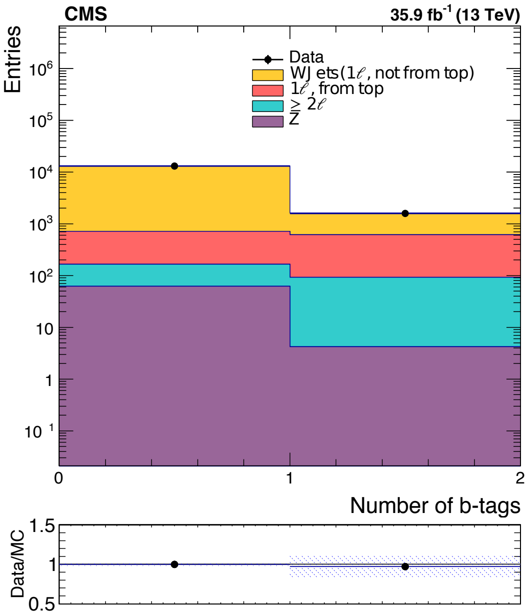

Figure 4.13: Number of b-tags compared between data and MC, in high-statistics crosscheck region. The second bin includes events with one or more b-tags. The uncertainty band illustrates a 50% uncertainty on the W+b cross section

Results

The full results of the single lepton from W background estimate, including systematic uncertainties, are presented in Table 4.12.

Table 4.11: Summary of systematic uncertainties on single lepton from W background estimate.

Region	Data Stats	MC Stats	CR Impurity	JES	W+b X-sec	b-tag (HF)	b-tag (LF)	Q^2	PDF	Total
A $250 < E_{\mathrm{T}}^{\mathrm{miss}} < 350$	9.2%	6.1%	23.4%	2.0%	22.8%	1.7%	2.5%	0.1%	1.0%	34.7%
A $350 < E_{\mathrm{T}}^{\mathrm{miss}} < 450$	13.7%	8.5%	20.6%	2.0%	21.0%	1.5%	3.1%	0.1%	0.6%	33.8%
A $450 < E_{\mathrm{T}}^{\mathrm{miss}} < 600$	20.6%	13.0%	16.7%	2.0%	25.1%	1.3%	2.9%	0.1%	1.0%	39.0%
A $E_{\mathrm{T}}^{\mathrm{miss}} > 600$	31.7%	21.0%	11.9%	2.0%	15.2%	0.9%	5.1%	0.2%	2.0%	43.1%
B $250 < E_{\mathrm{T}}^{\mathrm{miss}} < 450$	6.8%	6.7%	12.5%	2.0%	35.6%	2.2%	2.7%	0.6%	0.7%	39.2%
B $450 < E_{\mathrm{T}}^{\mathrm{miss}} < 600$	15.2%	11.0%	14.6%	2.0%	32.5%	2.5%	2.0%	1.4%	1.7%	40.5%
B $E_{\mathrm{T}}^{\mathrm{miss}} > 600$	21.5%	15.4%	9.2%	2.0%	35.6%	4.1%	1.7%	0.1%	1.0%	45.5%
C $250 < E_{\mathrm{T}}^{\mathrm{miss}} < 350$	9.8%	12.6%	85.9%	2.0%	17.5%	1.5%	2.3%	0.7%	0.5%	89.2%
C $350 < E_{\mathrm{T}}^{\mathrm{miss}} < 450$	21.5%	15.8%	61.8%	2.0%	17.5%	1.1%	2.9%	0.8%	1.6%	69.7%
C $450 < E_{\mathrm{T}}^{\mathrm{miss}} < 550$	46.6%	21.3%	79.6%	2.0%	23.0%	0.6%	2.0%	2.2%	0.8%	97.5%
C $550 < E_{\mathrm{T}}^{\mathrm{miss}} < 650$	61.7%	32.2%	28.1%	2.0%	15.7%	1.4%	4.3%	1.1%	1.6%	76.9%
C $E_{\mathrm{T}}^{\mathrm{miss}} > 650$	55.3%	30.7%	60.7%	2.0%	12.1%	1.0%	1.7%	6.9%	9.2%	89.3%
D $250 < E_{\mathrm{T}}^{\mathrm{miss}} < 350$	11.5%	9.3%	28.2%	2.0%	23.3%	2.3%	2.0%	3.2%	1.7%	39.8%
D $350 < E_{\mathrm{T}}^{\mathrm{miss}} < 450$	24.3%	17.6%	27.1%	2.0%	24.0%	2.1%	2.0%	3.6%	2.3%	47.4%
D $450 < E_{\mathrm{T}}^{\mathrm{miss}} < 550$	34.5%	23.1%	25.6%	2.0%	30.4%	2.2%	1.2%	1.1%	0.6%	57.6%
D $E_{\mathrm{T}}^{\mathrm{miss}} > 550$	31.4%	26.8%	31.5%	2.0%	18.0%	2.3%	1.9%	6.6%	6.1%	55.8%
E $250 < E_{\mathrm{T}}^{\mathrm{miss}} < 350$	20.3%	25.0%	38.6%	2.0%	17.4%	2.1%	2.0%	2.7%	1.9%	53.4%
E $350 < E_{\mathrm{T}}^{\mathrm{miss}} < 550$	28.7%	10.9%	23.1%	2.0%	18.9%	1.7%	2.8%	0.9%	1.3%	43.0%
E $E_{\mathrm{T}}^{\mathrm{miss}} > 550$	74.3%	26.9%	39.1%	2.0%	29.9%	0.8%	3.6%	0.7%	0.4%	93.2%
F $250 < E_{\mathrm{T}}^{\mathrm{miss}} < 450$	15.3%	11.4%	17.2%	2.0%	32.4%	2.1%	1.1%	0.1%	0.1%	41.5%
F $E_{\mathrm{T}}^{\mathrm{miss}} > 450$	45.8%	18.6%	25.3%	2.0%	33.2%	2.2%	2.2%	2.5%	3.1%	65.0%
G $250 < E_{\mathrm{T}}^{\mathrm{miss}} < 350$	39.1%	20.7%	70.5%	2.0%	22.1%	1.4%	1.8%	1.5%	5.9%	86.5%
G $350 < E_{\mathrm{T}}^{\mathrm{miss}} < 450$	51.8%	33.8%	28.8%	2.0%	23.9%	1.3%	2.1%	3.1%	2.8%	72.5%
G $450 < E_{\mathrm{T}}^{\mathrm{miss}} < 600$	60.3%	18.0%	32.7%	2.0%	21.6%	1.3%	4.1%	0.5%	1.4%	74.4%
G $E_{\mathrm{T}}^{\mathrm{miss}} > 600$	91.9%	49.1%	19.8%	2.0%	25.5%	1.4%	2.9%	5.6%	3.6%	109.3%
H $250 < E_{\mathrm{T}}^{\mathrm{miss}} < 450$	33.8%	16.0%	21.3%	2.0%	40.4%	1.9%	1.2%	0.7%	0.1%	59.2%
H $E_{\mathrm{T}}^{\mathrm{miss}} > 450$	38.8%	16.7%	19.0%	2.0%	35.2%	2.6%	2.3%	3.5%	0.1%	58.4%
I $250 < E_{\mathrm{T}}^{\mathrm{miss}} < 350$	14.3%	27.3%	33.6%	5.9%	8.2%	2.2%	5.3%	1.4%	2.8%	33.1%
I $350 < E_{\mathrm{T}}^{\mathrm{miss}} < 450$	30.2%	19.6%	29.9%	6.8%	4.3%	3.0%	2.7%	3.3%	9.6%	38.4%
I $450 < E_{\mathrm{T}}^{\mathrm{miss}} < 550$	44.7%	23.0%	40.6%	6.2%	14.8%	2.6%	2.4%	7.2%	14.4%	55.3%
I $E_{\mathrm{T}}^{\mathrm{miss}} > 550$	57.7%	23.2%	28.2%	4.5%	24.6%	3.1%	2.9%	5.4%	14.0%	68.9%

Table 4.12: Summary of the single lepton from W background estimate, and all its key components.

Region	$E_{\mathrm{T}}^{\mathrm{miss}}$ bin	Observed$_{\mathrm{CR}}$	Purity	TF_{btag}	SR Estimate
< 4 jets, $t_{\mathrm{mod}} \geq 10.0$, $M_{\ell b} < 175$	$250 < E_{\mathrm{T}}^{\mathrm{miss}} < 350$	151 ± 12.29	0.68 ± 0.03	0.07 ± 0.00	7.18 ± 0.79
< 4 jets, $t_{\mathrm{mod}} \geq 10.0$, $M_{\ell b} < 175$	$350 < E_{\mathrm{T}}^{\mathrm{miss}} < 450$	68 ± 8.25	0.71 ± 0.04	0.08 ± 0.01	4.06 ± 0.65
< 4 jets, $t_{\mathrm{mod}} \geq 10.0$, $M_{\ell b} < 175$	$450 < E_{\mathrm{T}}^{\mathrm{miss}} < 600$	31 ± 5.57	0.75 ± 0.08	0.07 ± 0.01	1.71 ± 0.42
< 4 jets, $t_{\mathrm{mod}} \geq 10.0$, $M_{\ell b} < 175$	$E_{\mathrm{T}}^{\mathrm{miss}} > 600$	11 ± 3.32	0.81 ± 0.08	0.09 ± 0.02	0.78 ± 0.30
< 4 jets, $t_{\mathrm{mod}} \geq 10.0$, $M_{\ell b} \geq 175$	$250 < E_{\mathrm{T}}^{\mathrm{miss}} < 450$	234 ± 15.30	0.80 ± 0.02	0.03 ± 0.00	5.64 ± 0.54
< 4 jets, $t_{\mathrm{mod}} \geq 10.0$, $M_{\ell b} \geq 175$	$450 < E_{\mathrm{T}}^{\mathrm{miss}} < 600$	49 ± 7.00	0.77 ± 0.04	0.04 ± 0.00	1.56 ± 0.29
< 4 jets, $t_{\mathrm{mod}} \geq 10.0$, $M_{\ell b} \geq 175$	$E_{\mathrm{T}}^{\mathrm{miss}} > 600$	27 ± 5.20	0.85 ± 0.08	0.04 ± 0.01	0.87 ± 0.23
≥ 4 jets, $t_{\mathrm{mod}} < 0.0$, $M_{\ell b} < 175$	$250 < E_{\mathrm{T}}^{\mathrm{miss}} < 350$	143 ± 11.96	0.37 ± 0.02	0.18 ± 0.02	9.65 ± 1.54
≥ 4 jets, $t_{\mathrm{mod}} < 0.0$, $M_{\ell b} < 175$	$350 < E_{\mathrm{T}}^{\mathrm{miss}} < 450$	31 ± 5.57	0.45 ± 0.05	0.18 ± 0.03	2.51 ± 0.67
≥ 4 jets, $t_{\mathrm{mod}} < 0.0$, $M_{\ell b} < 175$	$450 < E_{\mathrm{T}}^{\mathrm{miss}} < 550$	5 ± 2.24	0.39 ± 0.05	0.25 ± 0.05	0.47 ± 0.24
≥ 4 jets, $t_{\mathrm{mod}} < 0.0$, $M_{\ell b} < 175$	$550 < E_{\mathrm{T}}^{\mathrm{miss}} < 650$	3 ± 1.73	0.64 ± 0.14	0.14 ± 0.04	0.26 ± 0.18
≥ 4 jets, $t_{\mathrm{mod}} < 0.0$, $M_{\ell b} < 175$	$E_{\mathrm{T}}^{\mathrm{miss}} > 650$	4 ± 2.00	0.45 ± 0.11	0.24 ± 0.07	0.43 ± 0.27
≥ 4 jets, $t_{\mathrm{mod}} < 0.0$, $M_{\ell b} \geq 175$	$250 < E_{\mathrm{T}}^{\mathrm{miss}} < 350$	104 ± 10.20	0.64 ± 0.04	0.11 ± 0.01	7.52 ± 1.11
≥ 4 jets, $t_{\mathrm{mod}} < 0.0$, $M_{\ell b} \geq 175$	$350 < E_{\mathrm{T}}^{\mathrm{miss}} < 450$	27 ± 5.20	0.65 ± 0.10	0.09 ± 0.02	1.55 ± 0.47
≥ 4 jets, $t_{\mathrm{mod}} < 0.0$, $M_{\ell b} \geq 175$	$450 < E_{\mathrm{T}}^{\mathrm{miss}} < 550$	9 ± 3.00	0.66 ± 0.06	0.09 ± 0.02	0.56 ± 0.23
≥ 4 jets, $t_{\mathrm{mod}} < 0.0$, $M_{\ell b} \geq 175$	$E_{\mathrm{T}}^{\mathrm{miss}} > 550$	12 ± 3.46	0.61 ± 0.08	0.14 ± 0.04	1.02 ± 0.42
≥ 4 jets, 0.0 <tmod< 10.0, $M_{\ell b} < 175$	$250 < E_{\mathrm{T}}^{\mathrm{miss}} < 350$	54 ± 7.35	0.56 ± 0.09	0.19 ± 0.05	5.67 ± 1.83
≥ 4 jets, 0.0 <tmod< 10.0, $M_{\ell b} < 175$	$350 < E_{\mathrm{T}}^{\mathrm{miss}} < 550$	13 ± 3.61	0.68 ± 0.05	0.14 ± 0.02	1.25 ± 0.38
≥ 4 jets, 0.0 <tmod< 10.0, $M_{\ell b} < 175$	$E_{\mathrm{T}}^{\mathrm{miss}} > 550$	2 ± 1.41	0.56 ± 0.13	0.23 ± 0.06	0.26 ± 0.21
≥ 4 jets, 0.0 <tmod< 10.0, $M_{\ell b} \geq 175$	$250 < E_{\mathrm{T}}^{\mathrm{miss}} < 450$	51 ± 7.14	0.74 ± 0.05	0.08 ± 0.01	3.10 ± 0.59
≥ 4 jets, 0.0 <tmod< 10.0, $M_{\ell b} \geq 175$	$E_{\mathrm{T}}^{\mathrm{miss}} > 450$	5 ± 2.24	0.66 ± 0.07	0.07 ± 0.01	0.24 ± 0.12
≥ 4 jets, $t_{\mathrm{mod}} \geq 10.0$, $M_{\ell b} < 175$	$250 < E_{\mathrm{T}}^{\mathrm{miss}} < 350$	8 ± 2.83	0.41 ± 0.07	0.32 ± 0.07	1.06 ± 0.47
≥ 4 jets, $t_{\mathrm{mod}} \geq 10.0$, $M_{\ell b} < 175$	$350 < E_{\mathrm{T}}^{\mathrm{miss}} < 450$	7 ± 2.65	0.63 ± 0.22	0.16 ± 0.05	0.71 ± 0.44
≥ 4 jets, $t_{\mathrm{mod}} \geq 10.0$, $M_{\ell b} < 175$	$450 < E_{\mathrm{T}}^{\mathrm{miss}} < 600$	3 ± 1.73	0.60 ± 0.11	0.24 ± 0.04	0.43 ± 0.27
≥ 4 jets, $t_{\mathrm{mod}} \geq 10.0$, $M_{\ell b} < 175$	$E_{\mathrm{T}}^{\mathrm{miss}} > 600$	2 ± 1.41	0.72 ± 0.42	0.24 ± 0.12	0.34 ± 0.36
≥ 4 jets, $t_{\mathrm{mod}} \geq 10.0$, $M_{\ell b} \geq 175$	$250 < E_{\mathrm{T}}^{\mathrm{miss}} < 450$	10 ± 3.16	0.70 ± 0.08	0.14 ± 0.02	1.00 ± 0.37
≥ 4 jets, $t_{\mathrm{mod}} \geq 10.0$, $M_{\ell b} \geq 175$	$E_{\mathrm{T}}^{\mathrm{miss}} > 450$	7 ± 2.65	0.72 ± 0.06	0.09 ± 0.02	0.46 ± 0.19
Compressed search	$250 < E_{\mathrm{T}}^{\mathrm{miss}} < 350$	49 ± 7.00	0.50 ± 0.19	0.21 ± 0.06	5.03 ± 1.78
Compressed search	$350 < E_{\mathrm{T}}^{\mathrm{miss}} < 450$	11 ± 3.32	0.54 ± 0.20	0.14 ± 0.03	0.84 ± 0.33
Compressed search	$450 < E_{\mathrm{T}}^{\mathrm{miss}} < 550$	5 ± 2.24	0.42 ± 0.19	0.20 ± 0.05	0.42 ± 0.24
Compressed search	$E_{\mathrm{T}}^{\mathrm{miss}} > 550$	3 ± 1.73	0.56 ± 0.19	0.14 ± 0.05	0.24 ± 0.17

4.8.3 Single Lepton from Top

At the start of our search, before making any cuts to the data, the largest background to contend with was genuine single leptons that result from top quarks decaying to W-bosons, which in turn decay leptonically. However, as earlier sections have mentioned, our high $E_{\mathrm{T}}^{\mathrm{miss}}$ and M_{T} requirements are extremely effective at reducing this background component. So much so, in fact, that after event selections, the single lepton from top background (or 1ℓtop) becomes practically negligible in all our signal regions.

Unfortunately, there is no way to perform a robust, data-driven estimate of this background, because we cannot construct a control region that is enhanced in 1ℓtop processes (mostly $t\bar{t} \rightarrow 1\ell$, followed by single top quark production). Since this background was so strongly reduced by the M_{T} cut, one might consider a lower-M_{T} sideband region; however, as we discovered in the previous section, such a region contains a considerable number of 1ℓW events, and even lost lepton events. Therefore, we are forced to estimate the 1ℓtop background directly from Monte Carlo simulation.

As mentioned in Section 4.4, most 1ℓtop events that pass the M_{T} cut do so because of $E_{\mathrm{T}}^{\mathrm{miss}}$ resolution effects. Thus, by far the largest uncertainty on the 1ℓtop background component is the uncertainty on $E_{\mathrm{T}}^{\mathrm{miss}}$ resolution. Our studies in Appendix B show this uncertainty can be as high as 25%. In Figure 4.14, we show the $E_{\mathrm{T}}^{\mathrm{miss}}$ spectra of $t\bar{t} \rightarrow 1\ell$ events from Monte Carlo, both before and after fluctuating the $E_{\mathrm{T}}^{\mathrm{miss}}$ resolution according to the uncertainties from Appendix B. We note that the yields in the various bins may fluctuate enormously as the $E_{\mathrm{T}}^{\mathrm{miss}}$ resolution is varied within a realistic range. On that basis, we assign a flat 100% uncertainty to the 1ℓtop background component. All other uncertainties, including statistical, are insignificant by comparison, and should be covered by the 100% uncertainty we impose.

The final results of our single lepton from top background estimate are presented in Table 4.13.

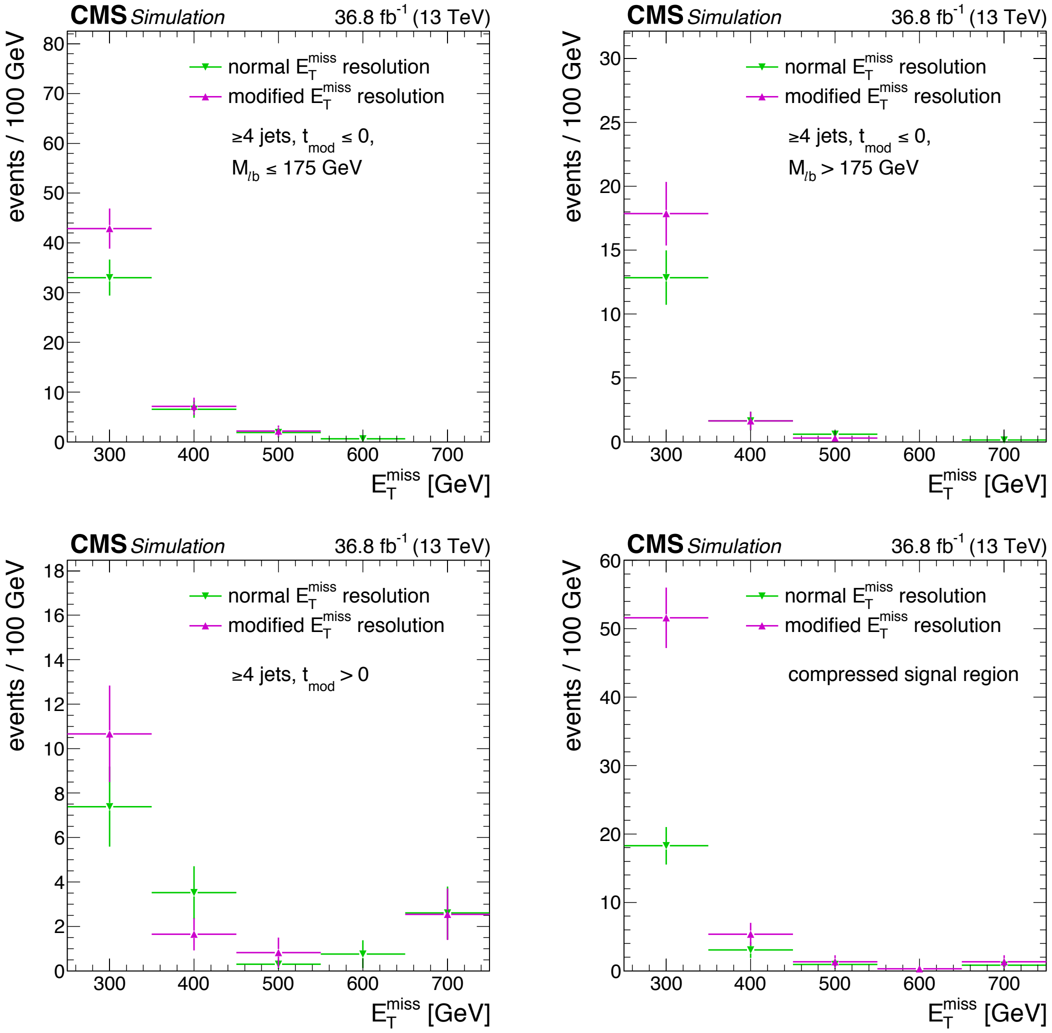

Figure 4.14: $E_{\mathrm{T}}^{\mathrm{miss}}$ distributions in $t\bar{t} \to 1\ell$ Monte Carlo, with and without fluctuated $E_{\mathrm{T}}^{\mathrm{miss}}$ resolution. The plots are made in the C regions, the D regions, the combined E/F/G/H regions, and the I (corridor) regions, respectively. The A/B regions have an insignificant $t\bar{t} \to 1\ell$ component, so are not shown.

Table 4.13: Results of the single lepton from top background estimate, with 100% uncertainty applied.

Region	$E_{\mathrm{T}}^{\mathrm{miss}}$ bin	SR Estimate
< 4 jets, $t_{\mathrm{mod}} \geq 10.0$, $M_{\ell b} < 175$	$250 < E_{\mathrm{T}}^{\mathrm{miss}} < 350$	—
< 4 jets, $t_{\mathrm{mod}} \geq 10.0$, $M_{\ell b} < 175$	$350 < E_{\mathrm{T}}^{\mathrm{miss}} < 450$	0.22±0.22
< 4 jets, $t_{\mathrm{mod}} \geq 10.0$, $M_{\ell b} < 175$	$450 < E_{\mathrm{T}}^{\mathrm{miss}} < 600$	0.13±0.13
< 4 jets, $t_{\mathrm{mod}} \geq 10.0$, $M_{\ell b} < 175$	$E_{\mathrm{T}}^{\mathrm{miss}} > 600$	0.28±0.28
< 4 jets, $t_{\mathrm{mod}} \geq 10.0$, $M_{\ell b} \geq 175$	$250 < E_{\mathrm{T}}^{\mathrm{miss}} < 450$	—
< 4 jets, $t_{\mathrm{mod}} \geq 10.0$, $M_{\ell b} \geq 175$	$450 < E_{\mathrm{T}}^{\mathrm{miss}} < 600$	—
< 4 jets, $t_{\mathrm{mod}} \geq 10.0$, $M_{\ell b} \geq 175$	$E_{\mathrm{T}}^{\mathrm{miss}} > 600$	—
≥ 4 jets, $t_{\mathrm{mod}} < 0.0$, $M_{\ell b} < 175$	$250 < E_{\mathrm{T}}^{\mathrm{miss}} < 350$	13.2±13.2
≥ 4 jets, $t_{\mathrm{mod}} < 0.0$, $M_{\ell b} < 175$	$350 < E_{\mathrm{T}}^{\mathrm{miss}} < 450$	2.3±2.3
≥ 4 jets, $t_{\mathrm{mod}} < 0.0$, $M_{\ell b} < 175$	$450 < E_{\mathrm{T}}^{\mathrm{miss}} < 550$	0.63±0.63
≥ 4 jets, $t_{\mathrm{mod}} < 0.0$, $M_{\ell b} < 175$	$550 < E_{\mathrm{T}}^{\mathrm{miss}} < 650$	0.09±0.09
≥ 4 jets, $t_{\mathrm{mod}} < 0.0$, $M_{\ell b} < 175$	$E_{\mathrm{T}}^{\mathrm{miss}} > 650$	—
≥ 4 jets, $t_{\mathrm{mod}} < 0.0$, $M_{\ell b} \geq 175$	$250 < E_{\mathrm{T}}^{\mathrm{miss}} < 350$	3.1±3.1
≥ 4 jets, $t_{\mathrm{mod}} < 0.0$, $M_{\ell b} \geq 175$	$350 < E_{\mathrm{T}}^{\mathrm{miss}} < 450$	0.59±0.59
≥ 4 jets, $t_{\mathrm{mod}} < 0.0$, $M_{\ell b} \geq 175$	$450 < E_{\mathrm{T}}^{\mathrm{miss}} < 550$	0.37±0.37
≥ 4 jets, $t_{\mathrm{mod}} < 0.0$, $M_{\ell b} \geq 175$	$E_{\mathrm{T}}^{\mathrm{miss}} > 550$	—
≥ 4 jets, $0.0 < t_{\mathrm{mod}} < 10.0$, $M_{\ell b} < 175$	$250 < E_{\mathrm{T}}^{\mathrm{miss}} < 350$	1.7±1.7
≥ 4 jets, $0.0 < t_{\mathrm{mod}} < 10.0$, $M_{\ell b} < 175$	$350 < E_{\mathrm{T}}^{\mathrm{miss}} < 550$	0.48±0.48
≥ 4 jets, $0.0 < t_{\mathrm{mod}} < 10.0$, $M_{\ell b} < 175$	$E_{\mathrm{T}}^{\mathrm{miss}} > 550$	0.33±0.33
≥ 4 jets, $0.0 < t_{\mathrm{mod}} < 10.0$, $M_{\ell b} \geq 175$	$250 < E_{\mathrm{T}}^{\mathrm{miss}} < 450$	0.30±0.30
≥ 4 jets, $0.0 < t_{\mathrm{mod}} < 10.0$, $M_{\ell b} \geq 175$	$E_{\mathrm{T}}^{\mathrm{miss}} > 450$	—
≥ 4 jets, $t_{\mathrm{mod}} \geq 10.0$, $M_{\ell b} < 175$	$250 < E_{\mathrm{T}}^{\mathrm{miss}} < 350$	0.75±0.75
≥ 4 jets, $t_{\mathrm{mod}} \geq 10.0$, $M_{\ell b} < 175$	$350 < E_{\mathrm{T}}^{\mathrm{miss}} < 450$	0.69±0.69
≥ 4 jets, $t_{\mathrm{mod}} \geq 10.0$, $M_{\ell b} < 175$	$450 < E_{\mathrm{T}}^{\mathrm{miss}} < 600$	0.10±0.10
≥ 4 jets, $t_{\mathrm{mod}} \geq 10.0$, $M_{\ell b} < 175$	$E_{\mathrm{T}}^{\mathrm{miss}} > 600$	0.65±0.65
≥ 4 jets, $t_{\mathrm{mod}} \geq 10.0$, $M_{\ell b} \geq 175$	$250 < E_{\mathrm{T}}^{\mathrm{miss}} < 450$	—
≥ 4 jets, $t_{\mathrm{mod}} \geq 10.0$, $M_{\ell b} \geq 175$	$E_{\mathrm{T}}^{\mathrm{miss}} > 450$	0.11±0.11
Compressed search	$250 < E_{\mathrm{T}}^{\mathrm{miss}} < 350$	5.3±5.3
Compressed search	$350 < E_{\mathrm{T}}^{\mathrm{miss}} < 450$	1.0±1.0
Compressed search	$450 < E_{\mathrm{T}}^{\mathrm{miss}} < 550$	0.12±0.12
Compressed search	$E_{\mathrm{T}}^{\mathrm{miss}} > 550$	0.13±0.13

4.8.4 Rare Standard Model Processes

The final component of our backgrounds is that from rare Standard Model processes. In practice, we define this background component as any events containing a Z boson that decays to two neutrinos (an "invisible" Z decay). The non-detection of a heavy particle such as the Z boson creates a considerable amount of real $E_{\mathrm{T}}^{\mathrm{miss}}$, helping the event to pass our selections.

The majority of this background comes from ttZ events where the Z decays to neutrinos, especially in the $\geq$4-jet regions. The next largest source is WZ production, which manifests primarily in the 2-to-3-jet regions. Note that the rare background category takes precedence over all others. For example, if an event has a $Z \to \nu\nu$ decay as well as one lepton from a top quark, it should always be classified as belonging to the rare background.

Estimation Method

Although the rare background is a relatively small component, we still attempt to estimate it using robust, data-driven methods. In contrast to the methods used for the lost lepton and 1ℓW backgrounds, we estimate the rare background using a technique more akin to that used in the top asymmetry measurements, as described in Section 3.6.

Our rare background estimate relies on the assumption that the relative normalization between data and MC is the same in our signal regions as in a three-lepton control region. So:

$$\frac{N_{\mathrm{rare}}^{\mathrm{SR}}}{M_{\mathrm{rare}}^{\mathrm{SR}}} = \frac{N_{\mathrm{ttZ,\ WZ}}^{CR3\ell}}{M_{\mathrm{ttZ,\ WZ}}^{CR3\ell}} \tag{4.15}$$

If we invert Equation 4.15, we can estimate our rare background component using the Monte Carlo yield in our signal region, times a normalization factor:

$$N_{\mathrm{rare}}^{\mathrm{SR}} = M_{\mathrm{rare}}^{\mathrm{SR}} \times NF_{\mathrm{ttZ,\ WZ}}^{CR3\ell} \tag{4.16}$$

where the normalization factor is just the data/MC ratio measured in the 3ℓ control region.

The normalization factors for ttZ and WZ production are derived using a simultaneous template fit, as shown in Figure 4.15. For ttZ, the factor is 1.14 ± 0.30, and for WZ, it is 1.26 ± 0.09. The uncertainties on these normalization factors include all the statistical and systematic factors that influence the template fit. The normalization uncertainty is taken as a systematic on the final background estimate.

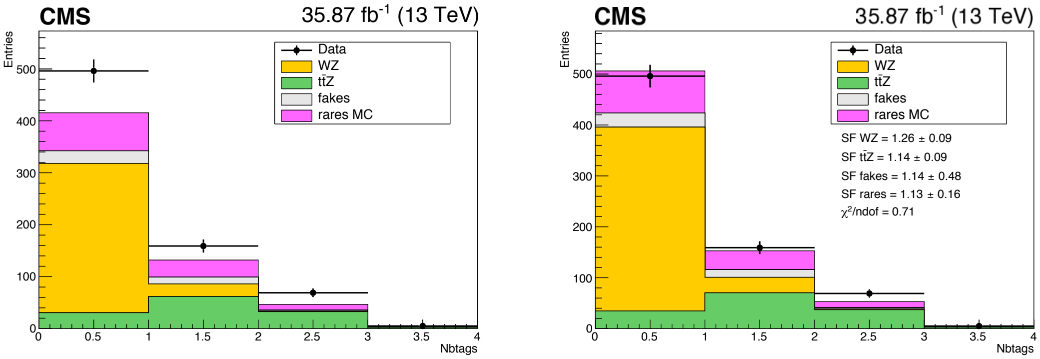

Figure 4.15: Distribution of number of b-jets in 3ℓ control region, before (left) and after (right) template fit, from 2016 same-sign dilepton search.

We do not derive these factors ourselves; rather, they are taken from a CMS internal note documenting changes and improvements to the 2016 same-sign dilepton search. The same-sign analysis was described in public documentation supporting ICHEP 2016 [75].

Control Region Definition

The control region used to select 3-lepton events for the same-sign analysis is formed from the following criteria:

- Require three leptons (e or μ) passing tight ID criteria. The first two must have $p_T > 25$ and 20 GeV, respectively, and the third must have $p_T > 10$ GeV.
- The third lepton must form an opposite-sign same-flavor pair with one of the first two leptons.

- The invariant mass of the paired leptons must be within 15 GeV of the Z-boson mass (which is 91.1876 GeV [3]).
- There must be at least two jets in the event. No requirement is made on the number of b-tags.
- The scalar sum of the p_T of the jets, known as H_T, must be > 80 GeV.
- $E_{\mathrm{T}}^{\mathrm{miss}} > 30$ GeV

Systematic Uncertainties

Because the rare background is estimated differently from the other backgrounds, we assess our systematic uncertainties in two different ways. The standard experimental systematics are evaluated the same way as for the lost lepton and 1ℓW backgrounds, except where explicitly stated otherwise. The experimental uncertainties include:

- Monte Carlo statistics
- b-tagging efficiencies (HF and LF)
- Lepton ID and isolation efficiencies
- JES
- ISR n_{jets} reweighting
- **Pileup reweighting:** this systematic is highly sensitive to the low MC statistics of this background, especially in the tail of the pileup distribution. To avoid large variations, we evaluate the uncertainty across all signal regions summed together, and see that it is $<1\%$. To be conservative, we assign a flat 3% systematic, expecting it will cover any variations due to signal region kinematics.

When evaluating the theory uncertainties, we only consider the effects they have on the shape of the background. We keep the normalization fixed to the values derived from the control region. And because the theory uncertainties are highly sensitive to our limited statistics, we merge several of the nominal regions together by removing the binning in $M_{\ell b}$ and t_{mod}. In effect, this leaves us with fewer regions, binned only in N_{jets} and $E_{\mathrm{T}}^{\mathrm{miss}}$. This merging is justified by studies showing that variations in the shapes of $M_{\ell b}$ and t_{mod} are small compared to uncertainties arising from the $E_{\mathrm{T}}^{\mathrm{miss}}$ distribution. The corridor regions are not merged in any way. The theory uncertainties evaluated in this manner are:

- Q^2
- PDF
- α_S

The systematic uncertainties on the rare background estimate are presented in Table 4.14.

Results

The full results of the rare standard model background estimate, including systematic uncertainties, are presented in Table 4.15.

Table 4.14: Summary of systematic uncertainties on the rare standard model processes background estimate.

Region	MC stat.	Lep. ID/Iso	b-tag (LF)	b-tag (HF)	PU	PDF	α_S	Q^2	ISR njets	JES	Norm.	Total
A $250 < E_{\mathrm{T}}^{\mathrm{miss}} < 350$	11.88%	0.31%	1.58%	1.23%	3.00%	0.23%	0.86%	3.86%	7.12%	2.55%	20.70%	25.60%
A $350 < E_{\mathrm{T}}^{\mathrm{miss}} < 450$	25.04%	0.35%	3.63%	0.77%	3.00%	3.33%	0.61%	1.31%	9.09%	0.37%	24.38%	36.61%
A $450 < E_{\mathrm{T}}^{\mathrm{miss}} < 600$	23.87%	0.37%	1.34%	1.34%	3.00%	0.45%	0.39%	2.47%	7.02%	0.46%	20.77%	32.71%
A $E_{\mathrm{T}}^{\mathrm{miss}} > 600$	51.43%	0.41%	2.87%	1.74%	3.00%	8.04%	0.36%	2.37%	5.13%	10.54%	16.77%	56.17%
B $250 < E_{\mathrm{T}}^{\mathrm{miss}} < 450$	29.98%	0.50%	1.67%	1.23%	3.00%	1.17%	0.76%	2.86%	3.97%	1.01%	14.74%	34.01%
B $450 < E_{\mathrm{T}}^{\mathrm{miss}} < 600$	86.04%	0.77%	5.28%	1.26%	3.00%	0.45%	0.40%	2.47%	4.00%	32.62%	15.46%	93.63%
B $E_{\mathrm{T}}^{\mathrm{miss}} > 600$	228.31%	2.65%	19.40%	1.64%	3.00%	8.03%	0.36%	2.37%	8.12%	44.04%	22.72%	234.76%
C $250 < E_{\mathrm{T}}^{\mathrm{miss}} < 350$	4.56%	0.45%	0.06%	0.68%	3.00%	0.81%	0.60%	1.77%	0.40%	4.78%	26.18%	27.26%
C $350 < E_{\mathrm{T}}^{\mathrm{miss}} < 450$	10.85%	0.35%	0.48%	0.66%	3.00%	2.01%	1.23%	5.00%	0.99%	6.85%	23.73%	27.73%
C $450 < E_{\mathrm{T}}^{\mathrm{miss}} < 550$	20.70%	0.31%	4.53%	0.26%	3.00%	1.89%	1.34%	4.86%	2.03%	4.52%	18.54%	29.25%
C $550 < E_{\mathrm{T}}^{\mathrm{miss}} < 650$	9.20%	0.38%	0.77%	0.38%	3.00%	4.90%	1.86%	3.67%	3.67%	2.14%	26.32%	29.09%
C $E_{\mathrm{T}}^{\mathrm{miss}} > 650$	12.73%	0.45%	0.20%	0.40%	3.00%	8.11%	3.08%	4.23%	4.92%	5.74%	26.32%	31.85%
D $250 < E_{\mathrm{T}}^{\mathrm{miss}} < 350$	19.82%	0.31%	0.72%	0.41%	3.00%	0.81%	0.60%	1.76%	0.82%	9.76%	20.24%	30.20%
D $350 < E_{\mathrm{T}}^{\mathrm{miss}} < 450$	27.58%	0.32%	1.82%	1.08%	3.00%	2.02%	1.23%	4.99%	1.63%	10.79%	17.33%	34.98%
D $450 < E_{\mathrm{T}}^{\mathrm{miss}} < 550$	47.40%	0.33%	4.96%	0.22%	3.00%	1.88%	1.33%	4.85%	2.24%	17.87%	17.31%	54.17%
D $E_{\mathrm{T}}^{\mathrm{miss}} > 550$	18.94%	0.44%	0.06%	0.83%	3.00%	7.53%	2.44%	2.55%	7.31%	7.15%	26.32%	35.14%
E $250 < E_{\mathrm{T}}^{\mathrm{miss}} < 350$	5.55%	0.42%	0.65%	0.74%	3.00%	0.81%	0.60%	1.77%	2.52%	3.80%	25.40%	26.66%
E $350 < E_{\mathrm{T}}^{\mathrm{miss}} < 550$	10.40%	0.40%	0.01%	0.83%	3.00%	1.97%	1.26%	4.96%	0.66%	7.23%	23.72%	27.63%
E $E_{\mathrm{T}}^{\mathrm{miss}} > 550$	87.72%	0.77%	7.05%	0.02%	3.00%	7.55%	2.47%	2.51%	2.26%	1.66%	24.61%	91.86%
F $250 < E_{\mathrm{T}}^{\mathrm{miss}} < 450$	16.02%	0.42%	0.06%	0.31%	3.00%	1.16%	0.78%	2.70%	2.10%	4.41%	24.07%	29.63%
F $E_{\mathrm{T}}^{\mathrm{miss}} > 450$	12.82%	0.47%	0.40%	0.57%	3.00%	3.72%	1.70%	3.91%	2.22%	3.37%	26.33%	30.26%
G $250 < E_{\mathrm{T}}^{\mathrm{miss}} < 350$	5.75%	0.39%	0.01%	1.71%	3.00%	0.81%	0.60%	1.77%	2.09%	3.44%	25.42%	26.68%
G $350 < E_{\mathrm{T}}^{\mathrm{miss}} < 450$	7.06%	0.43%	0.05%	1.35%	3.00%	2.01%	1.23%	5.00%	1.79%	9.62%	25.14%	28.63%
G $450 < E_{\mathrm{T}}^{\mathrm{miss}} < 600$	9.01%	0.37%	0.19%	1.27%	3.00%	2.63%	1.54%	4.72%	0.51%	5.15%	24.77%	27.64%
G $E_{\mathrm{T}}^{\mathrm{miss}} > 600$	7.00%	0.47%	0.19%	1.01%	3.00%	8.01%	2.34%	1.74%	0.68%	15.62%	26.32%	32.70%
H $250 < E_{\mathrm{T}}^{\mathrm{miss}} < 450$	9.94%	0.49%	0.05%	0.07%	3.00%	1.17%	0.79%	2.72%	2.06%	4.60%	26.32%	28.91%
H $E_{\mathrm{T}}^{\mathrm{miss}} > 450$	34.01%	0.43%	0.04%	0.88%	3.00%	3.71%	1.70%	3.91%	0.93%	2.41%	19.94%	40.03%
I $250 < E_{\mathrm{T}}^{\mathrm{miss}} < 350$	9.76%	0.38%	0.78%	0.47%	3.00%	0.21%	0.32%	3.91%	4.30%	5.32%	23.38%	26.72%
I $350 < E_{\mathrm{T}}^{\mathrm{miss}} < 450$	17.91%	0.35%	0.76%	0.60%	3.00%	1.99%	1.41%	5.88%	4.56%	6.05%	22.78%	30.79%
I $450 < E_{\mathrm{T}}^{\mathrm{miss}} < 550$	25.04%	0.51%	4.83%	0.35%	3.00%	1.89%	1.62%	4.90%	5.38%	4.89%	21.64%	34.80%
I $E_{\mathrm{T}}^{\mathrm{miss}} > 550$	29.62%	0.40%	0.22%	0.68%	3.00%	1.82%	1.55%	7.48%	4.76%	6.34%	20.76%	37.98%

Table 4.15: Summary of the rare standard model background estimate.

Region	ttZ	WZ	Total
A $250 < E_{\mathrm{T}}^{\mathrm{miss}} < 350$	3.33 ± 0.96	1.38 ± 0.58	4.71 ± 1.21
A $350 < E_{\mathrm{T}}^{\mathrm{miss}} < 450$	1.85 ± 0.53	0.21 ± 0.53	2.05 ± 0.75
A $450 < E_{\mathrm{T}}^{\mathrm{miss}} < 600$	1.15 ± 0.33	0.47 ± 0.39	1.62 ± 0.53
A $E_{\mathrm{T}}^{\mathrm{miss}} > 600$	0.36 ± 0.11	0.36 ± 0.41	0.71 ± 0.40
B $250 < E_{\mathrm{T}}^{\mathrm{miss}} < 450$	0.61 ± 0.18	0.93 ± 0.47	1.54 ± 0.52
B $450 < E_{\mathrm{T}}^{\mathrm{miss}} < 600$	0.15 ± 0.05	0.20 ± 0.34	0.35 ± 0.33
B $E_{\mathrm{T}}^{\mathrm{miss}} > 600$	0.09 ± 0.03	0.02 ± 0.26	0.11 ± 0.26
C $250 < E_{\mathrm{T}}^{\mathrm{miss}} < 350$	14.28 ± 3.84	0.10 ± 0.62	14.38 ± 3.92
C $350 < E_{\mathrm{T}}^{\mathrm{miss}} < 450$	3.83 ± 1.06	0.60 ± 0.48	4.43 ± 1.23
C $450 < E_{\mathrm{T}}^{\mathrm{miss}} < 550$	1.06 ± 0.31	0.73 ± 0.39	1.79 ± 0.52
C $550 < E_{\mathrm{T}}^{\mathrm{miss}} < 650$	0.40 ± 0.12	0.00 ± 0.00	0.40 ± 0.12
C $E_{\mathrm{T}}^{\mathrm{miss}} > 650$	0.20 ± 0.06	0.00 ± 0.00	0.20 ± 0.06
D $250 < E_{\mathrm{T}}^{\mathrm{miss}} < 350$	2.06 ± 0.56	0.95 ± 0.63	3.01 ± 0.91
D $350 < E_{\mathrm{T}}^{\mathrm{miss}} < 450$	0.62 ± 0.18	0.55 ± 0.40	1.18 ± 0.41
D $450 < E_{\mathrm{T}}^{\mathrm{miss}} < 550$	0.24 ± 0.07	0.21 ± 0.22	0.45 ± 0.24
D $E_{\mathrm{T}}^{\mathrm{miss}} > 550$	0.09 ± 0.03	0.00 ± 0.00	0.09 ± 0.03
E $250 < E_{\mathrm{T}}^{\mathrm{miss}} < 350$	7.88 ± 2.14	0.40 ± 0.44	8.27 ± 2.21
E $350 < E_{\mathrm{T}}^{\mathrm{miss}} < 550$	3.34 ± 0.94	0.52 ± 0.39	3.87 ± 1.07
E $E_{\mathrm{T}}^{\mathrm{miss}} > 550$	0.26 ± 0.08	0.03 ± 0.25	0.29 ± 0.26
F $250 < E_{\mathrm{T}}^{\mathrm{miss}} < 450$	0.98 ± 0.27	0.13 ± 0.17	1.11 ± 0.33
F $E_{\mathrm{T}}^{\mathrm{miss}} > 450$	0.21 ± 0.06	0.00 ± 0.00	0.21 ± 0.06
G $250 < E_{\mathrm{T}}^{\mathrm{miss}} < 350$	2.89 ± 0.78	0.14 ± 0.15	3.03 ± 0.81
G $350 < E_{\mathrm{T}}^{\mathrm{miss}} < 450$	2.51 ± 0.71	0.16 ± 0.18	2.67 ± 0.77
G $450 < E_{\mathrm{T}}^{\mathrm{miss}} < 600$	1.80 ± 0.50	0.16 ± 0.16	1.96 ± 0.54
G $E_{\mathrm{T}}^{\mathrm{miss}} > 600$	0.70 ± 0.20	0.00 ± 0.00	0.70 ± 0.23
H $250 < E_{\mathrm{T}}^{\mathrm{miss}} < 450$	0.37 ± 0.11	0.00 ± 0.00	0.37 ± 0.11
H $E_{\mathrm{T}}^{\mathrm{miss}} > 450$	0.33 ± 0.10	0.16 ± 0.17	0.49 ± 0.20
I $250 < E_{\mathrm{T}}^{\mathrm{miss}} < 350$	3.66 ± 1.01	0.66 ± 0.43	4.33 ± 1.16
I $350 < E_{\mathrm{T}}^{\mathrm{miss}} < 450$	1.57 ± 0.45	0.35 ± 0.34	1.93 ± 0.59
I $450 < E_{\mathrm{T}}^{\mathrm{miss}} < 550$	0.58 ± 0.17	0.19 ± 0.20	0.77 ± 0.27
I $E_{\mathrm{T}}^{\mathrm{miss}} > 550$	0.41 ± 0.13	0.17 ± 0.17	0.58 ± 0.22

4.9 Results

The results of the four background estimation procedures, as well as the yields of data in our signal regions, are presented in Table 4.16. The same numbers are presented graphically in Figure 4.16.

Table 4.16: Estimated background yields and measured data yields in our signal regions, based on the full 35.9 fb^{-1} of 2016 data.

N_J	t_mod	$M_{\ell\mathrm{b}}$ [GeV]	$E_\mathrm{T}^\mathrm{miss}$ [GeV]	Lost lepton	1ℓ (top)	1ℓ (not top)	$Z \rightarrow \nu\bar{\nu}$	Total background	Data
≤ 3	> 10	≤ 175	$250-350$	53.9±6.2	—	7.2±2.5	4.7±1.2	65.8±6.8	72
≤ 3	> 10	≤ 175	$350-450$	14.2±2.4	0.22±0.22	4.1±1.4	2.1±0.8	20.5±2.9	24
≤ 3	> 10	≤ 175	$450-600$	2.9±0.9	0.13±0.13	1.7±0.7	1.6±0.5	6.4±1.3	6
≤ 3	> 10	≤ 175	> 600	0.61±0.49	0.28±0.28	0.78±0.34	0.71±0.40	2.4±0.8	2
≤ 3	> 10	> 175	$250-450$	1.7±0.8	—	5.6±2.2	1.5±0.5	8.9±2.4	6
≤ 3	> 10	> 175	$450-600$	0.02±0.01	—	1.6±0.6	0.35±0.33	1.9±0.7	3
≤ 3	> 10	> 175	> 600	0.01±0.01	—	0.87±0.39	0.11±0.26	0.99±0.47	2
≥ 4	≤ 0	≤ 175	$250-350$	346±30	13.2±13.2	9.7±8.6	14.4±3.9	383±34	343
≥ 4	≤ 0	≤ 175	$350-450$	66.3±7.9	2.3±2.3	2.5±1.7	4.4±1.2	75.5±8.5	68
≥ 4	≤ 0	≤ 175	$450-550$	12.1±2.8	0.63±0.63	0.47±0.46	1.8±0.5	15.0±2.9	13
≥ 4	≤ 0	≤ 175	$550-650$	3.4±1.5	0.09±0.09	0.26±0.20	0.40±0.12	4.1±1.5	6
≥ 4	≤ 0	≤ 175	> 650	5.9±2.8	—	0.43±0.38	0.20±0.06	6.6±2.9	2
≥ 4	≤ 0	> 175	$250-350$	26.0±4.3	3.1±3.1	7.5±3.0	3.0±0.9	39.7±6.2	38
≥ 4	≤ 0	> 175	$350-450$	10.4±2.6	0.59±0.59	1.6±0.7	1.2±0.4	13.7±2.8	8
≥ 4	≤ 0	> 175	$450-550$	1.7±0.9	0.37±0.37	0.56±0.32	0.45±0.24	3.1±1.1	2
≥ 4	≤ 0	> 175	> 550	1.1±0.8	—	1.0±0.6	0.09±0.03	2.2±1.0	1
≥ 4	$0-10$	≤ 175	$250-350$	43.0±5.9	1.7±1.7	5.7±3.0	8.3±2.2	58.7±7.2	65
≥ 4	$0-10$	≤ 175	$350-550$	9.1±2.0	0.48±0.48	1.2±0.5	3.9±1.1	14.7±2.4	23
≥ 4	$0-10$	≤ 175	> 550	0.57±0.28	0.33±0.33	0.26±0.24	0.29±0.26	1.5±0.6	1
≥ 4	$0-10$	> 175	$250-450$	4.4±1.4	0.30±0.30	3.1±1.3	1.1±0.3	8.9±1.9	9
≥ 4	$0-10$	> 175	> 450	0.10±0.17	—	0.24±0.16	0.21±0.06	0.56±0.24	0
≥ 4	> 10	≤ 175	$250-350$	9.5±2.3	0.75±0.75	1.1±0.9	3.0±0.8	14.3±2.7	12
≥ 4	> 10	≤ 175	$350-450$	5.9±1.8	0.69±0.69	0.71±0.51	2.7±0.8	10.0±2.1	9
≥ 4	> 10	≤ 175	$450-600$	3.8±1.3	0.10±0.10	0.43±0.32	2.0±0.5	6.3±1.5	3
≥ 4	> 10	≤ 175	> 600	0.75±0.61	0.65±0.65	0.34±0.38	0.70±0.23	2.4±1.0	0
≥ 4	> 10	> 175	$250-450$	0.54±0.32	—	1.0±0.6	0.37±0.11	1.9±0.7	0
≥ 4	> 10	> 175	> 450	0.24±0.17	0.11±0.11	0.46±0.26	0.49±0.20	1.3±0.4	2
Corridor region			$250-350$	67.5±8.9	5.3±5.3	5.0±1.8	4.3±1.2	82.2±10.6	72
Corridor region			$350-450$	15.1±3.5	1.0±1.0	0.84±0.33	1.9±0.6	18.9±3.7	30
Corridor region			$450-550$	2.4±1.3	0.12±0.12	0.42±0.24	0.77±0.27	3.7±1.4	2
Corridor region			> 550	3.9±2.0	0.13±0.13	0.24±0.17	0.58±0.22	4.8±2.0	2

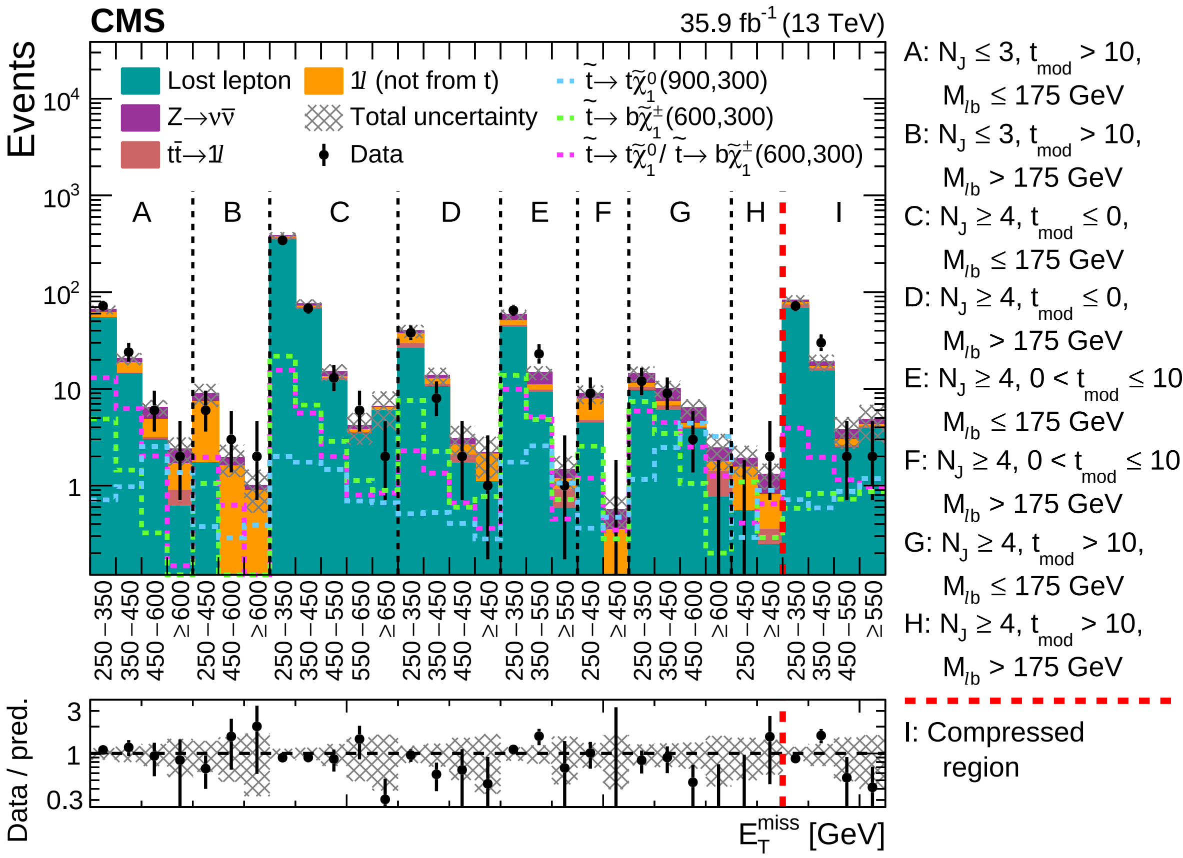

Figure 4.16: Estimated background yields, measured data yields, and selected signal predictions in our signal regions, based on the full 35.9 fb^{-1} of 2016 data. Hatched bands show the combined statistical and systematic uncertainties.

4.10 Interpretation

As Table 4.16 and Figure 4.16 show, our measured data are consistent with the predictions of the Standard Model. We must interpret these results in the context of our SUSY signal models.

4.10.1 Signal Estimate

As described in Table 4.3, our signal predictions are drawn from several Monte Carlo samples, all of which were produced using FastSim. In the course of routine data analysis, CMS scientists discovered certain anomalous events in the samples produced using FastSim. To prevent these anomalies from impacting our analysis, we filter out all simulated signal events that contain a reconstructed jet with the following attributes:

- Not matched to a generated jet within $\Delta R < 0.3$, and
- Charged hadron fraction (CHF) < 0.1

Systematic Uncertainties

Because our signal predictions are drawn from Monte Carlo simulations, we must assess many of the same systematic uncertainties for signal as we did for our background estimates. Although FastSim and FullSim have separate correction factors for a number of uncertainties, the method used to apply those corrections is generally the same as has been described for the background estimates.

For signal samples, we compute an uncertainty on the lepton veto efficiency separately. All our signal models have an efficiency of about 94% to accept true single-lepton events, with the 6% inefficiency due to fake leptons. We assess a 50% uncertainty on the efficiency of identifying these fake leptons, effectively giving a 3% systematic for lepton veto efficiency.

In addition, we must correct for the different modeling of $E_{\mathrm{T}}^{\mathrm{miss}}$ resolution in FastSim. To make such a correction, whenever $E_{\mathrm{T}}^{\mathrm{miss}}$ enters our measurements, we take the average of the reconstructed and generated $E_{\mathrm{T}}^{\mathrm{miss}}$ values. Effectively:

$$E_{\mathrm{T}}^{\mathrm{miss}}(\text{signal}) = \frac{1}{2}\left(E_{\mathrm{T}}^{\mathrm{miss}}(\text{reconstructed}) + E_{\mathrm{T}}^{\mathrm{miss}}(\text{generated})\right) \tag{4.17}$$

To evaluate the uncertainty on this $E_{\mathrm{T}}^{\mathrm{miss}}$ correction, we vary the $E_{\mathrm{T}}^{\mathrm{miss}}$ by half the difference between the reconstructed and generated $E_{\mathrm{T}}^{\mathrm{miss}}$ values.

A condensed summary of the uncertainties on the signal estimate is presented in Table 4.17.

Table 4.17: Summary of systematic uncertainties on signal yields. Uncertainties are given as typical values for an individual signal region. Low ΔM refers to the compressed regions. Table also indicates which uncertainties are treated as correlated between regions.

Systematic	Typical size		Correlated
	low ΔM	high ΔM	
Monte Carlo statistics	7–15%	5–25%	—
Luminosity	2.5%	2.5%	✓
Trigger	2–4%	2–4%	✓
Pile-Up	5–10%	5-10%	—
ISR	15%	1–8%	✓
Jet energy scale	1-20%	1-12%	✓
Q^2	2–4%	2-4%	✓
b-tagging	1–2%	1–7%	✓
Lepton ID/ISO	1%	1–2%	✓
Lepton veto efficiency	3%	3%	—
$E_{\mathrm{T}}^{\mathrm{miss}}$ modeling	2–7%	1–10%	—

Signal Contamination

Because our dilepton and 0-btag control regions are so similar to our signal regions, with only single cuts inverted, a number of signal events are reconstructed in those control regions instead of in the signal regions. This is known as *signal contamination*. This contamination could cause our background estimates to be artificially high, thus preventing us from noticing any excess of SUSY events in our signal regions. To account for this effect, we measure the number of signal events in our lost lepton and 0-btag control regions, and propagate those numbers through our estimation procedure, to figure out how the contamination would raise our background predictions. We then subtract those numbers from the signal yields predicted in the signal regions. This has the effect of reducing our sensitivity to SUSY signals in a way that approximates the effect of actual signal contamination.

Signal contamination in the lost lepton CRs results in a signal yield correction of 5-10% in the top and W corridor areas of parameter space, with corrections of 5% or less in the bulk regions. In the 0-btag CRs, signal contamination generally results in corrections of 3% or less, except for along the W corridor in the corridor search regions, where the correction tends to range from 20-40%. This heavy signal contamination along the W corridor appears because the kinematics of compressed T2tt decays make it difficult to tag b-jets. In essence, the 0-btag control regions act as fairly good signal regions themselves. Future researchers may wish to consider inverting the b-tag requirement and defining 0-btag signal regions to be used along the W corridor.

4.10.2 Limits

The statistical analysis of our results is performed using the CombinedLimit tool originally developed for the Higgs boson search at the LHC [76]. Using this tool, we combine our signal regions together using a modified frequentist approach [77]. As described in Section 4.7.2, we combine the four corridor signal regions (series I) when searching for T2tt signals in the range $100 < \Delta M < 225$ GeV; for other mass points in the T2tt search, and for all mass points in the T2bW and T2tb searches, we combine our 27 nominal signal regions (series A-H). When performing this combination, we account for the fact that some uncertainties, such as data and MC statistics, are totally uncorrelated from region to region, whereas other systematics, such as luminosity or JES, are correlated from region to region because they are derived from the same scale factors.

Because we do not see any large excesses of signal events over the Standard Model prediction, we set limits on the cross section for stop squark pair production decaying to single-lepton final states. At each mass point in the ($m_{\tilde{t}}$, $m_{\tilde{\chi}_1^0}$) parameter space, we calculate 95% confidence level (CL) exclusion limits for stop squark production using an asymptotic formulation of the $\mathrm{CL_s}$ method [78, 79].

In Figure 4.17, we show the 95% CL exclusion range for the process $pp \to \tilde{t}\tilde{t}^* \to t\bar{t}\tilde{\chi}_1^0\tilde{\chi}_1^0$ (the T2tt model), along with 95% CL upper limits on the production cross section for such signals. These numbers are produced assuming stop squarks are unpolarized. If the LSP is massless, we exclude production of stop squarks up to 1120 GeV in mass; the excluded LSP masses vary with stop mass, up to a maximum of 515 GeV for a stop mass of 950 GeV. Note that our exclusion curve does not have the “inlet” along the top corridor region seen in the Run I results, indicating the success of our compressed T2tt search strategy. The white band in the lower corner represents a region in which we set no cross section limit due to problems in the production of the signal Monte Carlo sample.

Figure 4.18 presents the same limits for the process $pp \to \tilde{t}\tilde{t}^* \to b\bar{b}\tilde{\chi}_1^{\pm}\tilde{\chi}_1^{\pm}$, with $\tilde{\chi}_1^{\pm} \to W\tilde{\chi}_1^0$ (T2bW model). In this case, we exclude stop squarks up to 1000 GeV for the case of a massless LSP, and LSPs up to 460 GeV for the case of an 800 GeV stop squark.

In Figure 4.19, we present the exclusion and cross section limits for the process $pp \to \tilde{t}\tilde{t}^* \to tb\tilde{\chi}_1^{\pm}\tilde{\chi}_1^0$, with $\tilde{\chi}_1^{\pm} \to W\tilde{\chi}_1^0$ (T2tb model). In this case, we exclude stops up to 1000 GeV for the case of a massless LSP, and LSP masses up to 390 GV for the case of an 850 GeV stop squark.

4.11 Conclusion

We have performed a search for three models of stop squark pair production and decay to single lepton final states using data from the CMS experiment. The data, collected in 2016, correspond to 35.9 fb^{-1} of luminosity. We selected events containing a single isolated electron or muon, multiple jets, and large $E_{\mathrm{T}}^{\mathrm{miss}}$. The results were consistent with the presence of Standard Model physics only. We set exclusion limits on these models; at the 95% confidence level, these exclusions include stop squarks up to about 1000 GeV for massless neutralinos, and neutralino masses up to 515 GeV for a stop mass of 950 GeV.

4.12 Acknowledgements

Although the bulk of this analysis was the work of a few physicists, the analysis would not be possible without the efforts of the entire CMS collaboration, more than 3,000 members

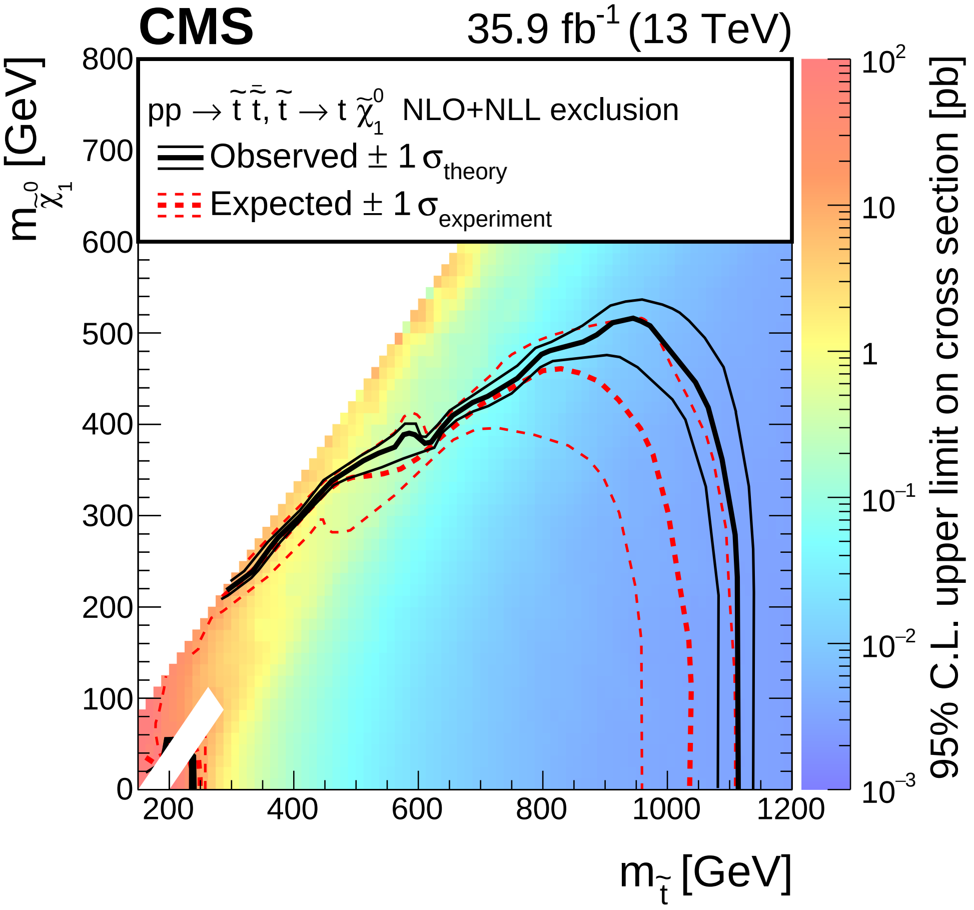

Figure 4.17: Exclusion limits at 95% CL (black line) and cross section upper limits at 95% CL (color scale) for production of stop squarks decaying to top quarks and LSPs.

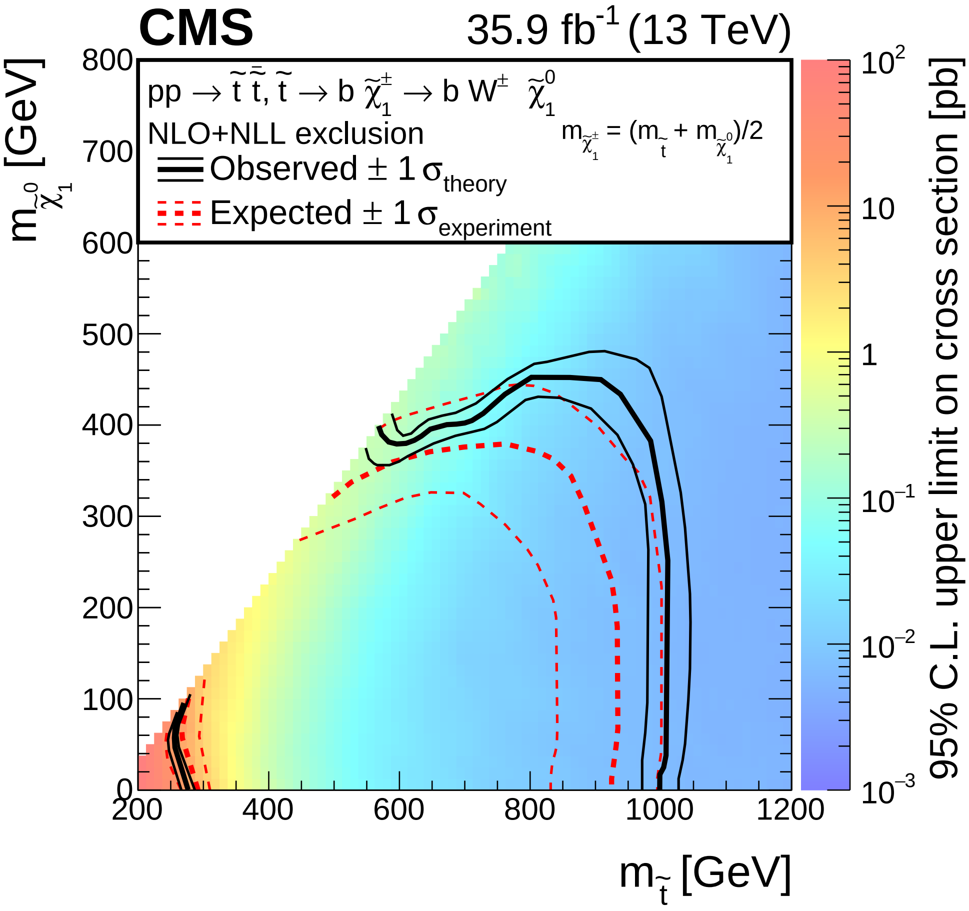

Figure 4.18: Exclusion limits at 95% CL (black line) and cross section upper limits at 95% CL (color scale) for production of stop squarks decaying to bottom quarks and charginos, with charginos decaying to W-bosons and LSPs.

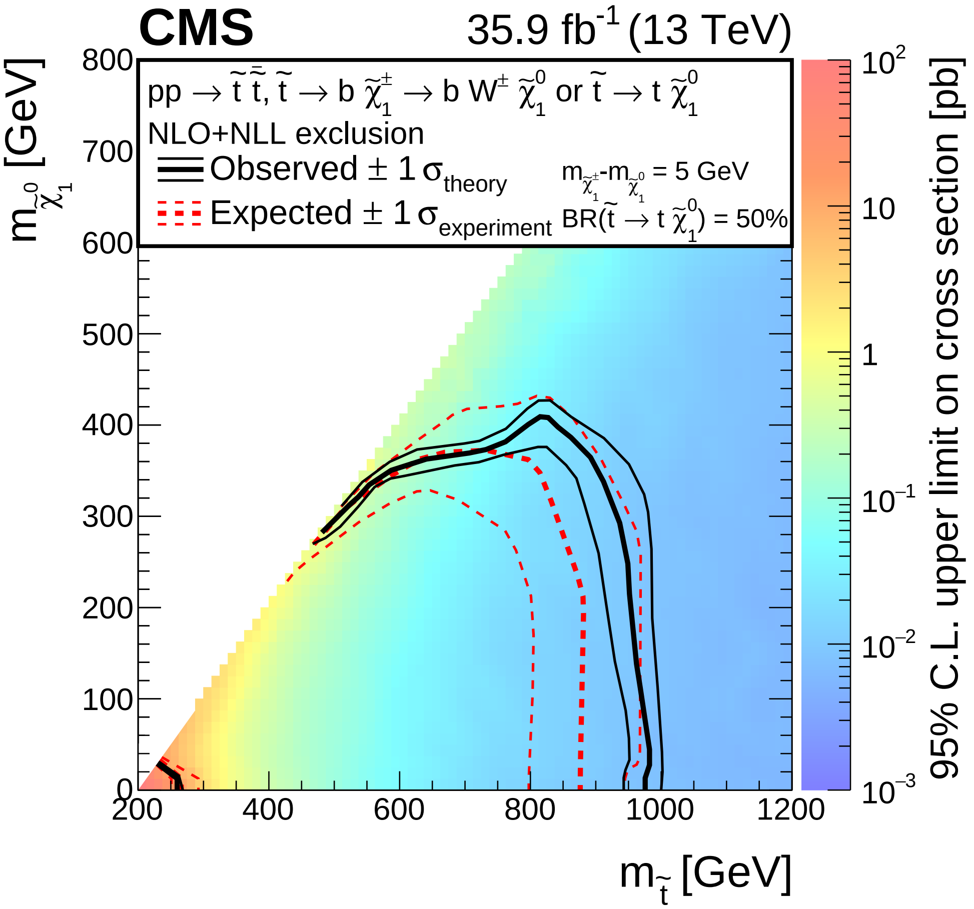

Figure 4.19: Exclusion limits at 95% CL (black line) and cross section upper limits at 95% CL (color scale) for production of stop squarks decaying half to top quarks and LSPs and half to bottom quarks and charginos.

strong. They were responsible for maintaining the detector, software, and computing platforms necessary to perform the analysis. In addition, numerous members contributed feedback that enhanced the quality of the analysis.

The 2016 analysis was published singly in JHEP [67], and an earlier version based on 2015 data was published, combined with an all-hadronic stop search, in EPJ [68].

Appendix A

Electron-Muon Crosscheck Studies

Our use of a dilepton control region to estimate the lost lepton background component in Section 4.8.1 is only useful if the physics of $t\bar{t}$ processes are correctly modeled. We know from Chapter 3 that our Monte Carlo simulations do a very good job of modeling $t\bar{t}$ processes on the whole, but our search for supersymmetry demands exacting precision. For that reason, we employ a set of e/μ crosscheck regions, enriched in $t\bar{t} \to \ell\ell$ and single top tW processes, to validate the physics of our lost lepton control regions.

Crosscheck Region Definitions

We define our crosscheck regions using the following criteria:

- Event must pass the standard $E_{\mathrm{T}}^{\mathrm{miss}}$ filters.
- Event must pass a mixed-flavor dilepton trigger (also known as MuonEG). The triggers we use are listed in Table 4.2.
- We must have exactly one medium electron and one tight muon.
  - The leading lepton must have $p_T > 30$ GeV, and the trailing, $p_T > 15$ GeV.
  - The leptons must have $|\eta| < 2.1$, and relative mini isolation < 0.1.

  - The leptons must have opposite charge.
  - The dilepton invariant mass must be > 20 GeV.
- The event must contain at least 2 jets.
- $E_{\mathrm{T}}^{\mathrm{miss}}$ must be > 50 GeV.

We create three overlapping regions, binned in number of b-tags: $\geq$0 tags, $\geq$1 tag, and $\geq$ 2 tags. The data and Monte Carlo yields in these regions are presented in Table A.1.

Table A.1: Data and Monte Carlo yields in the e/μ crosscheck regions, based on 35.9 fb^{-1} of luminosity.

Sample	≥ 0 b-tagged jets $E_{\mathrm{T}}^{\mathrm{miss}} > 50$	≥ 1 b-tagged jets $E_{\mathrm{T}}^{\mathrm{miss}} > 50$	≥ 2 b-tagged jets $E_{\mathrm{T}}^{\mathrm{miss}} > 50$
$t\bar{t}$, ≥ 2 leptons	123328.75 ± 106.86	96525.59 ± 93.60	35056.95 ± 55.22
$t\bar{t}$, 1 lepton	1504.44 ± 13.62	893.81 ± 10.35	135.22 ± 3.92
single t	6294.76 ± 22.06	4358.25 ± 18.09	1049.82 ± 8.69
DY+Jets$\rightarrow \ell\ell$	2788.03 ± 265.88	518.67 ± 91.55	43.46 ± 34.35
W+Jets$\rightarrow \ell\nu$	315.30 ± 27.79	51.68 ± 10.43	4.91 ± 3.17
diBoson	1947.21 ± 19.46	138.08 ± 5.04	9.89 ± 1.31
$t\bar{t}+W$	223.77 ± 0.86	166.85 ± 0.73	56.97 ± 0.42
$t\bar{t}+Z$	232.05 ± 0.76	176.28 ± 0.66	68.44 ± 0.40
All Background	136634.29 ± 289.71	102829.20 ± 133.08	36425.65 ± 65.82
Data, $ee/e\mu/\mu\mu$	127684 ± 357.33	96778 ± 311.09	35435 ± 188.24
Data/MC	0.93 ± 0.00	0.94 ± 0.00	0.97 ± 0.01
1 lepton, from W	363.69 ± 28.00	72.48 ± 10.51	7.47 ± 3.20
1 lepton, from t	1554.12 ± 13.78	913.48 ± 10.43	137.58 ± 3.94
≥ 2 leptons	134537.10 ± 288.03	101705.95 ± 132.26	36225.69 ± 65.62
$Z \rightarrow \nu\nu$	179.38 ± 0.73	137.30 ± 0.59	54.91 ± 0.36

We also check the efficiency of our e/μ triggers using a tag-and-probe method (see Section 3.5.3) in the $E_{\mathrm{T}}^{\mathrm{miss}}$ dataset. We measure the efficiency in both leading and trailing lepton p_T, as well as overall, and find in essentially all cases an efficiency of 0.86 ± 0.003.

Kinematic Checks

We compare the data and Monte Carlo distributions for a number of variables in our crosscheck regions. In general, we find fairly good agreement for number of jets, number of b-tags, and jet p_T, as shown in Figure A.1.

However, the $E_{\mathrm{T}}^{\mathrm{miss}}$ distribution in Figure A.1 shows significant disagreement in the last two bins. This discrepancy must be corrected, because we perform $E_{\mathrm{T}}^{\mathrm{miss}}$ extrapolation in some of our high-$E_{\mathrm{T}}^{\mathrm{miss}}$ control regions (see Section 4.8.1), and a disagreement between data and MC would skew our background estimate in those regions.

To correct the disagreement, we calculate the data/MC ratio in each $E_{\mathrm{T}}^{\mathrm{miss}}$ bin, as well as the data/MC ratio in our merged $E_{\mathrm{T}}^{\mathrm{miss}}$ bins used in the extrapolation. We rescale our Monte Carlo events so that the ratio in the individual bin equals the ratio in the merged bin. Because we only perform $E_{\mathrm{T}}^{\mathrm{miss}}$ extrapolation in a few $E_{\mathrm{T}}^{\mathrm{miss}}$ bins in the dilepton CRs, we only calculate and apply scale factors to $t\bar{t}$ and single-top tW events that have two leptons and that fall into one of the affected $E_{\mathrm{T}}^{\mathrm{miss}}$ bins. The uncertainties on the scale factors are used to evaluate a systematic uncertainty on the lost lepton background estimate in the bins where $E_{\mathrm{T}}^{\mathrm{miss}}$ extrapolation takes place. These scale factors and their uncertainties are presented in Table A.2.

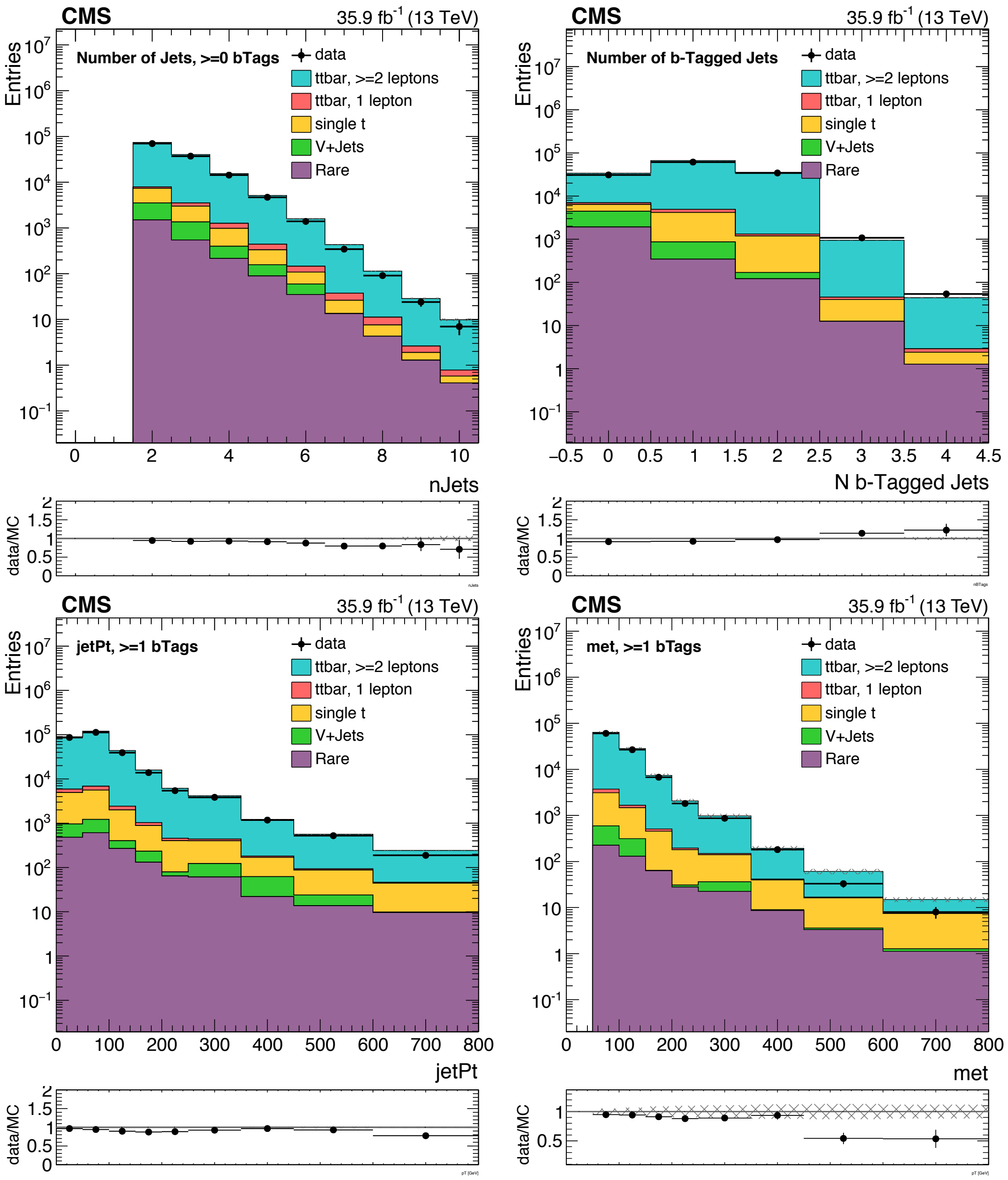

Figure A.1: Distributions of number of jets and number of b-tags in the ≥0 b-tag region, and jet p_T and $E_{\mathrm{T}}^{\mathrm{miss}}$ in the ≥1 b-tag regions. The $E_{\mathrm{T}}^{\mathrm{miss}}$ distribution contains a noticeable discrepancy in the last two bins.

Table A.2: Data and Monte Carlo yields, and yield ratios, in our $E_{\mathrm{T}}^{\mathrm{miss}}$ extrapolation regions.

Bin	Data	MC	Data/MC Norm	Scale Factor
Region B				
$450 < p_T < 800$	41 ± 6.4	75.9 ± 2.5	0.54 ± 0.09	—
$450 < p_T < 600$	33 ± 5.7	60.9 ± 2.3	0.54 ± 0.09	1.00 ± 0.24
$600 < p_T < 800$	8 ± 2.8	15.0 ± 1.1	0.54 ± 0.09	0.99 ± 0.39
Region E				
$350 < p_T < 800$	222 ± 14.9	269.4 ± 4.8	0.82 ± 0.06	—
$350 < p_T < 550$	209 ± 14.5	244.1 ± 4.5	0.82 ± 0.06	1.04 ± 0.10
$550 < p_T < 800$	13 ± 3.6	25.3 ± 1.4	0.82 ± 0.06	0.62 ± 0.18
Region F, H				
$250 < p_T < 800$	1092 ± 33.0	1246.5 ± 14.6	0.88 ± 0.03	—
$250 < p_T < 450$	1051 ± 32.4	1170.6 ± 14.4	0.88 ± 0.03	1.02 ± 0.05
$450 < p_T < 800$	41 ± 6.4	75.9 ± 2.5	0.88 ± 0.03	0.62 ± 0.10

Appendix B

$E_{\mathrm{T}}^{\mathrm{miss}}$ Resolution Studies

As various sections of Chapter 4 have noted, our Monte Carlo simulations may not do a perfect job reproducing the resolution of $E_{\mathrm{T}}^{\mathrm{miss}}$ reconstruction seen in actual data events. Such a shape difference has the potential to skew several of our background estimates. Mismodeling of the $E_{\mathrm{T}}^{\mathrm{miss}}$ resolution would be felt most strongly in the lost lepton background estimate. As Section 4.8.1 describes, we extrapolate from larger, merged $E_{\mathrm{T}}^{\mathrm{miss}}$ bins down to narrower, individual $E_{\mathrm{T}}^{\mathrm{miss}}$ bins. If the $E_{\mathrm{T}}^{\mathrm{miss}}$ resolution is not correctly modeled, this extrapolation may cause considerable migration of events between $E_{\mathrm{T}}^{\mathrm{miss}}$ bins. In addition, $E_{\mathrm{T}}^{\mathrm{miss}}$ resolution effects determine how many $t\bar{t} \to 1\ell$ events pass our M_{T} cut, thus affecting our single lepton from top estimate. And finally, $E_{\mathrm{T}}^{\mathrm{miss}}$ resolution plays an important role in estimating our single lepton from W background, because the W+jets process has a steeply falling $E_{\mathrm{T}}^{\mathrm{miss}}$ spectrum.

To correct the $E_{\mathrm{T}}^{\mathrm{miss}}$ resolution in our Monte Carlo simulations, and derive systematic uncertainties on this correction, we study $E_{\mathrm{T}}^{\mathrm{miss}}$ resolution effects using a sample of photon+jets events. Photons are generally well-measured within CMS. So if we treat photons as an analogue for neutrinos, we can model $E_{\mathrm{T}}^{\mathrm{miss}}$ using visible particles instead.

We begin by defining two analogous samples. As a sample of real $E_{\mathrm{T}}^{\mathrm{miss}}$, we select events from $t\bar{t} \to 1\ell$ and 2ℓ MC samples. We require a relatively loose cut of $E_{\mathrm{T}}^{\mathrm{miss}} > 55$ GeV, and accept

$\geq$0 b-tags. To be our $E_{\mathrm{T}}^{\mathrm{miss}}$ analogues, we select γ+jets events from simulation, as well as from data. The data are selected from the single photon datasets listed in Table 4.1, using the single photon triggers listed in Table 4.2. For these photon events, we require photon $p_T > 55$ GeV (motivated by triggers) and exactly 0 b-tags (to remove the influence of neutrinos produced in leptonic b-hadron decays). We select photons using the tight photon ID provided by the EGamma POG within CMS. We also account for trigger prescales.

From the $t\bar{t} \rightarrow 1\ell$ and 2ℓ samples, we extract the generator-level p_T spectrum of the single or double neutrinos. We normalize this spectrum and divide it by the normalized spectrum of the photon p_T, for both photon data and MC separately. This gives us a weighting function parameterized in p_T. We apply this weighting function to the photon data and MC samples, and plot a modified form of $E_{\mathrm{T}}^{\mathrm{miss}}$, defined to be the natural $E_{\mathrm{T}}^{\mathrm{miss}}$ in the events added vectorially to the p_T of the photon:

$$E_{\mathrm{T,mod}}^{\mathrm{miss}} = |\vec{E}_{\mathrm{T}}^{\mathrm{miss}} + \vec{p}_{\mathrm{T}}^{\gamma}| \tag{B.1}$$

Figure B.1 shows that the spectrum of $E_{\mathrm{T,mod}}^{\mathrm{miss}}$ looks considerably different with and without this reweighting to the neutrino p_T, indicating that the reweighting function is far from flat. Figure B.2 shows how the $E_{\mathrm{T,mod}}^{\mathrm{miss}}$ spectra compare between data and MC. Comparing the bottom ratio plots in each case, we can see that reweighting simulation to the true $E_{\mathrm{T}}^{\mathrm{miss}}$ spectrum is a much larger effect than the discrepancy between data and MC due to $E_{\mathrm{T}}^{\mathrm{miss}}$ resolution effects.

From the distributions of Figure B.2, we calculate the ratio of the number of events in a single $E_{\mathrm{T}}^{\mathrm{miss}}$ bin to the number of events in an inclusive $E_{\mathrm{T}}^{\mathrm{miss}}$ bin (i.e. $E_{\mathrm{T}}^{\mathrm{miss}} > 250$ GeV). We then define a $E_{\mathrm{T}}^{\mathrm{miss}}$ resolution scale factor, with associated errors, equal to the bin ratio in data divided by the bin ratio in Monte Carlo:

$$\mathrm{SF}_{\mathrm{MET\ res.}} = \frac{N_{\mathrm{bin}}/N_{\mathrm{inclusive}}(\mathrm{data})}{N_{\mathrm{bin}}/N_{\mathrm{inclusive}}(\mathrm{MC})} \tag{B.2}$$

The values and uncertainties of these scale factors in each bin are given in Table B.1. We apply

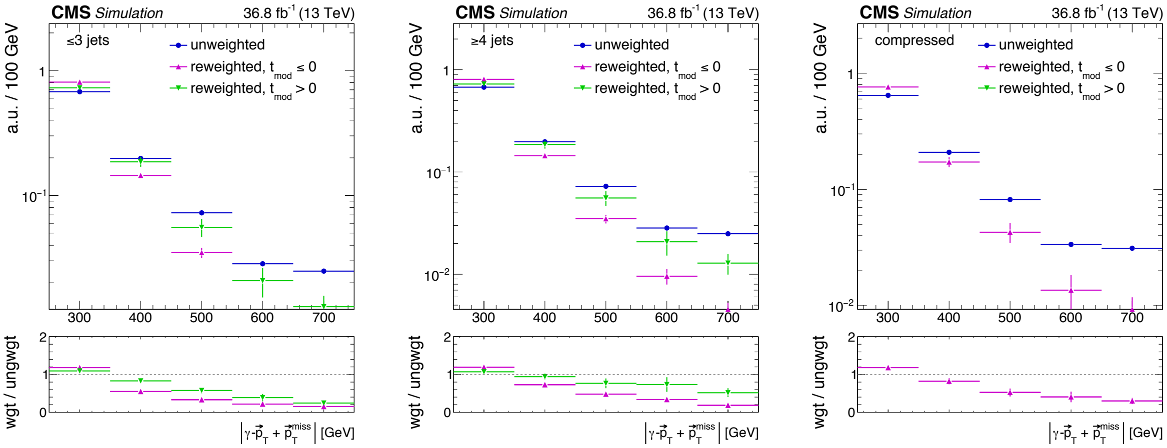

Figure B.1: Normalized distributions of $E_{\mathrm{T,mod}}^{\mathrm{miss}}$ in photon MC, before and after reweighting to the $t\bar{t}$ neutrino p_T spectrum. The plot at left shows a 2-3 jet region, at center a $\geq$4 jet region, and at right a $\geq$5 jet region.

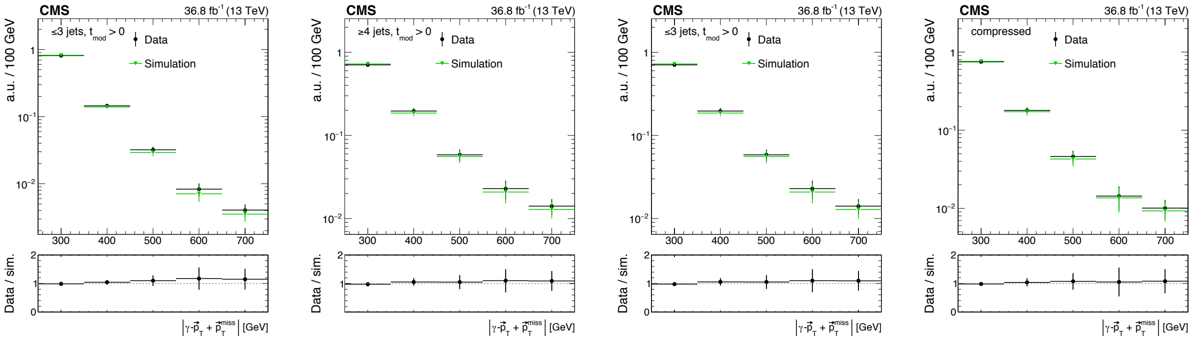

Figure B.2: Comparison of $E_{\mathrm{T,mod}}^{\mathrm{miss}}$ shapes in photon data and MC. The first plot shows a 2-3 jet region, the second shows $\geq$4 jets with t_{mod} $\leq$0, the third $\geq$4 jets with t_{mod} >0, and the last shows a $\geq$5 jet region.

these scale factors to all events in the $t\bar{t} \to 1\ell$, $t\bar{t} \to \ell\ell$, single top tW, and W+Jets Monte Carlo samples. Note that because the corridor signal regions overlap with the nominal signal regions, some events receive different weights when considered in a nominal SR versus in a corridor SR.

Table B.1: Scale factors derived to correct $E_{\mathrm{T}}^{\mathrm{miss}}$ resolution for each of our signal regions. The uncertainties are derived from the statistical uncertainties on the photon data and Monte Carlo.

Region	$\mathrm{SF}_{\mathrm{MET\ res.}}$
< 4 jets, $t_{\mathrm{mod}} \geq 10$, $M_{\ell b} < 175$, $250 < E_{\mathrm{T}}^{\mathrm{miss}} < 350$	0.99 ± 0.02
< 4 jets, $t_{\mathrm{mod}} \geq 10$, $M_{\ell b} < 175$, $350 < E_{\mathrm{T}}^{\mathrm{miss}} < 450$	1.04 ± 0.06
< 4 jets, $t_{\mathrm{mod}} \geq 10$, $M_{\ell b} < 175$, $450 < E_{\mathrm{T}}^{\mathrm{miss}} < 600$	1.11 ± 0.12
< 4 jets, $t_{\mathrm{mod}} \geq 10$, $M_{\ell b} < 175$, $E_{\mathrm{T}}^{\mathrm{miss}} > 600$	1.17 ± 0.23
< 4 jets, $t_{\mathrm{mod}} \geq 10$, $M_{\ell b} \geq 175$, $250 < E_{\mathrm{T}}^{\mathrm{miss}} < 450$	1.00 ± 0.02
< 4 jets, $t_{\mathrm{mod}} \geq 10$, $M_{\ell b} \geq 175$, $450 < E_{\mathrm{T}}^{\mathrm{miss}} < 650$	1.11 ± 0.12
< 4 jets, $t_{\mathrm{mod}} \geq 10$, $M_{\ell b} \geq 175$, $E_{\mathrm{T}}^{\mathrm{miss}} > 600$	1.17 ± 0.23
≥ 4 jets, $t_{\mathrm{mod}} < 0.0$, $M_{\ell b} < 175$, $250 < E_{\mathrm{T}}^{\mathrm{miss}} < 350$	0.99 ± 0.02
≥ 4 jets, $t_{\mathrm{mod}} < 0.0$, $M_{\ell b} < 175$, $350 < E_{\mathrm{T}}^{\mathrm{miss}} < 450$	1.05 ± 0.05
≥ 4 jets, $t_{\mathrm{mod}} < 0.0$, $M_{\ell b} < 175$, $450 < E_{\mathrm{T}}^{\mathrm{miss}} < 550$	1.07 ± 0.10
≥ 4 jets, $t_{\mathrm{mod}} < 0.0$, $M_{\ell b} < 175$, $550 < E_{\mathrm{T}}^{\mathrm{miss}} < 650$	1.10 ± 0.18
≥ 4 jets, $t_{\mathrm{mod}} < 0.0$, $M_{\ell b} < 175$, $E_{\mathrm{T}}^{\mathrm{miss}} > 650$	1.14 ± 0.18
≥ 4 jets, $t_{\mathrm{mod}} < 0.0$, $M_{\ell b} \geq 175$, $250 < E_{\mathrm{T}}^{\mathrm{miss}} < 350$	0.99 ± 0.02
≥ 4 jets, $t_{\mathrm{mod}} < 0.0$, $M_{\ell b} \geq 175$, $350 < E_{\mathrm{T}}^{\mathrm{miss}} < 450$	1.05 ± 0.05
≥ 4 jets, $t_{\mathrm{mod}} < 0.0$, $M_{\ell b} \geq 175$, $450 < E_{\mathrm{T}}^{\mathrm{miss}} < 550$	1.07 ± 0.10
≥ 4 jets, $t_{\mathrm{mod}} < 0.0$, $M_{\ell b} \geq 175$, $E_{\mathrm{T}}^{\mathrm{miss}} > 550$	1.11 ± 0.14
≥ 4 jets, $0.0 < t_{\mathrm{mod}} < 10$, $M_{\ell b} < 175$, $250 < E_{\mathrm{T}}^{\mathrm{miss}} < 350$	0.98 ± 0.04
≥ 4 jets, $0.0 < t_{\mathrm{mod}} < 10$, $M_{\ell b} < 175$, $350 < E_{\mathrm{T}}^{\mathrm{miss}} < 550$	1.06 ± 0.08
≥ 4 jets, $0.0 < t_{\mathrm{mod}} < 10$, $M_{\ell b} < 175$, $E_{\mathrm{T}}^{\mathrm{miss}} > 550$	1.10 ± 0.19
≥ 4 jets, $0.0 < t_{\mathrm{mod}} < 10$, $M_{\ell b} \geq 175$, $250 < E_{\mathrm{T}}^{\mathrm{miss}} < 450$	0.99 ± 0.04
≥ 4 jets, $0.0 < t_{\mathrm{mod}} < 10$, $M_{\ell b} \geq 175$, $E_{\mathrm{T}}^{\mathrm{miss}} > 450$	1.07 ± 0.13
≥ 4 jets, $t_{\mathrm{mod}} \geq 10$, $M_{\ell b} < 175$, $250 < E_{\mathrm{T}}^{\mathrm{miss}} < 350$	0.98 ± 0.04
≥ 4 jets, $t_{\mathrm{mod}} \geq 10$, $M_{\ell b} < 175$, $350 < E_{\mathrm{T}}^{\mathrm{miss}} < 450$	1.06 ± 0.09
≥ 4 jets, $t_{\mathrm{mod}} \geq 10$, $M_{\ell b} < 175$, $450 < E_{\mathrm{T}}^{\mathrm{miss}} < 600$	1.07 ± 0.15
≥ 4 jets, $t_{\mathrm{mod}} \geq 10$, $M_{\ell b} < 175$, $E_{\mathrm{T}}^{\mathrm{miss}} > 600$	1.08 ± 0.22
≥ 4 jets, $t_{\mathrm{mod}} \geq 10$, $M_{\ell b} \geq 175$, $250 < E_{\mathrm{T}}^{\mathrm{miss}} < 450$	0.99 ± 0.04
≥ 4 jets, $t_{\mathrm{mod}} \geq 10$, $M_{\ell b} \geq 175$, $E_{\mathrm{T}}^{\mathrm{miss}} > 450$	1.07 ± 0.13
Compressed search, $250 < E_{\mathrm{T}}^{\mathrm{miss}} < 350$	0.98 ± 0.05
Compressed search, $350 < E_{\mathrm{T}}^{\mathrm{miss}} < 450$	1.04 ± 0.10
Compressed search, $450 < E_{\mathrm{T}}^{\mathrm{miss}} < 550$	1.07 ± 0.20
Compressed search, $E_{\mathrm{T}}^{\mathrm{miss}} > 550$	1.07 ± 0.24

References

[1] D. J. Griffiths, "Introduction to Elementary Particles". Wiley VCH, second edition, 2008.

[2] J. Woithe, G. J. Wiener, and F. F. Van der Veken, "Lets have a coffee with the Standard Model of particle physics!", *Phys. Educ.* **52** (2017), no. 3, 034001, doi:10.1088/1361-6552/aa5b25.

[3] Particle Data Group Collaboration, "Review of Particle Physics", *Chin. Phys.* **C40** (2016), no. 10, 100001, doi:10.1088/1674-1137/40/10/100001.

[4] S. Durr et al., "Ab-Initio Determination of Light Hadron Masses", *Science* **322** (2008) 1224–1227, doi:10.1126/science.1163233, arXiv:0906.3599.

[5] F. Englert and R. Brout, "Broken Symmetry and the Mass of Gauge Vector Mesons", *Phys. Rev. Lett.* **13** (1964) 321–323, doi:10.1103/PhysRevLett.13.321.

[6] P. W. Higgs, "Broken Symmetries and the Masses of Gauge Bosons", *Phys. Rev. Lett.* **13** (1964) 508–509, doi:10.1103/PhysRevLett.13.508.

[7] G. S. Guralnik, C. R. Hagen, and T. W. B. Kibble, "Global Conservation Laws and Massless Particles", *Phys. Rev. Lett.* **13** (1964) 585–587, doi:10.1103/PhysRevLett.13.585.

[8] ATLAS, CMS Collaboration, "Combined Measurement of the Higgs Boson Mass in pp Collisions at $\sqrt{s} = 7$ and 8 TeV with the ATLAS and CMS Experiments", *Phys. Rev. Lett.* **114** (2015) 191803, doi:10.1103/PhysRevLett.114.191803, arXiv:1503.07589.

[9] S. P. Martin, "A Supersymmetry primer", doi:10.1142/9789812839657_0001,10.1142/9789814307505_0001, arXiv:hep-ph/9709356. [Adv. Ser. Direct. High Energy Phys.18,1(1998)].

[10] R. N. Cahn, "The Eighteen arbitrary parameters of the standard model in your everyday life", *Rev. Mod. Phys.* **68** (1996) 951–960, doi:10.1103/RevModPhys.68.951.

[11] G. Bertone and D. Hooper, "A History of Dark Matter", *Submitted to: Rev. Mod. Phys.* (2016) arXiv:1605.04909.

[12] Planck Collaboration, "Planck 2013 results. I. Overview of products and scientific results", *Astron. Astrophys.* **571** (2014) A1, doi:10.1051/0004-6361/201321529, arXiv:1303.5062.

[13] Supernova Cosmology Project Collaboration, “Measurements of Omega and Lambda from 42 high redshift supernovae”, *Astrophys. J.* **517** (1999) 565–586, doi:10.1086/307221, arXiv:astro-ph/9812133.

[14] Supernova Search Team Collaboration, “Observational evidence from supernovae for an accelerating universe and a cosmological constant”, *Astron. J.* **116** (1998) 1009–1038, doi:10.1086/300499, arXiv:astro-ph/9805201.

[15] E. J. Copeland, M. Sami, and S. Tsujikawa, “Dynamics of dark energy”, *Int. J. Mod. Phys.* **D15** (2006) 1753–1936, doi:10.1142/S021827180600942X, arXiv:hep-th/0603057.

[16] R. Davis, Jr., D. S. Harmer, and K. C. Hoffman, “Search for neutrinos from the sun”, *Phys. Rev. Lett.* **20** (1968) 1205–1209, doi:10.1103/PhysRevLett.20.1205.

[17] K. Lande, B. T. Cleveland, T. Daily, R. Davis, J. Distel, C. K. Lee, A. Weinberger, P. Wildenhain, and J. Ullman, “Solar neutrino observations with the Homestake ^{37}Cl detector”, *AIP Conf. Proc.* **243** (1992) 1122–1133, doi:10.1063/1.41548.

[18] SNO Collaboration, “Measurement of the rate of $\nu_e + d \rightarrow p + p + e^-$ interactions produced by ^8B solar neutrinos at the Sudbury Neutrino Observatory”, *Phys. Rev. Lett.* **87** (2001) 071301, doi:10.1103/PhysRevLett.87.071301, arXiv:nucl-ex/0106015.

[19] SNO Collaboration, “Direct evidence for neutrino flavor transformation from neutral current interactions in the Sudbury Neutrino Observatory”, *Phys. Rev. Lett.* **89** (2002) 011301, doi:10.1103/PhysRevLett.89.011301, arXiv:nucl-ex/0204008.

[20] Super-Kamiokande Collaboration, “Evidence for oscillation of atmospheric neutrinos”, *Phys. Rev. Lett.* **81** (1998) 1562–1567, doi:10.1103/PhysRevLett.81.1562, arXiv:hep-ex/9807003.

[21] M. C. Gonzalez-Garcia and M. Maltoni, “Phenomenology with Massive Neutrinos”, *Phys. Rept.* **460** (2008) 1–129, doi:10.1016/j.physrep.2007.12.004, arXiv:0704.1800.

[22] G. Jungman, M. Kamionkowski, and K. Griest, “Supersymmetric dark matter”, *Phys. Rept.* **267** (1996) 195–373, doi:10.1016/0370-1573(95)00058-5, arXiv:hep-ph/9506380.

[23] L. Evans and P. Bryant, “LHC Machine”, *JINST* **3** (2008) S08001, doi:10.1088/1748-0221/3/08/S08001.

[24] CERN Media and Press Relations, “Photos and images”. Accessed May 2018. http://press.cern/multimedia/photos-images.

[25] CMS Collaboration, “The CMS Experiment at the CERN LHC”, *JINST* **3** (2008) S08004, doi:10.1088/1748-0221/3/08/S08004.

[26] CMS Collaboration, “Detector | CMS Experiment”. Accessed May 24, 2018. https://cms.cern/detector.

[27] CMS Collaboration, G. L. Bayatian et al., "CMS Physics: Technical Design Report Volume 1: Detector Performance and Software". Technical Design Report CMS. CERN, Geneva, 2006.

[28] CMS Collaboration, "Particle-flow reconstruction and global event description with the CMS detector", *JINST* **12** (2017), no. 10, P10003, doi:10.1088/1748-0221/12/10/P10003, arXiv:1706.04965.

[29] R. Voss and A. Breskin, eds., "The CERN Large Hadron Collider, accelerator and experiments". CERN, Geneva, 2009.

[30] D. A. Matzner Dominguez, D. Abbaneo, K. Arndt, N. Bacchetta, A. Ball, E. Bartz, W. Bertl, G. M. Bilei, G. Bolla, H. W. K. Cheung et al., "CMS Technical Design Report for the Pixel Detector Upgrade", Technical Report CERN-LHCC-2012-016. CMS-TDR-11, CERN, 2012. doi:10.2172/1151650.

[31] L. Taylor, "Muon drift tubes", 11, 2011. Accessed May 9, 2018. http://cms.web.cern.ch/news/muon-drift-tubes.

[32] L. Taylor, "Cathode strip chambers", 11, 2011. Accessed May 9, 2018. http://cms.web.cern.ch/news/cathode-strip-chambers.

[33] L. Taylor, "Resistive plate chambers", 11, 2011. Accessed May 9, 2018. http://cms.web.cern.ch/news/resistive-plate-chambers.

[34] CMS Collaboration, "The CMS trigger system", *JINST* **12** (2017), no. 01, P01020, doi:10.1088/1748-0221/12/01/P01020, arXiv:1609.02366.

[35] W. Adam, B. Mangano, T. Speer, and T. Todorov, "Track reconstruction in the CMS tracker", Technical Report CERN-CMS-NOTE-2006-041, CMS-NOTE-2006-041, CERN, 2005.

[36] S. Cucciarelli, M. Konecki, D. Kotlinski, and T. Todorov, "Track reconstruction, primary vertex finding and seed generation with the pixel detector", Technical Report CERN-CMS-NOTE-2006-026, CERN, 2006.

[37] M. Cacciari, G. P. Salam, and G. Soyez, "The Anti-k(t) jet clustering algorithm", *JHEP* **04** (2008) 063, doi:10.1088/1126-6708/2008/04/063, arXiv:0802.1189.

[38] CMS Collaboration, "Identification of b-quark jets with the CMS experiment", *JINST* **8** (2013) P04013, doi:10.1088/1748-0221/8/04/P04013, arXiv:1211.4462.

[39] CMS Collaboration, "Identification of heavy-flavour jets with the CMS detector in pp collisions at 13 TeV", *JINST* **13** (2018), no. 05, P05011, doi:10.1088/1748-0221/13/05/P05011, arXiv:1712.07158.

[40] J. Alwall, R. Frederix, S. Frixione, V. Hirschi, F. Maltoni, O. Mattelaer, H. S. Shao, T. Stelzer, P. Torrielli, and M. Zaro, “The automated computation of tree-level and next-to-leading order differential cross sections, and their matching to parton shower simulations”, *JHEP* **07** (2014) 079, doi:10.1007/JHEP07(2014)079, arXiv:1405.0301.

[41] S. Alioli, P. Nason, C. Oleari, and E. Re, “A general framework for implementing NLO calculations in shower Monte Carlo programs: the POWHEG BOX”, *JHEP* **06** (2010) 043, doi:10.1007/JHEP06(2010)043, arXiv:1002.2581.

[42] T. Sjöstrand, S. Ask, J. R. Christiansen, R. Corke, N. Desai, P. Ilten, S. Mrenna, S. Prestel, C. O. Rasmussen, and P. Z. Skands, “An Introduction to PYTHIA 8.2”, *Comput. Phys. Commun.* **191** (2015) 159–177, doi:10.1016/j.cpc.2015.01.024, arXiv:1410.3012.

[43] GEANT4 Collaboration, “GEANT4: A Simulation toolkit”, *Nucl. Instrum. Meth.* **A506** (2003) 250–303, doi:10.1016/S0168-9002(03)01368-8.

[44] A. Giammanco, “The Fast Simulation of the CMS Experiment”, *J. Phys. Conf. Ser.* **513** (2014) 022012, doi:10.1088/1742-6596/513/2/022012.

[45] CMS Collaboration, “Measurements of $t\bar{t}$ charge asymmetry using dilepton final states in pp collisions at $\sqrt{s} = 8$ TeV”, *Phys. Lett.* **B760** (2016) 365–386, doi:10.1016/j.physletb.2016.07.006, arXiv:1603.06221.

[46] CMS Collaboration, “Measurements of t t-bar spin correlations and top quark polarization using dilepton final states in pp collisions at sqrt(s) = 8 TeV”, *Phys. Rev.* **D93** (2016), no. 5, 052007, doi:10.1103/PhysRevD.93.052007, arXiv:1601.01107.

[47] G. Mahlon and S. J. Parke, “Spin Correlation Effects in Top Quark Pair Production at the LHC”, *Phys. Rev.* **D81** (2010) 074024, doi:10.1103/PhysRevD.81.074024, arXiv:1001.3422.

[48] J. Ellis, “TikZ-Feynman: Feynman diagrams with TikZ”, *Comput. Phys. Commun.* **210** (2017) 103–123, doi:10.1016/j.cpc.2016.08.019, arXiv:1601.05437.

[49] CDF Collaboration, “Evidence for a Mass Dependent Forward-Backward Asymmetry in Top Quark Pair Production”, *Phys. Rev.* **D83** (2011) 112003, doi:10.1103/PhysRevD.83.112003, arXiv:1101.0034.

[50] D0 Collaboration, “Forward-backward asymmetry in top quark-antiquark production”, *Phys. Rev.* **D84** (2011) 112005, doi:10.1103/PhysRevD.84.112005, arXiv:1107.4995.

[51] CDF Collaboration, “Measurement of the top quark forward-backward production asymmetry and its dependence on event kinematic properties”, *Phys. Rev.* **D87** (2013), no. 9, 092002, doi:10.1103/PhysRevD.87.092002, arXiv:1211.1003.

[52] D0 Collaboration, “Measurement of the forward-backward asymmetry in top quark-antiquark production in ppbar collisions using the lepton+jets channel”, *Phys. Rev.* **D90** (2014) 072011, doi:10.1103/PhysRevD.90.072011, arXiv:1405.0421.

[53] CDF Collaboration, "Measurement of $t\bar{t}$ Spin Correlation in $p\bar{p}$ Collisions Using the CDF II Detector at the Tevatron", *Phys. Rev.* **D83** (2011) 031104, doi:10.1103/PhysRevD.83.031104, arXiv:1012.3093.

[54] D0 Collaboration, "Evidence for spin correlation in $t\bar{t}$ production", *Phys. Rev. Lett.* **108** (2012) 032004, doi:10.1103/PhysRevLett.108.032004, arXiv:1110.4194.

[55] D0 Collaboration, "Measurement of spin correlation in $t\bar{t}$ production using a matrix element approach", *Phys. Rev. Lett.* **107** (2011) 032001, doi:10.1103/PhysRevLett.107.032001, arXiv:1104.5194.

[56] D0 Collaboration, "Measurement of Leptonic Asymmetries and Top Quark Polarization in $t\bar{t}$ Production", *Phys. Rev.* **D87** (2013), no. 1, 011103, doi:10.1103/PhysRevD.87.011103, arXiv:1207.0364.

[57] ATLAS Collaboration, "Measurement of Top Quark Polarization in Top-Antitop Events from Proton-Proton Collisions at $\sqrt{s} = 7$ TeV Using the ATLAS Detector", *Phys. Rev. Lett.* **111** (2013), no. 23, 232002, doi:10.1103/PhysRevLett.111.232002, arXiv:1307.6511.

[58] ATLAS Collaboration, "Measurement of Spin Correlation in Top-Antitop Quark Events and Search for Top Squark Pair Production in pp Collisions at $\sqrt{s} = 8$ TeV Using the ATLAS Detector", *Phys. Rev. Lett.* **114** (2015), no. 14, 142001, doi:10.1103/PhysRevLett.114.142001, arXiv:1412.4742.

[59] W. Bernreuther and Z.-G. Si, "Top quark spin correlations and polarization at the LHC: standard model predictions and effects of anomalous top chromo moments", *Phys. Lett.* **B725** (2013) 115–122, doi:10.1016/j.physletb.2013.06.051,10.1016/j.physletb.2015.03.035, arXiv:1305.2066. [Erratum: Phys. Lett.B744,413(2015)].

[60] CMS Collaboration, "Search for top-squark pair production in the single-lepton final state in pp collisions at $\sqrt{s}$ = 8 TeV", *Eur. Phys. J.* **C73** (2013), no. 12, 2677, doi:10.1140/epjc/s10052-013-2677-2, arXiv:1308.1586.

[61] B. A. Betchart, R. Demina, and A. Harel, "Analytic solutions for neutrino momenta in decay of top quarks", *Nucl. Instrum. Meth.* **A736** (2014) 169–178, doi:10.1016/j.nima.2013.10.039, arXiv:1305.1878.

[62] CMS Collaboration, "Observation of the associated production of a single top quark and a W boson in pp collisions at $\sqrt{s}$ =8 TeV", *Phys. Rev. Lett.* **112** (2014), no. 23, 231802, doi:10.1103/PhysRevLett.112.231802, arXiv:1401.2942.

[63] G. Cowan, "A survey of unfolding methods for particle physics", in *Advanced Statistical Techniques in Particle Physics. Proceedings, Conference, Durham, UK, March 18-22, 2002*, volume C0203181, pp. 248–257. 2002.

[64] V. Blobel, "Unfolding for HEP experiments: Introduction to inverse problems.", (June, 2008). DESY computing seminar. http://www.desy.de/~blobel/itunfold.pdf.

[65] S. Schmitt, "TUnfold: an algorithm for correcting migration effects in high energy physics", *JINST* **7** (2012) T10003, doi:10.1088/1748-0221/7/10/T10003, arXiv:1205.6201.

[66] M. Botje et al., "The PDF4LHC Working Group Interim Recommendations", arXiv:1101.0538.

[67] CMS Collaboration, "Search for top squark pair production in pp collisions at $\sqrt{s} = 13$ TeV using single lepton events", *JHEP* **10** (2017) 019, doi:10.1007/JHEP10(2017)019, arXiv:1706.04402.

[68] CMS Collaboration, "Searches for pair production of third-generation squarks in $\sqrt{s} =$ 13 TeV pp collisions", *Eur. Phys. J.* **C77** (2017), no. 5, 327, doi:10.1140/epjc/s10052-017-4853-2, arXiv:1612.03877.

[69] CMS Collaboration, "Search for direct top squark pair production in the single lepton final state at $\sqrt{s} = 13$ TeV",. CMS-PAS-SUS-16-028.

[70] CMS Collaboration, "Search for direct top squark pair production in the single lepton final state at $\sqrt{s} = 13$ TeV",. CMS-PAS-SUS-16-002.

[71] ATLAS Collaboration, "Search for top-squark pair production in final states with one lepton, jets, and missing transverse momentum using 36 fb^{-1} of $\sqrt{s} = 13$ TeV pp collision data with the ATLAS detector", arXiv:1711.11520.

[72] M. L. Graesser and J. Shelton, "Hunting Mixed Top Squark Decays", *Phys. Rev. Lett.* **111** (2013), no. 12, 121802, doi:10.1103/PhysRevLett.111.121802, arXiv:1212.4495.

[73] CMS Collaboration, "Search for new phenomena with the M_{T2} variable in the all-hadronic final state produced in protonproton collisions at $\sqrt{s} = 13$ TeV", *Eur. Phys. J.* **C77** (2017), no. 10, 710, doi:10.1140/epjc/s10052-017-5267-x, arXiv:1705.04650.

[74] NNPDF Collaboration, "Parton distributions for the LHC Run II", *JHEP* **04** (2015) 040, doi:10.1007/JHEP04(2015)040, arXiv:1410.8849.

[75] CMS Collaboration, "Search for SUSY in same-sign dilepton events at 13 TeV",. CMS-PAS-SUS-16-020.

[76] ATLAS, CMS, LHC Higgs Combination Group Collaboration, "Procedure for the LHC Higgs boson search combination in summer 2011", Technical Report ATL-PHYS-PUB-2011-011, CMS-NOTE-2011-005, CERN, 2011.

[77] T. Junk, "Confidence level computation for combining searches with small statistics", *Nucl. Instrum. Meth.* **A434** (1999) 435–443, doi:10.1016/S0168-9002(99)00498-2, arXiv:hep-ex/9902006.

[78] A. L. Read, "Presentation of search results: The CL(s) technique", *J. Phys.* **G28** (2002) 2693–2704, doi:10.1088/0954-3899/28/10/313.

[79] G. Cowan, K. Cranmer, E. Gross, and O. Vitells, “Asymptotic formulae for likelihood-based tests of new physics”, *Eur. Phys. J.* **C71** (2011) 1554, doi:10.1140/epjc/s10052-011-1554-0,10.1140/epjc/s10052-013-2501-z, arXiv:1007.1727. [Erratum: Eur. Phys. J.C73,2501(2013)].